Experimental investigation and numerical modeling of plasma and laser microwelding processes

Mayuri Baruah

Department of Mechanical Engineering

Indian Institute of Technology Guwahati

January 2017

Experimental investigation and numerical modeling of plasma and laser microwelding processes

submitted in partial fulfillment of the requirements
for the degree of

Doctor of Philosophy

by

Mayuri Baruah

(11610311)

Supervisor:

Swarup Bag

Department of Mechanical Engineering

Indian Institute of Technology Guwahati

January 2017

Dedicated to

My father, sister, brother,

my teachers and my friends

Department of Mechanical Engineering
Indian Institute of Technology Guwahati
Guwahati-781039
INDIA

CERTIFICATE

It is certified that the work contained in the thesis entitled **"Experimental investigation and numerical modeling of plasma and laser microwelding processes"** submitted by **Miss. Mayuri Baruah** to the Indian Institute of Technology Guwahati for the award of the degree of doctor of Philosophy has been carried out under my supervision in the Department of Mechanical Engineering, Indian Institute of Technology Guwahati. This work has not been submitted elsewhere for the award of any other degree or diploma.

The thesis, in my opinion, has reached the standard fulfilling the requirements for the award of degree of Doctor of Philosophy in accordance with the regulations of the Institute.

Date: 9th January, 2017

Swarup Bag

Department of Mechanical Engineering, Indian Institute of Technology Guwahati, Guwahati, Assam 781039, India

Declaration

I declare that the present written submission is my thoughts in my own words. I have adequately been cited and referenced the original sources, where others' ideas have been involved. I also declare that I have followed to all principles of academic morality and honesty and have not neither fabricated nor falsified any idea/data in the present thesis. I realize that any defilement of the above will be cause for disciplinary action by the Institute and can also induce disciplinary action from the sources which have thus not been properly cited.

(Mayuri Baruah)

Date: 9th January, 2017 Roll No: 11610311

Abstract

Material joining at micro or nano scale is an essential and important aspect of manufacturing and assembly. In the growing technological field like micro-electro-mechanical systems (MEMS) and biomedical devices, the microwelding has potential application as encapsulation of miniature components. Adaptation or modification of new methodology brings the flexibility in microscale welding process with reduced defects and sound quality. However, the feasibility of microwelding depends on controlled and regulated heat source for manufacturing various miniature components. Micro plasma arc is one of such low cost but intense heat sources that have been successfully employed in microwelding of different materials. Laser processing offers unique advantages over other micro-fabrication techniques on account of its versatility, better control by selective range of pulse parameters. However, it is quite challenging task to achieve a defect-free joint in fusion welding because the complexity increases many folds with reduced thickness of the materials. On the other hand, understanding the synergistic interaction of the physical phenomena during microwelding of various materials is of practical significance. In this regards, a sophisticated mathematical model of microwelding is ever demanding since experimental investigation of the same is costly, expensive, and time consuming.

This thesis work is primarily motivated to develop plasma microwelding system for butt joining of different materials and the validation of the experimental results with the development of physics based numerical model. At first the major efforts are put forward to experimentally investigate the thermo-mechanical and microstructural behavior for joining of titanium alloy, stainless steel and low carbon steel. The heat input influences the mechanical properties, microstructural characteristics and finally the weld joint quality. For the same heat input, there is significant difference in weld geometry, residual distortion, and micro hardness. A comparative study between plasma and laser microwelding on titanium alloy put forward about the fundamental advantages over the processes. Using controlled and regulated arc current, the micro plasma arc welding process is specifically designed where the weld quality is assessed by carefully controlling the process parameters and by reducing the formation of oxides. A process window in terms of welding current and speed is evaluated to predict the defect-free microwelded joint. The plasma current range of 8 – 13 A produces high quality welded joints for all the selected materials. The weld joint quality is affected by specifically designed fixture that controls the oxidation of the joint and introduces high cooling rate. In laser microwelding of titanium alloy, high peak power is actually dampen by pulsation of Nd:YAG laser cratered to use in microwelding process. The feasible range of process parameters like laser scanning speed of 3-7 mm/s and peak power of 1-5 kW produces high quality weld joint.

Quantitative prediction by a sophisticated mathematical model of microwelding process is a daunting task due to several complex issues like heat source interaction, heat conduction and convection, solidification and phase changes, non-linearity in deformation. A 3D finite element based thermo-mechanical model is developed to study various aspects of plasma and laser microwelding processes. Large deformation theory is used to predict the distortion of microwelded joint. A dedicated pulse mode of heat flux model is developed for laser heat source. To analyze the heat transfer process by an ultra-short pulse laser, the 3D finite element based numerical model is developed assuming finite speed of thermal wave propagation with two phase lags. The transient heating and cooling phenomena are also analyzed for the effect of two relaxation times, variation of pulse width, and multiple pulses. The finite element modeling of laser transmission welding is developed using contact condition that accounts all physical phenomena such as heat radiation, thermal conduction, and convection heat losses. Material flow behavior in micro weld pool influences the temperature distribution to some extent. Hence, a well-tested 3D finite element based heat transfer and fluid flow model is used to analyze the flow behavior in laser microwelding process. A harmony search-based meta-heuristic algorithm is also integrated with the physics based numerical model to identify most suitable unknown model parameters in an inverse approach within overall kernel of optimization algorithm.

Chapter 1 provides the outline of the microwelding process and recent developments of the process. The key literature review on several issues on experimental investigation and numerical modelling of microwelding along with the microstructural changes, specifically of titanium alloy, are presented in Chapter 2. The theoretical background of thermal and mechanical model, material flow, contact condition and non-Fourier heat conduction using dual phase lag effects using finite element method is presented in Chapter 3. The experimental investigation on plasma and laser microwelding in terms of mechanical properties, macro and microstructural characteristics of the weld joint is presented in Chapter 4.The quantitative results from developed numerical model are mainly presented in Chapter 5. This chapter also demonstrates the validation of the numerical model with experimentally evaluated weld-zone macrograph and residual distortion. The last chapter presents the conclusions of present work and outline of the possible directions of future work.

Keywords: Plasma microwelding, laser microwelding, non-Fourier heat conduction, laser transmission welding, hourglass heat source, finite element model, pulse laser, heat input, fluid flow, distortion, residual stress, titanium alloy, stainless steel, low carbon steel, micro hardness, Harmony search algorithm

CONTENTS

List of Figures

List of Tables

Nomenclature

Symbol	Description	Unit
C	Specific heat of the material	J/kg K
$[C]$	Heat capacity matrix	-
$[\bar{C}]$	Velocity dependent convective transport matrix	-
$[C^{th}]$	Thermal stiffness matrix	-
C_B	Per cent carbon black	-
d	Gaussian power density distribution factor	-
d_{gap}	Gap clearance	mm
d_r	Roughness between the two contacting surface	-
$d\varepsilon$	Strain components	-
$d\varepsilon^E$	Elastic strain increment	-
$d\varepsilon^p$	Plastic strain increment	-
$d\varepsilon^T$	Thermal strain increment	-
$d\varepsilon^{TRIP}$	Strain increment due to volumetric change	-
$d\varepsilon^V$	Strain increment due to transformation plasticity	-
$\{d\sigma\}$	Incremental stress	N/mm^2
Δd_n	Minimum distance between the nodes	mm
G_D	Average grain diameter	mm
G_L	Length of line drawn over grains	-
G_d	Mean line average	-
G_N	Number of grain boundaries intercepted by the lines	-
$[D^{ep}]$	Elasto-plastic matrix	-
$[D^e]$	Elastic stiffness matrix	-
$[D^p]$	Plastic stiffness matrix	-
E^T	Local slope between stress and plastic strain of the specified material	-
E_m	Melting energy per unit volume	J/mm^3
E_{pl}	Pulse Energy	J
E_{pl}^{min}	Minimum energy of laser pulse	J

Symbol	Description	Unit
$\{F^{th}\}$	Thermal load vector	-
f	von-Mises yield surface	-
F	Pulse repetition rate	Hz
$\{f_{\dot{Q}}\}$	Load vector for accommodating volumetric heat source	-
$\{f_q\}$	Load vector for accommodating surface heat flux	-
f_L	Volume fraction of liquid metal along the weld pool top surface	-
F_i	Body force component	-
g	Gravitational acceleration	mm/s^2
G	Shear modulus	K/mm
g(t)	Temporal distribution of the pulse train	-
Gr	Grashof's number	-
h	Gap conductance	W/m^2K
h_{eff}	Lumped heat transfer coefficient	W/m^2
h(t)	Temporal variation of intensity	-
[H]	Heat conduction matrix	-
$[\overline{H}]$	Convective heat loss matrix	-
I	Current	A
[K]	Viscous diffusion matrix	--
$[\hat{K}]$	Penalty Matrix	-
k_{ij}	Components of thermal conductivity	-
k_g	Conductance coefficient of the gas	
L	Latent heat of fusion	J/Kg
L_r	Weld pool radius	mm
L_b	Characteristic length for the buoyancy force in the liquid pool	mm
Ma	Marangoni number	-
[M]	Mass matrix	-

Symbol	Description	Unit
[N]	Interpolation function or shape function	-
P	Pressure	Pa
{P}	Heat flow vector	-
p	Penetration depth	mm
P_{av}	Average power	W
P_{pk}	Peak power	W
Pe	Peclet number	W
P_{total}	Total laser power	-
$\dot{Q}$	Rate of internal heat generation	-
q_s	Heat flux	W/m^2
q	Gap heat transfer	W/m^2
q_c	Gas conductance heat transfer	W/m^2
q_r	Radiation heat transfer	W/m^2
q_0	Laser intensity at the center of the beam	W/m^2
R	Reflectivity of the material	-
R_a	Reynolds number	-
$R_{S/B}$	Ratio of surface tension Reynolds number to Grashof number	-
S_o	Laser spot overlap	mm
[S]	Heat capacitance matrix	-
r_{eff}	Effective radius of the heat source	mm
t	Welding time	s
t_p	Pulse on-time	s
T	Temperature of plate	K
T_0	Atmospheric temperature	K
T_m	Melting temperature	K
T_t	Fraction of laser energy transmitted	-
t_{on}^{max}	Minimal pulse duration	ms

Symbol	Description	Unit
t_{on}^{max}	Minimal pulse duration	ms
{T}	Temperature vector	-
ΔT	Temperature drop	K
Δt_c	Critical time step	s
U	Welding velocity	mm/s
{X}	Global displacement vector	-
x_i	Cartesian co-ordinates	-
V	Voltage	Volt
{V}	Velocity vector	-
v_i	Velocity components	-
V_r	Velocity of the weld pool	mm/s
V_{ST}^{max}	Maximal velocity under the influence of surface tension force	-
V_{ST}^{max}	Magnitude of the maximum velocity due to buoyancy driven flow	-
w	Thickness of the plate	mm
W_i^c and P_i^c	Computed values of weld penetration and width	mm
W_i^e and P_i^e	Obtained values of weld penetration and width	mm
Z_t, Z_b, Z_m	Depth of hourglass heat source model	
r_t, r_b, r_m	Radial distance of hourglass heat source model	
μ	Viscosity of the molten material	Pa-s
τ_q	Thermal lags for heat flux	-
τ_T	Thermal lags for temperature gradient	-
δ	Thermal diffusivity	m^2/s
ρ	Density of the material	Kg/mm^3
Ɛ	Emissivity of the surface	-
α	Absorption coefficient	-
η	Arc efficiency	-
β	Thermal expansion coefficient	K^{-1}
ε_{ij}	Element of the strain tensor	-

Symbol	Description	Unit
$u_{i,j}$	Displacement gradient	-
ε_v	Strain vector	-
σ_{ij}	Stress components	-
δ_{ij}	Knocker delta	-
λ	Penalty parameter	-
τ	Shear stress	N/m^2
γ	Surface tension coefficient	N/m
$\frac{d\gamma}{dT}$	Temperature coefficient of surface tension	N/m K
dT/dy	Average temperature gradient in the weld pool	K/m
ξ, η, ψ	Natural coordinates of a eight-node isoparametric element	-
ξ_i, η_i	Natural coordinates of i^{th} node	-
θ	Angular Distortion	-

Chapter 1

Introduction

1.0 General Background

Microjoining has become a significant field in recent era with increased miniaturization of the products. Effective microjoining has become one of the most critical technical prerequisites for success in manufacturing at ever-smaller scales. Microjoining is successfully employed for manufacturing many miniature components, devices, and systems such as medical implants, sensors and transducers, batteries and optoelectronics [Zhou, 2008]. There is no strict definition of micro joining. A working definition is employed to include the joining of sheet material's thickness or tubular material's diameter of less than 0.5 mm for applications in manufacturing of miniature products. The general configuration of micro joining is similar to conventional welding process. However, different variants of micro joining process are used by researchers. Several techniques have been utilized to achieve reliable microjoint with minimum distortion for fabrication in the industries. Newer methods are adapted for further advancing the science and technology, and economics of welding.

Fusion welds are achieved by application of an intense heat source and subsequent solidification of the molten metal. Fusion micro welding is the joining by fusion of parts where the dimension is less than or equal to 500 μm. The interaction between the heat source and the base material during fusion welding process results in a series of physical and chemical processes that influence the final geometry, microstructure and the mechanical properties of the weld joint. Energy balance is maintained by the heat flux from top surface and loss of heat by conduction and radiation. The molten pool is driven by surface and body forces. The driving force of liquid metal movement is the surface tension force that acts on the top surface of weld pool and the buoyancy force over volume of molten pool, and, also by the electromagnetic force when an electric arc is present. The solid region surrounding the weld pool experiences a

variation in temperature with time that may lead to various solid-state phase transformations, changes in grain structure and finally, in mechanical properties with respect to the original base material. For quantitative understanding of the aforementioned processes involved in fusion micro welding, a reliable mathematical model considering the underlying physics is better route in welding process design.

An accurate knowledge of the resulting fluid flow field and temperature distribution in the fusion zone are the prerequisites for the estimation of weld pool dimensions, weld thermal cycle, and distortion and residual stresses. However experimental determination of important parameters such as temperature and flow conditions in the micro scale weld pool is extremely difficult owing to the small size of the weld pool, high temperature gradient and high peak temperature and such methods are also costly. Theoretical investigation by mathematical modelling of the process provides better understanding of the complex phenomena. The numerical model that takes into account fluid flow is more close to the real welding process. The most common problem faced in the development of numerical process models is the consideration of all the physical phenomena associated with the process and integration of the same. With that aim, the temperature field in fusion welding is evolved either by solving conduction equation [Chang and Na, 2002; De *et al*., 2003; Frewin and Scott, 1999; Goldak *et al*., 1984; Kim *et al*., 2002] or through transport phenomena based heat transfer and fluid flow analysis [Cherepanov and Shapeev, 2009; He *et al*., 2004; He *et al*., 2005]. Computational complexities usually restrict the attempt towards the development and use of transport phenomena based comprehensive weld pool models [He *et al.*, 2004; He *et al.*, 2005]. However, a three dimensional finite element based sequentially coupled thermo-mechanical model is more useful to analyse the differential influence of process parameters that accounts a moving heat source and the associated physical phenomena such as heat conduction, convection, and radiation heat loss from the surface. The various physical phenomena are expressed through mathematical form of governing equations and corresponding boundary conditions. The mathematical framework calls for the solution of the equations of the conservation of mass, momentum and energy equations in a finite domain including the weld pool considering all material properties as temperature dependent. The analysis directs the reliable prediction of temperature and velocity field in the weld pool and the surrounding solid region, estimation of the shape and size of the fusion zone and the heat affected zone, and the rate of heating and cooling in the entire weld

area. Two fusion welding processes have been investigated in this present work i.e. micro plasma arc welding and laser micro welding.

Laser is a preferable heat source in micro joining because of the very small possible focussed beam as a form of spot or line welds during joining of metals and non-metals. The important characteristics of laser microwelding is very little distortion of final joint geometry, narrow heat affected zone, non-contact process, and precisely controlled intense heat source [Bag, 2011]. A wide range of materials with dimensions up to a few microns are welded by laser microwelding process. Laser welding involves several process parameters such as laser power, welding speed, beam diameter, pulse shaping, peak power, pulse energy, pulse duration, pulse repetition rate. However, the pulse characteristics are the most influencing element to control the weld joint quality in microwelding process. Nd:YAG laser is found to be suitable for welding in micro scale application due to its low operating wavelength (1.064 μm) which results in high absorptivity by the metals at such lower wavelength. At this wavelength extremely small focused fusion zone can be produced with an intensity of about 100 times higher than that of CO_2 lasers with the same emitted average power [Naeem, 2008].

The plasma process is also a suitable micro joining process which is equally suited to manual and automatic applications. It has been used in a variety of operations ranging from high volume welding of strip metal, to precision welding of surgical instruments, to automatic repair of jet engine blades, to the manual welding of kitchen equipment for the food and dairy industry. The plasma welding process was introduced to the welding industry in 1964 as a method of bringing better control to the arc welding process in lower current ranges. Today, plasma retains the original advantages it brought to industry by providing an advanced level of control and accuracy to produce high quality welds in miniature or precision applications and to provide long electrode life for high production requirements. Micro Plasma Arc Welding (MPAW) is a metal joining technique widely used in manufacturing of thin sheet components due to its inherent properties. MPAW is a variation of the PAW process and uses intensities lower than 15 A. The main advantages of plasma microjoining includes low amperage capability, stable, concentrated arc at low amps, gentle arc transfer (arc start) with no high frequency noise, high energy density and reduced heat affected zone, and flexibility of short weld time. The process parameters include welding current, speed, gas flow rate, stand-off distance, electrode diameter, nozzle diameter, shielding gas and gas flow rate. Current in MPAW can be applied continuously or in

pulsed mode. To enhance arc stability, pinhole constrained nozzle (0.6 - 1.2mm) and combined arc plasma is applied with different shielding gas. The narrow and stiff arc prevents arc wander and minimizes distortion of substrate material [Wu *et al.*, 2014]. Plasma arc can be readily used manually as the torch is compact and there is high tolerance to torch-to-work piece variation. The weld quality and productivity are controlled by the process parameters. The experimental effort is undertaken in the present work to perform micro plasma welding processes at varying welding conditions on titanium alloy, stainless steel, and low-carbon steel of 500 μm thicknesses.

Titanium and its alloys belong to the group of materials whose application in various industries is ever increasing. Titanium has found its niche in various industries owing to its excellent properties over competing materials like aluminium, steel, and superalloys. Gamma-TiAl super alloys have superior performance working at higher temperatures, having low density and better resistance to oxidation than alpha–beta titanium alloys. However, the strength and ductility of alpha–beta alloys are higher than gamma titanium alloys [Beranoagirre *et al.*, 2012]. One of the most widely used alpha-beta alloys is biocompatible Ti6Al4V alloy. Various fusion welding processes have been used for fabrication and joining of this alloy. Being biocompatible, Ti6Al4V has been the material of choice for biomedical application. It is also considered for many other applications where a combination of high strength, light weight, good corrosion resistance, and high toughness are required [Donachie, 2000]. Hence the microwelding of titanium alloy is practically significant for application in various sophisticated industry. The joining of titanium alloy at a micro scale level is not well established and there is lack of proper investigation in esteemed literatures. Titanium alloy is likely to form oxides, nitrides, and prone to high affinity towards other materials at high temperature. Thus, special care has to be taken in order to properly shield the molten weld pool [Donachie, 2000]. Porosity is also one of the main problems in the welding of titanium alloys which is caused by shielding gas entrapment in a solidified structure [Mueller *et al.*, 2006], and due to improper sample preparation and mechanical cleaning of the materials. It is observed that the porosity increases with increase in material thickness during welding of Ti6al4V alloy [Hilton *et al.*, 2007]. Therefore, it is practically important that the materials to be welded have to be properly shielded during welding to protect from contamination and oxidation which might cause embrittlement of the weld joint.

Low carbon steel and stainless steel are the two most widely used materials in today's world for various industrial applications. Similar and dissimilar welding of low carbon steel and

stainless steel are carried out by various processes since weldability of both the materials is relatively better. However, limited studies are observed on micro scale welding processes of these materials. In the present work, an attempt has been made to explore the possibility for the development of plasma microwelding process of stainless steel and low carbon steel. The analysis is carried out on comparative mode which may be helpful for the foundation of dissimilar joining between these two materials.

The complexity of joining materials enhances with reduction in sheet thickness. The present work put emphasis on MPAW and laser micro welding of 500 μm in butt joint configuration. Using controlled and regulated process parameters, the micro welding process is specifically designed to use in joining of thin sheet components over a wide range of process parameters. The weld quality is assessed by carefully controlling the process parameters and by reducing the formation of oxides. The combined effect of welding speed and current on the weld joint properties is evaluated for joining of Ti6Al4V alloy, SS304, and low carbon steel. The macro-microstructural characterizations of the weldment by optical microscopy as well as the evolution of mechanical properties by micro tensile and micro hardness test have been performed. The weld joint quality is affected by specifically designed fixture that controls the oxidation of the joint and introduces high cooling rate. Hence, the solidified microstructure of welded specimen influences the mechanical properties of the joint. The butt joint of titanium alloy by MPAW at optimal process parameters are of very high quality, without any internal defects and with minimum residual distortion.

The distortion is more serious problem mainly with thinner materials due to low stiffness and consists of transverse and longitudinal shrinkage, and angular rotations. Various attempts have been made to analyse the residual stresses and distortion in the welded structures [Deng and Murakuwa, 2008a, Long *et al.*, 2009; Wang *et al.*, 2008]. It is observed that Ti6Al4V weldment exhibits highly localized residual stress and the magnitude is very high in longitudinal direction. The former is due to its significant thermal diffusivity and the latter is because of its high yield strength [Shop *et al.*, 2014]. It is emphasized that the large-displacement theory predicts the distortion satisfactorily for microwelding process as compared to high thickness materials. The characteristics of temperature field, plastic strain distribution and the residual stress are also studied from the developed numerical model.

The integrated modeling approach learns the sensitivity of unknown parameters on final weld pool dimensions by minimizing the error between the predicted and experimental measured weld pool dimensions and find out most suitable set of unknown parameters. Finally, the optimized set of unknown parameters is used to calculate weld pool dimensions. It is however realized that the optimization algorithm, although a significant tool for the construction and organization of the integrated modelling approach, the real strength of the integrated model lie in the quality, completeness, and robustness of the numerical process model. However, with regard to the optimization tools, one major route is attempted – stochastic optimization tool. It is realized further that this algorithm is more effective in finding the global optima by avoiding the local minima. Hence, for the effective construction of integrated process model, a real-number based Harmony Search algorithm is interfaced with the numerical process model [Geem, 2009; Lee and Geem, 2005].

The validation of the computed results from the integrated model for a wide range of process condition is an important issue to endorse the level of efforts towards the development of such complicated mathematical modelling of fusion micro welding. The compatibility of the model to study the heat transfer and fluid flow behaviour in the weld pool in laser micro welding is verified by comparing the results of the computed weld pool dimensions with the experimental data reported in the independent literatures. The numerical model developed using ABAQUS is validated by comparing with experimentally measured weld pool dimensions and distortion pattern.

One of the greatest advances in the field of laser welding of dissimilar materials is joining of plastics. The laser source can be either Nd:YAG or direct diode, depending on the type of welding application and materials. The welding concept revolves around the top material being transparent to the laser, while the underlying material absorbs the laser. With minimal pressure on the joint the underlying material melts by absorbing the laser, and transfers heat to the top material that in turn melts and creates the weld. The laser light is absorbed at the surface of the lower material which causes heat to build up at the surface of the upper layer. In laser transmission welding (LTW), delivery of the thermal energy by laser beam is influenced by the process parameters, optical and material properties. If the parts to be joined do not receive enough heat, gaps can occur while excessive heat can cause polymer degradation. Thus the weld interface must be exposed to sufficient heat to melt the polymer and form strong weld. Thus

developing an accurate model to help understanding the process is very beneficial. An attempt has been made to simulate the laser transmission welding process for studying the effect of gap conduction due to the presence of any air gap at the rough surface of the weld interface. The algorithm is capable of calculating the contact conduction without approximating it based on roughness value and temperature developed at the two surfaces.

A thermal wave model with a single phase lag in which the temperature gradient established after certain elapse of time has been proposed by researchers [Eesley, 1983; Fujimoto, 1984]. In particular, as laser pulse duration approaches very small value, the effect of microscopic relaxation times among different energy carries i.e. in the mechanism of radiation absorption becomes important. Several authors have studied analytically the parabolic and hyperbolic models of heat conduction by laser heat source without a convective boundary condition [Cattaneo, 1958; Vernotte, 1958]. Using an inverse analysis, the two relaxation parameters and thermal diffusivity were estimated by comparing the experimental and simulated non-Fourier temperature response. The complicated photon electron interaction in space alternatively could be interpreted in terms of the lagging behaviour. However, most of the researchers presented either analytical solution or one dimensional solution of non-Fourier heat conduction model when the target is radiated by high power ultra-short pulse laser. There is always scope to enhance the phenomenological model that nearly represents actual process and is ever demanding for the application of micro/nano scale heat transport process. Hence, the motivation is to develop decent numerical heat transfer model for ultra-fast pulse laser heating. A finite element based three dimensional heat transfer model is developed for transient heating of ultra-short pulse laser. The numerical model accounts non-Fourier heat conduction using dual phase lag effect. The finite size of the solution domain is considered and a phase lag boundary condition is implemented.

Microjoining is an emerging technology with diverse application and an ever increasing demand. Adaptation of new technology brings the flexibility in microscale welding process with reduced defects and sound quality. However, microwelding depends on controlled and regulated heat source having high energy density with low heat input. Microplasma arc welding has been utilized recently to join various materials. Laser microwelding with its unique advantages is a prevalent technique for joining of different materials. However, the application is limited to joining materials like copper, stainless steel, etc. Thus both the methods are being utilized here to

join Ti6Al4V alloy whose application in various industries is increasing due to its extensive properties. Being biocompatible by nature and having high strength to weight ratio, Ti6Al4V alloy is the material of choice in various biomedical and aerospace applications. Also, understanding the various physical phenomena associated with microwelding of various materials is of practical significance. Hence the motivation of investigating the microwelding of various materials by micro plasma arc as well as by pulse laser.

1.1 Current Issues

It is thus obvious that the micro joining of materials has different philosophical basis in terms of thermo-mechanical, thermo-fluid, and macro-microstructural behaviour as compared to macro-scale welding process. The joining of biocompatible titanium alloy, stainless steel, and low carbon steel at a micro scale level is not well established and there is lack of proper investigation in esteemed literatures. However, the most obvious problem for fusion welding of titanium alloy is susceptibility to oxidation in welded components. Therefore, the development of suitable process for microwelding of titanium alloy using either plasma source or laser source is a challenging task to meet the demand of low level residual distortion and fairly acceptable mechanical properties.

Direct experimental realization of all physical parameters in microwelding process is proved to be extremely difficult or even impossible because of the complexity of the process. Although the numerical modelling approach for fusion welding process is attempted for several decades by several researchers, the complete realization of all the physical phenomena in a single mathematical model is absent. Hence the motivation is to develop the numerical models of increasing complexity and sophistication that can be used beneficially to understand the differential influences of process parameters. In laser transmission welding, the intimate contact between the upper and lower absorbing surfaces is important for appropriate temperature development at the heated interfacial zone to ensure good bonding. Therefore, the temperature simulation considering thermal contact resistance between two surfaces is an important aspect to correctly estimate temperature distribution. In pulse laser welding, the energy transfer to the substrate material is not continuous which is reflected by fluctuating temperature distribution. Averaging to continuous deposition of pulse energy actually dampen the pulse effect which is normally consider in process modelling of laser welding. Therefore, incorporation of actual pulse effect enhances the sophistication of numerical modelling approach. However, heat transfer in

ultra-short pulse laser has very different physical basis as compared to long pulse laser. The contemplation of finite speed of thermal wave propagation is necessary in order to precisely analyse the transient process for ultra-short pulse laser heating. The analysis accounts finite time lags for the solution of temperature which is different from Fourier's heat conduction model.

Though the small characteristic length in micro welding limits the liquid flow to some extent, yet convection is still an important mechanism of heat transfer in the weld pool. Few literatures have come up to study the heat transfer and fluid flow in micro joining. It is still in the premature stage and needs to be investigated from various aspects. Apart from correct interpretation of physical phenomena, the reliability of a numerical model greatly depends on the accuracy of the input parameters provided to such models. The input parameters required for modeling calculations are not readily available and can be obtained using an inverse approach by integrating mathematical model with multivariate optimization algorithm.

In summary, the development of the process window for microwelding of 500 µm thick titanium alloy, stainless steel, and low carbon steel using micro plasma arc welding is the major thrust of the present research work. The reduction of oxidation problem in joining of titanium alloy to get a successful weld joint is also a major contribution to develop plasma and laser microwelding processes. The experimental investigation of butt joint has been performed in terms of weld pool shape and size, residual distortion, mechanical strength, and micro-hardness of different heat affected zones. The relation between heat transfer phenomena in terms of heat input and the mechanical properties is established for titanium alloy through the microstructural characteristics at different welding conditions. The secondary objective of the present work is to develop a coupled thermo-mechanical model in micro joining process which takes into account more physical phenomena to predict distortion and residual stress in a solidified structure. A well tested thermo-fluid model is also used to investigate the material flow behaviour in laser microwelding process. Development of the numerical model for laser transmission welding using contact thermal resistance is also additional contribution in the present research work. The analysis of ultra-short pulse laser heating using dual phase lag effect in the frame of non-Fourier heat conduction is also a promising direction to develop ultra-short pulse laser welding system.

1.2 Research Objectives

The overall objective in this work is to establish plasma microwelding of titanium alloy, stainless steel, and low carbon steel through experimental as well as numerical investigation.

Additionally, the laser microwelding of titanium alloy using the effect of pulsation is established through thermo-mechanical analysis. To achieve the same the following modules are accomplished either simultaneously or sequentially which are developed over whole duration of research work.

- **Transient thermal analysis of fusion microwelding process**
  - Prediction of the temperature distribution, velocity fields, and the weld-pool dimensions.
  - Prediction of the effects of process parameters on temperature distributions.
  - A thermal model in the stimulation of temperature profile for ultra-short pulse laser heating process.
  - Studying and implementing a suitable method for bridging gap in micro welding mainly in Laser Transmission Welding where proper contact between the two parts is essential.
- **Optimization of the uncertain parameters**
  - Integrating mathematical model with multivariate optimization algorithm to identify the most suitable uncertain input parameters required for modelling calculations and are not readily available.
- **Thermo-mechanical analysis**
  - Prediction of the welding residual stresses and distortions.
  - Determination of the effect of welding parameters (current, welding speed, plate thickness) on residual stress and distortion.
- **Validation of the model**
  - The validation of the computed results from the integrated model for a wide range of process conditions with the experimentally measured values.
- **Experimental Investigation**
  - Experiments are also undertaken to perform plasma micro welding and pulsed laser welding at varying welding conditions on 500 μm thick Ti6Al4V. Plasma microwelding on stainless steel and low-carbon steel of 500 μm thicknesses is also carried out.
  - The aim of the experimental study has primarily been the development of the process map for a successful weld joint and secondarily the validation of the developed numerical process model.
  - A suitable fixture has been designed to reduce the oxidation problem in titanium alloy during welding.

- The weld joint performance is analysed by micro hardness, micro tensile test, and residual distortion. The macro-microstructural characterizations of the weldment are performed by optical microscopy. The weld joint quality is affected by specifically designed fixture that controls the oxidation of the joint and introduces high cooling rate. Hence the solidified microstructure of the welded specimen influences the mechanical properties of the joint. The weld joint quality is evaluated by oxygen concentration at the welded section. The solidified microstructure of the welded joint brings relatively better mechanical properties in micro plasma arc welding of titanium alloy.

1.3 Layout of the thesis

The present report consists of five chapters to elaborate and describe all the aspects aimed at research objectives. *Chapter 1* provides an introduction to the subject, the research objectives, and the overall layout of the report. *Chapter 2* includes the detailed literature survey of the work of previous researchers which is focused on various aspects of micro scale joining process in the perspective of practical application. First, experimental investigation on process conditions, materials, and feasibility of micro welding processes is reviewed. An extensive part of the article is devoted to the review of numerical process model and its complexities. A detailed reviewed work on welding of Ti6Al4V alloy is also carried out. Furthermore, an investigation of ultra-shot pulsed laser considering non-Fourier heat conduction analysis is done. The application and the role of different optimization algorithm in the integrated modelling are described next. Finally, the temperature induced distortion and residual stress analysis in weld joint are discussed with an aim to highlight the necessity of *a-priori* knowledge of expected temperature field in fusion welding to minimize welding distortion.

Chapter 3 presents the mathematical formulation to develop the thermo-mechanical model using finite element method. Thermal model followed by mechanical model was discussed. Typical 'hourglass' heat source model for over-penetrated weld is also developed to implement in laser microwelding process. A thermal model to stimulate the temperature profile for ultra-short pulsed laser joining process is also developed.

Chapter 4 depicts in details about the experimental investigation of micro plasma and laser microwelding processes. The effect of welding speed and current are analysed to estimate the feasible range of process parameters for a successful joint for micro plasma welding of 500 μm Ti6Al4V alloy, SS304 and low carbon steel. The role of fixture to minimize the oxidation

and weld induced distortion has been demonstrated in joining of titanium alloy. A study on laser microwelding using pulse Nd:YAG laser has also been carried out on 500 μm thick Ti6Al4V alloy in butt joint configuration. The influence of laser scanning speed and pulse energy is analysed to produce a defect-free joint. The critical assessment on the performance of the weld joint is evaluated by micro-tensile, micro-hardness and metallographic analysis.The micro scale butt joint by micro welding at optimal parameters are of very high quality, without any internal imperfections and with regular fusion zone. Thus, the present methodology developed for microwelding of 500 μm thick Ti6Al4V plate is good alternative for joining of thin sheets.

Chapter 5 presents the computed results and the validation of these results with the corresponding experimental data. A three-dimensional finite element based sequentially coupled thermo-mechanical model is developed to simulate the temperature distribution and the weld induced distortion of the joint. The large displacement theory which considers the non-linearity predicts well the distortion in microwelding. The temperatures are well below the vapourization temperature of the materials and hence it can be concluded that the conduction mode heat transfer prevails against keyhole formation within this power density range used for microwelding of 0.5 mm thick plate. An integrated modelling approach is presented in present course of action during reliable modelling of laser microwelding. The identification of unknown parameters using HS algorithm further strengthen the reliability of the numerical modelling. The analysis of various dimensionless numbers indicates that the fluid flow analysis is important even in micro-scale welding process. To analyse the heat transfer process by an ultra-short pulse laser, a three dimensional finite element based numerical model is developed assuming finite speed of thermal wave propagation with two phase lags using phase lag boundary conditions. The transient heating and cooling phenomena are analysed for the effect of two relaxation times, variation of pulse width, and multiple pulses. The model results are validated with ultra-short pulse laser heating of a thin gold film. A more general 3-D finite element model for LTW for similar and dissimilar materials is developed including the effect of contact resistance due to the presence of any air gap and roughness at the weld interface.

Chapter 6 outlines the summary and conclusions that are envisaged as a part of the present work. Further scope of taking the present effort forward is also documented in this chapter. The list of references is presented at the end.

Chapter 2

Literature Review

2.0 General Background

Fusion welding is a complex process that involves several interactive physical phenomena. The evolution of the temperature profiles, geometric shape and size of the molten pool and flow behavior are evidently affected by various phenomenological realities occurs during welding. The heat flux received by the substrate material from the heat source, the formation of a dynamic molten pool, energy leaving the substrate by convection, radiation, evaporation, and vaporization of the alloying elements account the process. The mechanism of microwelding is a miniature version of conventional fusion welding process. Since heat input used in the microwelding is very low compared to the macro scale process, the weld zone and heat effected zone produced is much narrower. For the same heat input, there exists wide variation of temperature gradient, solidification rate and geometric shape and size of the weld pool which brings the difference in microstructure and properties between micro and macro welded structure. As micro technology advances, the need for joining of miniaturized components is rapidly increasing. The field of microjoining has come into existence because of this driving force. Microjoining is a growth area and critical to the successful performance of many components in a wide variety of industries. Though little advancement has come up in this field as compared to conventional fusion welding process, yet microjoining is in the immature stage and needs to be investigated from various aspects.

A detailed review of the fusion microwelding processes on the basis of experimental and computational works are addressed by different researchers [Zhou, 2008]. Several microjoining techniques have been used successfully aiming at to reduce the weld induced distortion. The fusion microwelding system has been developed mainly five different types (Fig. 2.1). However, in this section, an extensive review is focused on current achievement and challenges in laser and

plasma microwelding processes. Low input power, but high flux density heat source is an important practical aspect for welding of small components since it is restricted to relatively small area [Kou, 2003]. Thus, autogenous welding process with highly concentrated energy sources, such as laser beam and electron beam are receiving increasing interest on microscale application. In particular, with laser welding, much simpler fixturing would be beneficial in comparison with electron beam welding where a vacuum is needed and X-rays are produced [Mazumder and Steen, 1980]. However, micro plasma welding with a highly constricted and flexible heat source having high energy density is preferable for micro welding application due to low cost of equipment as compared to laser and electron beam welding.

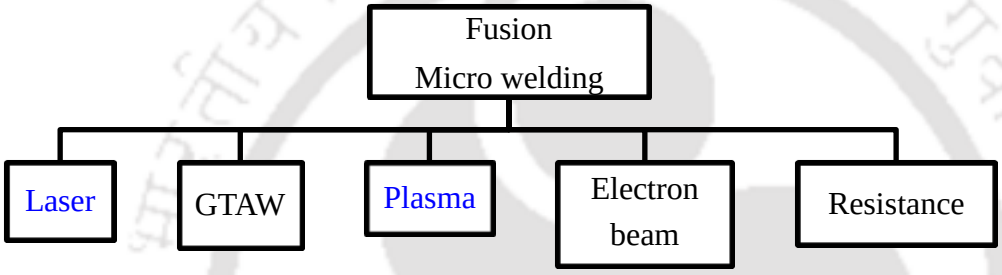

Fig. 2.1 Types of fusion microwelding [Zhou, 2008].

2.1 Microwelding

In the era of miniature, microwelding has been evolving as a prospective smaller scale manufacturing process. If the geometric dimension of the solidified fusion zone is roughly less than 500 μm, the joining process can be categorized as microwelding. Therefore, the literature review is focused on various aspects of micro scale joining process in the perspective of practical application. The experimental investigation on process conditions, materials and feasibility of microjoining processes is reviewed here. It is anticipated that at ultra-shot pulsed laser, the phase lag behavior is more appropriate to signify rapid propagation of heat wave into the substrate material. In fusion microwelding, most of the works is mainly focused on experimental investigation to study the effect of process parameters on feasibility of micro welding process. The controlled and regulated heat source has been used in microwelding system. Out of several microjoining processes, the laser and plasma microwelding processes in case of metals and non-metals are reported here. In a nutshell, an overview of microjoining process is highlighted here which is required for promising development of microsystem technology.

2.1.1 Laser microwelding

As a comparatively new process, laser microjoining has potential future prospects in manufacturing industry and hence it is realized to congregate both the theoretical and practical aspects of the processes. Laser processes has already been established as a high precision and versatile manufacturing process due to availability of very high quality laser with excellent process automation abilities. Laser microwelding is an efficient technique where the joining has been performed by the application of very small, highly focused and precisely controlled intense heat source [Zhou, 2008]. Laser welding can be used in both continuous and pulse mode to join a wide range of materials with dimensions up to few microns. The process involves precisely controlled several parameters like beam power, scanning speed, beam diameter, pulse shape, pulse energy, pulse duration, and pulse repetition rate that individually affect the weld joint quality. However the pulse characteristics are the most influencing element to control the weld joint quality in microwelding process. A study on the process parameters that influence the quality of weld joint in pulsed laser welding is shown in Fig. 2.2 [Tzeng, 2000]. It is also highlighted that the final weld joint quality depends on the interactive combination of a number of factors.

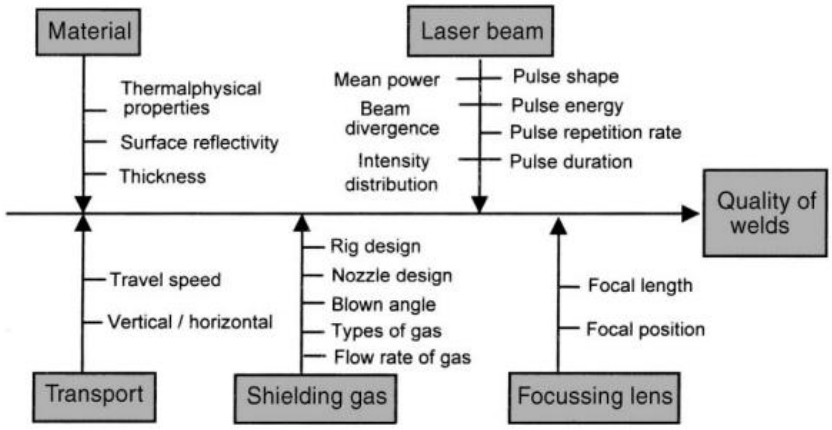

Fig. 2.2 A diagram demonstrating the effect of process parameters on the quality of pulse laser welding [Tzeng, 2000].

When using laser for welding purposes, energy is transferred from the laser to the work-piece through two different ways or modes. The laser welding mode can be either the conduction mode or the keyhole mode depending upon the power density. In conduction mode, the low energy density basically heats the surface of the material being welded. The size of the weld on the surface is generally larger, and the depth of penetration of the weld is generally shallower. In

conduction mode, power densities lie below 10^6 W cm^{-2}. In keyhole mode laser operation, the power density is above conduction mode. A narrow, deeply penetrating vapour cavity, or keyhole, is formed due to local vaporization. The keyhole is surrounded by a thin layer of molten material. This layeris maintained by equilibrium between vapour pressure, surface tension and hydrostatic pressure. Keyhole mode laserwelding is generally followed in the industry due to better energy coupling, higher welding speed, and thicker-section welding capability [Benyounis *et al.*, 2005; Tzeng, 2000].The conduction mode of welding is also advantageous in minimizing distortion, loss of alloying elements, as well producing fine grain structures through rapid solidification. This mode of welding is well suited for thin sheets because the laser beam spot size is comparable to the sheet thickness.

During last few decades, a considerable research has been endeavored in laser joining at the level of macro scale. This section has been categorized according to the various laser sources used, the similar kind of metal joining like steels, aluminum and titanium alloys, and non-metal joining like plastic that most commonly used in the industry, the joining of dissimilar materials like metal with polymer mostly used in biomedical application and dissimilar polymer joining like glass with silicon having potential application in joining of semiconductor devices. Semak *et al.* [2003] proposed a theoretical criterion in terms of threshold pulse energy and beam intensity required for the possibility of laser microwelding. They indicated that with a focused beam diameter of few ten microns and pulse durations shorter than 1 ms may enable microwelding of fusion zones of the order of or smaller than 100 μm. Nicholas [1969] addressed the suitability of lasers for practical application in microwelding in dates back to 70's. Considerable development in laser technology has been achieved for micro scale joining of various kinds of metals and non-metals with outstanding quality. Bag [2011] did an extensive review on laser microjoining process in the perspective of current application and modeling aspects. A recent review on laser microwelding has been performed by Guo [2009] who presented an overview of laser microwelding process as a small part of the whole work.

Ventrella *et al.* [2010] investigated the quality and reliability on micro joining of stainless steel foil using pulsed Nd:YAG laser. It was observed that micro hardness was almost uniform across the parent material and the shape and size of fusion zone was very much sensitive to gap between foils. Rohde *et al.* [2010] demonstrated micro weld between two different grade of aluminum alloy using pulsed Nd:YAG laser. However, the overall quality of the welding seams

was sensitive to the temporal pulse shaping. Kim *et al.* [2002] also investigated the optimum pulse shape during joining of thin aluminium sheet. Abe *et al*. [2005] investigated the butt welding of 100µm and 50µm thick stainless steel with a direct diode laser system. At an output power of 100W, 100µm and 50µm thick stainless steel plates could be welded with a velocity of 6m/min and 18m/min respectively. They bead widths of 100 µm which was narrower than the beam size of the laser. No spatter or plasma plume was observed even without the use of an assist gas. The tensile strength of the weld bead was nearly the same as the base metal. Naeem [2008] investigated the suitability of laser characteristics on micro joining of various materials. The author performed experiments using lamp pumped pulsed Nd:YAG laser and continuous wave (CW) single mode fiber laser. The single mode fiber laser produced good micro joint for stainless steel and titanium alloys up to 1mm thick foil. However, to weld reflective materials like aluminium and copper base alloys it needed to increase the power level. The report indicated that to produce good quality of welds for highly reflectivity materials and dissimilar materials, pulsed Nd: YAG laser needed to control proper pulse shape and pulse energy. Kleine *et al.* [2004] investigated on the power stability of pulsed fiber laser during welding of stainless steel and titanium. A superior pulse-to-pulse energy stability was achieved during these experiments by fiber lasers. The weld penetration and weld bead width is sufficient for many welding applications in the medical and electronics industry. Ismail *et al*. [2011] experimentally investigated the characteristics of laser micro-welding of thin stainless steel sheets by using a single mode continuous fiber laser with high-speed scanning system. It was clarified that the welding bead width and depth increased with increasing the scanning velocity under a constant energy density condition. The utilization of shielding gas is very effective to obtain smooth fusion bead and the combination of micro beam spot and high-speed laser scanning made, it was possible to obtain good overlap welding of ultra-thin stainless steel sheets. A faster and high quality welding could be achieved by using a single-mode fiber laser with micro-beam and high-speed scanning.

Laser is also being employed in the micro joining of various dissimilar materials. Mys and Schmidt [2006] investigated the stability of micro joint between aluminum and copper using filler material. It was found that use of silver and tin as filler materials yields to a considerable improvement of the static and dynamic mechanical stability of welded joints. The authors also claimed that even small amount of suitable filler material addition helps to reduce brittle

intermetallic phases on the interface between copper and solidified melt in the welded joints. Majumdar *et al.* [1997] studied the formation of a crack-free joint between Ti alloy and Al alloy by using a high-power CO_2 laser. Laser power, welding speed and offset of the laser with respect to the joint are considered as variable parameters. It was found that intermetallic compounds are formed in the fusion zone depending on the amount of Al or Ti melted by the laser. This intermetallic compounds are very brittle and solid state cracks are formed because of the stress developed after the solidification. Formation of cracks is more sensitive to amount of aluminum present in the fusion zone. In order to minimize the dissolution of Al and to increase the toughness of the intermetallic phases Nb foil is used as a buffer between the two alloys. It was observed that the partially melted Nb act as a barrier to dissolve Al and thus a strong weld is formed. Chan *et al.* [1984] studied the effects of three processing parameters, laser power, and welding speed and offset distance of the laser beam from the interface during fibre laser welding of Ti6Al4V to Inconel 718. Experimental results indicated that when welding sheets of Ti6Al4V to Inconel 718 with an IPG 1 kW fibre laser, crack-free welds could be readily obtained by a higher laser power and welding speed. A better quality weld with less hardness variations and less chance of cracks can be generated by offsetting the laser beam approximately 35 μm from the interface to the Inconel 718 side and using a combination of a higher laser power and a higher welding speed. This is attributed to this method suppressing the formation of Ti-Ni intermetallic brittle phases.

In the last decade, most successful achievement in the field of micro scale joining is the joining of similar and dissimilar non-metallic materials such as glass, silicon and plastics. These non-metallic materials are generally joined by transmission welding. With ever demand of dissimilar biocompatible material joining, researchers have found promising future in the joining of polymer to metal by transmission laser micro joining. Mian *et al.* [2005] conducted experimental studies to find good bonding strength between polyimide (PI) and titanium (Ti) using near-infrared diode lasers. They observed line widths of 200 to 300 μm using fiber lasers of 2.2 and 3.8 W. Georgiev *et al.* [2005] investigated micro joining between polyimide (PI) and titanium-coated borosilicate glass (BSG), respectively. It was observed that the formation of the joints was a result of the creation of strong chemical bonds between Ti-containing species and certain polymeric functional groups. Mechanical tensile-strength-failure testing showed that such joints experience some degradation as a result of soaking in artificial cerebrospinal fluid (CSF).

Newaz *et al.* [2006] also conducted comparative study between the performance of glass/polymide and titanium/polyamide micro joint in CSF. Mahmood *et al.* [2007] investigated the joining between PI and Ti with a wider range of scanning velocity of fiber laser. The authors optimized the suitable combination of laser power and scanning speed to find good bonding when the maximum temperature at the centre of laser beam was above the melting point but below the burnout point of the PI. This kind of joining is significant in bio encapsulation of medical implant devices and neural implant devices. According to the practical need researchers investigated micro joining of two different geometric components. Chung and Lin [2005] conducted micro joining of pin-to-plate using pulsed Nd:YAG laser and filler material. This kind of work is significant in dot matrix printing pin joint. The authors demonstrated that micro-pin were successfully joined to the thin plate in the better condition of laser peak power of 600 W, spot size of 0.6 mm and pulse duration of 10 ms.

Thus laser is being employed variably in the microwelding of both similar and dissimilar materials. It is realize from the experimental evidence that the size and shape of weld fusion zone developed during welding depends on input power density, thermal diffusivity and weld duration. Weld sizes grows till it reaches a steady state once the balance between heat absorbed and heat dissipation is established. Short duration pulse of high peak power produces a deeper weld but can also lead to excessive spatter. On the other hand, pulse of low peak power and longer duration produce a shallower weld with fewer spatters. Hence an optimum calibration of pulse characteristics is necessary to obtain successful joint. Nd:YAG laser is found to be suitable for welding of metals in micro scale application due to its low operating wavelength (1.06 μm) which results in high absorptivity by the metals at such lower wavelength(Fig.2.3). At this wavelength extremely small focal diameter can be produced with an intensity of about 100 times higher than that of CO_2 lasers with the same emitted average power [Naeem, 2008]. A 400 W pulsed Nd:YAG laser welds 30–40% deeper in stainless steel than a pulsed CO_2 laser operating at the same average power over the entire range of parameters [Bagger, 1992]. Furthermore, Nd:YAG lasers can be transmitted through fibers. This flexibility makes these lasers more useful for welding delicate electrical components and small wires in medical equipment. The need for more efficient, compact and high beam quality lasers for very fine microwelding has fuelled the rapid growth for developing fiber lasers. These lasers operate at near IR spectral region and offer multitude of advantages over conventional lasers and shows greater promise to open up new

micro welding applications. Assuncao and Williams [2013] compared the pulse welding and continuous laser welding conditions. They concluded that the pulse welding laser showed higher efficiency under the same welding conditions.Table 2.1 depicts the overview of the laser conditions and object materials used in microjoining between similar or dissimilar metals (approximate data) [Bag, 2011]. It is obvious from the critical analysis of experimental work that fiber laser and Nd:YAG laser have been applied in microjoining with low and high peak power, respectively.

Table 2.1 Laser conditions corresponding to joining of metals [Bag, 2011].

Laser conditions								**Object material**			
Type	**Mean power (W)**	**Pulse energy (J)**	**Pulse length (ms)**	**Pulse frequency (Hz)**	**Spot size (µm)**	**Power density (W/cm^2)**	**Speed (mm/s)**	**Type of joint**	**Material**	**Thickness (µm)**	**Weld dimensions (µm)***
Pulsed Nd:YAG	125	~ 17	0.1-20	1000	60	-	8.3 – 38.3	Bead-on-plate	SS304	500 - 2000	-
CW fiber	100	-	-	-	30	$100x10^6$	30 - 800		SS304	50 - 500	
	200					-	833 - 3333		SS304	150 - 500	
							500 - 2667		Aluminium	150 - 300	
							167 - 833		Copper	110 - 150	
Pulsed Nd:YAG	-	1 – 2.25	4	39	200	-	8.75	lap	AISI 316L	100x100	480-750 (W) 100-240 (D)
Pulsed Nd:YAG	102	-	-	40	80	$\sim 2x10^6$	1.6	Bead-on-plate	AlMg3	200	150-350 (W) 230-460 (D)
Direct diode	50	-	-	-	300x 1800	$\sim 9.2x10^3$	100-125	butt	SUS304H	50	-
	100					$\sim 19x10^3$	250-300			50	
	100						50-100			100	
	300					$\sim 57x10^3$	225-350			100	
Pulsed fiber	40 - 100	-	2 - 4	200	25	-	4	Bead-on-plate	SS304	260	65- 430 (D) 60-250 (W)
	80	-	4	200	-	-	4	lap	Titanium	260x260	300 (W) 350 (D)

*W – width; D – depth of penetration

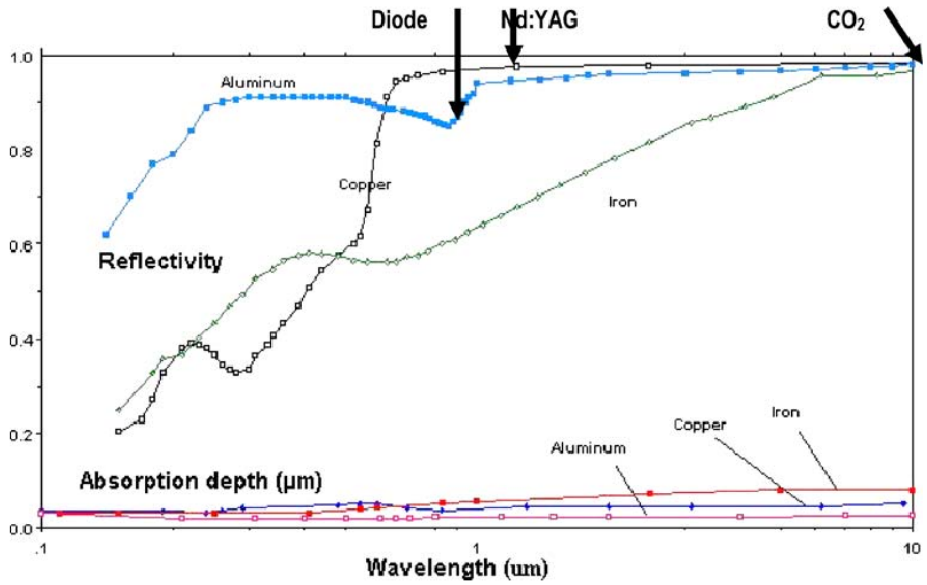

Fig. 2.3 Reflectivity of metals as a function of wavelength of laser beam [Chen and Molian, 2008].

2.1.2 Micro plasma arc welding

In plasma welding (PAW) an arc (electrical discharge) is ignited between the electrode and the work piece that locally melts the work piece. The electrode tip is positioned carefully inside a plasma gas nozzle, through which the plasma gas is fed which reduces arc expansion from the electrode to the work piece, i.e. acts to constrict the arc. Thus, higher power densities are achieved in PAW than in GTAW, where the arc is unconstricted. The other processes such as laser beam welding (LBW) and electron beam welding (EBW) have also been available for many years whose power density is even higher than for PAW. But PAW is a cost effective process than the LBW and EBW processes which require large and expensive equipment and are thus often infeasible. Furthermore, precautions need to be taken when operating these processes to protect against potentially harmful radiation. In addition, an important disadvantage of EBW is that it needs to be operated in vacuum. Another disadvantage of LBW is its small fit-up tolerance due to the small beam sizes. This puts strong requirements on pre-welding workpiece preparation, which increases production cost. PAW is more tolerant to misalignment etc. due to its larger anode contact area. Micro Plasma Arc Welding (MPAW) is a metal joining technique widely used in manufacturing of thin sheet components due to its inherent properties. The weld

quality and productivity are controlled by the process parameters. To enhance arc stability, pinhole constrained nozzle (0.6-1.2mm) and combined arc plasma is applied with different shielding gas. Thus, micro-plasma can become a highly concentrated heat source. Table 2.2 shows the wide variety of metals and alloys that can be welded by micro-plasma process [Jiang *et al.*, 2008].

Table 2.2 MPAW parameters of some metals and alloys [Jiang *et al.*, 2008].

Assembly		Torch equipment		Gases used (L/min)					Current (A)	Welding Speed (cm/min)
Material	Thickness (mm)	Electrode diameter (mm)	Nozzle diameter (mm)	plasma Argon	Annular Ar%	H_2%	He%	L/min		
Stainless steel	0.06	1	0.8	0.15	95	5	0	4/6	2	65
Constantan	0.10	1	0.8	0.15	95	5	0	4/6	3	50
Iron/Nickel	0.80	1.6	1.5	0.20	95	5	0	5/7	15	45
Cupronickel	0.50	1.6	1.2	0.20	95	5	0	5/7	10	60
Nickel Silver	0.30	1.6	1.8	0.20	0	0	100	7	45	60
Titanium, Tantalum, Zirconium	0.50	1.6	1.2	0.20	0	0	100	7	25	70
Gold	0.20	1	1	0.15	95	5	0	4/6	5	40

Yoshioka *et al.* [1993] investigated the high-power-density plasma arc welding of stainless steel plate of 0.1 and 0.3 mm thickness. Suitable combinations of welding current and welding speed required for successful welding was evaluated. It was concluded that large position tolerance of the torch exists in plasma arc welding as the process is of DCEN (direct current electrode negative type where most of the thermal energy is released on the workpiece. Comparative study of micro plasma and GTAW welding of 0.8 mm thick SS304L welded structure using micro-plasma arc and tungsten inert gas (TIG) welding process was performed by Batool *et al.* [2015]. Micro-plasma arc welding was concluded to be the suitable process for welding of thin 304L sheets over GTAW process owing to applicability at higher welding speed. Sanchez-Tovar *et al.* [2011] concluded that the microstructure of the stainless steel is modified due to the micro-plasma arc welding procedure. Voropai *et al.* [1971] developed a technique of pulsed micro plasma butt welding of the shells of asbestos-metal gaskets made of Aluminum (thickness 0.2-0.3mm). Pulsed micro plasma welding results in steady burning of the arc on low

current and in the destruction of the oxide film on the joined metal. In this method, argon of a purity of not less than 99.8% is used as plasma forming gas and helium of a purity of not less than 99.5% as protective gas. Sepokurov *et al.* [1971] developed a controller that permits the smooth control of welding current over the 1-10A range, so that it can be used for welding thin components and for hard facing small components. The effect of the process parameters such as arc current, welding speed, arc length, shielding gas, and clamp distance of MPAW on the morphology and quality of 0.1mm thick 304 stainless steels edge joint were investigated by Tseng *et al.* [2013]. In MPAW the volt–ampere characteristic curve is almost flat i.e. it can provide an arc that is stable at very low currents and thus is suitable for welding thin metals. Thus, high quality welds having very smooth surfaces can be achieved by this process. The weld morphology had a low sensitivity to variations in the nozzle stand-off distances due to the collimated shape of the low current plasma arc. Zhang *et al.* [2009] applied artificial neural network to model the plasma arc welding of aluminum. A novel dynamically controlled plasma arc welding process was introduced by Chen and Pan [2011],which is able to minimize heat input into the work piece materials while maintaining desired full penetration, and it was used to weld Ti-6Al-4V alloy sheets. Comparing with welds such as gas tungsten arc and conventional plasma arc processes, the experimental results revealed the improvements when using the present process. The effects of pulsing current parameters on weld pool geometry, namely front width, back width, front height and back height of pulsed current in micro plasma arc welded Nickel alloy (Inconel 625) were analyzed by Prasad *et al.*[2012a, 2012b].Contour plots are drawn to study the interaction effect of the input process parameters. It is understood that grain size and ultimate tensile strength are more sensitive to peak current and pulse rate. It showed that grain size and ultimate tensile strength are inversely proportional; *i.e.* smaller the grain sizes higher the ultimate tensile strength of the weld joint. Prasad *et al.* [2014] studied and compared the weld quality characteristics like weld bead geometry, grain size, hardness and ultimate tensile strength of MPAW welded joints of various austenitic stainless steels. It was concluded that with similar welding conditions, AISI 304L has achieved sound weld bead geometry, highest tensile strength and hardness than the other grades of austenitic steel.

In summary, the researchers have tried to find the most feasible input parameters for a successful micro weld through experimental investigation. However in current study, two methods are investigated carefully-pulsed laser welding by Nd:YAG laser and microplasma

welding. The material of choice is Ti6Al4V alloy. Several methods have been utilized for fabrication of this alloy to obtain reliable joints [Donachie, 2000]. The joining technique of this material at a micro scale is not yet properly established. But very few literatures are available to join thin sheets of Ti6Al4V.

2.2 Weldability of Ti6Al4V Alloy

Titanium and its alloys belong to the group of materials whose application in various industries is ever increasing. The titanium alloys are common, readily available engineered metals that compete directly with stainless, copper alloys, nickel based alloys and composites. In the majority of these and other engineering applications, titanium has replaced heavier, less serviceable or less cost-effective materials. Titanium is available in different grades.Ti6Al4V, also known as grade 5, Ti6Al4V or Ti 6-4, is the most commonly used titanium alloy. It has a chemical composition of 6% aluminum, 4% vanadium, 0.25% (maximum) iron, 0.2% (maximum) oxygen, and the remainder titanium. It is a two phase α+β alloy, with aluminum as the alpha stabilizer and vanadium as the beta stabilizer. Being a relatively new metal and expensive to produce, its outstanding properties of high strength to weight ratio and excellent corrosion and heat resistance have made titanium and its alloys well established engineering materials [Donaiche, 2000]. Being a non-corrosive and biocompatibility material, titanium is one of the most widely used materials in aerospace [Boyer, 1996] and medical industry [Donachie, 2000]. It is also considered for many other applications where a combination of high strength, lightweight, good corrosion resistance, and high toughness are required. The primary attributes of titanium alloys with respect to its specific application in various industries is summarized below [Boyer, 1996, Donaiche, 2000; Faller and Sam Froes, 2001; Veiga *et al.*, 2012; Peters *et al.*, 2003].

High structural efficiency is the primary incentive for selection and design into aerospace engines and airframe structures and components. Exceptional corrosion resistance provided by a thin, invisible but extremely protective surface oxide film. This property provides the prime motivation for chemical process, marine and industrial use. Its excellent elevated temperature properties attributes to the application in hot gas turbine and auto engine components. It's nontoxic, non-allergenic and fully biocompatible with the body and tissue has driven its wide use in body implants, prosthetic devices and jewelry, and in food processing. Low modulus of

elasticity of the alloy (flexibility) makes it suitable for bending and cyclic stresses in deflection-controlled applications, making it ideal for springs, bellows, body implants and dental fixtures. Low thermal expansion coefficient allows for improved interface compatibility with ceramic and glass materials and minimizes wrapage and fatigue effects during thermal cycling. High melting point is responsible for its good resistance to ignition and burning in air, making it a choice light weight armor material for military equipment. It is essentially nonmagnetic (very slightly paramagnetic) and is ideal where electromagnetic interference must be minimized. Excellent cryogenic properties possess very low ductile-to-brittle transition temperatures and have therefore, been attractive materials for cryogenic vessels and components. Thus Ti6Al4V alloy has been used in various industries based on its various properties.

Weld ability of commercial pure titanium and most titanium alloys is fairly good. Ti6Al4V has the best weldability among the various alpha-beta alloys. This weldability can be attributed to the formation of good strength and better ductility [Ahmed and Rack, 1998]. Also, Ti6Al4V exhibited low hardenability when cooling from solution treatment temperature allowing the formation of more desirable Widmanstatten alpha-plus-retained beta. Due to its single phase mode of solidification (i.e. absence of low melting point eutectics), Ti6Al4V is highly resistant to solidification related cracking. Despite of its good weldability special cares must be taken during the welding process to avoid the following:

- The most instinct problem with welding of titanium as compared to other materials is the strong affinity with surrounding elements at high temperature. During heating, titanium becomes highly reactive and readily combines with oxygen, nitrogen, hydrogen, and carbon to form oxides that causes embrittlement of the weldment. Therefore, all parts of the heat-affected zone (HAZ) are necessary to shield from the atmosphere until the temperature drops below 650 K. Thus, additional shielding is generally provided for welding of titanium alloy [Donachie, 2000].
- Porosity is also one of the main problems in the welding of titanium alloys which is caused by shielding gas entrapment in a solidified structure [Donaiche, 2000]. The weld shape that primarily depends on laser power and scanning speed may be affected by porosity formation due to improper sample preparation and mechanical cleaning of the materials [Mueller *et al.*, 2006]. It is observed that the porosity increases with increase in material thickness during welding of Ti6al4V alloy [Hilton *et al.*, 2007]**.** Therefore, it is practically important that the

materials to be welded have to be properly shielded during heating and cooling period to protect from contamination and oxidation which might cause embrittlement of the weld joint.

- The electrical and thermal conductivity (16.4 W/mK) of titanium is relative low, and significantly affects the thermal cycle of welding, thus the cooling rate of weld metal and heat affected zone (HAZ) is relative low. The low cooling rates usually leads to grain growth of weld metal and HAZ as well. In a case of overheating of the joint, when the heat input of welding is too high, the brittle phases may be formed at the stage of low rate cooling resulting in hardness, brittleness increase. Additionally, as a result of high temperature gradients, significant stresses in the weld metal and HAZ may occur and sometime even cracks.

Various welding processes have been utilized in fabrication of this alloy at a macro scale level. The fusion welding processes most widely used for joining titanium are gas tungsten arc welding [Thomas *et al.*, 1992; Lathabai and Jarvis, 2001; Zhou and Chew, 2003], gas metal arc welding [Zhang and Li, 2001], plasma arc welding [Chen and Pan, 2011; Akbari*et al.*, 2014], laser beam welding [Fraser, 1982; Liu *et al.*, 2002; Caiazzo *et al.* 2004]and electron beam welding [Barreda*et al.*, 2001; Wang and Wu, 2012]. These processes characteristically deliver various amounts of heat energy in terms of heat input. An extensive research for comparing the influence of various welding process has been reported. Sun *et al.* [2002] compared the GTAW, plasma, and CO_2 laser welding of 5-mm-thick sheets of Ti6Al4V alloy and concluded that though laser welding is more efficient welding procedure. Pulsed and continuous GTAW welding are utilized and compared with welding of 2mm thick plate of Ti4Al5V [Mehdi *et al.*, 2016]. An investigation is carried out to determine the changes in the welding joint of 3 mm rolled plates of Ti6Al4V by GTAW and LBW processes [Raja *et al.*, 2009]. It was found that the LBW produced much smaller welds. Gao *et al.* [2013] reported a study aiming at comparing the properties of the Ti6Al4V titanium alloy joints with a thickness of 0.8 mm between pulsed Nd:YAG laser welding and GTAW. It can be concluded that pulse Nd:YAG laser welding is much more suitable for welding the thin Ti6Al4V titanium alloy plate than GTAW. It was also reported that compared to the joint formed by GTAW and EBM of 0.5mm thick Ti6Al4V alloy, welded by LBW has many advantages such as narrower weld-seam and fine grains [Yunlian *et al.*, 2000]. 5.4 mm Ti6Al4V alloy were evaluated for high vacuum electron beam welding, CO_2 laser beam welding and gas tungsten arc welding [Balasubramanian *et al.*, 2011]. The results

indicated that the electron beam welding is more suitable for Ti6Al4V sheet welding. A direct comparison was made of electron beam, laser beam and arc welding processes in Ti6Al4V alloy in nominal thicknesses of 0.10, 0.15, 0.20 and 0.6µcm [Banas, 1974]. The program described herein was undertaken as an initial step in establishing an evaluation framework which would permit a priori selection of advanced welding processes for specific applications. Researchers are also carried out Nd:YAG laser welding on 4mm thick Ti6Al4V alloy [El-Batahgy andDebRoy, 2014] and compared it to that of GTAW. The comparative study of micro plasma and GTAW of 0.8 mm thick SS304L welded structure was performed by Batool *et al.* [2015]. MPAW was concluded to be the suitable process for welding of thin 304L sheets over GTAW process owing to applicability at higher welding speed. Sanchez-Tovar *et al.* [2011] concluded that the microstructure of the stainless steel is modified due to the micro-plasma arc welding procedure. When GTAW is applied to titanium sheet exceeding 2 mm in thickness, the welding efficiency decreases because of the high thickness [Otani *et al.*, 2006]. Therefore, the application of GMAW in this case is a highly efficient welding technique which permits welding medium-thickness titanium sheets exceeding 2 mm in thickness in a single pass.

It is thus obvious from literature review that the titanium alloy is variably welded by different welding process. Laser welding was most widely used for welding of this alloy. Different processes exhibited different joint characteristics due to the difference in heat source delivering different heat input, different cooling and solidification rate. Thus, a lot of literatures have come up for welding of this alloy at the macro-scale level. However, the joining of titanium alloy at a micro-scale is not well established and there is lack of proper investigation in esteemed literatures.

2.2.1 Laser welding of Ti6Al4V alloy

Nd:YAG laser has been variably applied for welding of Ti6Al4V alloy. Blackburn *et al.* [2010] produced the welds with high internal quality in Ti6Al4V up to 3.25 mm in thickness by using Nd:YAG laser source. They inferred that the key to achieving an excellent weld quality is the appropriate choice of waveform, modulation frequency and modulation amplitude. Experiments have been carried out to find out the influence of welding parameters for joining of 3mm thick titanium alloy using Nd:YAG pulse laser [Akman *et al.*, 2009]. The peak temperature in the system controls the penetration depth for a pulse laser. Increase in pulse duration at

constant peak power impact on weld width enlarged with no substantial increment of the penetration depth. At too high peak power, the crater formation takes place on the surface of the materials as the temperature of the work pieces exceeds the evaporation point of the Ti6Al4V alloy. Akbari *et al.* [2014] performed experimental measurement of the temperature and HAZ dimensions in Nd:YAG laser welding of 3mm thick Ti6Al4V sheets. The molten pool geometry as well as peak temperature decrease with increase in the welding speed.1mm and 2 mm thick sheets of annealed Ti6Al4V alloy have been welded using a 4 kW Nd:YAG laser to study the effect of welding speed [Cao and Jahazi, 2009]. The width and area of fusion zone decreases with increase in welding speed. Although some welding defects such as underfill and porosity have been observed in butt joint of Ti6Al4V alloy (3.175 and 5.08 mm) using continuous wave Nd:YAG laser, high quality welds have been obtained using a high power laser where the joint efficiency has been achieved between 95 - 105 % [Kabir , 2013]. The effect of welding speed and laser power on weld quality of 1.6 mm thick Ti6Al4V in butt joint configuration using Nd:YAG laser was reported by Squillace [2012]. The keyhole mode welding predominant when heat input per unit length exceeds 30 kJ/m. Gao *et al.* [2013] studied the comparative analysis for 0.8mm thickTi6Al4V welded joint using pulsed Nd:YAG laser and GTAW. Laser welding produced less residual distortion, fine microstructure, narrow heat-affected zone (HAZ), high hardness and higher strength as compared to GTAW. Therefore, precisely controlled pulse laser welding is much more suitable for welding thin Ti6Al4V alloy than GTA welding. On 1.2 mm thick Ti6A14V alloy, high input produces H shape weld cross-sectional profile while low heat input produces V shape [Gao. *et al*., 2014]. The microstructure in the fusion zone (FZ) consisted of a fine acicular martensitic α′ solidification structure within the prior-β grains which resulted in maximum hardness in the FZ. The V-shaped welded joint had lower tensile strength and fractured at the HAZ zone whereas H-shaped welded joint fractured at the base metal. Researchers are also carried out Nd:YAG laser welding on 4mm thick Ti6Al4V alloy [El-Batahgy and DebRoy, 2014]. A shift of the focal point up to 2mm below the specimen surface considerably improved the laser square butt weld profile. Laser welding having lower heat input produced smaller weld zone with less distortion. Literatures indicate that Nd:YAG laser welding has been utilized and studied extensively to achieved reliable welds for various thickness of Ti-6Al-4V alloy. But no literature yet has reported the welding of Ti-6Al-4V sheet of thickness below 0.5mm or 500 μm.

2.2.2 Micro plasma welding of Ti6Al4V alloy

Baker [1985] has reported tensile, fracture toughness and fatigue crack propagation (FCP) data for PAW of 4 mm thick Ti6Al4V sheet. The welded specimens were generally fractured in the parent metal. Due to the high cooling rate, the formation of hard martensitic structure was observed in the fusion zone. As a result, the fracture toughness of the weld was lower than that of the parent material. Welding of 0.8 mm thick Ti6Al4V have been carried out by Karimzadeh *et al.* [2005; 2006]. A critical energy input was observed, below which the width of fusion zone remained almost constant and beyond that the width increased continuously with an increase in energy input. With the reduction of sheet thickness, the welding energy becomes critical and important factor for Ti6Al4Valloy because of its effect on solidification behavior, possibility of porosity formation and quality of welded structure. The dynamically controlled plasma arc welding process was developed that was able to minimize heat input into the workpiece materials while maintaining the desired full penetration to weld Ti6Al4V sheets [Chen and Pan, 2011]. Comparing with welds such as gas tungsten arc and conventional plasma arc processes, the experimental results revealed the improvements when using the present process. A parametric envelope for stable keyhole plasma arc welding was evaluated by Despande *et al.* [2012] to relate the primary welding parameters, i.e. current, traverse speed, plasma gas flow rate on 2.1mm titanium alloy. The plasma gas flow rate can be selected to ensure full penetration but does not generate significant undercut. The current and traverse speed can be selected to give smaller weld size. A faster traverse speeds results in increased cooling rate and reduced grain size. Experimental investigations were conducted to determine the influence of nozzle orifice diameter on weld width and weld stability for a range of substrate thicknesses in Ti6Al4V (2.1 mm, 3 mm, 6 mm) [Short *et al.*, 2011]. The nozzle orifice diameter has a pronounced yet differing effect on the formation and stability of keyhole welds in thin and thick substrates. Stable keyhole welds are difficult to form in thin substrates when welding with a relatively large nozzle orifice diameter as it resulted in larger weld dimensions, reduced weld pool penetration, greater changes to the weld dimension in response to an increased current, reduced weld pool stability and greater undercut. Traverse speed and current (i.e. specific heat input) have been shown to have a significant effect on weld width. Increasing the plasma gas flow rate has been shown to have a limited effect on the top and bottom widths [Short, 2009]. Various experimental trials are conducted on Ti6Al4V alloy of 2 mm thickness to obtain the full

penetration weld using plasma arc welding [Dhinakaran *et al.*, 2015]. Sun *et al.* [2014] reported an experimental-research work on prediction and optimization of the keyhole plasma arc welding process of thin (2.1 mm) Ti6Al4V structures.The experimental investigations include the determination of keyhole plasma arc welding process parameter envelopes using robotic welding and the measurements of thermal histories.

Thus quite a few investigations based on experiments have been performed on thin titanium alloy. However experimental determination of important parameters such as temperature and flow conditions in the micro scale weld pool is extremely difficult, owing to the small size of the weld pool, high temperature gradient and high peak temperature and such methods are also costly [DebRoy& David, 1995; Zhao *et al.*, 1999; Pitscheneder *et al.*, 1997]. Theoretical investigation by mathematical modeling of the process provides better understanding of the complex phenomena involved in welding. In parallel, it is also necessary proper understanding of the process model that involves thermal analysis of the joint as well as mechanical attributes such as distortion and residual stress. So, sophisticated computational model of laser welding is required for a wide range of process conditions that incorporates mutual interaction of various phenomena.

2.3 Structures and Properties of Micro joint

The quality and performance of welded joints depend on the weld geometry, the metallurgy of the welded zone and the heat affected zone, and any presence of welding defects. For obtaining an acceptable weld profile and satisfactory mechanical properties, control of weld bead shape is essential. The weld bead shape is influenced by combination of a number of welding parameters and the corresponding amount of heat input into the workpiece [Benyounis *et al.*, 2005]. Henceforth, it is an utmost necessity to determine the influence of the welding parameters on weld morphology as well as to identify the sources of welding defects which would help to identify the optimum combination of welding parameters.

The weld structure and properties are investigated by various researchers in micro welding especially that of laser micro welding. As compared to conventional welding process, laser welding produces much narrower heat-affected zones (HAZ). Ventrella *et al.* [2010] investigated the micro weld structure of stainless steel (AISI 316L) as a function of pulse energy. Higher pulse energy extended the HAZ and the grains in HAZ were coarsening as the pulse

energy increased. It was observed that the grains in the solid state were coarsening with decreasing parent material thickness. Thus, in thin foil welding, HAZ play significant role for welded joint quality. He *et al.* [2004] studied the weld metal composition change in micro joining of 304 stainless steel by Nd:YAG pulse laser and the composition changes were analysed by electron microprobe analysis. They concluded that concentrations of manganese and chromium in the weld pool decreased, whereas the concentrations of iron and nickel increased at the end of weld and the alloying element vaporization was most pronounced toward the end of the pulse. Tamaki *et al.* [2006] investigated the joint strength of glass using an amplified femtosecond fiber laser. For similar type of glass substrate, the maximum joint strength was achieved as 9.87MPa. However, during micro welding between non-alkali glass and silicon substrate, the joint strength was achieved as 3.74 MPa. El Kadiri *et al.* [2006] investigated the tensile and creep properties of laser micro-welded thin Fe-Cr-Al foil. The laser bead shows higher tensile resistance than the base material. At higher temperature, the bead creeps significantly higher than the base material. It is realized from the experimental evidence that the size and shape of weld fusion zone developed during welding depends on input power density, thermal diffusivity, and weld duration. Weld sizes grows till it reaches a steady state once the balance between heat absorbed and heat dissipation is established. Short duration pulse of high peak power produces a deeper weld but can also lead to excessive spatter. On the other hand, pulse of low peak power and longer duration produce a shallower weld with fewer spatters. Hence, an optimum calibration of pulse characteristics is necessary to obtain successful joint.

Few literatures have also come up to investigate the microplasma welding joint characteristics. Comparative study of the weld geometry, distortion, microstructure, and mechanical properties of 0.8 mm thick SS304L welded structure using micro-plasma arc and tungsten inert gas (TIG) welding process was performed by Batool *et al.* [2015]. Micro-plasma arc welding was concluded to be the suitable process for welding of thin 304L sheets over GTAW process owing to applicability at higher welding speed. Moreover, the welded samples had higher tensile strength, higher ductility, narrow heat affected zone and lower distortion. Shiv Prasad *et al.* [2014] studied and compared the weld quality characteristics like weld bead geometry, grain size, hardness and ultimate tensile strength of MPAW welded joints of various austenitic stainless steels. It was concluded that with similar welding conditions, AISI 304L has achieved sound weld bead geometry, highest tensile strength and hardness than the other grades

of austenitic steel. Sanchez-Tovar *et al.*[2011]concluded that the microstructure of the stainless steel is modified due to the micro-plasma arc welding procedure.

Ishida [1987] investigated the interfacial microstructures and intermetallic compounds produced by plasma arc butt fusion welding of aluminium to mild steel. Experiments were carried out on 5mm thick mild steel and aluminium plates. An intermetallic compound alloy layer formed at the interface region between mild steel and aluminium. Luo [2002] analysed the surface microstructure and the anodic polarization curves in a sulphuric acid solution of a Cr19Ni9 stainless steel submerged arc welded joint before and after surface melting using a 4 A micro-plasma arc. The results showed that both the heat-affected zone and the weld metal of the as-welded joint had a lower corrosion resistance than the as-received parent material, while the arc melted joint had a significantly increased corrosion resistance. This increase in corrosion resistance is attributed to a rapid solidification of the melted layer. Rapid solidification of the melted layer refines its microstructure, decreases micro segregation, and inhibits the precipitation of chromium carbides at the grain boundaries.

2.3.1 Micro structural and mechanical characterization of Ti6Al4V joints

Ti6Al4V is a two phase (α+β)alloy with around 6% aluminum (wt. %) stabilized the α phase and about 4% (wt. %) vanadium stabilized the β phase. Fig.2.4 shows the Ti-6Al and V phase diagram for Ti6Al4V (1) illustrating the β transus and the weight percent (wt. %) alpha within the two-phase region at different temperatures.

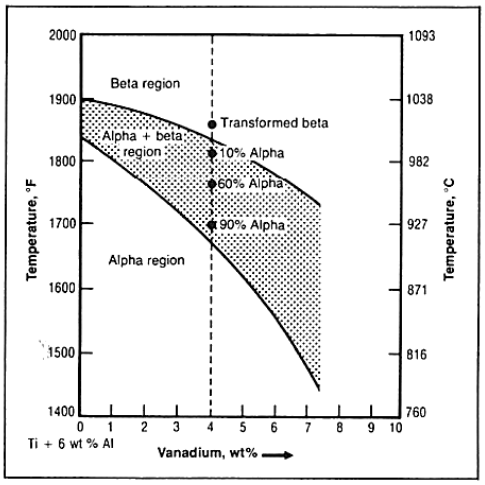

Fig. 2.4 Phase Diagram for Ti6Al4V [Donaiche, 2000].

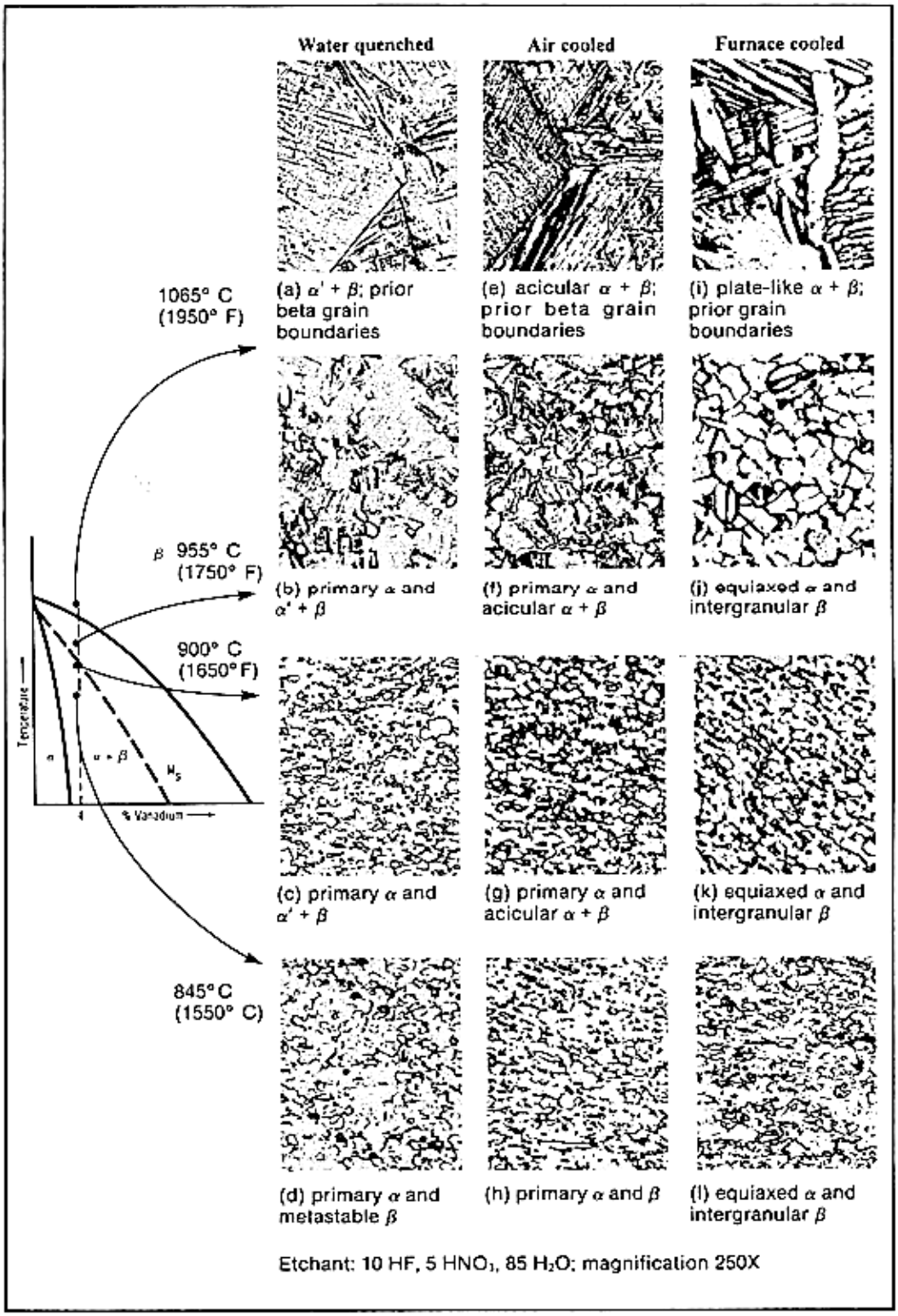

Fig. 2.5 Different Ti6Al4V Microstructures [Donaiche, 2000].

Figure 2.5 shows different microstructures that can be formed in this alloy, depending on the cooling rate. The variation of microstructure in the different zones can be attributed to the heating and the cooling cycle of Ti6Al4V alloy. In welding of Ti6Al4V, $\alpha \rightarrow \beta$ phase transformation during rapid heating and the decomposition of the $\beta \rightarrow \alpha$ phase during cooling [Donaiche, 2000]. At the end of solidification, the structure is completely beta. As the cooling process commences, transformation of beta to alpha occurs at temperatures below the alpha solves. The variation of microstructure in the different zones can be attributed to the heating and the cooling cycle of Ti-6Al-4V alloy. Thus the microstructure that is formed after the welding process in the different zones is dependent on the cooling rate as a function of the heat input. If the cooling rate is higher than the critical cooling rate (~ 623K/s) of Ti6Al4V, α' martensite is formed (diffusionless transformation). At slower cooling rate, diffusion controlled nucleation takes place resulting in the growth of secondary lamellae [Fan *et al.*, 2005; Ahmed and Rack, 1998]. Some β phase is always retained irrespective of the cooling rate. Proper studies on the microstructure–mechanical properties relationships of welded joints would enhance the materials development and optimization process of titanium alloys.

During slow cooling rate, diffusion phase transformation takes place. Diffusional phase transformations consist of three phases: nucleation, growth and saturation. They are usually assumed to follow the well-known Johnson-Mehl-Avrami equation with specific parameters *n* and *k* for different transformations and materials:

$$f_{\alpha}(t) = f_{\alpha}^{ini}(1 - e^{[-kt]^{n}}) \qquad (2.1)$$

where *f* is the volume fraction of the new phase, *t* is the isothermal time duration, *k* is a coefficient dependent on the temperature, composition of parent phase, and grain size, and *n* is also a coefficient dependent on the type of phase transformation and grain growth.

When the material is heated above the beta transus and cooling below the martensitic start temperature at sufficient high cooling rate, martensite is formed and transformation is given by diffusionless phase transformation, which is commonly simulated by the Koinstinen-Marburguer equation:

$$f_m = f_\beta(1-\psi e^{\left[-k(M_S-T)\right]}) \tag{2.2}$$

In a welding process of titanium alloy, especially fusion modes, temperature gradient, high peak temperatures, and rapid thermal fluctuation occur as a welding heat source passes through the material [Wong *et al.*, 1997; Wu, 1981]. These temperature fluctuations non-uniformly alter the microstructure of the material and create the heat affected zone (HAZ) with the large beta grain size adjacent to the weld fusion zone (FZ) and causes deterioration of the microstructure and mechanical properties of the original material in the joining region [Baeslack *et al.*, 1990; Nordin *et al.*, 1987]. Welding processes with low heat input such as EBW and LBW cause high cooling rates that result in low toughness welds [Zhou and Chew, 2003; Wang *et al.*, 2003; Liu *et al.*, 2002; Fraser, 1982; Barreda *et al.*, 2001]. Welding processes with high heat input such GTAW and GMAW produce poor fusion zone ductility [Zhang, Y.M and LI, P.J., 2001; Thomas *et al.*, 1992; Keshava *et al.*, 1998].

Several studies have been performed which aimed at understanding the process-microstructural relationship and optimizing the mechanical properties [Liu *et al.*, 2015; Cao and Jahazi, 2009, Khurram and Shehzad, 2012]. Several researches have also been done to compare the microstructure and mechanical properties obtained by various methods. The welding technique used for fabricating the Ti6Al4V makes a significant effect in the microstructure of the weldments. The microstructural changes are significant, since it determines the properties, behavior and reliability of the welded joints. Sun *et al.* [2002] compared the parameters and microstructures for GTAW, plasma, and CO_2 laser welding of 5-mm-thick sheets of Ti6Al4V alloy. The depth and width of the welds produced by laser welding were found to decrease with increasing welding speed. In terms of microstructure, higher current levels for GTAW and plasma, as well as lower speeds for laser welding produced larger grain sizes due to the increase in heat input. Laser welds produced much smaller grains than either GTAW or plasma. The hardness of the fusion zone increased with increasing welding current for both plasma and GTAW welds, and with increasing welding speed for laser. Laser welding produced much harder welds than either plasma or GTAW welding due to the high cooling rates.A comparative study of evaluation in 2mm thick in Ti6Al4V alloy by pulsed and un-pulsed GTAW welds was carried out [Mehdi *et al.*, 2016]. Increasing the pulse frequency in pulsed GTAW refines the prior-grain size in the fusion zone of Ti6Al4V alloy compared to un-pulsed process. An investigation was

done to determine the changes in the microstructure of butt joints prepared from 3 mm rolled plates by GTAW and LBW processes [Raja *et al.*, 2009]. It was found that the LBM produces smaller heat affected zone with high hardness. Gao *et al.* [2013] concluded that the joint obtained by laser beam welding has the characters of fine microstructure, narrow HAZ, and high Vickers hardness. It was also reported that compared to the joint welded by GTAW or EBW, titanium alloy welded by LBW produces narrower weld-seam with fine grains [Yunlian *et al.*, 2000]. Balasubramanian *et al.*, 2011 indicated that the EBM electron beam welding is more suitable for Ti6Al4V sheet welding as compared to GTAW and CO_2 laser welding. Electron beam and laser welds were formed at substantially lower energy inputs per unit weld length than either plasma arc or GTAW. For this reason the former experienced much more rapid cooling rates and therefore exhibited finer fusion zone grain structure than the latter. On the other hand, the rapid cooling rates encountered in electron and laser beam welds led to increased weld zone hardness and decreased fracture toughness in comparison to arc welds. Researchers are also carried out Nd-YAG laser welding on 4mm thick Ti6Al4V alloy [El-Batahgy and DebRoy, 2014] and compared it to that of GTA welding. The welded samples produced by laser welding exhibited much lower distortion and smaller fusion zone size than the GTA welded samples. However, the laser welded samples had higher hardness in the fusion zone due to higher amount of acicular alpha prime martensite which resulted from the higher cooling rate but better impact and corrosion properties. Thus, it can be concluded that that properties of the welded joints were influenced not only by the microstructure but also by the fusion zone size.

Several studies have come up to investigate the weld joint characteristics of Ti6Al4V joint mainly formed by Nd:YAG laser. Squillace *et al.* [2012] investigated the influence of the LBW process parameters on weld morphology. They explained the origin of the main geometrical features of butt joints such as underfill and face and root reinforcement. Independence of the specific heat input, this defect showed a maximum, which separates two different welding regimes: keyhole welding, at low heat input, and a welding regime where heat conduction around the keyhole is predominant, at high heat input. The weldability of 5.1-mm thick Ti6Al4V sheets in the mill-annealed condition was investigated using a continuous wave 4 kW Nd:YAG laser at various welding speeds and defocusing distances [Kabir *et al.*, 2010]. Although some welding defects such as underfill and porosity were observed, sound welds without cracks can be obtained using a high power Nd:YAG laser. The hardness was found to be

maximum in the fusion zone (FZ) and the heat affected zone (HAZ) near the fusion boundary, beyond which a gradual decrease occurred to the base material. Annealed Ti6Al4V alloy sheets with 1 and 2 mm thickness are welded using a 4 kW Nd:YAG laser system [Cao and Jahazi, 2009]. Weld joints without or with minor cracks, porosity and shape defects were obtained indicating that high-power Nd:YAG laser welding is a suitable method for Ti6Al4V alloy. The fusion zone consists mainly of acicular α' martensite leading to an increase of approximately 20% in hardness compared with that in the base metal. The heat-affected zone consists of a mixture of α' martensite and primary α phases. Significant gradients of microstructures and hardness are obtained over the narrow heat-affected zone. The laser welded joints have similar or slightly higher joint strength but there is a significant decrease in ductility. The loss of ductility is related to the presence of micro-pores and aluminum oxide inclusions. Joints with regular shapes, without visible cracks, pores, and geometrical defects were achieved during laser beam welding of Ti6Al4V alloy [Kashaev *et al.*, 2016]. Tensile tests revealed high joint integrity in terms of strength and ductility for both the butt joint and T-joint geometries. Fracture always occurred in the weld without any plastic deformation in the base material outside the weld. The V-and H shaped weld cross-sectional profiles were obtained under low and high heat input, respectively in pulse Nd:YAG laser welding of 0.8mm Ti6A14Valloy [Gao *et al.*, 2014]. The microstructure in the fusion zone (FZ) of V-and H-shaped welded joint consisted of a fine acicular martensitic α′ solidification structure within the prior-β grains, responsible for the maximum hardness in the FZ. Tensile tests revealed that the V-shaped welded joint fractured at the near heat-affected zone (HAZ)/base metal (BM) interface, but the H-shaped welded joint fractured in the BM. Furthermore, the tensile strength of the V-shaped welded joint was lower than that of the H-shaped welded joint. This was attributed to the fact that the heterogeneity of strain distribution at the interface of HAZ and BM of the V shaped welded joint was greater than that of the H-shaped welded joint during tensile process. Krasnoperov *et al.*, [2004] observed that the widths of the weld bead on the upper and lower surfaces were almost similar at high heat input; however, the weld bead was wider at the top than at the bottom at low heat input. Thus, heat input plays an important role to decide the weld bead geometry.

Not much investigation have come up on the use of intermediate energy input welding processes, thus, an intermediate heat input welding process such as microplasma arc welding can be selected as a base process to study the effect of controlled microstructural development in the

titanium alloy. Baker [1985] reported plasma arc welding (PAW)of 4 mm thick Ti6Al4V sheet. The welded specimens were generally fractured in the parent metal. Due to the high cooling rate, the formation of hard martensitic structure was observed in the fusion zone. As a result, the fracture toughness of the weld was lower than that of the parent material. Karimzadeh *et al.* [2005; 2006] investigated the effect of MPAW process parameters on grain growth and porosity distribution of 0.8 mm thin sheet of Ti6Al4V alloy. The welding energy is a critical and important factor in joining of Ti6Al4V thin sheet because of its effect on weldment growth, grain growth, porosity distribution, and quality of welded structure. Metallographic characterization has shown that coarse primary beta grains exist in the fusion zone. This is due to the fact that these grains have nucleated epitaxially upon coarsened beta grains in the near heat affected zone (NHAZ) and grown competitively into the molten weld pool. Evaluation of grain size indicates that there is a threshold energy input for phase transformation of →β in the HAZ. In the case of lower energy input, grain growth of phase inthe HAZ could be restricted by phase. The presence of small quantities of this phase at high peak temperatures in the weld cycle is sufficient to prevent beta grain growth of HAZ and fusion zone (FZ). The SEM and optical metallographic examinations also indicated that porosity occurs in FZ. The dynamically controlled plasma arc welding process was developed that was able to minimize heat input into the work piece materials while maintaining the desired full penetration to weld Ti6Al4V sheets [Chen and Pan, 2011].

Thus Ti6Al4V has been reported to have good weldability, but its strength, ductility, and toughness may be significantly varied, depending on the thermal cycling history during manufacturing. The welding process used, the amount of specific heat input, the cooling rate and the peak temperature have a definite effect on its structure and properties. Thus, the fusion welding of this alloy has to be carefully carried out under controlled combination of process parameters to get the desirable good joints. Modeling of the complex phenomenon by numerical method may provide the real picture of the complicated process including the effect of individual process parameter as well as the interaction of different parameters.

2.4 Theoretical Model

Welding is complex process that involves interactions of thermal, mechanical and metallurgical phenomena. An assumed physical picture of the process can be modeled mathematically and the robustness of the model can be validated by comparing with experimental results. A model capable of predicting experimental results means that previously immeasurably parameters can be estimated. The most important data that needs to be estimated in metal welding are (1) the thermal cycle at each location in the fusion and heat affected zone (HAZ), which defines the extent of any phase change, (2) the peak temperature distribution, and (3) the cooling rates which would affect the formation of metastable structures such as martensite. Without a mathematical model the values of these parameters are very difficult to obtain.

Various analytical models of welding phenomenon exist from early date backs with lots of simplifications and assumptions [Rosenthal, 1941, Nguyen *et al.*, 1999]. The restrictive assumptions will however limit the practical utility of the results. Analytical models are useful for only simple geometries and tend to ignore factors such as fluid flow, actual heat source distribution, latent heat, and the temperature dependence of physical properties. Thus various computational models have evolved in the recent decades and made numerical modeling more practical oriented. Several numerical methods such as finite element [Bag *et al.*, 2009; Tsirkas *et al.*, 2003], finite difference [Kim *et al.*, 2002; Mazumder and Steen, 1980; Cherepanov, *et al.*, 2006], and finite volume [He *et al.*, 2004; Taylor *et al.*, 2002] are extensively used for the simulation of welding process. Moreover most of the work is restrictive by the assumption of conductive heat transfer [Chang and Na, 2002; De *et al.*, 2003; Frewin and Scott, 1999; Goldak *et al.*, 1984; Kim *et al.*, 2002]. Molten material flow within small weld pool may have significant effect on heat transfer and influence the overall temperature field of whole solution domain [Cherepanov and Shapeev, 2009; He *et al.*, 2004; He *et al.*, 2005]. This precise estimation of temperature field in microwelding is significant to estimate residual stress and distortion of final weld joint. The microjoining process relates the following simplified blocks of physical phenomena which are necessary for the development of numerical process model.

- Heat transfers from the torch to substrate material. So a substantial heat source model is necessary when the beam or arc interact with actual parent material to be joined. The intensity of the heat source defines the shape of the molten pool.

- The beam or arc produces a dynamic weld pool of liquid metal. Within the weld pool the heat transfer and fluid flow occurs and the rest of the domain are subjected to heat conduction only.
- After removal of the heat torch, the rapid cooling and solidification occurs in the whole solution domain. The rate of cooling and solidification decides the final microstructure and structural properties of the joint.
- Finally, a permanent distortion and residual stress occurs in the joint. The nature of the stress level can be linked with the structural change of material when it changes phase such as austenite to martensite in welding of steels.

2.4.1 Heat source model

An accurate description of the heat source and the appropriate choice of the relevant parameters are essential to the numerical simulation of thin-plate welded structures [Sun *et al.*, 2014]. The heat transfer model for laser welding represents the solution of heat conduction equation when two work-pieces are joined. The heat source is applied on the top surface of the work-piece and rest of the workpiece is subjected to the convection and radiation heat losses.Various heat source models have been proposed so far for welding process. Most of the researchers employed a Gaussian distribution of heat flux (W/m^2) deposited on the surface of the workpieces. One of the early numerical models using finite difference method starts with Mazumder and Steen [1980] by assuming a Gaussian distribution of beam intensity on the top of weld surface which is treated as a surface heat flux. They also assumed further energy absorption within high penetration weld pool by following Beer-Lambert's law, $q_z = q_0 e^{-\beta z}$, where β is the absorption coefficients and q_z and q_0 are the heat intensities at depth z and on the surface, respectively. This model can be used to simulation of the initiation of the keyhole.The Gaussian heat flux is represented by following:

$$\dot{Q} = \frac{\alpha d P}{\pi r_{eff}^2} \exp\left[-d\frac{x^2+y^2}{r_{eff}^2}\right] \quad (2.3)$$

where P refers to laser power, r_{eff} is effective radius of laser beam on the workpiece surface, d is the power density distribution factor of heat source. To reduce the number of process parameters, it is generally assumed 1 – R = α, R and α are reflectivity and absorption coefficient of the

material.The simulated results were obtained by solving three dimensional transient heat conduction equations which is expressed as

$$\frac{\partial}{\partial x}\left(k\frac{\partial T}{\partial x}\right)+\frac{\partial}{\partial y}\left(k\frac{\partial T}{\partial y}\right)+\frac{\partial}{\partial z}\left(k\frac{\partial T}{\partial z}\right)+\dot{Q}=\rho C_p\frac{\partial T}{\partial t} \tag{2.4}$$

where ρ , C_p and k refer respectively to density, specific heat and thermal conductivity of substrate material; T and t refer to temperature and time variable respectively. The term $\dot{Q}$ refers to the internal heat generation per unit volume per unit time. .

However, only surface heat flux may not produce sufficient weld depth during simulation of temperature profile. Although such a surface mode of heat source may be used for the shallow penetration arc welding processes it is not suitable for deeper penetration. Goldak *et al.* [1984] proposed a double-ellipsoidal heat source model, which has the capability of analyzing the thermal history of deep penetration welds like GMAW. However, the double-ellipsoidal distribution of heat intensity is still not applicable to the high-density welding processes with high ratio of the weld penetration to width, such as keyhole PAW. Hence researchers often encounter this problem by the use of a volumetric heat source term [Chang and Na, 2002a; Chang and Na, 2002b; Goldak *et al.*, 1984; Kaplan, 1994; Frewin and Scott, 1999; Bag *et al.*, 2009; De *et al.*, 2003].

The model of Mazumder and Steen [1980] was combined with a heat flux equation and used for internal heat generation in the case of deep penetration welding [Neto and Lima, 1994] . The combined heat source equation is presented as follows:

$$\dot{Q}=\frac{2\beta P}{\pi r_{eff}^{\,2}}\exp\left[-2\frac{r^2}{r_{eff}^{\,2}}-\beta z\right] \tag{2.5}$$

where an the effective radius r_{eff} is assumed at which the intensity falls to 13.5% of the peak value. Sonti and Amateau [1989] also treated the laser weld heat input as an internal heat source rather than a surface flux by using the relation:

$$\dot{Q}=\frac{9P}{\pi\hat{z}r_{eff}^{\,2}}\exp\left[-3\frac{r^2}{r_{eff}^{\,2}}-\frac{3z}{\hat{z}}\right] \tag{2.6}$$

Thus, the heat source was assumed to have a Gaussian distribution in the radial direction with exponential decay in the thickness direction. An effective radius and depth of the energy source, r_{eff} and $\hat{z}$, respectively, were assumed at which the intensity falls to 5% of the peak value. In another model, it was proposed that the volumetric heat source has a Gaussian transverse distribution, corresponding to the laser intensity profile and that this distribution extends uniformly with depth into the material for a distance d_k, forming a 'Gaussian rod' [Mueller, 1994] which is represented as

$$\dot{Q} = \frac{P}{\pi d r_{eff}^2} \exp\left[-2\frac{r^2}{r_{eff}^2}\right] - u(z) \tag{2.7}$$

where r_{eff} an effective radius is assumed at which the intensity falls to 37% of the peak value, u(z) = 1 for $0 \leq z \leq d$ and u(z) = 0 otherwise. The distance *d* is the maximum keyhole depth, or maximum penetration of the vaporization isotherm into the material, and must be determined iteratively as part of the model.An adaptive volumetric heat source term was introduced which may be appropriate to simulate heat transfer analysis in micro scale joining processes shown in Fig.2.6 [Trivedi *et al.*, 2013, Bag *et al.*, 2009].

$$\dot{Q} = \frac{6\sqrt{3}P\alpha}{\pi a^2 b\sqrt{\pi}} \exp\left[-3\frac{r^2}{a^2} - 3\frac{z^2}{b^2}\right] \tag{2.8}$$

where $a = \begin{cases} r_{eff} & for\ a < r_{eff} \\ w_i & for\ a > r_{eff} \end{cases}$

$b = p_i$

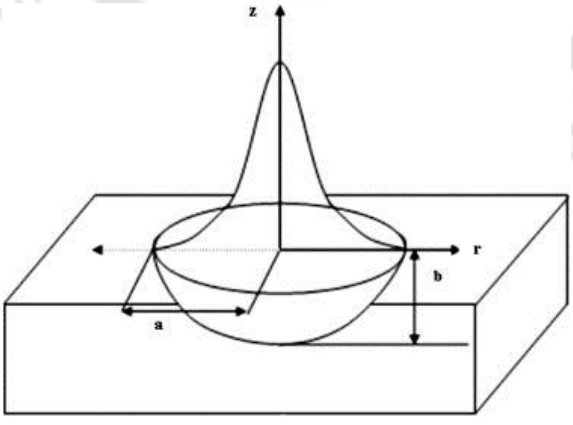

Fig. 2.6 Adaptive heat source model [Trivedi *et al.*, 2013, Bag *et al.*, 2009].

Several researchers used finite element based commercial software to simulate temperature profile in microjoining process using heat conduction equation. Chang and Na [2002a; 2002b] investigated various heat source equations to simulate laser spot welding for thin stainless steel plates using ABAQUS. The results suggest that temperature profiles and weld deformation vary according to the heat source equation of the laser beam. Therefore, it is essential to incorporate an accurate model of the heat source for precision analysis in microwelding. They considered a two dimensional finite element based heat conduction model with pulsed laser energy as a volumetric heat source. The laser energy is mathematically expressed as:

$$\dot{Q}(r,z,t) = (1-R)\frac{2P}{\pi r_{eff}^2}\exp\left(-\frac{2r^2}{r_{eff}^2}\right)\exp(-\eta z) * H(t) \qquad (2.9)$$

where R is the reflectivity, P the laser output power and r_{eff} the effective radius of laser beam at the workpiece surface, r represents the coordinate along radial direction, z stands for coordinate along vertical direction, t denotes time, η denotes laser absorption coefficient and H(t) represents the time variation of the pulse and the unit step input is expressed as

$$H(t) = \begin{cases} 1 & \text{for } 1 < t < t_p \\ 0 & \text{for } t > t_p \end{cases} \qquad (2.10)$$

where t_p is the pulse duration. Chung and Lin [2005] used similar volumetric energy expression during microjoining of pint to plate using ANSYS. Chang and Na [2002a] investigated various heat source equations to simulate laser spot welding for thin stainless steel plates. The results suggest that temperature profiles and weld deformation vary according to the heat source equation of the laser beam. Kim *et al.* [2002] used finite difference method to simulate microjoining of thin A3003 Al sheet by a pulsed Nd:YAG laser beam. The authors demonstrated that the welding stability as well as evaporation is greatly affected by the modulation of laser pulse shape for the same laser energy and welding parameters. Three-dimensional conical heat source is a volumetric heat source that considers the heat intensity distribution along the workpiece thickness. As shown in Fig.2.7, the heat intensity deposited region is the maximum at the top surface of workpiece, and is the minimum at the bottom surface of workpiece. Along the thickness of the workpiece, the diameter of the heat density distribution region is linearly

decreased. But the heat density at the central axis (z-direction) is kept constant. At any plane perpendicular to z-axis, the heat intensity is distributed in a Gaussian form. Thus, in fact, it is the repeated addition of a series of Gaussian heat sources with different distribution parameters and the same central maximum values of heat density along the workpiece thickness.

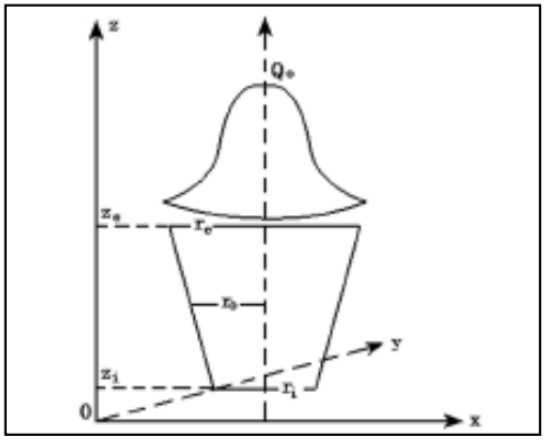

Fig. 2.7 Conical heat source model [Goldak and Akhlaghi, 2005].

Du *et al.* [2004] used a heat source model compromising a Gaussian plane heat source to the top surface and a cylindrical heat source along the z-direction to simulate the geometry profile of weld pools during laser beam welding for titanium alloys. The combined heat source they used can reflect the deep penetration of laser beam welding, but the cylinder heat source cannot accurately predict the reducing of the molten width along the z-direction of a laser beam welding bead. In some cases, the selection of an appropriate model is not obvious. Although a conical heat source may be used for simulation of the full penetration laser welding process, it does not reflect the action of surface tension on both the top and bottom weld pool surface, so it is not suitable for modeling hourglass-like weld pool shape [Casalino *et al.*, 2015]. The power intensity for combined heat source model can be calculated:

$$Q_o = \frac{\eta P}{\int f_1 dV_{1+} \int f_2 dV_2} \tag{2.11}$$

where η is the thermal efficiency, P is the laser power, and f_1 and f_2 are the heat intensity distribution for the two heat sources, V_1 and V_2 and are the volumes of the two heat sources, respectively. A new heat source model for quasi-steady state temperature field in keyhole PAW

is developed to consider the "bugle-like" configuration of the keyhole and the decay of heat intensity distribution of the plasma arc along the direction of the workpiece thickness [Wu *et al.*, 2006]. Researchers have illustrated several adaptive heat source models for predicting the weld dimensions and distribution of heat intensity strike through along the workpiece thickness during PAW process [Wang *et al.*, 2005; Wu *et al.*, 2006] to make it more general and close to the reality. The adaptive volumetric term is defined by mapping the instantaneous value of the computed weld dimensions (length, width and depth) with respect to time step (transient) or load step(steady-state) and thus, the requirement of a-priori definition of the source geometry is avoided [Bag and De, 2010].

Thus, over the time, the researchers have tried to adopt a suitable heat source model for modeling of accurate heat input being transferred to the material. However, an accurate heat source model to consider the heat transfer in thin plate welding is not well established. Still, there is a need of investigation whether a surface or volumetric heat source in plasma or laser microwelding process is appropriate.

2.4.2 Conduction heat transfer model

To determine the thermal fields during the welding process, the equation of energy conservation is required. The heat transfer of laser beam welding is usually calculated by applying classical heat conduction theory. Conduction heat transfer based models are simpler, computationally inexpensive and yet can provide fairly reliable results in several simple welding systems [Trivedi *et al.*, 2013; Goldak*et al.*, 1984; Frewin and Scott, 1999; De *et al.*, 2003]. Thus, conduction heat transfer based models are often preferred to the convective heat transport based weld pool simulations for smaller weld pool sizes and joining processes involving rapid melting and solidification. The conduction heat transfer based weld pool models also find tremendous application in the calculations of weld distortion and residual stress [Teng *et al.*, 1998; Deng *et al.*, 2007; Trivedi *et al.*, 2013; Deng, 2009], where the temperature field over a very large domain is of greater importance in comparison to its local variation in weld pool. In conduction based heat transfer analysis, a volumetric heat source is often used further too numerically compensate the influence of convection heat transport in weld pool and effectively describe the heat source phenomenon in the weld pool [Li *et al.*, 2013].

There are several numerical studies on the effect of different welding parameters on thin plate welding of other materials based on conduction based heat transfer. The laser welding modes such as conduction, conduction–penetration, and keyhole welding, are studied at different beam energy levels. A three-dimensional finite-element model is developed to analyze the transient heat flow for AISI304 stainless steel [Buvanashekaran *et al*, 2009]. The heat input to the developed model is assumed to be a three-dimensional conical Gaussian heat source. Finite-element simulations are carried out by using finite-element code, SYSWELD, and FORTRAN subroutines available within the code are used to obtain the numerical results. Several studies on the welding of Ti6Al4V have been conducted numerically based on conduction mode weld pool neglecting the complex phenomenon associated with convective heat. Frewin and Scott [1999] produced a time-dependent 3D model of heat flow during pulsed Nd:YAG laser welding. They found that the fusion and HAZ produced numerically were extremely close to those produced experimentally. Uncoupled steady-state and transient heat transfer analyses were performed to predict fusion zones and thermal histories of titanium sheets to investigate the relationships between the primary welding parameters, i.e. current, traverse speed, plasma gas flow rate and the weld efficiency, using inverse finite element modeling [Deshpande *et al.*, 2012]. The numerical modeling was conducted focusing the attention on the model of the laser-material interaction, which allowed predicting the temperature distribution during the thermal cycle and the related phase transformations [Casalino *et al.*, 2015]. Numerical simulations are carried out with conical heat source and modified conical heat source, using finite element method to predict the weld bead geometry during plasma arc welding of thin sheets of titanium alloy [Dhinakaran *et al.*, 2015]. The effect of trailing gas shielding, latent heat, and radiative and convective heat transfer are taken into account while performing the transient thermal analysis which significantly alters the sensitivity and accuracy of the model. A numerical investigation of laser welding of titanium alloy (Ti6Al4V) for modeling the temperature distribution to predict the heat affected zone (HAZ), depth and width of the molten pool is performed by Akbari *et al.*, 2014. The complex physical phenomenon causing the formation of keyhole has not been considered. Yang *et al.* [2010] provided a finite element model to predict the depth and width of HAZ in laser heating of Ti6Al4V alloy plate and found that the depth and width of HAZ were decreased with an increase of laser scan speed.

However, the explorations on the development of a numerical model which simulates the welding of thin sheets of titanium alloy are limited and confined to primordial and elemental stage.

2.4.3 Convective based weld pool model

The numerical model that takes into account fluid flow is more close to the real welding process. Though the small characteristic length in microwelding limits the liquid flow to some extend yet convection is still an important mechanism of heat transfer in weld pool. Although a few literatures have come up to study the heat transfer and fluid flow in micro joining, till it is in the premature stage and needs to be investigated.Convective flow of liquid metal within weld pool is the most important factor to influence the pool geometry, change in pool shape, composition and the aspect ratio. The shape and size of weld pool are decided by the nature of circulation of liquid metal that are driven by electromagnetic, surface tension gradient and buoyancy forces. An extensive review of the physical processes prevalent in fusion weld pool was studied by Debroy and David [1995].According to the authors, the convective flow in weld pool is driven by surface tension, buoyancy and when electric current is used, electromagnetic forces. Aerodynamic drag forces of the plasma jet might also be contributed to the convective flow in the weld pool. Buoyancy effects originate from the spatial variation of the liquid-metal density, mainly because of temperature variation, and, to a lesser extent, from local composition variations. Electromagnetic effect is a consequence of the interaction between the divergent current path in the weld pool and the magnetic field that it generates. This effect is important in arc and electron-beam welding, especially when a large electric current passes through the weld pool. In arc welding, a high velocity plasma stream impinges on the weld pool. The friction of the impinging jet on the weld pool surface can cause significant fluid motion. The spatial gradient of surface tension results in a driving force, referred to Marangoni stress, along the top surface of the weld pool. The spatial variation of the surface tension at weld-pool surface may arise owing to variations of both temperature and composition [He *et al.*, 2004]. Frequently the main driving force for convection is the spatial gradient of surface tension at the top surface of the weld pool from its center to the periphery. For such a situation, the Marangoni stress can be expressed as [DebRoy and David, 1995]:

$$\tau = \frac{d\gamma}{dT} \cdot \frac{dT}{dy} \qquad (2.12)$$

where τ is the shear stress due to temperature gradient, γ is the interfacial tension, T is the temperature, and y is the distance along the surface from the axis of the heat source. The nature of liquid convection in weld pool and the shape of the weld pool due to different driving forces are schematically shown in Fig. 2.8. Due to the variations of temperature and composition, the temperature coefficient of surface tension may be positive or negative as shown in Figs 2.8(b) – (c) and the shape of the weld pool is influenced subsequently.

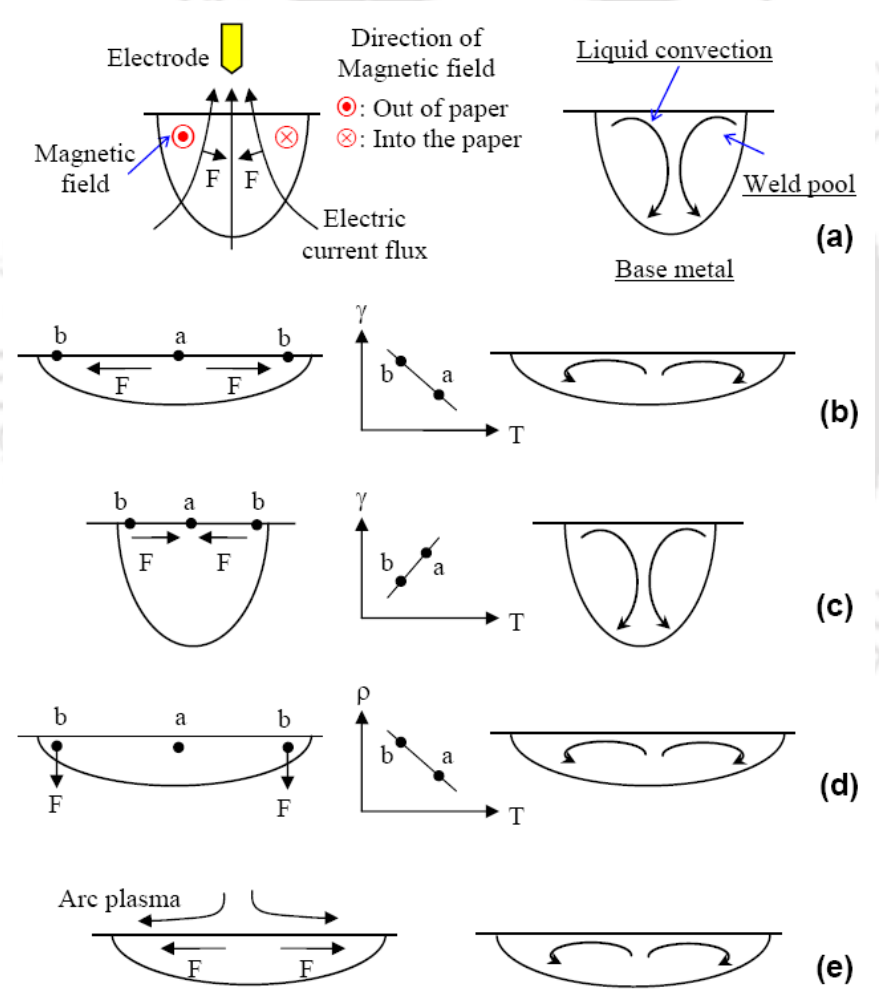

Fig. 2.8 Various driving forces and resulted liquid convection in weld pool (a) electromagnetic force, (b) and (c) surface tension force, (d) buoyancy force, and (e) arc plasma force [Schauer *et al.*, 1978].

Though, the dynamics of molten pool is an important phenomenon in a sophisticated weld pool model, very few have attempted to simulate velocity field and their differential effects on the formation of weld pool in laser microwelding process. An excellent literature review on thermal modeling of laser welding was performed by Mackwood and Crafer [2005]. However, to what extend the flow dynamics influences the formation of weld pool in microjoining is still not understood due to difficulty in experimental observation of the same. Hence, the flow dynamics is generally analysed by numerical models that solved the conservation of mass, momentum, and energy in the molten region. Rohde *et al.* [2010] performed numerical simulation of microjoining using the finite-volume method which is based on the Semi-Implicit Method for Pressure Linked Equations (SIMPLE) algorithm.A transient three dimensional model to study heat transfer and fluid flow during laser spot micro welding of a 304 stainless steel was stimulated by He *et al*. [2005]. It is seen during most of the welding time Peclet number was greater than unity which showed the importance of convection in heat transfer analysis. Brockmann *et al.* [2001] developed a model to study the temperature field induced by laser on moving thin foils. Effects of evaporation, melting and solidification of sheet material is taken into account. Convective and radiation cooling, nonlinear effects connected with temperature dependencies of material properties are included into the model. In order to include the Marangoni effect into the model, the heat conductivity of melted metal to solid metal is increased several times. He *et al*. [2004] studied the composition change of stainless steel during micro joining with short laser pulse. Using the computed temperature fields, vaporization rates of various alloying elements resulting from both concentration and pressure driven transport of vapours and the resultant composition change of the alloy were calculated. The vaporization took place mainly from a small region near the centre of the beam-work piece interaction zone, where the temperatures were very high. Furthermore, the alloying element vaporization was most pronounced toward the end of the pulse. Fig.2.9 shows the computed three-dimensional temperature and velocity fields for a typical linear Nd:YAG laser microweld of 304 stainless [He *et al.*, 2005]. Since the temperature coefficient of surface tension $d\gamma/dT$ is negative, the molten metal flows from the middle to the periphery of the liquid pool. As a result, the convection aids in the transport of heat in the weld pool. The calculated maximum temperature and liquid velocity along the *y* direction in the weld pool are 2119 K and 440 mm/s, respectively. Compared with large welds, smaller weld pool size for laser microwelding restricts the liquid velocities, but convection still remains an important

mechanism of heat transfer [He *et al.*, 2005; Bag and De., 2010]. There is little evidence to experimentally measure liquid flow velocity within weld pool. Pitscheneder *et al.* [1997] attempted to experimentally measure the flow velocity in laser welding of thick material. However, in microwelding there does not exists any such attempt in current literature and these may be because of complexity of the rapid process itself and of small scale component size. It is also evident that the presence of surface active elements in parent material has great influence in the formation of weld pool shape [Pitscheneder *et al.*, 1996; Bag and De, 2010] and these phenomena is still unclear in the microjoining process.

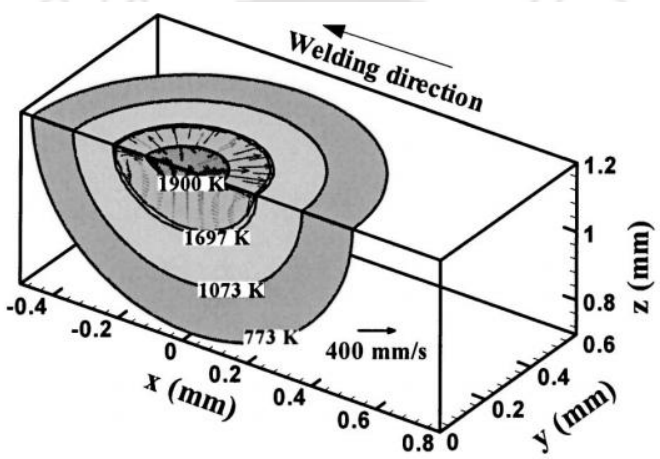

Fig. 2.9 Calculated temperature and velocity fields in three dimensions in a 304 stainless steel sample. Laser power: 100 W, beam radius: 100 mm, and welding speed: 1 mm/s [He *et al.*, 2005].

Not much work has come up yet in the field of theoretical modeling of micro plasma arc welding. Tam *et.al* [1989] studied the process of mechanized plasma arc butt welding of thin gauge mild steel sheets. McKellit[1990] developed a mathematical model to predict the velocity, temperature and electromagnetic fields inside an inductively coupled plasma torch, as well as the motion and thermal histories of particle injected into the torch. Keanini [1993] presented a three dimensional finite element model of the plasma arc welding process. The model allows calculation of three dimensional flow and temperature fields, and solid phase temperature distribution. The flow in vertical cross sections is dominated by a large jet driven vortex, competition between surface tension and jet shear produces a stagnation region near the top of the pool. Flow in horizontal planes is largely determined by the plate's motion and buoyancy is a secondary driving force within the plasma arc weld pool. Xu *et.al* [2009] developed a model to

simulate the electromagnetic phenomena and flow field in low current micro plasma arc welding process.

Together with the aforementioned literature on microjoining, various authors developed integrated models in order to keep a complete vision of the welding problems [Sudnik *et al.*, 1996; Ye and Chen, 2002].But most of the all of the models mainly focused on the study on the steel materials or aluminum alloys. Not much investigation was found to predict the weld profile of the laser weld for titanium alloy. With the special materials properties, the weld geometry of titanium alloys appears difference characters with other materials. A thorough investigation of flow in the weld pool can meet the needs for exactly controlling the profile of the weld, which is very important for the titanium alloy products of various industries. Rai *et al.* [2008] calculated and compared the temperature fields, thermal cycles, weld geometry, and fluid flow of laser and electron beam welded joints of Ti6Al4V and stainless steels. The fusion zone size in Ti6Al4V alloy was larger than that of the 21Cr6Ni9Mn stainless steel during both the electron beam and laser beam welding. In the EBW of both the alloys, there were significant velocities of liquid metal along the keyhole wall driven by the Marangoni convection. In contrast, during LBW, the velocities along the keyhole wall were negligible. A comprehensive fluid flow model is developed to simulate the geometric profile of the laser beam welding of titanium alloys [Du *et al.*, 2004]. The result confirmed that the momentum interpolation system with under-relaxation parameter based on non-staggered grid technology can effectively eliminate the pressure oscillations. The calculated results showed that the molten pool becomes shorter and wider with the Marangoni effect. It also indicated that the metal flow is the main reason for forming the typical “hourglass” cross-section profile.

A comparison between computed weld dimensions using both conduction heat transfer and transport phenomena based model in laser spot welding was carried out by Bag and De [2010] to relate the relative importance of both the model as depicted in Fig. 2.10. It is demonstrated that the conduction model predicts weld geometry well in case of small geometry (low on-time) and material having low weight percent of sulfur whereas the transport phenomena based heat transfer and fluid flow model predicts bigger weld pool (high on-time) better. Also, the conduction based model fails to predict the weld geometry for the material having considerable amount of surface active elements (0.015 wt % of sulfur). Thus, it can be accepted

that for thin plate welding especially below 0.5 mm conduction mode with a suitable heat source would be preferable. Moreover Ti6Al4V has no content of sulphur. Thus, conduction mode heat transfer model with a suitable heat source would be better for simulation of weld pool of Ti6Al4V.

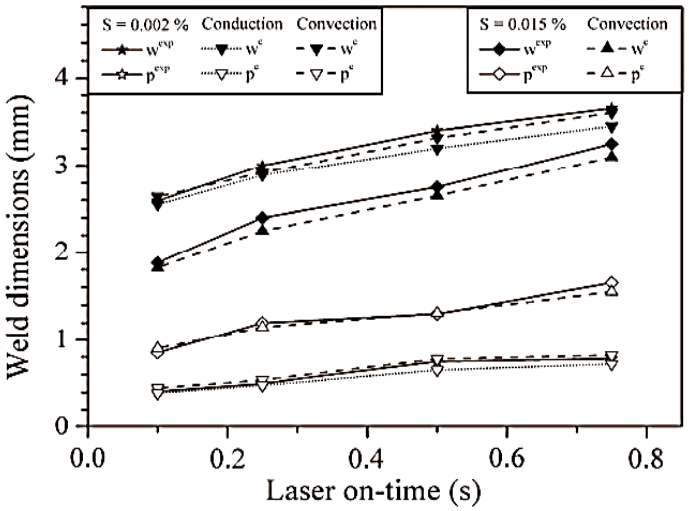

Fig. 2.10 Comparison of weld geometry prediction between conduction model and transport phenomena based heat transfer and fluid flow model in spot welding [Bag and De, 2010].

2.4.4 Non-Fourier heat conduction

It is obvious that researchers have considered classic Fourier heat conduction for heat transfer analysis where basic assumption is that heat propagates in a medium with an infinite speed and a thermal disturbance responses instantly everywhere in the medium. However, this assumption breaks down with very fast laser pulsed heating when strong phonon-scattering or phonon-electron interactions occurs. To describe these micro scale effects on heat transfer, researchers proposed two temperature models [Chen *et al.*, 2002; Hu *et al.* 2011] and phase lag models [Cattaneo, 1958; Vernotte, 1958; Tzou, 1998; Tzou and Chiu, 2001] using damped version of Fourier's law of heat conduction.

Lee and Kannatey-Asibu [2008] investigated the microwelding at uultrafast lasers of sub picosecond pulse duration. They used the two-temperature method to model heat transfer analysis of laser microwelding process using finite element based commercial software

ABAQUS. In this model the electron and lattice ware treated as two separate heat baths. The governing equations of two temperature method are expressed as [Hu *et al.*, 2011]:

$$\begin{aligned} C_e \frac{\partial T_e}{\partial t} &= -\nabla \cdot q_e - E(T_e, T_l) + Q \\ C_l \frac{\partial T_l}{\partial t} &= E(T_e, T_l) \\ E(T_e, T_l) &= G \cdot (T_e - T_l) \end{aligned} \tag{2.13}$$

where suffix 'e' and 'l' indicate electron and lattice, respectively, T is the temperature, C is heat capacity, q is heat flux, Q is heat source, E takes into account the energy interactions between electron and lattice, and G is electron-phonon coupling factor. The numerical value G depends on the specific combination of laser and material. Researchers [Cattaneo,1958; Qui and Tien, 1993] also developed various phase lag models assuming relaxation of both heat flux and temperature gradient by following the constitutive relation:

$$q(r, t + \tau_q) = -k \nabla T(r, t + \tau_T) \tag{2.14}$$

where r is the radial vector, τ_q and τ_T are the characteristic relaxation times in the heat flux and temperature gradient, respectively. These relaxation times are intrinsic properties of materials like thermal conductivity. At the same time, the local energy balance also exists between the heat flux and temperature fields. Qui and Tien [1993] used single phase lag model by assuming relaxation only in heat flux which is originally proposed by Cattaneo [1958]. By expanding eq. (2.14) in first order and assuming relaxation time is very small, the governing equation for single phase model is expressed as

$$q(r, t) + \tau_q \cdot \frac{\partial q(r, t)}{\partial t} = -k \cdot \nabla T(r, t) \tag{2.15}$$

The relaxation time parameter τ_q is defined as α / c^2, where c is the speed of thermal wave propagation in the medium, and the thermal diffusivity α is $k/\rho C_p$. However, it is to noticed that for $\tau_q = 0$, the constitutive equation becomes the standard heat conduction equation.

The analysis on the existing work on numerical modeling of heat transfer in microwelding process suggests that the traditional Fourier heat conduction model is valid for continuous as well as long pulse laser heat source. However, extremely short pulse laser processing for microwelding of thin foil cannot be adequately described by classic Fourier heat conduction law. There is a lack of enough evidence in the literature to clearly distinguish the domain of heat transfer analysis using Fourier or non-Fourier heat conduction in terms of laser pulse characteristics. It may be feasible to point out that if the laser pulse duration is more than the electron-phonon coupling time, a thermal equilibrium establishes and Fourier heat conduction law still valid. If the pulse duration is smaller, non-equilibrium thermal balance exists and hence non-Fourier heat conduction analysis is appropriate. However, a unified thermal model is necessary to bring the robustness in the simulation of temperature profile for pulsed laser joining process.

2.4.5 Laser transmission welding and gap-conduction

One of the greatest advances in the field of laser welding of dissimilar materials is joining of plastics. Precise prediction of gap/contact between surfaces is necessary in dissimilar material joining [Yovanovich, 2005].The welding concept revolves around the top material being transparent to the laser, while the underlying material absorbs the laser (Fig. 2.11). With minimal pressure on the joint the underlying material melts by absorbing the laser, and transfers heat to the top material that in turn melts creating the weld. Intimate contact between the upper and lower absorbing surfaces is important for appropriate temperature development at the heated interfacial zone to ensure good bonding. There are various methods of making the lower plastic absorb the laser energy. The absorptive properties are realized by adding soot or pigmentation. The most common, and best, absorbing additive is carbon black which determines the optical penetration depth. As this technology become more prevalent, however, a variety of other additives have been developed specifically for laser polymer welding. Additives are available in two forms: either as an additive that can be incorporated into the resin used to mould the actual part, or as a coating that is applied to the joint interface prior to welding. The process is effectively applied in number of applications such as in automotive industries for producing sensor housing, lighting, instrument clusters, interior panels, fluid control devices, for

manufacturing various medical devices such as catheters, micro fluidics, and many others. The Laser source generally used are CO_2, YAG laser and diode laser.

The laser beam can be delivered to the joint interface by various methods. In simultaneous welding, the entire weld interface is irradiated with laser energy for the duration of welding cycle. In quasi-simultaneous welding, mirrors are used to move the beam rapidly and repeatedly over the weld interface and create meltdown. In contour welding the beam moves at a relatively slow speed along a predefined path with only a fraction of the total weld line length molten at any time. In laser transmission welding (LTW), delivery of the thermal energy by laser beam is influenced by the process parameters, optical and material properties. If the parts to be joined do not receive enough heat, gaps can occur while excessive heat can cause polymer degradation. Thus the weld interface must be exposed to sufficient heat to melt the polymer and form strong weld. Thus developing an accurate model to help understanding the process is very beneficial. A number of attempts are already been made to simulate the laser transmission welding process for studying the process characteristics.

Various analytical models of welding phenomenon exist in the literature. Kennish *et al.* [2002] established an analytical heat transfer model of laser transmission welding process to predict the process capabilities and weld characteristics. In 2003, Grewell and Benatar [2003] compared two theoretical models for a 3-D transient temperature field in LTW. These two analyses were based on the assumption that light energy is absorbed on the weld interface. Coelho *et al.* [2000] developed a theoretical model describing the temperature distribution in thin thermoplastic material during the laser welding process. The heat conduction equation is solved analytically by the Green function method and thermal stresses are taken into consideration. The approach, based on the Green function method, allows successful prediction of the temperature distribution in the material to optimize the welding parameters. Russek et al. [2004] presented an analytical thermodynamic model of LTW. The equation of energy conservation is solved for different steps of approximation to indicate the influence of the convective as well as the diffusive heat flow on the energy density distribution. Ho *et al.*[2010] presented an analytical approach to thermal behavior of laser welding of polymers. However, nnumerical modelling of the LTW process can provide a relatively precise quantitative prediction of temperature and deformation in LTW. Prabhakaran *et al.*[2003]. used a 1-D finite-difference method to calculate

the transient temperature distributions in contour LTW of an over-lap weld made of PA6GF using a 940 nm wavelength diode laser. Becker and Potente [2002]. simulated the temperature field in contour welding of PP using a 2-D transient thermal model. The Bouguer-Lambert law was used to describe the heat source in the laser absorbent part. ABAQUS software was applied in this analysis. A fitted temperature-dependent laser-absorption coefficient was used to predict the melt layer thickness. Light absorption in the laser-transparent part was not considered in the model. Kritskiy [2009] created a 2-D axi-symmetric FEM model in COMSOL to simulate temperature distribution and weld width during the welding of the transparent nylon tube to the absorbent nylon plaque. Potente and Fiegler [2004] reported a FEM model for simulation of laser transmission welding of PA6. Potente *et al.* [2006] developed a model that described the temperature development in the transparent and the absorbent. According to this, more energy is transferred to the absorbent component than to the transparent one. This high temperature gradient in the contact area results in a non-uniform temperature distribution in both components. Mayboudi *et al.* [2007] simulated transient heat transfer of PA6 with diode lasers using finite element method. Simulation results using the theoretical estimation of the absorption coefficient improved the prediction accuracy of the melt layer thickness. Scattering of the laser light through the laser-transparent part was treated by a linear widening of the beam. Mahmood *et al.* [2007] developed a numerical method using finite element technique to determine the optimum condition of jointing two dissimilar materials namely titanium and polyimide.In this case, the mating surfaces at the interface had been considered two separate sets of nodes belong to two different element sets corresponding to two different materials. Similar approach was followed by Dhorajiya *et al.* [2010] during thermal simulation of titanium and polyimide. Acherjee *et al.* [2010] developed a three-dimensional finite element (FE) thermal model to simulate the laser transmission welding process for joining polyvinylidene fluoride to titanium using a distributed moving heat flux. All the major physical phenomena associated with the LTW process, such as, heat radiation, thermal conduction and convection heat losses are taken into account in the model development. Acherjee *et al.* [2012] also investigated the influence of carbon black content on temperature distribution and weld profile, during laser transmission contour welding of polymers.

Most of literature assumed perfect contact between the two parts neglecting any gap due to roughness value. The heat required for melting of the top layer and subsequent successful joining

of the two parts depend on the upward heat transfer from the uppermost layer of the bottom half. The heat transfer between the two parts relies on the gap conductance at the interface. The value of thermal contact conduction depends on the surface roughness and the material properties as well as the temperature and pressure at the interface and the type of fluid trapped at the interface. Few literatures has been reported which account for the contact conduction between the joined parts. Ven and Erdman [2007a; 2007b] simulated the transient heat transfer and gap bridging at the weld interface during the contour LTW of the T-joint made of polyvinyl chloride (PVC) using a 2D numerical model. The model introduced contact conductance at the weld interface reflecting the influence of contact pressure, surface roughness, and elastic modulus. Contact pressure and gap bridging at the weld interface were calculated based on a simplified 1D thermal expansion of polymers along the part thickness. Taha *et al.* [2009] developed a mathematical model for laser transmission welding of polyethylene in lap geometry considering the effect of the clamping pressure on weld geometry and thermal profile. They invoked the contact resistance to obtain a realistic thermal profile for a given thermal input and applied pressure, characterized by an average heat transfer coefficient. Cheng [2009] developed a 3D Quasi-static FEM model to simulate the heat transfer and thermal deformation in contour gap bridging welding of PC, PA6, and PA6GF. In order to reduce the computing time, a mass flow was introduced in the model so that a time-dependent contour welding process was solved as a time independent heat transfer problem. Kawahito *et al.* [2007] developed an adaptive and in process method for reduction of harmful effects of gaps.It has been emphasized that better gap bridging can be achieved through optimized laser parameters such as pulse length, duration, and energy [Norris *et al.*, 2005]. Long pulse durations at low energies generating low peak powers were found to create the highest percentage of gap bridging ability. Gas shielding using Argon was also found to greatly impact gap-bridging ability.

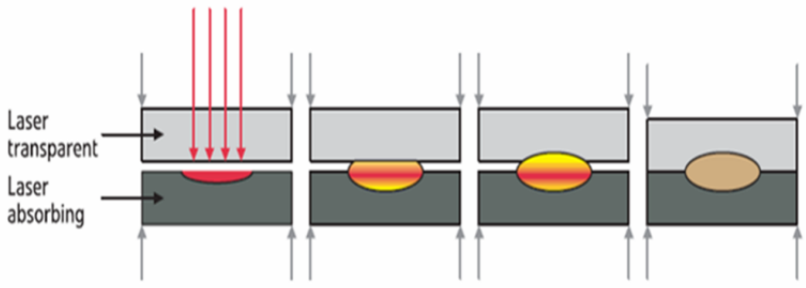

Fig. 2.11 Mechanics of laser transmission welding [Mayboudi *et al.*, 2007].

2.5 Distortion and Residual Stress in Fusion Welding

In joining of materials, the distortion is generated due to differential expansion and shrinking, and the residual stress is produced when weld joint is restricted against deformation. Residual stresses are locked-in stresses present in the engineering components. When the maximum value of residual stresses exceed the elastic limit of the metal leads to plastic deformation and thus residual stresses greater than elastic limit are accommodated in the form of distortion of components. Residual stresses in welded joints primarily develop due to differential weld thermal cycle (heating, peak temperature and cooling at the any moment during welding) experienced by the weld metal and region closed to fusion boundary i.e. heat affected zone (Fig. 2.12). Type and magnitude of the residual stresses vary continuously during different stages of welding i.e. heating and cooling (Fig. 2.13). During heating primarily compressive residual stress is developed in the region of base metal. After attaining a peak value compressive residual stress gradually decreases owing to softening of metal being heated. Compressive residual stress near the faying surfaces eventually reduces to zero as soon as melting starts and a reverse trend is observed during cooling stage of the welding. During cooling as metal starts to shrink, tensile residual stresses develop and their magnitude keeps on increasing until room temperature is attained. In general, greater is degree of constraint and elastic limit of melt higher will be the value of residual stresses [Desai and Bag, 2014]. The variation in temperature and residual stresses owing to movement of heat source along the centerline of weldment is shown schematically in Fig. 2.13. The residual stress along the weld is generally tensile in nature while balancing compressive residual stress is developed adjacent to the weld in heat affected zone on cooling to the room temperature as evident from the Fig. 2.13(b). The non-uniform temperature distribution produced during welding give rise to incompatible strains which in turn results in generation of self-equilibrating residual stresses and its distribution that remain in the structure after cooling down to ambient temperature.

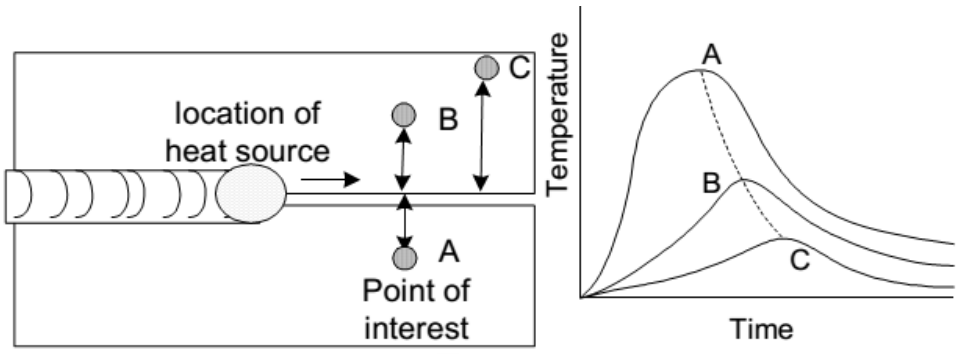

Fig. 2.12 Weld thermal cycle of: a) locations A, B, C and b) temperature vs. time relation of A, B and C.

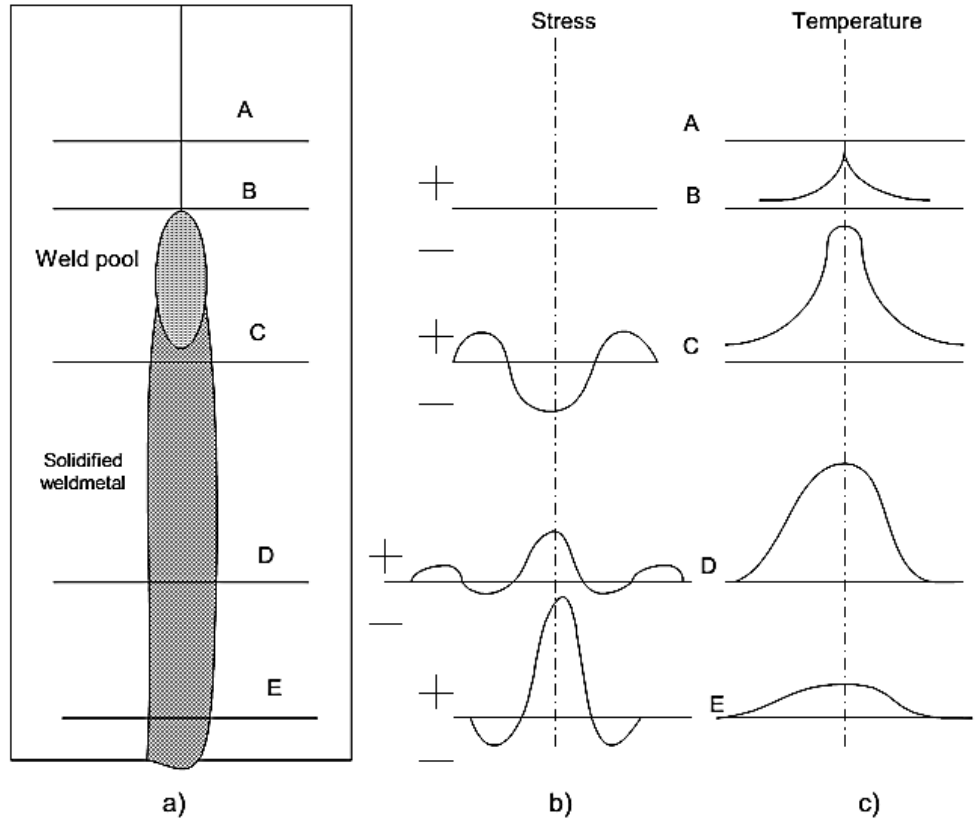

Fig. 2.13 Schematic diagram showing: a) plate being welded; b) stress variation across the weld centerline at different locations and c) temperature of different locations [Masubuchi, 1953].

A distortion is more serious problem mainly with thinner materials due to low stiffness. Also metals with greater thermal expansion and lower thermal conductivity are more susceptible to distortion [Mcdill *et al.*, 1990; Wang *et al.*, 2008]. The estimation and reduction of welding distortion is one of the most important criteria in the industry as it creates problem not only in the

assembling process but also in the final product quality. Theoretically, there are three categories of factors that significantly affect welding distortion. The first class is called as material-related factors, which are the thermal properties (e.g. thermal conductivity, density, and specific heat capacity) and mechanical properties (e.g. Young's modulus, Poisson's ratio, yield strength, and thermal expansion coefficient). Mcdill *et al.* [1990] discussed the effect of material properties of carbon and stainless steel and concluded that thermal properties play a larger role in distortion. Wang *et al.* [2008] also inferred that when heat input is same material properties plays a significant role in distortion. The second class is design-related factors, which involves the type of weld joint, thickness of plate, dimensions of joint or structure, etc. [Choobi *et al.*, 2013; Deng *et al.*, 2007]. The third class is process-related factors, which includes welding method, heat input, preheating, welding sequence, external constraint, etc. [Choobi *et al.*, 2013; Lindgren, 2007, Teng *et al.*, 1998; Despande *et al.*; 2011; Mollicone, *et al.*, 2008]. Direct and interaction effects of the process parameters were analyzed and presented on the distortion were variably studied in the past [Kihara and Masubuchi, 1954; Watahnabe and Satoh, 1958]. It is very important to simulate the welding process using a suitable heat source model which takes into account the actual heat input in order to obtain reliable results of the distortion [Deng and Murakawa, 2008a; Wang *et al.*, 2014]. Also, in case of numerical analysis, a correct thermal analysis is mandatory to predict welding induced distortions and residual stresses [Spina *et al.*, 2007; Long *et al.*, 2009]. There is a strong influence of clamps on the distortion, and that the distortion can be controlled to some extent by appropriate selection of the clamping conditions [Schenk *et al.*, 2009; Choobi *et al.*, 2010; Desai and Bag, 2014]. Initial gap and misalignment has significant influence on welding distortion [Deng *et. al.*, 2007b]. Because the stiffness is relatively low in a thin welded structure, the geometrical nonlinearity should also be considered if a numerical model is used to simulate welding deformation [Deng and Murakuwa, 2008, Long *et al.*, 2009; Wang *et al.*, 2008]. This will bring a larger challenge to the development of numerical model. Generally speaking, the welding induced distortion of thin plate welded structures can be divided into in-plane and out-of plane distortion. Welding shrinkage is the typical in-plane type. Out-of-plane welding distortion may be divided in two different kinds: bending distortion and buckling distortion. Figure 2.14 shows all typical welding distortions of a thin plate butt welded joint. In particular, buckling distortion can take various modes. Welding distortion will not only degrade the performance of a welded structure, but also delay the

production schedule and increase fabrication cost when it is mitigated. It is very difficult to completely eliminate or correct welding distortion because of the non-linear irreversible nature of the welding [Wang *et al.*, 2014]. Correcting distortion especially buckling distortion is a time-consuming work that adds little value and tends to degrade the quality of the welded structures as well. Therefore, control or prevention of such distortion in a thin plate structure is more meaningful and more important than correction of deformation after welding.

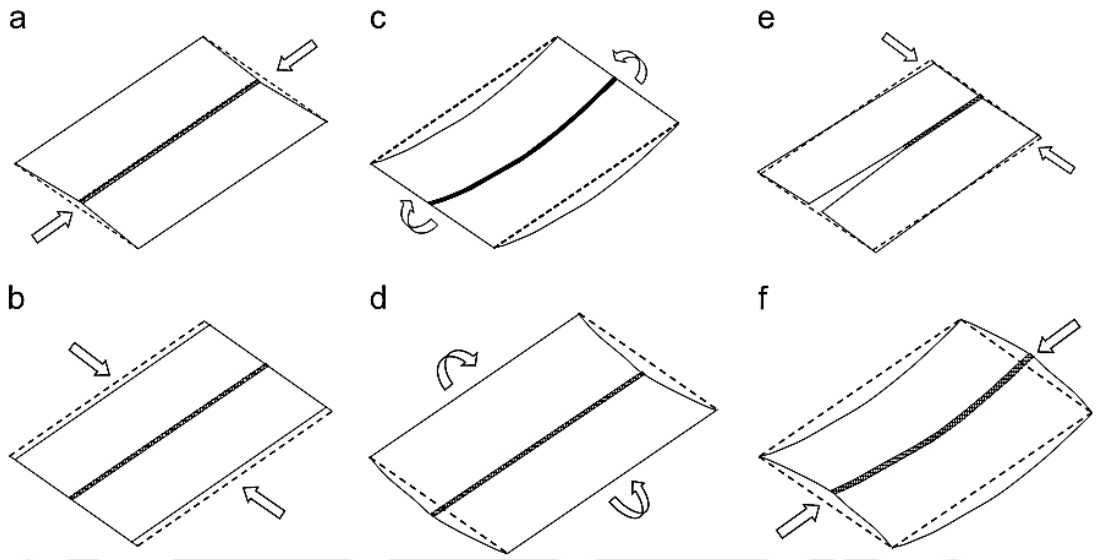

Fig. 2.14 Basic types of welding distortion in thin plate butt welded joint: (a) longitudinal shrinkage; (b) transverse shrinkage; (c) longitudinal bending; (d) transverse bending; (e) rotational deformation; and (f) buckling deformation [Wang *et al.*, 2014].

It would be more preferable if welding deformation can be predicted and controlled both at design stage and at manufacturing stage through designing reasonable positions for the joints and/or by adjusting the thickness of plate. Also, controlling heat input and adopting appropriate assembling sequence can reduce the welding-induced deformation to some extent at the manufacturing stage. Accurate quantitative estimation of residual stress in welded fabrications is of significant interest. To minimize the negative effect of welding process on fabrication quality, research on welding distortions and residual stresses has been a continuous interest among researchers [Kong *et al.*, 2011; Mollicone, *et al.*, 2008]. Thus, it is necessary to develop advanced predictive tools for determining accurately welding residual stresses. A detailed discussion on this issue is well described by De and Debroy [2011].Such stresses are often

calculated using finite element method where different physical phenomena are taken into account such as elastic plastic, material behavior or elasto-visco-plastic, material behavior due to mechanical and thermal resistance. Various attempts have been made to analyze the residual stresses and distortion in welded structures both experimentally [O'Brien, 2007; Watanabe and Satoh, 1957] and theoretically [Sarkani *et al.*, 2000; Ueda *et al.*, 2007]. However, there is very limited literature describing the prediction and measurement of welding deformation in the thin plate welded structures especially for these welded structure whose plate or wall thickness is less than 3.0 mm.

2.5.1 Experimental investigation

A lot of literatures have come up for experimental investigation of welding induced distortion. The destructive and nondestructive techniques to evaluate residual stresses are X-ray diffraction method [Withers and Bhadhesia, 2001], neutron diffraction method [Park*et al.*, 2004; Owen *et al.*, 2003; Song *et al.*, 2014], layer-removal method, sectioning method, ultrasonic and magnetic methods, and hole drilling method [Schajer, 1988; Roy *et al.*, 2003; Atma Raj and Joy Varghese, 2014]. However, these methods are extremely complicated with limited application owing to cost or accuracy. However these investigations are mainly for thick plates. Few literatures on thin plates have also come up. Masubuchi [1953] conducted experiments of buckling type deformation of thin plates due to welding, and presented the critical buckling wave length as influenced by the size of plate and welding conditions. Watanabe and Satoh [1957] conducted a series of experiments of bead-on-plate welding on thin plates and observed welding induced buckling distortion, the so-called concave–convex or convex–concave type. The critical buckling force and the moment when buckling occur in welded plates with different aspect ratios are measured [Watanabe and Satoh, 1958]. Pattee [1975] indicated that thin plate can buckle during and after welding due to thermal and residual welding stresses. Critical residual buckling stresses are calculated for a number of different boundary conditions and a test program is conducted to partially verify the predictions. Terasaki *et al.* [1998] also investigated plate buckling behavior caused by welding and had reported that welding-induced buckling is affected by the welding conditions, size of plate and material properties. Liang *et al.* [2004; 2005] have established a number of databases of welding inherent deformations for typical thin plate welded joint using experimental method and inverse analysis method, and some meaningful

achievements have been obtained. The deflection of 1 mm thick low carbon steel welded by gas metal arc welding was carried out by Deng and Murakawa [2008a]. Figure 2.15 shows a schematic image of a simple method for measuring the deflection in the butt-welded joint generally adopted. Approximately, w/2 can be regard as the deflection at the center of the welding line.

Experiments were done to measure and compare the welding deformation of carbon and stainless steel [Wang *et al.*, 2008]. Both bead-on-plate and fillet joints were done by CO_2 gas metal arc welding. The angular distortion, longitudinal stress and transverse shrinkage were measured before and after welding at specific points both on the top and bottom surface of the welded joints. Experiments were carried out to measure and compare the transverse shrinkages and the deflection (out-of-plane deformation) induced by LBW and CO_2 gas arc weldingof 2.3 mm thick plate of low carbon steel [Sun *et al.*, 2014]. The final deformation in the specimen by LBW is very small, while the CO_2 gas arc welding has a significant bending deformation. Deng et al. [2013] investigated the influence of heat input on welding distortion in a 2 mm thin-plate bead-on-joint induced by CO_2 gas arc welding. Nelias *et al.* [2010] experimentally measured the in-plane displacements during by laser beam welding in a 2.5 mm thin-plateAA6065T4 joint by using linear variable differential transformer (LVDT) sensors were placed to measure. The experiments on 2.88mm carbon steel plates showed that buckling with saddle type is produced by welding, and a thin plate stiffened welded structure is deformed with twisting type buckling due to welding [Wang *et al.*, 2014].

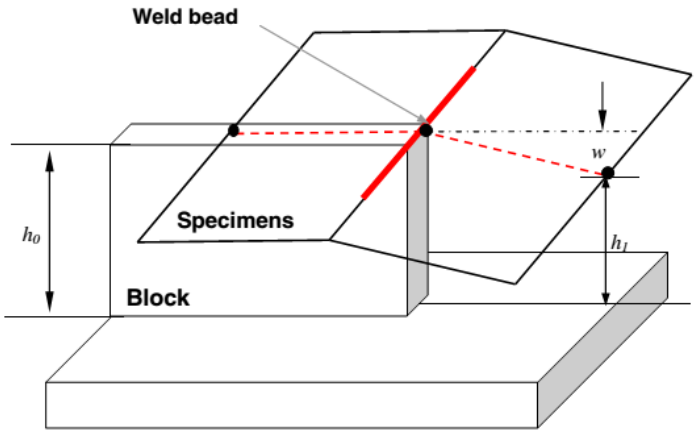

Fig. 2.15 Schematic image of measuring the deflection in the butt-welded joint [Deng and Murukuwa, 2008a].

2.5.2 Numerical Investigation

Developing a reliable model that can predict the welding distortions effectively and easily under certain conditions is of great necessity. With the help of modern simulation software and use of numerical techniques, complex phenomenon of welding can be understood and both weld thermal cycles experienced by the weld and distortion resulting from this can be predicted with reasonable accuracy. From modeling point of view, it will be very useful if the parameters of interest which contribute to the residual stresses and distortions in various types of welded joint and structure application can be simulated numerically so that welding performance with respect to the various aspects could be assessed and evaluated in an efficient manner [Goldak and Akhlagi, 2005; Lindgren, 2007]. Finite element based deformation simulation using software like ABAQUS, ANSYS, SYSWELD etc. and Elastic FE analysis using inherent deformation and shell elements model of welded structures proved to be a proficient tool to predict welding distortion and residual stresses in welded structures [Khurranm and Sehzad, 2012; Mollicone *et al.*, 2008; Sarkani *et al., 2000*.; Mackerle, 2002].

Camilleri *et al.* [2005] predicted angular distortions caused by fusion butt welding of thin plates using finite element method. A thermo-elastic–plastic analysis on 1 mm thick low carbon steel was carried out by Deng and Murakawa [2008a; 2007]. The finite element based numerical model using inherent strain theory and assuming large deformation predicts well the experimentally measured values and indicates the importance of the geometrically nonlinear problem for simulating thin plate deformation. The prediction method of welding distortion, which combines thermo-elastic-plastic finite element method (FEM) and large deformation elastic FEM based on inherent strain theory and interface element method, was developed [Deng and Murakawa, 2008b]. The result from this study showed that the initial gap between skin plate and stiffener is one of the factors that can contribute to welding distortion. Wang *et al.* [2008] carried out comparison of welding deformation of stainless steel and carbon steel by 3D thermo-elastic plastic method using an in house finite element iterative substructure method. The iterative substructure method has the advantage the nonlinearity region is confined within a small area while rest of the model is linear which reduces the computation time significantly. The distortion and residual stress distribution during CO_2 gas arc welding of 2 mm thick plate was carried out by considering elastic–plastic material behavior and temperature dependent material

properties under the condition without any external constraint by [Deng *et al*., 2013]. Simulation results show that longitudinal shrinkage, transverse shrinkage and deflection increase with heat input. The buckling propensity of thin plate is bound to occur during welding which increases with the heat input. The comparison between predictions and measurements shows that the computational approach developed in the present work can successfully capture the features of welding distortion and residual stress in the thin plate joint. Long *et al.* [2009] investigated the transverse, longitudinal and angular distortions induced in thin butt gas metal arc welded low carbon steel plates of 2.5 mm and 3 mm. It was predicted that the welding speed and plate thickness are significant parameters on weld-induced distortions and residual stress in gas metal arc welding of thin plate structure. It can be seen that the longitudinal and transverse shrinkages are increased when the welding speed is reduced. The comparative study of weld distortion induced by laser beam welding and CO_2 gas arc welding was carried out by Sun *et al.* [2014]. The distortion and longitudinal residual stress generated by laser beam is much smaller as compared to CO_2 gas welding. The welding distortion predicted by large deformation theory is different from that simulated by small deformation theory to some extent. Moreover, the deflections predicted by the large deformation theory are in good agreement with the measured data. Huang *et al.* [2016] predicted the CO_2 laser welding induced deformation in 1.33 mm thick SS301 thin sheets. It was concluded that at the same welding condition, the out-of-plane welding deformation greatly increases with the plate length. Nelias *et al.* [2010] studied laser welding induced on 2.5mm thin sheets of AA 6056-T4 by means of decoupled computational approach. The process was divided into two steps; in first step, determination of residual stress by thermo-mechanical analysis was carried out and in second step the critical buckling stress and buckling mode with Eigen value was obtained. Darcourt *et al.* [2004] and Josserand *et al.* [2007] have attempted to predict residual stresses and out-of plane displacements for aluminum alloy on thin sheets. Del *et al.* [2010] predicted residual stress and distortion by GTAW of two different stainless steel specimens for comparing mode of distortion and magnitude. A thermal-elastic-plastic finite element analysis is introduced to study the deformation of laser welding of bridge steel Q235 of thickness 1.2 with consideration of varying constraints conditions [Zeng, *et al.* 2013]. Finite element modeling of GTAW is performed using SYSWELD for a butt joint of SS304sheets by Deshpande *et al.*, [2011]. An increase in convective heat transfer coefficient, the out-of-plane longitudinal distortion was predicted to decrease whereas angular distortion was

predicted to increase. Clamp release immediately after the welding step predicted higher longitudinal residual stresses and subsequently larger cambering than with extended clamping times. Starting from the middle portion of the plates to the end of the plates was found to predict significantly less distortion than the sequences starting from the edges of the plates. Monfared [2012] validated the distortion results with experimental angular distortion and longitudinal bending of CT3 steel. The welding induced buckling of 2.88m thick carbon steel plate is investigated using the eigenvalue analysis based on inherent deformation theory [Wang *et al.*, 2014]. Although the longitudinal inherent shrinkage is the dominant reason of welding induced buckling in flat welded joint, inherent bending deformation and initial deflection are considered to act as imperfections that trigger buckling and influence the magnitude of the out-of-plane welding distortion. A modeling procedure was developed with consideration of bead shape and the initial imperfection of the plate for predicting buckling distortion in the MIG welding of 3mm sheet [Yang *et al.*, 2000].

The development of artificial neural network provides an alternative for realizing this idea that is the base of this research. Choobi *et al.* [2010] investigated welding-induced angular distortions in 2mm thin SS304 using artificial neural network methods. In order to predict angular distortions, a multilayer feed forward neural network based on back propagation error correction method was created. Tian *et al.* [2014] developed a back propagation neural network model coupled with finite element based simulation to predict the angular distortion and transverse shrinkage in GTAW. The findings indicates that the distortion increases at a maximum point with threshold of heat input and then decreases with further increase in heat input.

It is obvious that a lot of research has been done on residual stress and deformation analysis of different thickness plates. However, the survey reflects that the thickness of most of the materials is usually 2mm or more. A limited number of works has been reported in the literature to estimate the residual stress and distortion produced during microjoining at continuum scale. Chung and Lin [2005] simulated the thermal stress during joining of pin to plate material by assuming thermo-elastic plastic theory and the materials ware assumed to be isotropic strain hardening followed by Von-Mises yield criteria. It was observed that higher thermal stress exists between the base of the pin and the plate, and the place near the heat source also. Mian*et al.* [2005] followed two material models for stress analysis in joining titanium and

polyimide. A simple linear elastic model was used for titanium, and a linear elastic-plastic model was used for polyimide. Dhorajiya *et al.* [2010] analysed the stress level generated during joining of PI and Ti using elastic-plastic material model. It was observed that higher tensile stress (transverse) built up near the centreline of the laser travel on the Ti surface and compressive stress (transverse) built up near the centreline on the PI surface. The magnitudes of the tensile stresses on the Ti surface ware higher than the magnitudes of the compressive stresses on the PI surface. This was due to the fact that Ti remained in solid state over the entire laser heating whereas PI subjected to melting and solidification. The material models follow isotropic hardening rule and Von- Mises yield criteria.

Till date, even though a considerable progress has been made in computational welding mechanics, but there are a number of key problems i.e. how to develop advanced material model to roundly consider the influence of microstructural changes on welding residual stress and deformation in certain steels is still a difficult problem. It has been recognized that the solid-state phase transformation has significant influences on welding residual stress especially in medium carbon steel or alloy steels with a certain carbon equivalent. During the phase transformation of cooling stage, the volume of weld metal and heat-affected zone (HAZ) expands because face centered cubic (FCC) structure changes into body-centered cubic (BCC) or body-centered tetragon (BCT) structure. The volume change due to phase transformation in the course of heating and cooling is schematically shown in Fig. 2.16. When a pearlite-ferrite carbon steel is heated over A1 temperature (cementite disappearance temperature) during the heating phase of welding, its microstructure starts to transform into austenite, and when the temperature reaches A3 (a-ferrite disappearance temperature), pearlite-ferrite completely changes into austenite. Pearlite-ferrite steel has a BCC structure, whereas austenite has a FCC structure. During austenite transformation, the steel undergoes a reduction in volume. When the steel cools down rapidly just after the heating phase and a certain temperature is reached, austenite begins to transform into martensite with a BCT structure, and the volume increases. The quantity of martensite transformed from austenite depends on the temperature reached upon cooling. Depending on the peak temperature that a particular point has reached during heating process, the decision is made whether the point undergoes the austenite to martensite transformation or not, i.e. all points whose peak temperature is higher than the temperature A3 are considered to undergo martensitic transformation when cooling to the onset temperature M_s. It is assumed that

when cooling to the end temperature M_f, the martensitic transformation is complete and the austenite fully transforms into martensite. Meanwhile, the mechanical properties such as yield strength drastically alter especially when austenite changes into martensite [Lee and Chang, 2009; Deng, 2009; Deng and Murakuwa, 2006; Deng and Murakuwa, 2008a]. Thus, the inclusion of volumetric strain due to phase transformation like austenite to martensite improves the estimated residual stress in numerical modelling of the same. Few recent works has been reported in the literature to include the effect of phase transformation induced strains in the modelling of residual stress. A detailed discussion on this issue is well described by De and Debroy [2011].

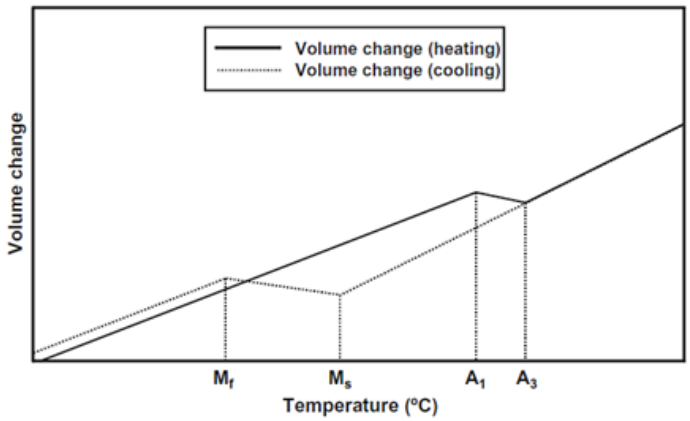

Fig. 2.16 Volume change due to phase transformation [Lee and Chang, 2009].

From the above description it is clear that the thermal cycles during the fusion welding process are responsible for the solid-state phase transformation which induces volumetric changes and yield stress changes in the metal. Therefore, the total strain increment can be written as the sum of the individual components of the strain or strain rate as follows:

$$\Delta\varepsilon = \Delta\varepsilon^{E} + \Delta\varepsilon^{P} + \Delta\varepsilon^{T} + \Delta\varepsilon^{Vol} + \Delta\varepsilon^{TRP} \tag{2.16}$$

$\Delta\varepsilon^{E}$, $\Delta\varepsilon^{P}$, $\Delta\varepsilon^{T}$, $\Delta\varepsilon^{Vol}$, $\Delta\varepsilon^{TRP}$represent the strain or strain rate components due to elastic, plastic, thermal loading, volumetric change and transformation induced plasticity, respectively.

Thus, in addition to the strain induced by microstructure evolution during solid-state phase transformation along with the thermal strain, transformation-induced plasticity is also produced. Transformation induced plasticity (TRIP) is significant during a phase change. For an

externally applied load for which the corresponding equivalent stress is small compared to the normal yield stress of the material, plastic deformation occurs. Unlike austenitic transformation, the formation of martensite, which involves shear and is displacive in nature, induces transformation plasticity. It is usual to describe transformation plasticity by equating the induced strain rate under constant and small applied stress in the equation:

$$\varepsilon^{TRP} = 3K\left(1-\mathrm{f_M}\right)\Delta \mathrm{f_M} \mathrm{s_{ij}} \tag{2.17}$$

where f_M and Δf_M are fraction of martensite and its increment, respectively; s_{ij} is stress deviator; and K is the coefficient of transformation plasticity. This parameter can be measured by experiment. The coefficients of transformation plasticity (K parameter) of steels measured by experiment are seen very limited. However, the K parameters for several steels are summarized in [Lee and Chang,2009]. It is observed that the K parameter is of the order of10^{-4} MPa^{-1}. Oddy *et al.* [1990] has given a concise description of TRIP. The simulation with and without the strain component indicate that neglecting the effect of TRIP may lead to residual stresses that are incorrect both in magnitude and direction [Bamman *et al.*, 1995].A computational approach was developed to predict welding residual stress in low temperature phase transformation steel with considering volume change and TRIP by [Deng and Murakawa, 2008; Deng and Murakawa, 2006; Deng, 2009]. In the developed approach, the TRIP was considered based on Inoue model [Bamman *et al.*, 1995; Bortoleto *et al.*, 2000]. According to Inoue model, stress state related to the yielding of the austenite (parent phase) is affected by the daughter phase (martensite). The plasticity of austenite is controlled by the yield function in the form:

$$F = f\left(\sigma, T, \varepsilon^{p}, \kappa, \mathrm{f_M}\right) \tag{2.18}$$

where σ, T, ε^P, K and f_M are uniform stress, current temperature, plastic strain, inelastic hardening parameter, and phase fraction of martensite, respectively.

Two particular conclusions can be arrived from this issue of transformation induced residual stress. First, the kinetics of phase transformation during welding is still complicated area for multicomponent alloys which demands precise metallurgical model. Effects of volume change due to austenite–martensite transformation on the final residual stress and the welding

distortion are important for certain materials and cannot be neglected. Deng [2009] revealed that the final residual stress and the welding distortion in low carbon steel do not seem to be influenced by the solid-state phase transformation. However, for the medium carbon steel, the final residual stresses and the welding distortion seems to be significantly affected by the martensitic transformation.Secondly, the transformation induced residual stress may be significant in micro scale joining process as compared to macroscale or large scale joining. Finally, evidence from the current literature suggests that there is a lack of comprehensive work to estimate the residual stress in micro scale joining process that includes the effect of phase transformation kinetics. Enough investigation is necessary in this aspect.

From the discussion of a limited number of papers on laser microwelding, it can be summarised as follows. Most of the thermo-mechanical models discussed above, consider sequentially coupled thermal and mechanical analysis. This may be due to the fact that fully coupled analysis is computationally more involved because of the adoption of coupling strategies between thermal, mechanical and metallurgical analysis. Also, the material models follow isotropic hardening rule and Von-Misses yield criteria to judge plastic zone. Elastic FE analysis using inherent deformation and shell elements model of welded structures is an ideal and practical computational approach for predicting welding distortion due to its high computational efficiency and accurate computed results. Fig. 2.17 summarizes the general computation procedures of the elastic FEM for welding deformation [Huang, *et al.*, 2016]. At the beginning, the basic data such as welding conditions and material properties need to be prepared. The sectional macrostructure is helpful in determination of the heat efficiency and validation of the thermal analysis results. Thermal–mechanical test such as a gleeble test can be performed to get the stress–strain curves of base material under different temperature. Secondly, in order to obtain inherent strain for the prediction of welding deformation in a real size welded structure, thermo-elastic-plastic analysis is carried out on a small size model of typical welded joints which is here called as a local solid model. Alternatively, two-dimensional plane strain model can also be used to calculate residual strains to save computation time. After thermo-mechanical analysis is completed, inherent deformation is calculated by integration of residual strains through the transverse section. Sometimes, the inherent deformation can be directly obtained from

experiment instead of numerical analysis. In the last step, the global structural analysis for prediction of welding deformation is performed by the elastic FEM.

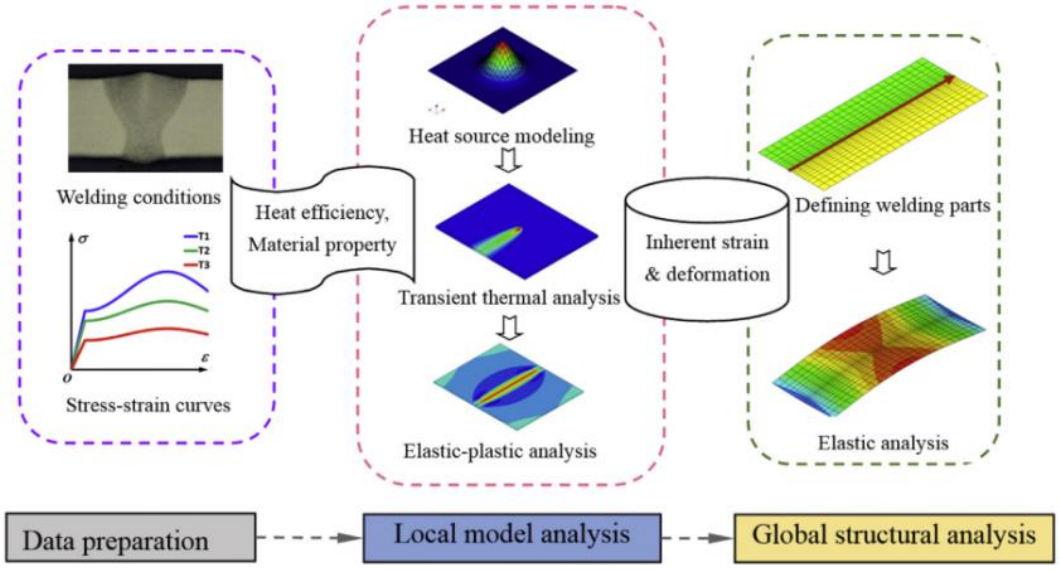

Fig. 2.17 Computation procedures of structural welding deformation [Huang *et al.*, 2016].

Therefore, for the modern fabrication procedure to produce high quality welded structure and decrease the fabrication cost, welding distortion controlling and mitigation by computational prediction in advance has been widely accepted and practiced. However, it is anticipated from the current literature that there is a lack of complex thermo-mechanical-metallurgical models in microjoining process which takes into account more physical phenomena to predict distortion and residual stress in a solidified joint structure. It is observed that Ti6Al4V weldment exhibits highly localized residual stress and the magnitude is very high in longitudinal direction. The former is due to its significant thermal diffusivity and the latter is because of its high yield strength [Song *et al.*, 2014]. However, literature lacks proper investigation on distortion and residual stress for microwelding of reduced sheet thickness.

2.6 Summary

This chapter describes various aspects of microwelding processes in the perspective of practical application. First, experimental investigation on laser and plasma micro welding processes is reviewed. An extensive part of the chapter is devoted to address the issues on

welding of Ti6Al4V alloy. Secondly, several approaches on numerical modeling of micro welding process is discussed. It is also anticipated that the non-Fourier heat conduction analysis is more appropriate to signify rapid propagation of heat wave in case of ultra-shot pulse laser. Finally, the residual stress and distortion analysis in microwelding process is reviewed including the effect of phase transformation. In a nutshell, this chapter provides an overview on thermo-mechanical analysis of laser and plasma micro welding processes which is extracted from literature and is required for promising development of microsystem technology. The key findings from this chapter are summarized as:

- It has been realized that a lot of researches have come up in the field of microwelding to find out an envelope of the physical parameters for successful joints. The individual and combined effect of various welding parameters on the weld joint shape and morphology has been investigated. It is established that a low heat and high energy density is preferable for microwelding process. Most of the works on microsystem is mainly focused on laser as a heat source. Very few literatures come up with micro plasma arc welding in micro scale welding process. Also the microwelding of the common materials like stainless steel, copper, and aluminum are tried to establish. Titanium and its alloys have found a niche in various industries where the properties are greatly altered with the processing of the materials. Not much work has been found in esteemed literature on welding process of titanium alloy at a micro scale.
- The literature indicates that the selection of welding process, amount of heat input, cooling rate, peak temperature reached and welding process parameters have a definite effect on the shape and final structure of the weld joint and in turn affects the mechanical properties of the joint. Thus, the researchers have targeted to find an optimum combination of the welding parameters which ensures the required quality of the final joint with minimum defects.
- Lot of literatures has come up to study the experimental investigation of fusion micro welding processes. However, experimental determination of important parameters such as temperature and flow conditions in the micro scale weld pool is extremely difficult, owing to the small size of the weld pool, high temperature gradient and high peak temperature and such methods are also costly. The effective construction of a reliable numerical model is an utmost necessity to investigate the fusion micro welding phenomenon. Such a model will help to understand and relate the welding process phenomenon even at the design and

manufacturing stage. This will help to reduce the cost and cumbersome experimental effort associated with the experimental investigation.

- The basic assumption of Fourier heat conduction model breaks down with very fast laser pulse heating when strong phonon-scattering or phonon-electron interactions occurs. To describe these micro scale effects on heat transfer phenomena, researchers proposed two temperature models and phase lag models using damped version of Fourier's law of heat conduction.
- Thin sheets with its low stiffness are more susceptible to distortion. Quite a few literatures have come up to predict distortion of thin sheets mainly using the finite element based software. However, most of this model is limited to analyze 2 mm thick materials. The buckling deformation which occurs during the assembly process is becoming the most critical mode of welding deformation compared with other deformation modes for the thin plate welded structures.
- There is a lack of complex thermo-mechanical-metallurgical models in micro joining process which takes into account more physical phenomena to predict distortion and residual stress in a solidified joint structure. Microstructure of the final weld structure, presence of surface active elements in parent materials in the formation of the weld pool shape, effect of fixtures in joining micro parts are still to be looked into. The phase transformation effect is important to predict residual stress and distortion in fusion welding process.

2.7 Scope of Present Work

Based on the survey of existing work in literature, the objectives of the present work are summarized as:

- The initial aim of the present work is the experimental investigation of laser and plasma micro welding processes and to bring out an envelope of suitable combination of process parameters required for successful joints. It is further attempted to analyze the effect of process parameters on the quality of the final weldment. The primary focus is mainly on micro welding of Ti6Al4V alloy along with stainless steel and low carbon steel.
- The present work also aims to develop numerical model for better understanding of differential influence of process parameters in microwelding process. The conduction mode heat transfer with an effective heat source model is sufficient to represent the numerical model micro scale welding process which simplifies the calculation by removing the

complexities associated with convection mode of heat transfer. However, the transport phenomena based heat transfer and fluid flow mode will help to enhance the understanding of the overall temperature field. Also, the incorporation of temperature dependent material properties and latent heat of fusion has significant effect on the solution of temperature and fluid flow field.

- The numerical heat transfer and fluid flow models in fusion welding often fail to provide with reliable predictions as a number of input variables, that are specifically required for modeling calculations, are rarely known with confidence. In general, values of such input parameters are obtained either from past experience or through a huge volume of numerical experiments. The use of optimization algorithm assisted numerical models that can inherently learn the suitable values of such uncertain model parameters has just started. The present work has aimed at extensively using this concept to develop a reliable integrated process model.
- The present work also attempts to analyze the distortion and residual stress developed during the micro welding process. For this purpose sequentially coupled thermo-mechanical is attempted to develop. However successful prediction of residual stress depends greatly on accurate simulation of temperature fields.
- It is often required to consider the phase lag effect in heat transfer mechanism during ultra-short pulse laser processing. The heat is not transferred to the substrate material instantaneously i.e. Fourier heat conduction model fails to explain this phenomena. Therefore, an attempt has been made to simulate the ultra-shot pulse laser heating process by non-Fourier heat conduction. The experimental data were however adopted from independent literature to validate the numerical model.

Chapter 3

Theoretical Formulation

3.0. Introduction

Theoretical investigation by mathematical modelling provides better understanding of underlying physics involved in the process. In the present work, finite element based numerical model is developed for micro scale welding process. The thermal analysis is performed considering either Fourier heat conduction or non-Fourier heat conduction. Sequentially coupled thermo-fluid and thermo-elastic–plastic finite element model is also developed to simulate the micro plasma arc and laser microwelding processes. The commercial finite element code ABAQUS multi-physics is used to obtain temperature field, weld induced distortion and residual stresses. However, a well-tested thermo-fluid model is used to analyse the material flow in laser microwelding process. The in-house developed non-Fourier heat conduction model is used to analyse the heat transfer aspect in a thin nano scale film limited to surface heating using a ultra-short pulse laser. An attempt has been made to consider contact thermal condition between two mating surfaces and is implemented in laser transmission welding process. The numerical model is validated with micro welding experiments for several materials like low carbon steel, stainless steel, and titanium alloy.

The coupled analysis procedure is divided into two steps. First, a transient nonlinear uncoupled heat flow analysis is performed to determine the temperature distribution in the entire weldment for the entire welding process and predict the fusion and heat-affected zones (HAZs). The stress analysis considers thermal history as input and predicts distortion and residual stress of the welded joint. Direct coupled heat transfer and fluid flow model help to simulate the evolution of temperature and velocity fields during micro welding processes. Temperature dependent material properties and latent heat of melting and solidification are incorporated in the

numerical model. In addition to the process variables, the numerical model require an additional set of parameters as input, which cannot be specified with confidence based on the scientific principles alone. The most suitable values of some of these significant uncertain input parameters are estimated by integrating HS (Harmony Search) based global optimization algorithm with the numerical model. The integrated model minimizes the sensitivity of the error in the prediction of weld pool dimensions, obtained from a few known welding experiments, and identifies their suitable values. The optimized values of these parameters are next used with greater confidence for the heat transfer and fluid flow calculations.

3.1 Conduction Mode Heat Transfer Analysis

It is well-known fact that consideration of transport phenomena based models in fusion welding are physically superior to only conduction based heat transfer analysis. However, in microwelding process, the conduction heat transfer is often preferred due to insignificant volume of molten zone that directly reduces the computational cost. To approximate the influence of convective transport of heat in weld pool in the conduction heat transfer based thermal analysis, a volumetric heat source term is often used. However, heat transfer in micro/nano scale has very different physical basis as compared to macro scale process. Most of the problems of short pulse laser welding and heating are described and analysed by Fourier's law of heat conduction that assumes infinite speed of thermal wave propagation i.e. whenever heat transfer occurs in certain location within a continuum of the material it is felt everywhere instantaneously. This assumption is incorrect since it is observed experimentally that the thermal wave propagates with a finite speed. When the order of magnitude of time and space of the system is extremely small, Fourier's law fails to precisely predict the transient temperature distribution. This is exactly the case in ultra-short pulse laser processing where the time of heat transfer is extremely small (~ 10^{-15}s) and the heat affected zone is also very small (~ 10^{-9}m).

3.1.1 Fourier heat conduction

The heat input into the work piece is approximated by a surface heat source with constant shape. The mathematical formulation of the model is based on the following assumptions:

- The top surface of the weld pool is considered to be flat, neglecting the effect of plasma arc and shielding gas. As keyhole formation is not expected, the energy absorption of the plasma can be neglected.
- The welded sheets are considered as solid deformable bodies in the FE simulation.
- Only half of the geometry is considered due to symmetry along the weld line. This effectively reduces the computational time.
- The thermal properties have been considered as temperature dependent.
- The initial temperature of the workpiece is considered as 298 K.

Governing equation and boundary conditions

An estimation of the temperature at the interface is required for establishing the welding process parameters. The mechanism of heat conduction resulting in transient temperature field generated during welding is determined based on the basic principles of thermal transfer and conservation of energy:

$$\rho C\left(\frac{\partial T}{\partial t}\right) = U\frac{\partial T}{\partial x_1} + \frac{\partial}{\partial x_i}\left(K_{ij}\frac{\partial T}{\partial x_j}\right) + \dot{Q} \qquad (3.1)$$

where ρ is the density, T is the temperature, C is the specific heat, $\dot{Q}$ is the rate of internal heat generation, K_{ij} the component of thermal conductivity tensor and U is the welding velocity. The term on the left side refer to the transient nature of the heat transfer process. The term on the right side infer to the conductive heat transfer in the three directions.

Figure 3.1 schematically shows one sheet of butt joint geometry to be welded along the interface 2-3-7-8 along with the mesh pattern utilized for the present model. The heat source is irradiated on the top surface along 3-2. The developed model comprises the whole welding process including the heating and the cooling phase.1-2-3-4 is the symmetric surface.

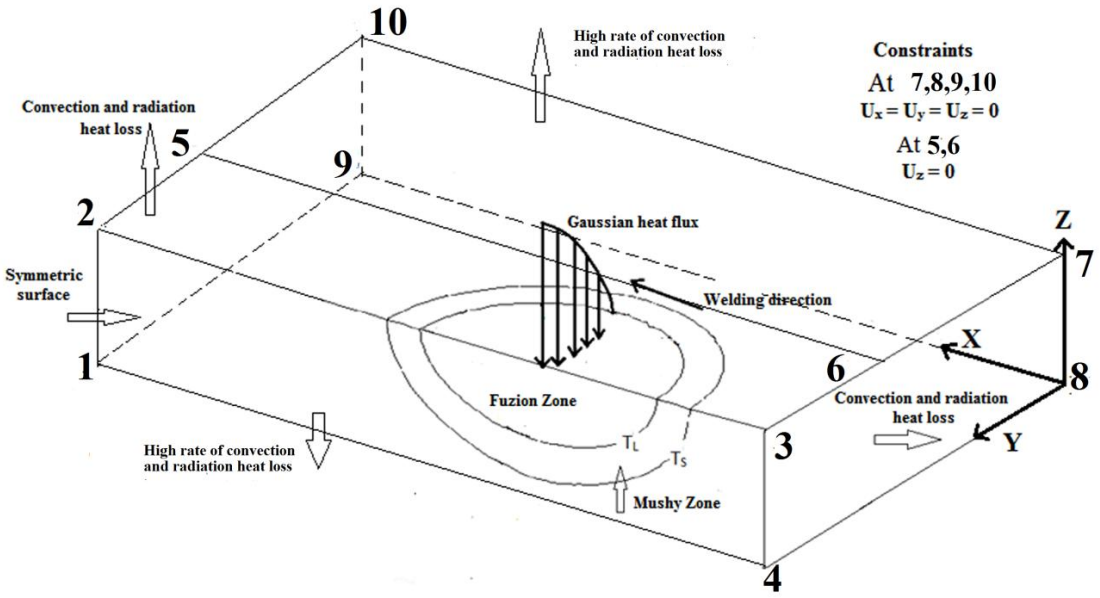

Fig. 3.1 Schematic representation of the solution geometry and boundary interactions.

Boundary conditions

For heat transfer between the workpieces and the surrounding medium, the following boundary condition is considered.

a) Initial boundary condition where the temperature at the boundary is specified,

At time $t = 0$, $T(x, y, x, 0) = T_0$ (3.2)

b) At the symmetric surface, there is no gradient

i.e. $\frac{\partial T}{\partial y} = 0.$ (3.3)

c) Mathematically heat interactions of all the surfaces can be expressed as:

$$K\frac{\partial T}{\partial n} + q_s + \varepsilon(T^4 - T_0^4) + h_c(T - T_0) = 0 \quad (3.4)$$

where q_s defined by a Gaussian heat distribution, n denotes the direction normal to the surface, h_c is the heat transfer coefficient, and T_0 is the ambient temperature. The first term denotes the heat conduction to the boundary surface, the second surface the heat flux from the heat source on the top surface, the second and third terms represent the heat loss by radiation and convection, respectively, ε is the emissivity. The surfaces which are in direct contact with air are assigned coefficient of convective heat transfer of air. However, at the surfaces 1-4-8-9 and 5-6-7-10, the

workpiece is in tight contact fixture and copper backing plate, having high thermal conductivity. Therefore, these interfaces are assigned with a high heat transfer coefficient.

Heat source model

The modelling of heat source helps to accurately predict the required weld pool shapes and temperature profiles. It is noteworthy that the surface heat flux does not produce adequate weld penetration until a well-defined heat source model is defined as in welding process the power of the beam decreases with increasing depth of the penetration, which should be taken into account in numerical modelling. The heat source is considered as Gaussian distribution over the volume such that flux density decreases in depth of penetration. However, to provide a better representation of weld bead at higher heat input, an hourglass-like heat source model is more suitable to describe the unique shape of laser microwelding instead of commonly used conical heat source model. As the heat input is increased more energy is deposited; an equivalent heat source is defined in the volume by finding a satisfactory spatial distribution. The simplest method is to identify the distribution from the weld bead shape. In the present model, the general heat source model is defined by:

$$\dot{Q}(x,y,z,t) = q_o h(t) \exp\left[-d\frac{(x-Ut)^2+y^2}{r_{eff}{}^2}\right] \exp[\omega - z] \tag{3.5}$$

where r_{eff} is the effective radius of the heat source falling on the top surface, and U is the laser scanning velocity along x direction, ωis the thickness of the plate, and q_0 is the laser intensity at the center of the beam, which is defined as:

$$q_o = \frac{\alpha d P_{total}}{\pi r_{eff}{}^2 p} \tag{3.6}$$

where P_{total} is the total power and p is the weld depth and η is the absorption coefficient, d is the power density distribution factor. For micro plasma welding, the maximum intensity is expressed as:

$$q_0 = \frac{d\eta VI}{\pi r^2 p} \tag{3.7}$$

where V is the voltage, I is the current,η is the arc efficiency and r_{eff} is the arc radius at the workpiece surface. In Eq. (3.5), h(t) shows the temporal variation of intensity. In case of

continuous welding h(t) is 0 for the whole cycle. In the pulse laser, the value of h(t) is equal to 1 at pulse on-time and else zero during pulse off-time. The frequency of the welding determines the number of time steps that the pulse was on. However, it is revealed from the laser micro welding from the macrograph that the shape of weld pool of the full penetrated welds cannot be accurately characterized by the assumed heat source when the heat input is increased, especially in the bottom of welds. To represent the shape of full penetration welds, an hourglass like heat source with Gaussian power density distribution is developed. The schematic diagram of hourglass-like heat source model is shown in Fig. 3.2 where the volumetric shape consists of two combined frustums. Thus the volumetric heat source distribution becomes:

$$\dot{Q}(Z,r) = \frac{3d\eta P_{total}}{\pi.[1-\exp(-d)].(Z_t-Z_m)[r_m{}^2+r_m.r_t+r_t{}^2]} h(t)\exp\left[-d\frac{(x-Ut)^2+y^2}{r_{eff}{}^2}\right]; \text{ for upper cone } (Zo \geq Zm) \quad (3.8)$$

$$\dot{Q}(Z,r) = \frac{3d\eta P_{total}}{\pi.[1-\exp(-d)].(Z_m-Z_b)[r_m{}^2+r_m.r_t+r_t{}^2]} h(t)\exp\left[-d\frac{(x-Ut)^2+y^2}{r_{eff}{}^2}\right]; \text{ for lower cone } (Zo < Zm) \quad (3.9)$$

where z and r represent the z-axis coordinate and the radial distance from the axis, the subscript "t", "m" and "b" represent the top surface, middle surface, and bottom surface of the heat source, respectively. The effective radius of the cones is defined as:

Upper truncated cone: $r_{eff} = \frac{Z_o-Z_m}{Z_t-Z_m}(r_t - r_m) + r_m$ (3.10)

Lower truncated cone: $r_{eff} = \frac{Z_o-Z_b}{Z_m-Z_b}(r_b - r_m) + r_m$ (3.11)

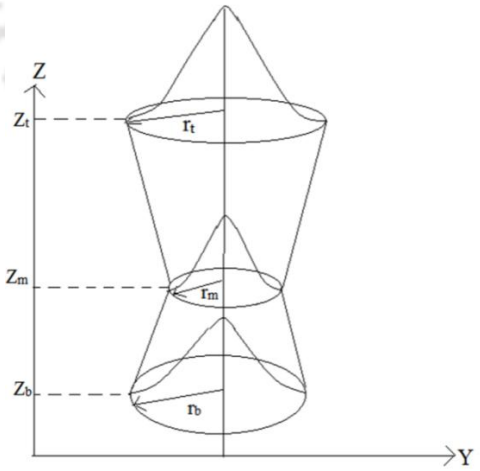

Fig. 3.2 Hourglass like heat source model.

3.1.2 Distortion and residual stress model

Once the thermal model is produced, the development of the mechanical model will enable the prediction of the welding distortions and material residual stresses to be calculated. The deformation of the structure after welding is resulted from the plastic deformation at elevated temperature and the thermal expansion and contraction.

- The temperature dependent mechanical properties such as thermal expansion coefficient, Young's modulus, yield stress, ratio between the tangential modulus and Young's modulus, and Poisson's ratio respectively, are considered.
- For mechanical analysis, the material is assumed to follow the bi-linear isotropic hardening law. The strain-rate independent plasticity is assumed.
- The material is considered to be elasto-plastic behaviour.
- The plastic deformation obeys the von-Mises criterion, the yield function of the material.

Neglecting the effect of phase transformation, the total strain can therefore be decomposed into three components as follows:

$$\{d\varepsilon^{Total}\} = \{d\varepsilon^{E}\} + \{d\varepsilon^{P}\} + \{d\varepsilon^{T}\} \quad (3.12)$$

where dε represent the incremental strain components due to elastic, plastic, thermal loading respectively. The elastic strain increment $d\varepsilon^{E}$ is calculated using the isotropic Hook's law with temperature-dependent Young's modulus and Poisson's ratio. For the plastic strain increment $d\varepsilon^{P}$, a rate-independent elastic-plastic constitutive equation is considered with the von-Mises yield criterion and temperature dependent mechanical properties. The thermal strain increment $\Delta\varepsilon^{T}$ is computed using the coefficient of thermal expansion as

$$d\varepsilon^{T} = \beta\Delta T \quad (3.13)$$

where β is the thermal expansion coefficient and ΔT is the change in temperature.

Two cases are performed in mechanical simulation for the analysis of deformation behaviour that occurs during welding related to two different deformation theories: Case A describes infinitesimal strain theory or small deformation theory where strains and rotations are both small. Case B defines the finite strain theory or large deformation theory, deals with deformations in which both rotations and strains are arbitrarily large. In case A the strains can be expressed as a linear function of displacement. When case B is considered, Green–Lagrange

strain which is the nonlinear function of the displacement is required. The Green Lagrange Strain tensor as a function of the displacement gradients can be expressed as [Deng *et al.*, 2008a]

$$\varepsilon_{ij} = \frac{1}{2}\left(u_{i,j} + u_{j,i} + \sum_{k=1}^{3} u_{k,i}u_{k,j}\right), \quad i,j = 1,2,3 \tag{3.14}$$

where ε_{ij} are the element of the strain tensor ε and $u_{i,j} = \delta u_i / \delta x_j$ is the displacement gradient. The strain tensor is symmetric and can be used to define the following strain vector:

$$\varepsilon_v = [\varepsilon_{11}\ \varepsilon_{22}\ \varepsilon_{33}\ \varepsilon_{12}\ \varepsilon_{13}\ \varepsilon_{23}]^T \tag{3.15}$$

In this vector, ε_{ij} for i = j are the normal strains and ε_{ij} for i ≠ j are the shear strains. The first two terms represents the linear response and the third term in Eq. (3.14) is the product of gradients in displacement, and is thus second order and describes the non-linear behaviour under large deformation. This term is neglected as long as the displacement gradients are small compared to unity as in case A.

A rate independent plasticity is used as the material is subjected to high temperature for a relatively short time. The von-Mises yield surface is defined as:

$$f = \frac{1}{\sqrt{2}}[(\sigma_{11} - \sigma_{22})^2 + (\sigma_{22} - \sigma_{33})^2 + (\sigma_{33} - \sigma_{11})^2 + 6(\sigma_{23}^2 + \sigma_{31}^2 + \sigma_{12}^2)]^{1/2} \tag{3.16}$$

where the longitudinal stress is expressed as σ_{11} and transverse stress is σ_{22}.

3.1.3 Computational methods

The finite element analysis of the process has been conducted using the FE code ABAQUS. Finite element involves solving a differential equation by its application on a discretized domain. When solving the non-linear heat conduction equation by FEM, the equation is first discretized in the spatial region followed by the temporal region (time domain). The material properties are taken into consideration and the equations are applied to individual discretized elements. These set of equations are then assembled to generate a global set of equations which are then solved to obtain the solution at any individual discretization. The discretized form of heat conduction equation is written as:

$$[H]\{T\} + [C]\{\dot{T}\} = \{P\} \tag{3.17}$$

where [H] is the heat conduction matrix, {T} is the temperature vector, [C] is the heat capacity matrix and {P} is the heat flow vector. The stress model directly considers the temperature distribution from thermal model and solve for displacement field by considering the incremental mode of strain. Following Prandtl-Reuss flow rule and von-Mises yield criteria, the incremental stress can be represented as [Singh *et al.*, 2014]:

$$\{d\sigma\} = [D^{ep}]\{d\varepsilon\} - \left[C^{th}\right]\{dT\} \tag{3.18}$$

$$\text{where } [D^{ep}] = [D^{e}] - [D^{p}];\ \left[C^{th}\right] = \{\alpha\}[D^{e}] \tag{3.19}$$

$[D^{ep}]$ is elasto-plastic matrix, $[D^{e}]$ is elastic stiffness matrix, $[D^{p}]$ is plastic stiffness matrix, $\left[C^{th}\right]$is thermal stiffness matrix and {dT} is the temperature increment. The elasto-plastic matrix is expressed as:

$$[D^{ep}] = \left([D^{e}] - [D^{e}]\left\{\frac{\partial f}{\partial \sigma}\right\}\left\{\frac{\partial f}{\partial \sigma}\right\}^{T}[D^{e}]\frac{1}{3G+E_T}\right) \tag{3.20}$$

where $[D^{e}]$ depicts the elasticity matrix which consists of mechanical properties like Young's modulus and Poisson's ratio, G is shear modulus and E^{T} is local slope between stress and plastic strain of the specified material. The elasto-plastic matrix is due to recovery of elastic response when the material is in plastic deformation zone. The second term on the right hand side of Eq. (3.20) becomes zero when the material is in elastic zone only. The function "f" predicts the yield surface and the evolution of the yield surface are governed by the hardening rule. According to the minimization of potential energy of the system, the following equation is used from standard procedure as [Singh *et al.*, 2014]:

$$[K]\{X\} = \left\{F^{th}\right\} \tag{3.21}$$

where {X} is the global displacement vector, [K] refers to stiffness matrix, and $\left\{F^{th}\right\}$ is the thermal load vector.

A distributed heat flux is applied on the material body on which the laser is being focussed. The moving heat flux is implemented into ABAQUS through DFLUX subroutine

which has been written to describe the spatial and temporal variation of the heat source. The time is calculated based on the welding speed and heat source location. Thus, a nodal temperature history is obtained as a function of time. This nodal temporal field is given as a load for the mechanical analysis. Thus effectiveness of the mechanical model is reflected by the robustness of the thermal model.

A three dimensional sequentially coupled thermo-elastic–plastic finite element model is developed to simulate microplasma welding process as well as laser micro welding process. The finite element code is used to calculate temperature field, welding residual stress, and welding deformations. The analysis procedure is divided into two steps. First, a transient nonlinear uncoupled heat flow analysis is performed to determine the temperature distribution in the entire weldment for the entire welding process and predict the fusion and heat-affected zones (HAZs). And then stress analysis taking thermal history as input. The overall model is shown in Fig.3.3. Few of the important steps are delineated below:

- The solution domain is created and discretized into a finite number of elements in such a way that fine meshes are created near the weld centreline and coarser meshes away from the centre.
- The thermo-mechanical properties are considered to be temperature dependent.
- The process parameters are defined and a suitable heat source model with prior knowledge of the weld dimension is adapted. The moving heat source is implemented through the DFLUX subroutine.
- The total weld time is divided into small time-steps and then the analysis is implemented for each time step explicitly.
- The output of the thermal model is the thermal cycles.
- Temperature histories obtained from thermal analysis were applied as thermal loads in the subsequent mechanical analysis. The mesh in the mechanical analysis should be exactly same as in thermal analysis to facilitate data mapping between thermal and mechanical analysis.
- Von-Mises yield criteria with strain rate dependent bilinear isotropic hardening is considered.
- The residual stress and distortion are predicted from the mechanical model.

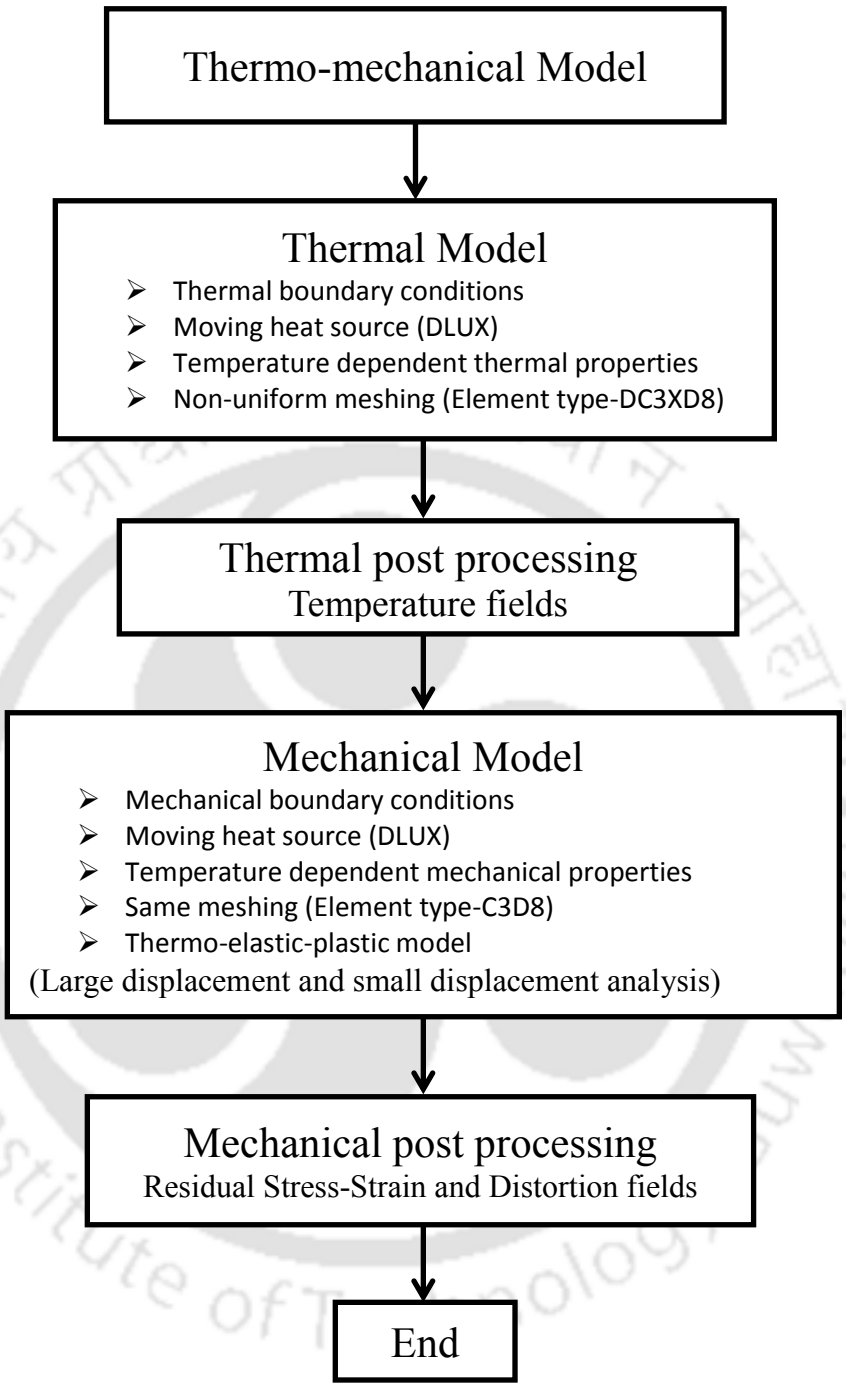

Fig. 3.3 Overall flowchart of thermo-mechanical analysis.

3.1.4 Non-Fourier heat conduction

To account the finite time of heat propagation, researches have proposed to upgrade Fourier equation from parabolic to hyperbolic nature of governing equation. Thus, a hyperbolic

non-Fourier model with finite thermal wave speed has to be considered for the analysis of heating by ultra-short pulse laser. Present study is focused on dual phase lag (DPL) model which accounts for non-zero time required by the heat flux and temperature gradient to gradually become established in response to thermal disturbance by ultra-short pulse laser. When the duration of heat transfer approaches of the order of femtosecond, the assumption of Fourier law i.e. thermal wave having infinite speed is no longer valid. An idea of relaxation time is introduced in single phase lag (SPL) model where one relaxation time accounts for heat flux. Cattaneo [1958] and Vernotte [1958] proposed the single phase lag model (SPL) which accounted only one relaxation time. This model was accurate in analysing of heat transfer through short pulse laser. For ultra-short pulse laser where the heat effected zone is very small (in the order of micro/nanometres), the dual phase lag (DPL) model provides more accurate results than SPL model. In DPL model two non-zero time is required by heat flux and temperature gradient to gradually become established in response to thermal disturbance (i.e. imposed heat flux). In contrast, Fourier's law assumes heat flux and temperature gradient becomes established immediately (i.e. the relaxation time is zero).

Governing equations and boundary conditions

The Fourier's law of heat conduction in one-dimensional form is represented as

$$q = -k\frac{\partial T}{\partial x} \tag{3.22}$$

where q is the heat flux, k the thermal conductivity and $\frac{\partial T}{\partial x}$ the temperature gradient. Assuming first order Taylor series expansion, one dimensional DPL equation relating to relaxation in heat flux and temperature gradient is expressed as

$$q + \tau_q \frac{\partial q}{\partial t} = -k\left\{\frac{\partial T}{\partial x} + \tau_T \frac{\partial}{\partial t}\left(\frac{\partial T}{\partial x}\right)\right\} \tag{3.23}$$

where thermal lags or delays τ_q and τ_T are approximately are time required for gradual response of heat flux and temperature gradient, respectively. Further $\partial q/\partial t$ and $\partial^2 q/\partial t\,\partial x$ represents the transient behaviour of heat flux and temperature gradient during this response. Once the gradual

response completes, the heat flux and temperature gradient achieve the value given by Fourier's Law. In general $\tau_q$and τ_T are interpreted as non-zero time accounting for the effect of thermal inertia and microstructural interaction, respectively. Hence τ_q is the delay in establishing heat flux and associated conduction through solid. This delay tends to induce thermal wave with sharp wave front separating the heated and unheated zone in the solid. Where τ_T is the delay in establishing the temperature gradient across the solid during which conduction occurs through its small scale structure. The values of thermal lags are typically very small for continuous solid which implies immediate response of temperature development. For gold, $\tau_q$and τ_t are in the order of subpicosecond to picosecond (10^{-13}to10^{-12}) whereas for non-continuous solids the lag can be relatively large i.e. in the order of seconds [Banerjee *et al.*, 2005].

Fourier's Law can provide accurate approximation except for very small period of time after thermal disturbance. One-dimensional unsteady state heat conduction without internal heat generation is expressed as

$$\frac{\partial^2 T}{\partial x^2} = \frac{\rho c}{k}\frac{\partial T}{\partial t} \tag{3.24}$$

Eq. (3.23) reduces to the non-Fourier Cattaneo-Vernotte model [Yang, 1991] i.e. SPL model following hyperbolic heat conduction by setting $\tau_t = 0$. The Eq. (3.23) can be reduced to Fourier's Law for steady state condition even when τ_T and τ_q are zeros (immediate response). The DPL model in three dimensional form is written as

$$\dot{T} + \tau_q \ddot{T} - \alpha\left(\frac{\partial^2 T}{\partial x^2} + \frac{\partial^2 T}{\partial y^2} + \frac{\partial^2 T}{\partial z^2}\right) - \tau_T \delta\left(\frac{\partial^2 \dot{T}}{\partial x^2} + \frac{\partial^2 \dot{T}}{\partial y^2} + \frac{\partial^2 \dot{T}}{\partial z^2}\right) = 0 \tag{3.25}$$

where δ is the thermal diffusivity and T represents temperature variable. The detail derivation of Eq. (3.25) is described in Appendix A. The initial condition of the process is considered as

$$T(t) = T_0 \text{ at } t = 0 \tag{3.26}$$

where T_0 is the reference temperature. Since the solution domain has finite boundary, it is necessary to define the boundary conditions. The phase lag boundary condition as a function of time is expressed as

$$k_n \left\{\frac{\partial T}{\partial n} + \tau_T \frac{\partial}{\partial t}\left(\frac{\partial T}{\partial n}\right)\right\} = q + \tau_q \frac{\partial q}{\partial t} - h_{eff}(T - T_0) \tag{3.27}$$

where h_{eff} is lumped heat transfer coefficient, q is imposed heat flux on the surface due to laser heat source, k_n is the thermal conductivity normal to the surface. The Eq. (3.27) can be assumed as heat conducted from the top surface of the work piece is equal to heat supplied from the ultra-short pulse laser on the surface minus heat lost from the surface by convection or radiation to the surrounding at ambient temperature. The second term of left hand side of Eq. (3.27) indicates the transient lagging of temperature gradient on the boundary. The second term of right hand side also indicates the lagging in heat flux on the surface. The lumped heat transfer coefficient is combined effect of convection and radiation heat loss form the surface and is expressed as [Desai and Bag, 2014]:

$$h_{eff} = 2.4 \times 10^{-3} \varepsilon \times T^{1.61} \tag{3.28}$$

where T is temperature (K) and ε is emissivity. Gaussian distributed surface heat flux model is used to simulate the temperature distribution. The heat flux model is expressed as

$$q(r,t) = \begin{cases} \frac{\alpha P k}{\pi r_{eff}^2} \exp\left(-\frac{dr^2}{r_{eff}^2}\right) g(t) & \text{if} \quad r \le r_{eff} \\ 0 & \text{if} \quad r > r_{eff} \end{cases} \tag{3.29}$$

where P is the laser power, r_{eff} is the laser spot radius and r is the radial distance from the heat source centre, α is the laser absorption coefficient, and d is the distribution coefficient. The temporal distribution of the pulse train g(t) is approximated as a rectangular pulse and is expressed as:

$$g(t) = \begin{cases} P(t) & \text{if} \quad t \le t_p \\ 0 & \text{if} \quad t > t_p \end{cases} \tag{3.30}$$

where P(t) is the peak power and t_p is the pulse on-time.

Finite element discretization

The governing equation along with boundary condition is discretized using Galerkin's weighted residue technique over the solution domain. The hyperbolic nature of equation for an element (superscript 'e') is represented as

$$[K^e]\{T^e\} + [M^e]\{\ddot{T}^e\} + [C^e]\{\dot{T}^e\} = \{F^e\} \tag{3.31}$$

$$[K^e] = [K^e]_v + [K^e]_s \tag{3.32}$$

$$[C^e] = [C^e]_{v1} + [C^e]_{v2} + [C^e]_{s1} \tag{3.33}$$

$$\{F^e\} = \{F^e\}_1 + \{F^e\}_2 \tag{3.34}$$

The subscript 'v' and 's' represents over elemental volume and surface respectively. The detail derivation of discretized form is expressed in Appendix B. For an 8 nodded brick element, the elemental form of the Eq. (3.31) is written as

$$[K_{ij}]_v = \iiint k\left(\frac{\partial N_i}{\partial x}\frac{\partial N_j}{\partial x} + \frac{\partial N_i}{\partial y}\frac{\partial N_j}{\partial y} + \frac{\partial N_i}{\partial z}\frac{\partial N_j}{\partial z}\right) dxdydz \tag{3.35}$$

$$[M_{ij}]_v = \iiint \tau_q \rho c N_i N_j dxdydz \tag{3.36}$$

$$[C_{ij}]_{v_1} = \iiint \rho c N_i N_j dxdydz \tag{3.37}$$

$$[C_{ij}]_{v_2} = \iiint k\tau_T\left(\frac{\partial N_i}{\partial x}\frac{\partial N_j}{\partial x} + \frac{\partial N_i}{\partial y}\frac{\partial N_j}{\partial y} + \frac{\partial N_i}{\partial z}\frac{\partial N_j}{\partial z}\right) dxdydz \tag{3.38}$$

where N represents the shape function and "dxdydz" indicates the elemental volume over global coordinate system. The values of $[K_{ij}]$, $[M_{ij}]$, $[C_{ij}]$ are evaluated from numerical integration. Gauss quadrature method is used for numerical integration. The terms related to the boundary condition are obtained for specified boundary

$$[K_{ij}]_S = \iint h_{eff} N_i N_j dxdy \tag{3.39}$$

$$[C_{ij}]_{s_1} = \iint \tau_q k\left(N_i \frac{\partial N_j}{\partial x} + N_i \frac{\partial N_j}{\partial y} + N_i \frac{\partial N_j}{\partial z}\right) dxdy \tag{3.40}$$

$$\{F_i\}_1 = \iint qN_i dxdy \quad (3.41)$$

$$\{F_i\}_2 = \iint h_{eff}\, T_0 N_i dxdy \quad (3.42)$$

The value of $[K_{ij}]_S, [C_{ij}]_{s_1}, [C_{ij}]_{s_2}, \{F_i\}_1, \{F_i\}_2$ are further obtained through numerical integration using gauss quadrature method.

3.1.5 Contact conduction

A gap can exist between the contact surface of the fixture and the sheets to be joined. Also gap is a more serious problem when plates are joined in lap joint configuration as the joining process is mainly depended on heat conduction between the two surfaces. Thus gap conduction has to be modelled accurately for better accuracy. Thus in the present model the relevance of contact conduction has been modelled for a welded joint in lap joint configuration. For accurate simulation of the process attention must be paid to the thermal contact conductance. The thermal contact can be treated as either contact between two surfaces touching each other (perfect contact) or surfaces with a gap between them. In the FE modelling, the contact is defined between two nodes or a node from the slave surface and a projection of this node to the nearest element face from the master surface. Using the FEM the gap conductance coefficient must be specified for achieving the heat transfer between two interfaces in a contact. In general a gap exists between the two joining parts, which worsen or prevent the heat flow. The surfaces of the joining partners as well as the gap are generating a thermal resistance. The existence of a finite contact resistance is primarily due to a surface roughness effect. Heat transfer is therefore due to conduction across the actual contact area and also due to conduction and/or radiation across the gaps. For the modelling it is assumed the original gap has a homogeneous width d_{gap} and it is filled with air.

Heat transfer between the two materials has been modelled by using the user subroutine GAPCON implemented into surface interaction technique option in ABAQUS, as physically these materials are in contact with each other; however, they have large and distinct temperatures on each side. The heat transfer between contacting interfaces in ABAQUS is defined as:

$$q = h(T_1 - T_2) \quad (3.43)$$

where q is the heat transfer between corresponding nodes 1 and 2, h is the gap conductance. The heat transfer equilibrium equation is given by:

$$q = q_c + q_r \tag{3.44}$$

where q is the gap heat transfer, q_c is the gas conductance heat transfer and q_r is the radiation heat transfer. The gas conductance heat transfer is given by [Chen 2009]**:**

$$q_c = \frac{k_g(T_1 - T_2)}{d_{gap} + d_r} \tag{3.45}$$

where: k_g is the conductance coefficient of the gas, T_1 and T_2 are the temperatures at nodes 1 and 2, d_{gap} is the gap clearance and d_r is due to the roughness between the two contacting surface. The radiation heat transfer between two nodes in contact is given by [Chen 2009]:

$$q_r = Sf(T_1^4 - T_2^4) \tag{3.46}$$

where f is the radiation factor, S = 5.6697×10^{-8} W/(m^2K^4) is the Stefan-Boltzmann constant, T_1 and T_2 are the temperatures in nodes 1 and 2 and they must have units in K. The radiation factor can be given as a function of the emissivity [Chen 2009]:

$$f = \frac{1}{\left(\frac{1}{\varepsilon_1} - \frac{1}{\varepsilon_2} - 1\right)} \tag{3.47}$$

where ε_1 and ε_2 are the emissivity coefficients for surfaces 1 and 2. Thus equation (3.44) can be rewritten as:

$$h(T_1 - T_2) = \frac{k_g (T_1 - T_2)}{d_{gap} + d_r} + \frac{S(T_1^4 - T_2^4)}{\left(\frac{1}{\varepsilon_1} - \frac{1}{\varepsilon_2} - 1\right)} \tag{3.48}$$

$$\text{i.e. } h = \frac{k_g}{d_{gap} + d_r} + \frac{S(T_1^4 - T_2^4)}{\left(\frac{1}{\varepsilon_1} - \frac{1}{\varepsilon_2} - 1\right)(T_1 - T_2)} \tag{3.49}$$

The gap conductance coefficient from Eq. (3.48) is implemented into the user defined GAPCON subroutine. This subroutine is called in each time increment of the coupled temperature displacement analyses in ABAQUS. Contact in ABAQUS can be defined between a node from the slave surface and the nearest node to it from the master surface. The nodal temperature calculated through the DFLUX subroutine is implanted in this subroutine. The mating surfaces at the interface have been modelled by with same sets of nodes.

Laser Transmission Welding

Gaps at part interfaces pose a major challenge for laser transmission welding (LTW) of thermoplastics due to the reliance on contact conduction between the absorptive and transmissive parts. In industrial applications, gaps between parts can occur for a variety of tolerance and process control reasons. Previous experimental and modelling work in LTW has focused on gap-free joints, with little attention to bridging a gap with thermal expansion of the absorbing material. The absorbing part must be heated slowly to allow conduction into the bulk of the material, which will increase the thermal strain and allow the two parts to meet. Achieving the necessary thermal strain is not trivial because the thermal conductivity of polymers is relatively low and during a longer weld time, the possibility of thermal decomposition becomes greater .A three-dimensional comprehensive numerical model simulated bridging gaps in LTW. Using the model, operating parameters were selected for welding across different gaps by creating sufficient thermal strain to bridge the gap and form a weld. Designing a laser transmission weld to bridge a gap requires careful consideration of the heating distribution.

The transient temperature field generated during laser welding is determined based on the mechanism of heat conduction. At the initial condition when t = 0 s, the workpieces are at uniform ambient temperature. The environmental temperature is chosen as T_o = 300 K. For heat transfer between the workpieces and the surrounding medium the boundary condition is represented by Eq. (3.4). The heat source model is depicted by:

$$q_s = \begin{cases} 0; & \text{for transparent material} \\ \frac{(1-R)PT_t\alpha d}{\pi r_{eff}^2} \exp\left[\frac{-d(x_s^2+y_s^2)}{r_{eff}^2}\right] \exp[\alpha z_s]\,; & \text{for absorbing material} \end{cases} \quad (3.50)$$

where P refers to laser power, r_{eff} is effective radius of laser beam on the work piece surface, d is the power density distribution factor of heat source, R_a and α are reflectivity and absorption coefficient of the absorbing material and T_t is the fraction of laser energy transmitted through the top material. In Eq. (3.50) the heat flux at any penetration depth follows Gaussian distribution. The term actually used in Eq. (3.50) is volumetric heat source term and is incorporated in Eq. (3.1) through internal heat generation term. The absorption coefficient of polymer increases linearly with the carbon black (CB) content. Absorption coefficients of material for different level of carbon black concentration are linearly extrapolated using following linear regression equation [Acherjee *et al.*, 2012]:

$$\alpha = 82C_B \tag{3.51}$$

where α is the absorption coefficient (mm^{-1}) of the material containing C_B per cent carbon black by weight. Lower CB content caused higher melt depths, although more line energy was needed to obtain high strength welds. The effect of CB particle size on weld strength has been studied [Schulz and Haberstroh, 2000; Haberstroh and Lutzeler, 2001]. Both of them found that, under the same laser power irradiation, smaller carbon black particle sizes result in higher butt joint weld strengths. For reference, the primary sizes of CB used were 20 nm and 60 nm. They also mentioned that the dimensions of the CB aggregates can reach several hundreds of nanometres. Shultz and Haberstroh [2000] welded PMMA to ABS at a CB level of 0.5 wt. %. Haberstroh and Lutzeler [2001] explained that smaller particle size of CB could absorb more light energy and transform it into heat for the same amount of irradiated laser power. It would have been more informative if the dimensions of the CB aggregates in the polymers, as well as the laser absorption coefficient of the polymers were measured and reported at the same time.

3.2 Three Dimensional Heat Transfer and Fluid Flow Analysis

In laser welding, an intense heat is focused on substrate material that forms the weld pool and subsequently solidifies with advancement of laser. Hence a quasi-steady state analysis is sufficient to gain in computational time. In quasi-steady state, a fixed shape of weld domain exists during welding process along the direction of laser scanning velocity vector. Hence, the analysis is performed over space domain in moving Cartesian coordinate system. Figure 3.1

depicts the solution domain and the interaction of various physical phenomena that occurs during welding process. Energy balance is maintained by heat flux on top surface of the specimen and loss of heat by conduction and radiation. The driving force for liquid metal movement is surface tension force that acts on the top surface of weld pool and the buoyancy force over volume of molten pool. This physical phenomenon is expressed through mathematical form of governing equations and corresponding boundary conditions.

Governing equations and boundary conditions

To analyse transport phenomena based heat transfer and fluid flow in laser micro welding, the conservation of mass, momentum and energy equations need to solve. The liquid molten material is assumed as an incompressible, Newtonian, and laminar flow. It is also assumed that laser is moving at a speed of v_w along x_2 direction. The conservation of mass is represented as [Reddy and Gartling, 2010]

$$\frac{\partial v_i}{\partial x_i} = 0 \tag{3.52}$$

where v_i denote the velocity components along x_1 (i =1), x_2 (i = 2) and x_3 (i = 3) directions. Conservation of momentum is also expressed as [Reddy and Gartling, 2010]

$$\rho\left(v_j \frac{\partial v_i}{\partial x_j}\right) = \frac{\partial}{\partial x_j}\left[-P\delta_{ij} + \mu\left(\frac{\partial v_i}{\partial x_j} + \frac{\partial v_j}{\partial x_i}\right)\right] - \rho U \frac{\partial v_j}{\partial x_2} + F_i \tag{3.53}$$

where P is the pressure, ρ is the density, F_i is the body force component, δ_{ij} is knocker delta, μ is the viscosity of molten material. The conservation of energy is expressed as [Reddy and Gartling, 2010]

$$\rho C\left(v_j \frac{\partial T}{\partial x_j} - V_w \frac{\partial T}{\partial x_2}\right) - \frac{\partial}{\partial x_i}\left(k_{ij} \frac{\partial T}{\partial x_i}\right) - \dot{Q} = 0 \tag{3.54}$$

where T is the temperature, C is the specific heat of material, $\dot{Q}$ the rate of internal heat generation, and k_{ij} the component of thermal conductivity tensor. The body force in laser welding consists of buoyancy force only. Considering Boussnesq approximation [McLay and Carey, 1989] the body force vector in Z-direction (i = 3) is expressed as

$$F_3 = -\rho\beta g\left(T - T_0\right) \tag{3.55}$$

where β is the coefficient of thermal expansion, g is the gravitational acceleration and T_o is the reference temperature. To avoid computational difficulty the free surface is considered as flat. The free surface of weld pool is subjected to surface tension and the velocity component normal to this surface is zero. The following boundary conditions are imposed for free surface.

$$\mu\frac{\partial v_1}{\partial x_3} = f_L\frac{\partial\gamma}{\partial T}\frac{\partial T}{\partial x_1}; \qquad \mu\frac{\partial v_2}{\partial x_3} = f_L\frac{\partial\gamma}{\partial T}\frac{\partial T}{\partial x_2}; \quad v_3 = 0 \tag{3.56}$$

where $\frac{\partial\gamma}{\partial T}$ is the temperature coefficient of surface tension, f_L is the volume fraction of liquid metal along the weld pool top surface, and v_1 , v_2 , v_3 are the velocity along X, Y and Z directions respectively. The solid-liquid interface surface is subjected to zero velocity components and is expressed as

$$v_1 = 0;\ v_2 = 0;\ v_3 = 0 \tag{3.57}$$

On the symmetric surface, a slip boundary condition is expressed as

$$v_1 = 0;\ \frac{\partial v_2}{\partial x_1} = 0;\ \frac{\partial v_3}{\partial x_1} = 0 \tag{3.58}$$

The boundary interaction for energy transport is expressed mathematically by Eq. (3.4). It is noteworthy thathigh penetration laser, the surface heat fluxis not sufficient to produce adequate weld penetration until a well-defined heat source model is defined without much

information about conduction or key-hole mode laser micro welding. In the frame of condition mode laser welding, the heat source model is defined by

$$\dot{Q} = \frac{(1-R)\,\mathrm{P}_{total}\,d}{\pi \mathrm{r}_{eff}^{\,2}\,p} \exp\left[\frac{-d(x_1^2 + x_2^2)}{\mathrm{r}_{eff}^{\,2}}\right] \exp\left[-\alpha(t - x_3)\right] \tag{3.59}$$

where Q refers to laser power, r_{eff} is effective radius of laser beam on the work piece surface, d is the power density distribution factor of heat source, p is the weld depth, and t is the thickness of plate. R and α are reflectivity and absorption coefficient of the material. In Eq. (3.59) the heat flux at any penetration depth follows Gaussian distribution. The flux also varies in exponential way along the depth direction till x_3 equals to the thickness of plate. The first term (except the exponential terms) in Eq. (3.59) represents the maximum intensity of heat flux at the centre of heat source. For simplicity and to reduce the number of process parameters, it is assumed $1 - R = \alpha$. The term actually used in Eq. (3.59) is volumetric heat source term and is incorporated in Eq. (3.54) through internal heat generation term.

Finite element discretization

The solution domain is discretized using 8 noded isoparametric brick element. Galerkin's weighted residue technique is used to generate linear system of equations. The penalty finite element method is used [Reddy and Gartling, 2010; Oden *et al.*, 1982; Zienkiewicz *et al.*, 1971] to solve momentum equations. By this method the pressure variable is linked with continuity equation in following way

$$P = -\lambda\left(\frac{\partial v_i}{\partial x_i}\right) \tag{3.60}$$

where λ is the penalty parameter that is set equal to a large number so that it can satisfy the continuity equation. Eq. (3.60) is treated as constraint on the velocity field. In this method the constraint problem is reformulated as unconstraint problem. To avoid nonlinearity due to the presence of the velocity components in the convective term (first term of Eq. 3.54) while solving

the momentum equations, the convective velocities are made independent of the nodal velocity variables. Hence the convective velocity for an element is calculated as average of the corresponding nodal velocity components. This method is useful primarily because the pressure term is not used in the formulation thereby reducing the number of unknowns. However an approximation of P can be obtained from the computed values of the velocity components using Eq. (3.53). The velocity and temperature may be approximated in an 8-noded element as:

$$\begin{aligned} v_i &= \sum_{n=1}^{8} N_n \, \mathrm{v}_n^i = \left[N_1 \mathrm{N}_2 \, \mathrm{N}_3 \ldots\ldots\ldots\ldots\ldots \mathrm{N}_8\right]\left\{v_1^i \, v_2^i \, v_3^i \ldots\ldots\ldots v_8^i\right\}^T = \left[N\right]\left\{\mathrm{v}_{ne}^i\right\}; \\ T &= \sum_{n=1}^{8} N_n T_n = \left[N\right]\left\{T_{ne}\right\} \end{aligned} \tag{3.61}$$

where i = 1, 2, 3 and N is the interpolation function or shape function. The momentum equation for a specific element is ‘e’is written as:

$$\left\{\left[\mathrm{M}^{\mathrm{e}}\right]+\left[\overline{\mathrm{C}^{\mathrm{e}}}\right]+\left[\hat{K}^e\right]+\left[K^e\right]\right\}\left\{V\right\}=\left\{\mathrm{F}^{\mathrm{e}}\right\} \tag{3.62}$$

where the coefficient matrices are defined as:

$$\begin{aligned} &\left[\mathrm{M}^{\mathrm{e}}\right]=-\int_{\Omega^{\mathrm{e}}} \rho v_m \left[N\right]\frac{\partial\left\{N\right\}}{\partial x_2} d\Omega; \quad \left[\hat{K}^e\right]=\int_{\Omega^{\mathrm{e}}} \lambda \frac{\partial\left\{N\right\}}{\partial x_i}\frac{\partial\left[N\right]}{\partial x_j} d\Omega \\ &\left[K^e\right]=\int_{\Omega^{\mathrm{e}}} \mu \frac{\partial\left\{N\right\}}{\partial x_i}\frac{\partial\left[N\right]}{\partial x_j} d\Omega; \quad \left[\overline{\mathrm{C}^{\mathrm{e}}}\right]=\int_{\Omega^{\mathrm{e}}} \rho \sum_{i=1}^{3}\left(v_i^0\left\{N\right\}\frac{\partial\left[N\right]}{\partial x_i}\right) d\Omega \\ &\left\{\mathrm{F}^{\mathrm{e}}\right\}=\int_{\Omega^{\mathrm{e}}} \left\{N\right\}F_i \, d\Omega; \quad \left\{V\right\}=\left\{v_1 \; v_2 \; v_3\right\}^T \end{aligned} \tag{3.63}$$

However, in the derivation of Eq. (3.63), the integral term involving the penalty function i.e. $[\hat{\mathrm{K}}]$ matrix should be under-integrated (one point less) than the viscous and the convective terms i.e. [K] and $[\overline{\mathrm{C}}]$ matrices [Reddy and Gartling, 2000]. By similar mathematical treatment of momentum equations, the energy equation can be represented in matrix form for any specific element ‘e’ as:

$$\left\{\left[H^e\right]+\left[C^e\right]+\left[S^e\right]+\left[\bar{H}^e\right]\right\}\{T\}=\left\{f_{\dot{Q}}^e\right\}+\left\{f_h^e\right\} \tag{3.64}$$

where various terms are defined by:

$$\left[H^e\right]=\int_{\Omega^e} k\sum_{i=1}^{3}\left(\frac{\partial\{N\}}{\partial x_i}\frac{\partial[N]}{\partial x_i}\right)d\Omega;\quad \left[C^e\right]=\int_{\Omega^e}\rho C\sum_{i=1}^{3}\left(v_i^0\{N\}\frac{\partial[N]}{\partial x_i}\right)d\Omega$$
$$\left[S^e\right]=-\int_{\Omega^e}\rho v_w C\{N\}\frac{\partial[N]}{\partial x_2}d\Omega;\quad \left[\overline{H^e}\right]=\int_{\Gamma^e} h_{eff}\{N\}[N]d\Gamma \tag{3.65}$$
$$\left\{f_{\dot{Q}}^e\right\}=\int_{\Omega^e}\{N\}\dot{Q}\,d\Omega;\quad \left\{f_h^e\right\}=\int_{\Gamma_1^e} h_{eff}\{N\}T_0 d\Gamma$$

After assembling the elemental matrix, the linear systems of equations are solved to obtain nodal temperature distribution and velocity vector. However, the solution domain for thermal analysis and flow analysis are different. The flow analysis domain is decided by the isotherm of solidus temperature.

3.3 Optimization of Uncertain Model Parameters

The estimation of uncertain parameters involves some sort of inverse analysis where the numerical model is integrated with Harmony Search (HM) algorithm and an optimum set of uncertain parameters comes out from this integrated approach. HM is a real number based metaheuristic algorithm where the concept of improvisation technique of the musicians is used [Geem, 2009]. Each musician (decision variable) plays a note under certain pitch range in search of best harmony i.e. optimum solution. This algorithm has been successfully used to solve global optimization problem in several areas [Madhavi *et al.*, 2007; Zou *et al.*, 2011]. In present problem the unknown parameter set is defined by

$$\boldsymbol{X}=\{\eta \quad k^* \quad \mu^*\} \tag{3.66}$$

where **X** is the unknown variable set. The objective function for minimization problem is defined by:

$$f(\mathbf{X}) = \sum_{i=1}^{n} \left(\frac{W_i^c - W_i^e}{W_i^e}\right)^2 + \left(\frac{P_i^c - P_i^e}{P_i^e}\right)^2 \quad (3.67)$$

where 'W' and 'P' corresponds to weld width and penetration, respectively. 'e' indicates experimental value and 'c' numerically computed values, 'n' refers to number of experimental data considered for this analysis. The HS algorithm which was developed for solving optimization problems, utilises just like musical harmony is improved time after time, solution vector is improved iteration by iteration. The HM algorithm is implemented in present problem by following approach. The harmony memory (HM) is prepared with randomly generated initial population with predefined number of individuals that is called harmony memory size (HMS). The objective function is also calculated corresponding to each individual from

$$f(\mathbf{X}) \text{ subject to } x_i^L \leq x_i \leq x_i^U \quad (i = 1,2,3) \quad (3.68)$$

where x_i^L and x_i^U are the lower and upper bounds for each decision variable respectively. The HM is represented as:

$$HM = \begin{bmatrix} x_1^1 & x_2^1 & x_3^1 \\ x_1^2 & x_2^2 & x_3^2 \\ \vdots & \vdots & \vdots \\ x_1^{HMS-1} & x_2^{HMS-1} & x_3^{HMS-1} \\ x_1^{HMS} & x_2^{HMS} & x_3^{HMS} \end{bmatrix} \quad (3.69)$$

The algorithm parameters are then set. HS contains algorithm parameters including, harmony memory considering rate (HMCR), pitch adjusting rate (PAR), maximum improvisation (MI), and fret width (FW).Next, a new harmony vector is generated based on three mechanisms such as memory selection, harmonic memory consideration rate (HMCR)and pitch adjustment rate (PAR). Generating a new harmony is called improvisation. The decision variables of new solution vector is chosen from historically stored values in HM with probability HMCR or from entire possible range with (1 – HMCR) probability. Every component obtained

by the memory considerationis pitch-adjusted into neighbouring values by adding certain amount to the value, with probability of PAR. The pitch-adjusted decision variable is modified as:

$$x_i = x_i \pm rand(\quad) * BW \tag{3.70}$$

where rand() is a random number between 0 and 1, and BW is the arbitrary distance bandwidth. If the new harmony is better than the existing worst harmony vector, then it is included in the HM and the worst harmony vector is excluded. The steps are repeated until termination criteria are satisfied.

Figure 3.4 describes the overall solution algorithm of integrated model. The initialpopulation of unknown parameters are created first. All sets of unknown parametersare used to calculate the weld dimensions with the help of numerical model.Next, the numerical value of objective function is estimated along with initial HM.Afterwards, the HM is improvised for randomly selected individual. If the value ofobjective function is better than worst value in HM, the individual is replaced by worstvalued objective function. This process continues up to a predefined number of generations.

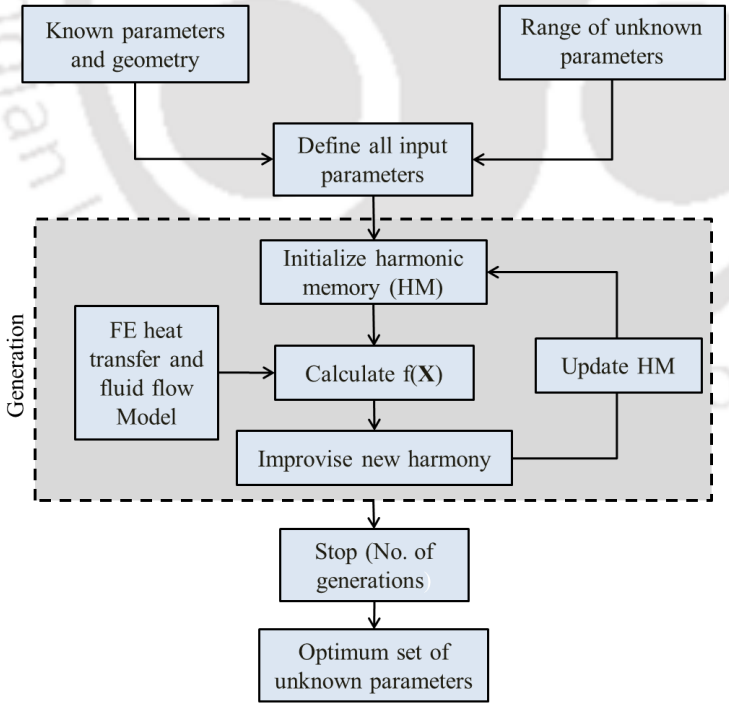

Fig. 3.4 Overall solution algorithm of integrated model.

3.4 Summary

Theoretical formulation of heat transfer, fluid flow, and distortion analysis in microwelding process is outlined in this chapter. The intention of the present work is to develop a general numerical model of the micro welding process which will be capable of predicting the significant effects of the process on the basis of known behaviour of the material and known parameters of the process. The Fourier heat conduction is suitable to predict the temperature distribution in continuous mode laser or plasma arc welding whereas extremely short pulse laser creates the phase lag in heat transfer and hence non-Fourier heat conduction is suitable. The sequencely coupled thermo-mechanical model predicts the distortion of micro welded structure using large displacement theory.A three dimensional numerical heat transfer and fluid flow model has been developed to simulate the evolution of temperature and velocity fields during micro welding. Harmony search algorithm is utilized to identify the suitable values of a set of unknown variables that are required for modeling calculations.A 3D numerical model using ABAQUS is also developed which accounted for all physical phenomena associated with the LTW. A model involving moving distributed heat flux for laser transmission welding has been implemented into FE thermal simulations to predict temperature field during the process. The heat transfer process for ultra-short pulse laser heating is simulated using Non-Fourier dual phase lag heat conduction model over nanometre film thickness. The various features of the developed numerical model have been illustrated by quantitative analysis of transient heat transfer.Anattempt has been made to understand the physical significance of two relaxation parametersandtheir effect on the time-temperature history. However, the influence of pulse shape on heating process is important to make the model more reliable and robust that precisely controls the temperature of nanoscale system.

Chapter 4

Experimental Investigations

4.0 Introduction

The experimental studies are undertaken in the present work to primarily create a reliable database for elaborate and extensive validations of the computed results from the numerical models. The complexity of joining enhances with reduction in sheet thickness. The present work put emphasis mainly on micro welding of 500 μm thick Ti6Al4V alloy. The basic requirement for microjoining is a low heat input process with high energy density [Kou, 2003]. The processes of investigation in the current study are laser micro welding and micro plasma arc welding (MPAW). 500 μm thick sheets of SS304 and mild steel are also joined by MPAW process. Both bead on plate welding and butt welding are performed. An indigenous experimental set up is developed at the central workshop, IIT Guwahati, India to conduct MPAW experiments. The experiments were carried out using a plasma arc welding machine with a 0.05 – 50 A DC power supply (MP – 50, EWM, Germany). The laser welding experiments were conducted at the CSIR manufacturing laboratory, Durgapur, INDIA.

Using controlled and regulated parameters, both the processes are specifically designed to use in joining of thin sheet components over a wide range of process parameters. The weld quality is assessed by carefully controlling the process parameters and by reducing the formation of oxides. The combined effect of welding speed and current on the weld joint properties is evaluated. The macro-microstructural characterizations of the weldment by optical microscopy as well as the analysis of mechanical properties by micro tensile and micro hardness test have been performed. The weld joint quality is affected by specifically designed fixture that controls the oxidation of the joint and introduces high cooling rate. Hence the solidified microstructure of welded specimen influences the mechanical properties of the joint. The butt joint obtained at

optimal process parameters are of very high quality, without any internal defects and with minimum residual distortion. Few experimental data are also extracted from independent literature [Kleine *et al.*, 2004] to validate the heat transfer and fluid flow model. In this present chapter, a brief outline of all the experimental results is presented.

4.1 Materials

The material of choice in the current investigation is Ti6Al4V, SS304 and low carbon steel. Both micro plasma welding and laser welding are performed on Ti6Al4v alloy. Ti6Al4V is a two phase (α+β) alloy with around 6% aluminium (wt. %) stabilized the α phase and about 4% (wt. %) vanadium stabilized the β phase. The microstructure of the as-received sheet of 500 µm thickness consists of intergranular β (BCC) outlining the α (HCP) grains as shown in Fig. 4.1(a). The beta transus temperature of this alloy is 1273K [Donaiche, 2000]. X-ray diffraction (XRD) and Energy dispersive X-ray (EDX) analysis of the alloy before welding are also performed to quantify the phases and elements of the alloy. The phase composition of the specimen is evaluated by XRD by filtered CuK_{α} radiation in the scanning regime where the angle range 2θ varies from 20° to 100° with a scanning step size of 0.033 s. Standard chart is used in the qualitative phase analysis using the values of the integral intensity of diffraction lines (Fig.4.1.b). The XRD patterns considered directly on the Ti6Al4V prior to welding are reported as hexagonal α-Ti and cubic β-Ti. The diffraction pattern is dominated by the HCP α-Ti diffraction peaks since the alloy contains approximately 88% α-phase at room temperature. The small amount of β-phase in the starting microstructure is characterized by only two of these peaks, BCC (110) and BCC (200). Figure 4.1(c) shows the elemental distribution of parent material as a result of EDX analysis. The presence of carbon is inherent to the technique as the carbon tape is used for holding the sample. EDX analysis confirms the presence of the alloying elements (Ti, Al, and V). Certain amount of oxygen concentration is also found in the sample. Thus, the samples are cleaned properly prior to welding. The chemical composition of Ti6Al4V is estimated and is provided in the Table 4.1. Titanium has high affinity towards interstitial elements like oxygen, nitrogen and absorbs them readily at elevated temperature. To avoid the reaction with environment, the molten pool is protected with a special custom made fixture to work in open air during welding. The copper because of its high conductivity cools down the material rapidly resulting in lesser oxidation. The fixture also has provision to provide an inert atmosphere under

the substrate (bottom purging). Industrially pure argon gas is used for shielding as well as plasma producing gas. The plates are cleaned before welding using acetone solution to remove any oil attached and dried properly. The color of the welded specimen provides an indication of the effectiveness of the inert gases to protect the solidified pool from the atmospheric gases.

Table 4.1 Chemical composition of Ti6Al4V (wt. %).

Element	Content (wt. %)
Al	5.5 - 6.75
V	3.5 - 4.5
H	0.015 max
Ti	Balance

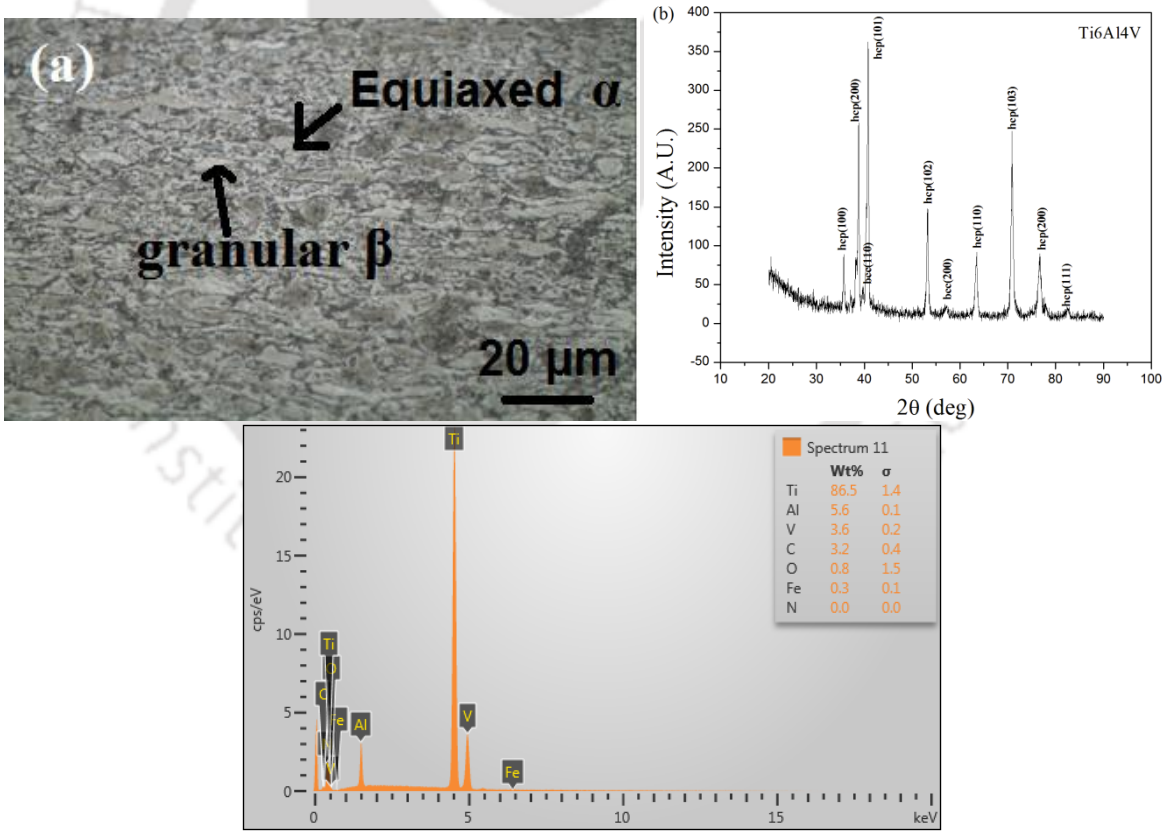

Fig. 4.1 Ti6Al4V alloy: base material (a) microstructure, (b) XRD pattern, and (c) EDX pattern.

The MPAW of SS304 and low carbon steel have been carried out and the analysis has been performed in a comparative mode. The microstructure of these materials is shown in Fig. 4.2(a) and Fig. 4.3(a). The phase composition of the specimen is evaluated by XRD by filtered CuK_{α} radiation in the scanning regime where the angle range 2θ varies from 20° to 90° with a scanning step size of 0.033s. Standard chart is used in the qualitative phase analysis using the values of the integral intensity of diffraction lines (Fig. 4.2b). As shown in Fig. 4.2(b), the XRD pattern exhibits peaks at 2Θ = 44.67˚ (110), 2Θ = 65.02˚ (200) and 2Θ = 82.33˚ (211) corresponding to the cubic crystalline metallic iron structure. From the result of XRD, as shown in Fig. 4.3b, the diffraction peaks are (111), (200), and (220), which agree with the profiles found in XRD database. It tells us that 304SS is a single phase solid solution of Fe with Cr and Ni elements. It has face-centered cubic (FCC) crystal lattice. The chemical composition of the two materials is shown in Table 4.2 and Table 4.3, respectively.

Table 4.2 Chemical composition of SS304 (wt. %).

C	Si	Mn	S	P	Ni	Cr	Mo	V	Ti	Cu	Nb	Al	Fe
0.05	0.13	1.24	0.005	0.03	8.01	18.6	0.13	0.09	0.01	0.31	0.04	0.01	Bal.

Table 4.3 Chemical composition of low carbon steel (wt. %).

C	S	Mn	P	Si	Cr	Ni	Mo	Nb	Fe
0.12	0.045	0.6	0.045	0.011	0.008	0.035	0.003	0.001	Bal.

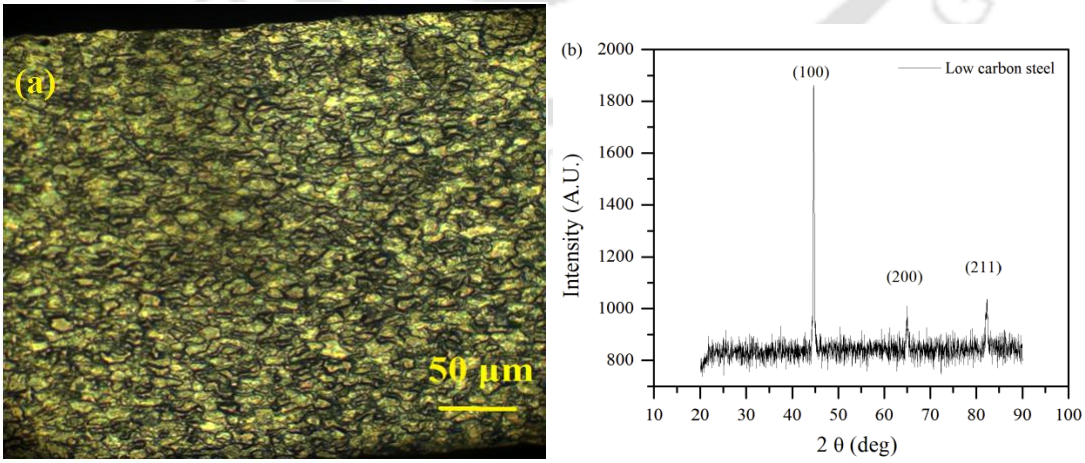

Fig. 4.2 (a) Microstructure and (b) XRD pattern of low carbon steel.

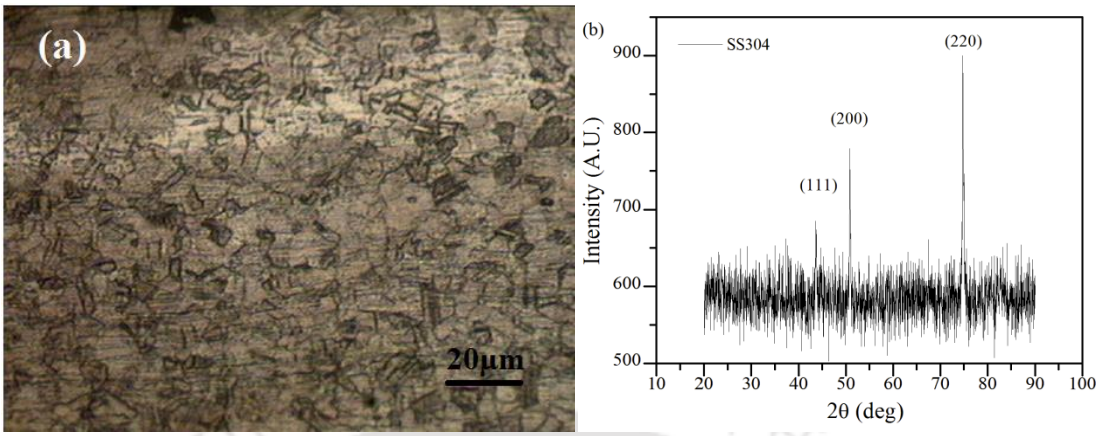

Fig. 4.3 (a) Microstructure and (b) XRD pattern of SS304.

4.2 Micro plasma arc welding

The experimental setup of MPAW is shown in the Fig. 4.4. Experiments are conducted using 0.05–50 A plasma arc welding machine with direct current electrode negative (DCEN) mode. The heat of fusion is produced by the constricted plasma arc which is delivered by the plasma torch that melts and joins the metals. The welding torch is fixed while the workpiece moves at constant speed with the help of a rail guided motor powered platform. The suitable combination of welding parameters is required to produce stable and defect-free weld. Industrially pure argon gas is used as shielding gas as well as plasma gas. It is apparent that the amount of care has to be taken for welding thin sheets increases with decrease in welding sheet thickness. The welding of thin sheets has been carried out under carefully selected parameters because the stable welding conditions exist in narrow regions. Therefore, very tight control of the heat input is required in this case. Bead-on-plate welding for current in the ranges of 8 - 13 amperes is carried out at constant plasma gas flow rate to evaluate the proper ranges of process parameters. Bead on plate welding eliminates the effect of the joint gap on shape and size of the weld bead. Trials runs are carried out by varying one parameter while keeping other parameters as constant. The quality of the weld primarily depends on the combinations of welding current, speed and plasma gas flow rate. However, the plasma arc welding is less sensitive to unintentional arc length variations [Yoshioka *et al.*, 1993]. Welding speed is decided first by the trial on minimum speed and then varied at regular interval. The stable welding current for successful joints decided after a lot of trials. It is observed that the minimum welding speed is

2.33 mm/s and the minimum current is 7 A for stable welding. The arc is unstable below 7A current. Thus the current is varied from 7 A until the burn out of the material occurs. Smooth appearance of the bead and absence of any visible defects were taken as the criteria for selection of the working range of the process parameters.

Fig. 4.4 Experimental set-up for micro plasma arc welding.

4.2.1 MPAW of Titanium alloy

In the present work, micro plasma arc welding is carried out on 500 μm thick Ti6Al4V, SS304 and low carbon steel individually. Figure 4.5(a) shows the weld beads of Ti6Al4V alloy obtained by bead on plate welding at a speed of 4.2 mm/s and current 11 A without the effect of extra shielding gas supply. The decolourization of the specimen is due to the formation of oxide film which leads to the degradation of mechanical properties. This is serious problem for welding titanium alloys. Several favorable activities have been followed to improve the joining system of titanium alloy using micro plasma arc welding process. In addition to proper shielding, the samples are cleaned using acetone solution to remove any oil attached and dried properly. The use of intensive fixture is an essential requirement for producing a good weld joint. A

suitable fixture was designed and constructed for the operation of welding procedure in open air to prevent both oxygen contamination and distortion of the workpiece. The fixture which is made of copper is shown in the Fig. 4.5(b)**.**The gap left for welding is kept to a minimum only to allow the movement of the plasma torch. If the gap is large, the misalignment of the sheets at the joint occurs since the workpieces are very thin. The backing plate of the fixture is made of copper which ensures low angular distortions of the joint due to intensive heat transfer [Klimpel and Lisiecki, 2007]. Also the problem of oxidation is reduced due high rate of heat diffusion through copper. The flow rate of the shielding gas is kept higher side (~ 2 lpm) to protect the molten weld pool against oxidation. The flow rate is adjusted in such a way so that it protects the weld pool without blowing up of the molten metal. The welding electrode is made of Tungsten (W) with 2 wt. % Thorium (Th) of diameter 1.2 mm and the copper nozzle is of 1 mm diameter. The flow rates of plasma and shielding gas are selected as 6 lpm (litre per minute) and 0.6 lpm, respectively. The MPAW process is carried out at a range of current (7A-13A) and welding speed (2.33 - 6.67 mm/min) with a vertical torch position. Figure 4.5(c) demonstrates the welding cycle used in present case. The welding current is given to increase (upslope current) and decrease (downslope current) gradually during the welding procedure. This reduces the wear of the electrode and increases its lifetime. Both the upslope and downslope currents are taken as 4s.

Fig. 4.5 (a) Bead-on-plate welding at 11 A, 4.2 mm/s; (b) Copper fixture used in present investigation; (c) Welding cycle.

Autogenous welding is performed on square butt joint configuration on Ti6Al4V sheets of 100×50×0.5 mm at different power and welding speed based on the preliminary tests of bead on plate welding. The sheets to be joined are clamped tightly by a copper fixture so that there is minimum gap between two sheets. Edge preparation was done properly to keep the gap at the

joint at a minimum level. The MPAW process parameters are presented in Table 4.4. Figure 4.6 (a) - (c) shows the weld joint obtained at different parameters. The surface seems bright silver that indicates there is no reaction with atmospheric gases during the cooling phase and during the actual welding. It is obvious that with increase in welding current the weld bead increases while an increase in welding speed decreases the weld bead. This is due to the fact that increase in current and decrease in speed leads to increase in heat input and subsequently results in bigger molten pool [Watanabe and Satoh, 1957]. Thus proper heat input is necessary to obtain a stable welding. From Fig. 4.5(b) and Fig. 4.6(b), it is observed that the weld bead decreases marginally with similar process parameters. This is due to presence of slight gap between two sheets (Fig.4.6b) for actual butt joint as compared to bead-on-plate welding. While identifying parametric envelops for a weld joint, three modes i.e. heating, stable and burnt through welding are identified to characterize the joint (Table 4.5).

Table 4.4 MPAW process parameters used in present investigation.

Welding Parameters	**Values**
Welding current (A)	8 - 13
Welding speed (mm/s)	2.33, 2.75, 4.2, 5.62, 6.67
Copper Nozzle diameter (mm)	1.2
Electrode diameter(mm)	1.2
Plasma gas flow rate(lpm)	6
Nozzle to plate distance (mm)	2
Shielding gas flow rate (lpm)	0.4
Pre Flow (s)	4
Post Flow(s)	4
Torch Position	Vertical

Welding current and speed are the most influential parameter because it affects bead shape, heat affected zone, the depth of penetration, and the amount of base metal melted. The total molten area increases with the increase in welding current. If the current is too high at a given welding speed, the fusion area will also be too high so that the resulting weld may tend to melt through the thickness. This over-welding increases weld shrinkage and causes greater

distortion. If the current is too low, inadequate penetration or incomplete fusion may result. Too low current also leads to unstable arc, inadequate penetration, and overlapping. Figure 4.7 shows the feasible domain of welding speed and arc current for a successful weld joint. There is positive correlation between welding speed and welding current. It is found that at a speed of 2.33 mm/s and 8 A, a stable welding of the material occurs while at a speed of 6.67 mm/s and even at 11 A, no bead is formed and subsequently higher current is required to weld the material. When the welding speed is increased, the proper welding current range shifts towards the higher-current side. The stable welding is obtained under the combination of weld current and speed. Beyond a certain limit of the current, burn out of the material occurs. The selective welding speed and arc current indicates that there may be a process map that creates a domain of successful joints in plasma micro welding process. This graph can be used to determine the type of weld at different parameters and can further be used for predicting the types of welds at higher current and welding speed.

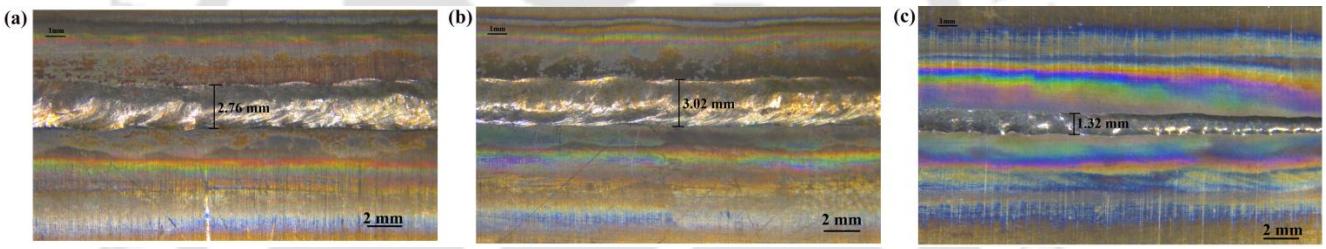

Fig. 4.6 Weld beads for butt joint obtained at: (a) 10 A, 4.2 mm/s, (b) 11 A, 4.2 mm/s, and (c) 10 A, 5.26 mm/s.

Table 4.5 Symbols used for categorization on type of welding.

Category	Symbol	Weld surface	Cross-section
Heating	■	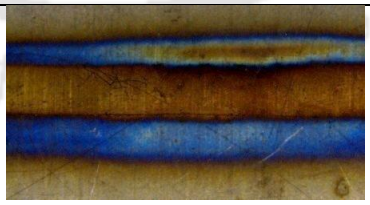	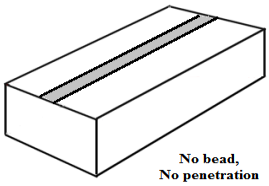

Stable welding	●	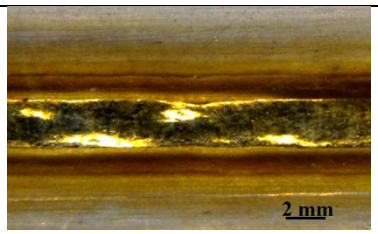	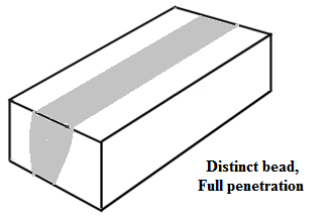
Burnt through	▲		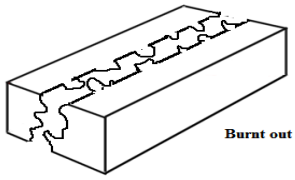

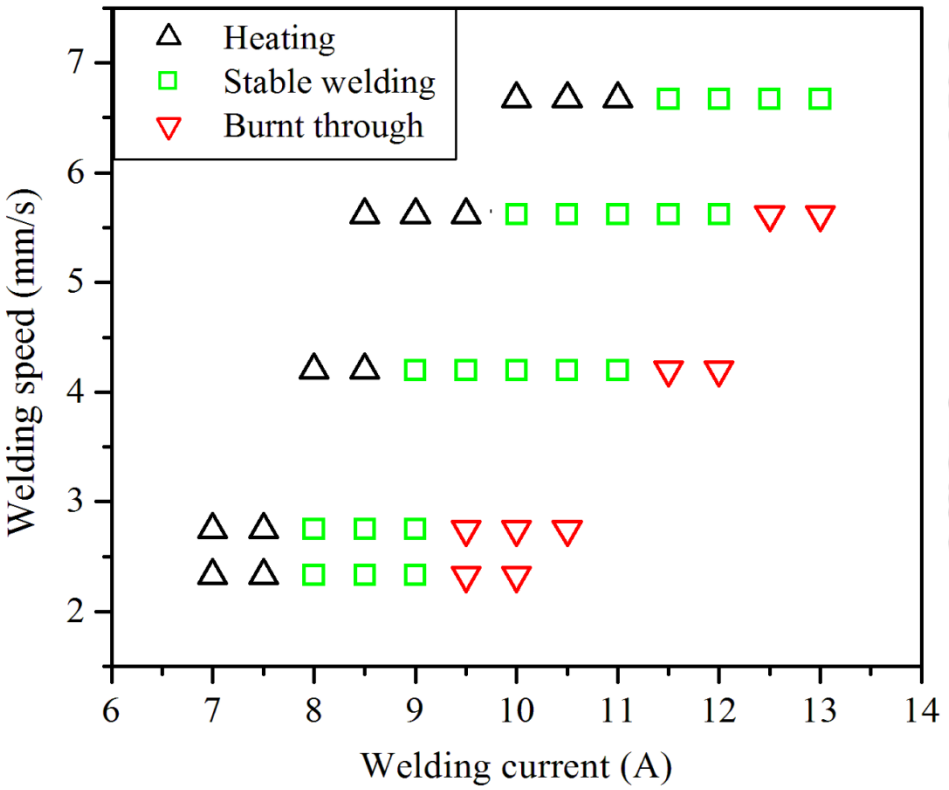

Fig. 4.7 Process map for micro plasma welding of Ti6Al4V butt joint configuration as a function of welding current and speed.

In arc welding, sufficient amount of energy has to be supplied to create the weld pool by fusion. The relative measure of the energy transferred per unit length of is heat input and is expressed as:

$$Q = VI/U \quad (4.1)$$

where V, I, U represents the voltage, current and speed respectively. It is an important characteristic since it governs the cooling rate which may affect the mechanical properties and metallurgical structure of the weld and the HAZ. Fig.4.8 shows the influence of heat input per unit length (combined effect of welding power and welding speed) on weld dimensions. It is observed that at lower heat input weld bead increases more rapidly and the steepness decreases towards higher heat input. The trend indicates that the weld bead converges towards a fixed value with increase in heat input per unit length. Beyond certain heat input (~ 85 J/mm) there may not be any increment of weld width.

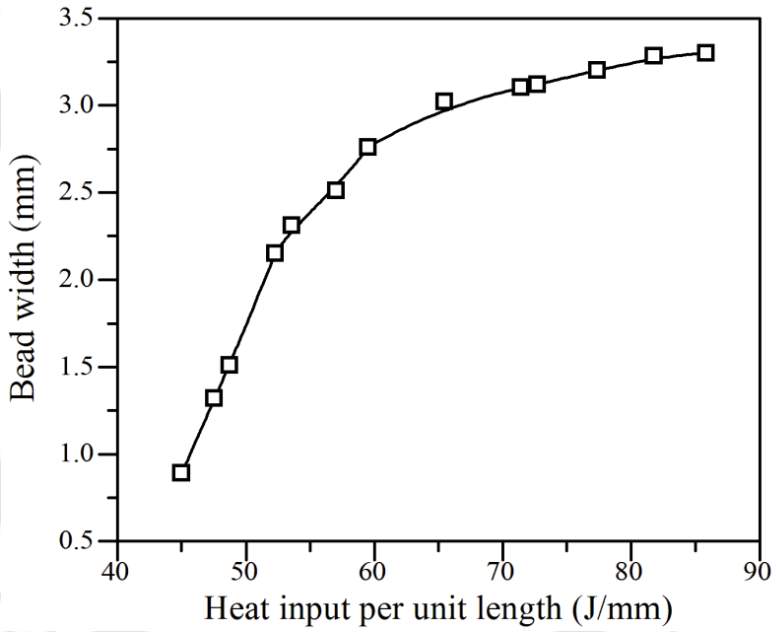

Fig. 4.8 Weld bead dimensions with heat input.

4.2.1.1 Macro and microstructural study

The detailed microstructural observation is conducted for each welded specimen using optical microscopy to determine the variation of grain size and presence of any weld defect. The microstructural analysis is preceded by fine polishing in emery paper followed by polishing in velvet cloth by suspension of alumina powder over it. Macro etchants differentiates major portions of specimen only like welded zone and normal surface. The macro etchant that is used

for Ti6Al4V is HCL+H_2O in 1:1 ratio. The micro etchant used is Kroll's reagent i.e. distilled water, nitric acid, and hydrofluoric acid in the ratio of 46:3:1.

The strength and toughness of Ti6Al4V alloy are quite sensitive to microstructure. Figures 4.9 and 4.10 show the macrographs for the welded Ti6Al4V sheets. The Fig.4.9 reveals the grain refinement at three zones corresponding to welding conditions of of 53.57 J/mm heat input per unit length. The boundary of the fusion zone is difficult to identify due to the narrow transformation kinetics for Ti6Al4V [Donaiche, 2000]. Macrograph demonstrates no sharp interface between FZ and HAZ suggesting epitaxial growth phenomenon in FZ from HAZ [Karimzadeh *et al.*, 2005]. However, the shape of the fusion zone is regular and symmetric, and is clearly defined by semi-circular cross-sectional boundary. In all the cases, the fusion zone is elliptical in shape. It is found that the fusion zone size increases with increase in heat input. It is also reflected that full penetration and no unacceptable porosity and cracks are observed in the fusion (FZ) or heat-affected (HAZ) zone at any welds. This indicates that proper selection of welding conditions is implemented in all the cases. The depth/width ratio reveals a conduction mode welding for the investigated weld with elliptical shape of fusion zone. This is due to the fact that low heat input (~ 45-90 J/mm) of the plasma arc is not enough to produce a keyhole. This conduction mode welding along with full and effective protection of the weld pool using argon shielding gas employed in the present case restricts high peak temperature of the system and reduces the reaction with air. Figure 4.10(d) shows a misaligned sample due to mis-fitting of the fixture. Excessive heat input during welding can cause considerable distortion, particularly in thin sheets. Thus very careful edge preparation and fitting of the sheets to be joined is required especially for thin sheets.

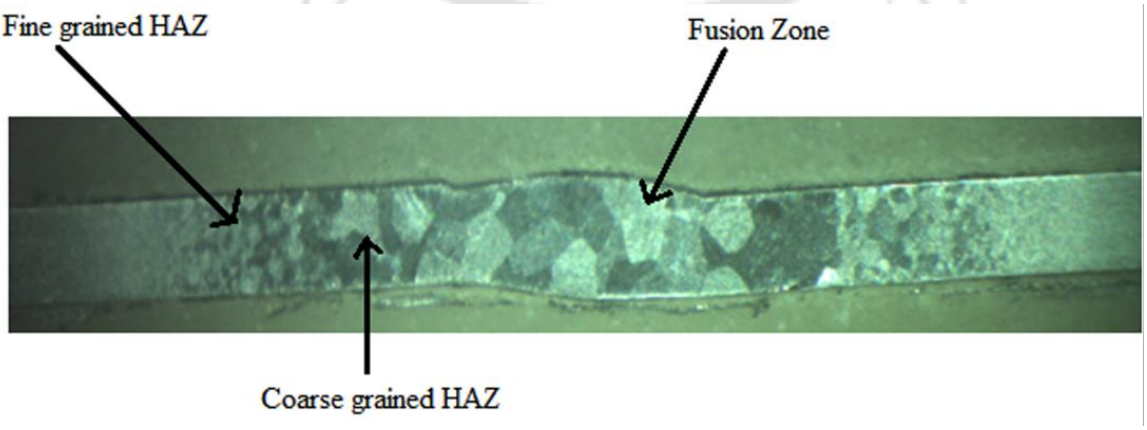

Fig. 4.9 Macrograph of weld cross-section at welding condition of 53.57 J/mm.

After metallographic sample preparation, grains in a specific alloy are often analyzed via microscopy, where the size and distribution of these grains can demonstrate the quality of the sample. Grain size measurement is carried out by using line intercept method since the grains are not equiaxed. The measurements are carried out using an optical microscope with digital photo capturing facilities and analysis software. In this method, five line of known length 'G_L' is drawn and number of grain boundaries intercepted by the lines is counted (designated as G_N). The mean line average is given by:

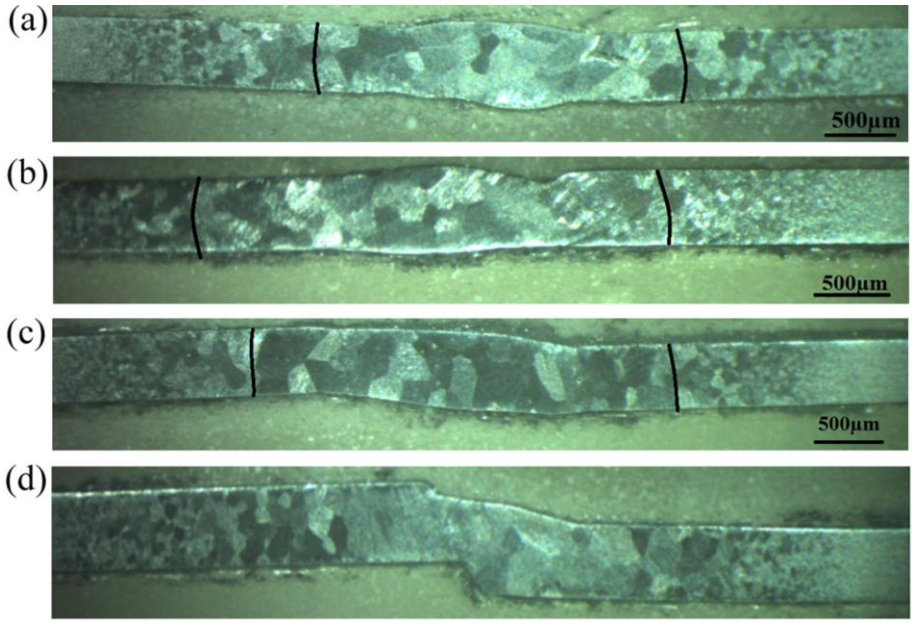

Fig. 4.10 Cross-sectional macrograph at welding condition of: (a) 48.7 J/mm; (b) 65.5 J/mm; (c) 72.72 J/mm; (d) 85.5 J/mm.

$$G_d = \frac{G_L}{G_N} \tag{4.2}$$

Assuming reasonable shape of grains and obtaining a mean diameter of rotation, the average grain diameter is given by:

$$G_{Dd} = 1.75 \times G_d \tag{4.3}$$

The weld fusion zone in titanium alloy is characterized by coarse, columnar, prior-beta grains that originate during solidification. In full penetration plasma welding, the columnar beta grains solidify inward from the base metal in a direction nearly parallel to the workpiece surface, ultimately impinging to form a vertical grain boundary at the weld centerline. The fusion zone beta grain size depends primarily on the weld energy input where a higher energy input promotes larger grain size. The weld joint mechanical properties, particularly ductility, can be degraded by a coarse prior beta grain [Karimzadeh *et al.*, 2006]. Therefore, it is important to maintain fine grain structure by minimizing the weld energy input. In the heat affected zone, the grain size is significantly smaller than that of the fusion zone (Fig. 4.11a). The base metal exhibits an average

grain size of ~ 15 μm. From Fig. 4.11(a) it can be observed that very large prior-β grains in the FZ with an average size of 214 μm exist. It is also observed that a significant grain growth in the HAZ where the average prior-β grain size is~ 67 μm. The evolution of the grain size of the prior-β phase in the HAZ and the FZ with respect to heat input is represented in Fig. 4.11(c). The change in heat input causes some prior-β grain refinement in the FZ. Indeed, the average of prior-β grain size increases from 151 μm to approximately 297 μm when the heat input increases from 44.4 J/mm to 96.6 J/mm. It is also noteworthy that minor refinement of prior-β grain is observed in the HAZ due to change in heat input. In this region, the average prior-β grain sizes that are corresponding to the lowest (~ 44.5 J/mm) and the highest (~ 96.6J/mm) heat input are of 54 μm and 74 μm, respectively. However, the refinement of grains in HAZ zone is not as significant as in the fusion zone. These results demonstrate that the heat input strongly affects grain growth and the large grain size can be avoided by using smaller energy input whenever possible. In general, large temperature variation takes place within a small length along its width. The molten zone is subjected to a very high temperature which is confined within a small area. This promotes grain coarsening at the fusion zone. Also due to the low thickness of the plate, the heat flow is limited along the width direction. Thus, wide variation of grain size occurs along the width. However, increasing the speed or reducing the heat input per unit length, can reduce the difference of grain size in the three zones as is reflected in Fig. 4.11(b).

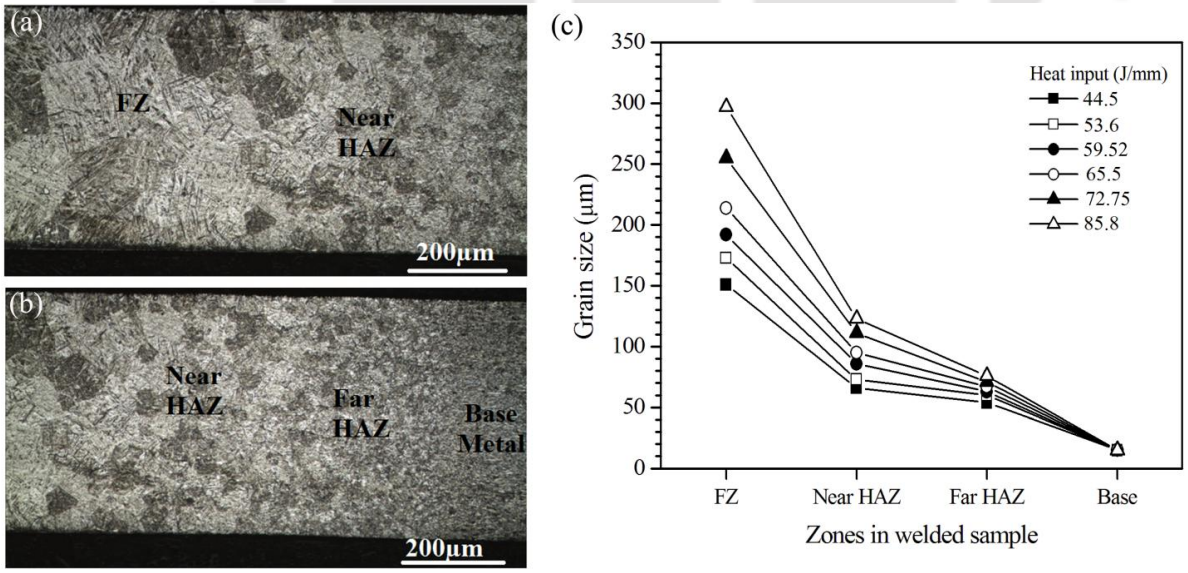

Fig. 4.11 (a) – (b) Macrographs showing different zones for Ti6Al4V weldment at heat input of 65.5 J/mm; (c) Prior-β grain size in the FZ and HAZ for the different welding conditions.

In welding of Ti6Al4V, $\alpha \rightarrow \beta$ phase transformation during rapid heating and the decomposition of the $\beta \rightarrow \alpha$ phase during cooling greatly depends on heating or cooling rate. If the cooling rate is higher than the critical cooling rate (~ 623K/s) of Ti6Al4V, α' martensite is formed (diffusionless transformation). At slower cooling rate, diffusion controlled nucleation takes place resulting in the growth of secondary lamellae [Fan *et al.*, 2005]. Some β phase is always retained irrespective of the cooling rate. Due to the high thermal conductivity of copper, the cooling rate of the material is considerably increased. However, the typical cooling rate is ~100 K/s for PAW process which is approximately increased to 700 K/s using copper as a fixture which greatly affects the formation of microstructure and is sufficient to form a martensitic structure. The microstructure observed in Fig. 4.12 reveals that all these samples exhibit very similar microstructures in the fusion zone consisting of fine acicular martensitic α' structure within the β grains. This microstructure forms when the structure is quenched from the β phase above the beta transus temperature (1253K), at a cooling rate higher than the critical cooling rate [Ahmed and Rack, 1998]. Thus, it may be concluded that there is not much difference in the cooling rate in the investigated region. Although each location contains α' martensite, the amount, size and distribution differ at each location. The α' phase is a martensitic phase with an HCP crystal structure and similar lattice parameters to the α phase. The dark etching phase appears within the martensitic structure is retained β phase. However, the microstructure in different zones is indirectly dependent on heat input.

Figure 4.12(a) shows the microstructure in the fusion zone at heat input of 48.7 J/mm. At this magnification, the microstructure appears to be composed entirely of martensite oriented in different direction in prior beta, where the length of many of the needles exceeds 100 µm. This microstructure has very less retained β, and appears to form entirely through diffusionless martensitic transformation. Figure 4.12(b) represents the microstructure of fusion zone at heat input of 53.6 J/mm where length of the α' martensite increases and the distributions becomes finer that exhibits relatively better strength [Ahmed and Rack, 1998].It is observed that martensitic length decreases with further decrease in heat input (Fig. 4.12c) corresponding to heat input of 65.5 J/mm. At a higher heat input (Fig. 4.12d), it shows completely different microstructure. The formation of a second morphology i.e. α-β lamellar structure with α-phase lamellae in a β-phase is observed in the fusion zone. The α lamellae is arranged in a Widmanstatten/basket weave structure also called Thomson structures with different sizes and

orientations, and forms alpha platelet colonies within the columnar grains [Rafi *et al.*, 2003]. This may be presumably due to moderate cooling rate slightly lower than critical cooling rate because of the high heat input [Elmer *et al.*, 2003]. The fusion zone at high heat input shows mixed mode of transformation which consists of initial mode of transformation and subsequent martensitic transformation. Such structure has lower strength than the α' martensitic structure [Ahmed and Rack, 1998]. Thus, it may be concluded that the percentage of martensitic structure decreases with increase in heat input. The lowest heat input which has the highest cooling rate has the highest martensitic fraction. Only α' is present in the fusion zone formed by the lowest heat input while both α' and transformed α+β are formed in the fusion zone obtained from highest heat input [Elmer *et al.*, 2003]. From Fig. 4.12(a) and Fig. 4.12(b) it can be concluded that the average martensite length increases from 50 µm to 100 µm, however the density becomes coarser. Again from Fig. 4.12(c) and Fig. 4.12(d) shows that the average martensite length reduces to 30 µm.

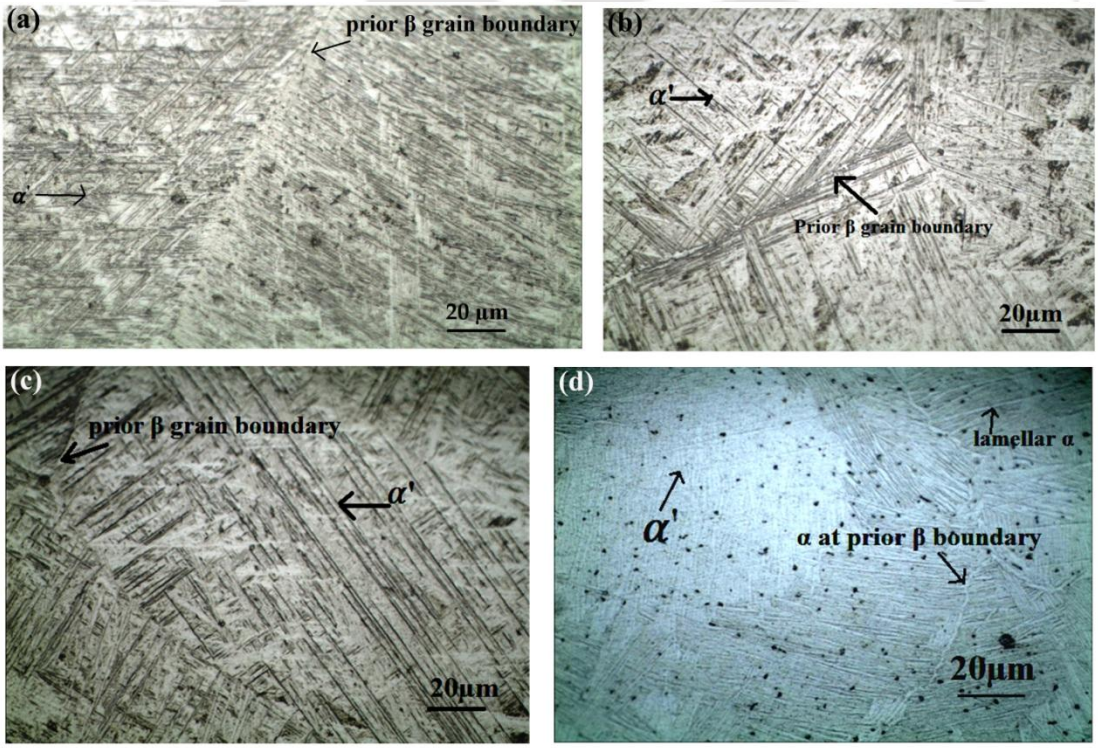

Fig. 4.12 Microstructure of fusion zone for Ti6Al4V weldment at welding conditions of: (a) 44.96 J/mm (12A, 6.67 mm/s); (b) 53.6 J/mm (9 A and 4.2 mm/s); (c) 65.5 J/mm (11 A and 4.2 mm/s); (d) 85.83 J/mm (8 A, 2.33mm/s).

The peak temperature and cooling rate decreases away from the weld centerline. The heat affected zone (HAZ) experienced significant phase transformations during the welding process due to different peak temperature, and heating and cooling rates. It is observed from Fig. 4.13(a) and Fig. 4.13(b) that far away from the weld center line, the blocky secondary phase is produced under a lower cooling rate along with some primary α and few traces of retained β . However, Fig. 4.13(c) reveals that the martensitic α' is substantially formed due to high cooling rate at the near HAZ zone. It is also observed that the content of acicular α' is decreased significantly from the region near the fusion zone to region near the base material. This is because that the high temperature gradient exists in the narrow HAZ due to low heat input of the process (48.7 J/mm). Fig. 4.13(b) demonstrates that the primary phase exists in the middle of the HAZ that contains secondary Widmanstatten α, having morphology of a blocky appearance with a heavily dislocated internal substructure and with a small amount of primary α. The appearance of the original α phase and β phase in the HAZ signifies partially transformed region [Elmer *et al.*, 2003] i.e. the region may not be heated to the beta transus temperature (1253K). Fig.4.14 highlights the microstructure of HAZ zone corresponding to the highest heat input of 96.6 J/mm. The HAZ for this welding condition is entirely different from low heat input (~ 48.7 J/mm). This is because of high heat input causing slower cooling rate resulting in diffusion controlled transformation. Figure 4.14(a) shows the near-HAZ region which also has a microstructure similar to the fusion zone, consisting almost entirely of the transformed grains with a lamellar structure. With further away from the fusion zone as shown in Fig. 4.14(b), an increase in the volume fraction of this morphology is observed due to the reduction in cooling rate resulting in the further growth of the grain boundary Widmanstatten α plates into the center of grains and formation of the classical 'basketweave' Widmanstatten morphology. In the far-HAZ region (Fig. 14.14c), with increasing distance from the FZ boundary, the fraction of the transformed β with a lamellar structure decreases whereas the primary equiaxed α fraction increases.

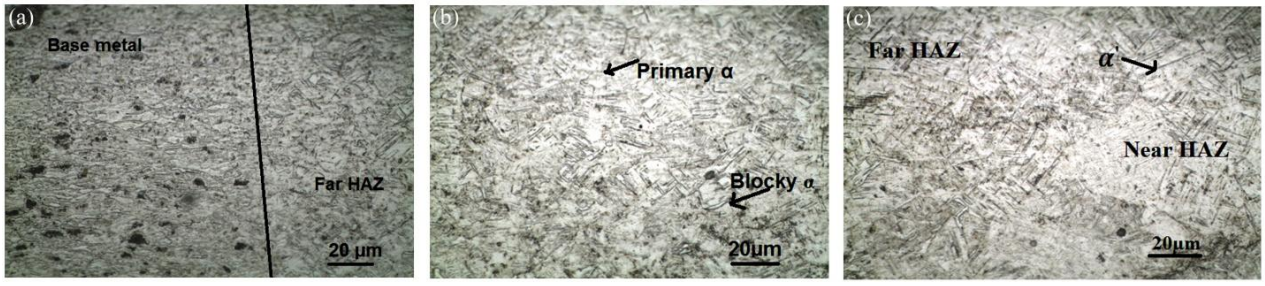

Fig. 4.13 Microstructure of the HAZ for heat input of 48.7 J/mm.

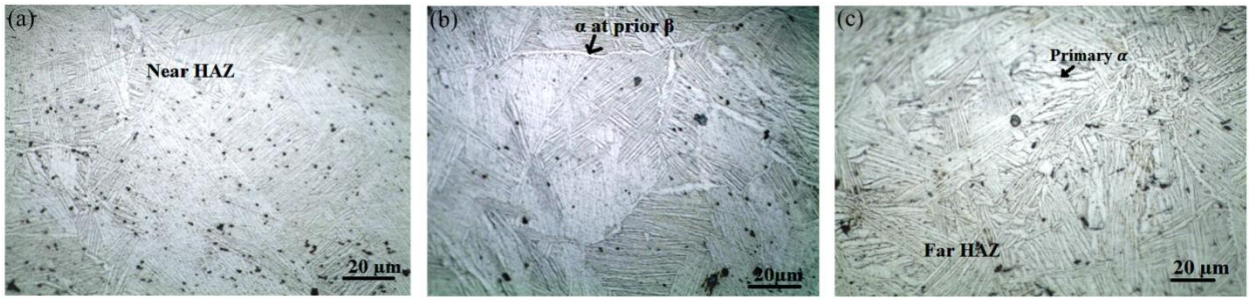

Fig. 4.14 Microstructure of HAZ zone corresponding to heat input of 85.83 J/mm.

4.2.1.2 Oxygen concentration in weld joints

Energy dispersive X-ray (EDX) analysis is performed to find out the elemental distribution at the weld region (Fig. 4.15) in order to estimate the oxidation rate. Due to interaction of plasma arc with substrate material at high temperature, the oxygen concentration might increases at the weld joint. It might make the material brittle and reduces its strength that is impractical for the use in industry. It is found that the oxygen concentration is more for lower speed and high heat input (~ 12.2 – 17.0% oxygen) as compared to higher welding speed and low heat input (~ 9.8 – 10.8 % oxygen). At lower welding speed more time is available for reaction with molten pool and as such more amount of oxygen is absorbed from the atmosphere. Also at high heat input, the temperature of the molten material is very high and thus prone to enhance oxidation. However, at moderate welding speed (4.2 mm/s) and heat input (~ 53 – 65 J/mm) the oxygen concentration is minimum (~ 5.9 – 6.5%).All the welding conditions of the present system, the cooling rate is probably same due presence of high conductive copper backing plate and fixed rate of purging gas flow. At moderate welding speed, the system creates well balance between heat input and rate of cooling that result in minimum reaction time for oxidation. The presence of oxides at the weld joint influences the mechanical behavior of solidified material. It is observed that the maximum oxygen percentage is around 17.3 %. It is thus obvious that the process shielding procedure with specifically designed fixture for titanium alloy and use of suitable process parameters are effective to produce defect free weld at open atmospheric condition.

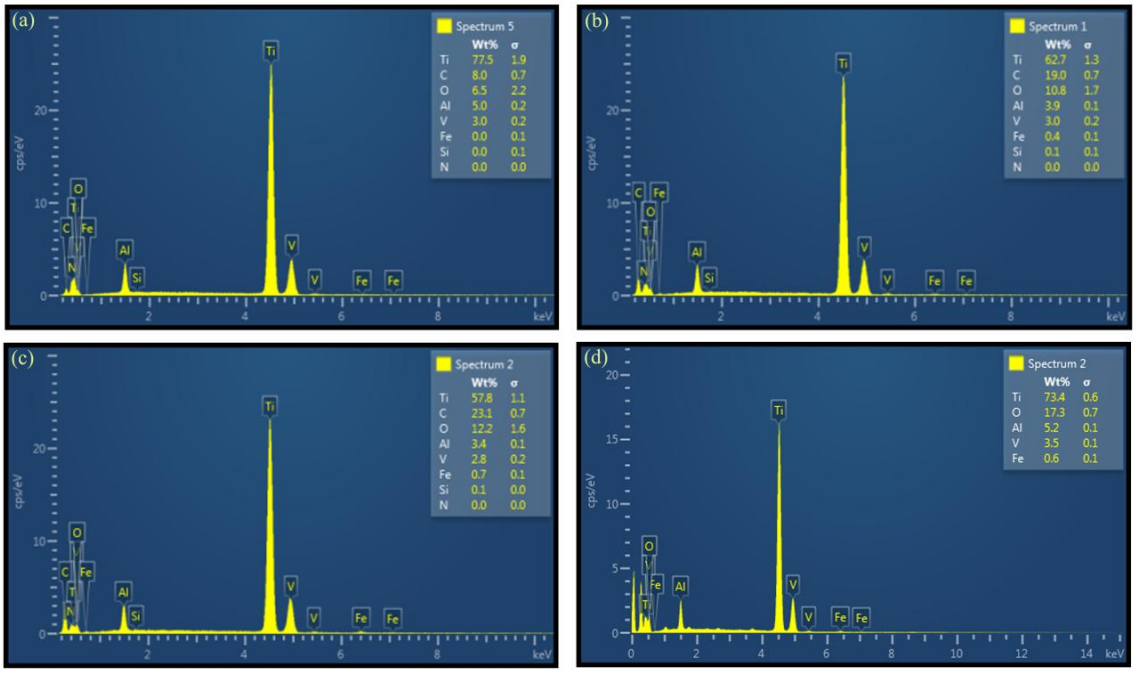

Fig. 4.15 EDX results of Ti6Al4Vafter welding corresponding to welding conditions of :(a) 65.5 J/mm; (b) 48.7 J/mm; (c) 85.8 J/mm;(d) 85.83 J/mm.

4.2.1.3 Mechanical properties

Tensile test is carried to evaluate the strength of the weldment. The ultimate tensile strength and elongation which is a measure of ductility is evaluated. The joint efficiency is defined by the ultimate tensile strength (UTS) of a joint with respect to the strength of the base material. It is expressed as

$$\text{Joint efficiency} = \frac{Joint\ strength}{Base\ material\ strength} \times 100\% \quad (4.4)$$

The tensile property of the sample is evaluated according to ASTM E-08 standard. The specimen is prepared according to Gao *et al.* [2014] is prepared to determine the strength and elongation of the weld joint. Two tensile specimens are prepared for each welding condition and the average value is considered here. The test was carried at a constant rate of 0.2 mm/min. The stress-strain curve of welded joint at six different welding conditions is described in Fig. 4.16(a). The yield strength and the ultimate strength do not differ much for all the cases indicating low strengthening by deformation due to lack of effective hardening mechanism. The ultimate tensile strength of the welded specimen is found to be comparable to the base metal (1090 MPa). The tensile strength of butt joint is not lower than that of base material because all testing samples are

broken at HAZ zone. It is observed from Fig. 4.16(b) that the ultimate tensile strength first increases, reaches an optimum value, and then decreases slightly with the increase in heat input. The strength of the α' martensite is very high which results in high strength of the joint [Elmer *et al.*, 2003]. As the martensitic α' becomes coarser and longer, the strength becomes highest in case of moderate heat input [Gao *et al.*, 2014]. With further increase in heat input, the growth of lamellar alpha takes place which have relatively weaker strength resulting in reduction of overall strength in case of the highest heat input. The yield stress follows similar trend to that of the ultimate tensile strength. The elongation of weld joint is less than the base metal for all the conditions. This suggests that there is a reduction in ductility due to the welding of materials. The maximum percentage of the reduction in ductility is 12% and the minimum is 9.1%. However, at heat input of 59.3 J/mm, the ductility is found to be the highest (~ 14.4%) which is much higher than the base material. The highest elongation in this case indicates the presence of greater fraction of diffusional α in the FZ as the cooling rate reduces with increase in heat input [Kabir *et al.*, 2012]. However, the joint efficiency of the welded samples with reference to ultimate tensile strength is more than 100 % in most of the cases. It is thus obvious that the micro plasma arc welding for titanium alloy with present system under favorable process parameter produces high quality joint without much appreciable reduction in ductility.

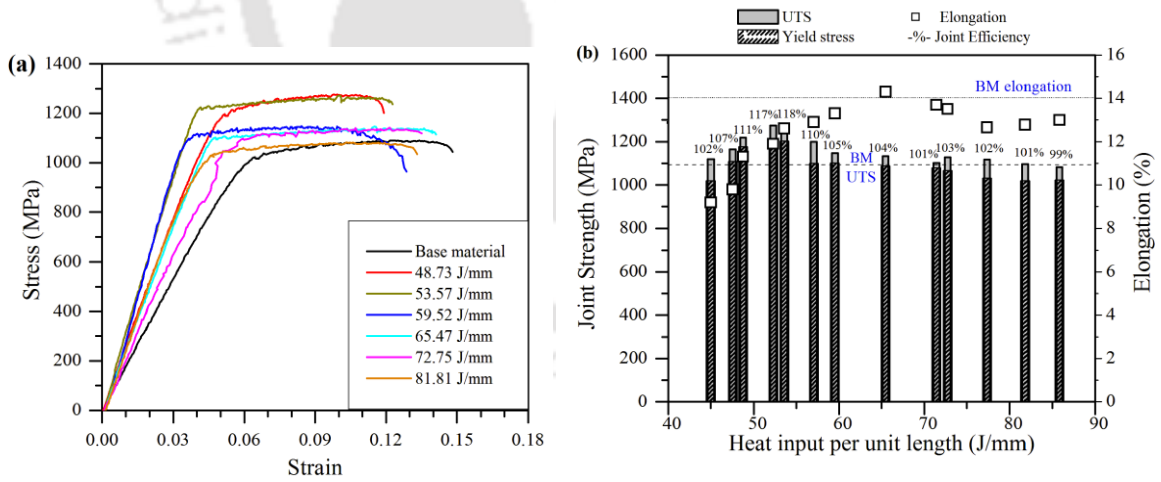

Fig. 4.16 Mechanical properties of butt joint corresponding to different welding condition: (a) tensile stress-strain curve, (b) strength, elongation and joint efficiency.

Fractured surface of the tensile test specimens is characterized by using scanning electron microscope (SEM) to understand the failure pattern. The SEM fractographs of a welded joint for

different heat input is shown in Fig. 4.17 that exhibits numerous dimples with different depth and sizes on the fractured surfaces reflecting the mode of failure for the tensile load is ductile. Thus, the specimens are subjected to large plastic deformation prior to failure. Some dimples are deep and accumulate in stripes while others are shallow [Kabir *et al.*, 2014]. At low heat input (Fig. 4.17a), the dimples are quite shallow with certain secondary dimples. Since the structure is full of hard particles α', the secondary cracks appear in various location. From the same figure a localized area of cleavage is also obtained. This is indicative of the fact that α' does not fracture in a completely ductile pattern but exhibited a mixed mode of failure. Fig. 4.17(b) reveals parallelly aligned finer dimples with secondary dimples at the lip of the dimples or at the valley of the dimples which could be the reason for the highest ductility with intermediate tensile strength for the welded joint of moderate heat input. Fig. 4.17(c) indicates that the entire surface shows dimpled fracture of fine and equiaxed α phase that ruptured in ductile shear and the secondary dimples is also evident.

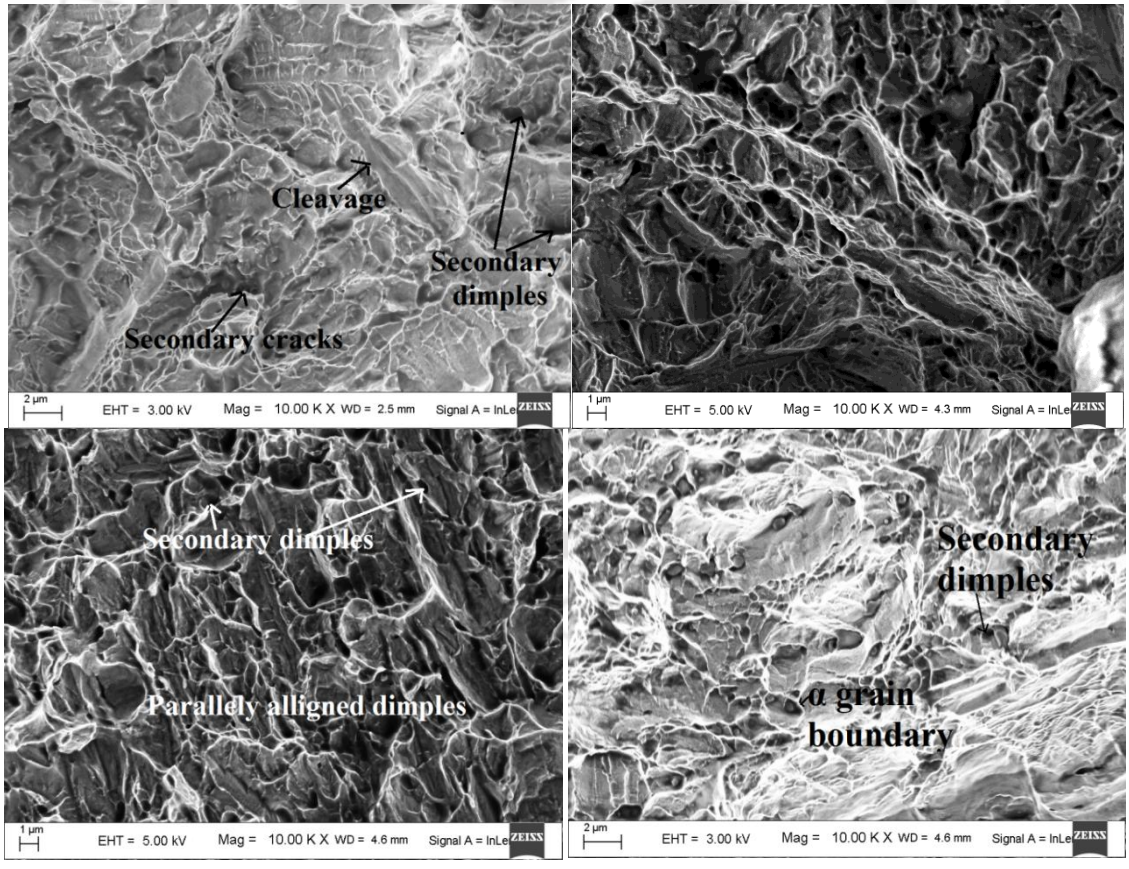

Fig. 4.17 Fracture surface of fusion zone of Ti6Al4V joints corresponding to heat input: (a) 48.7 J/mm; (b) 59.52 J/mm; (c) 65.5 J/mm;(d)85.83 J/mm.

The micro hardness tests in three distinct zones i.e. fusion zone (FZ), heat-affected zone (HAZ) and base metal (BM) are done. The Vickers (H_V) micro hardness measurements are made using an indentation load of 500 g, a dwell time of 20 s. The Vickers hardness number (H_V) is the ratio of applied load to the surface area of the indent. Hardness values are surveyed across the weld joint at an interval of 0.5 mm and at 0.25 mm from the top surface. The average hardness values of a welded sample are taken and plotted in Fig. 4.18. The hardness is found to be highest at the HAZ zone for all the cases and is the highest for moderate heat input (~ 53.6 J/mm) which may be due to the formation of coarse α' martensite at that process condition. The hardness value is the lowest for the highest heat input as in this process condition the microstructure contains lamellar α and very less amount of martensitic α' which exhibits very less hardness comparable to the primary alpha [Wang and Wu, 2012].It is thus obvious that the hardness primarily depends on the size and distribution of martensitic phases.

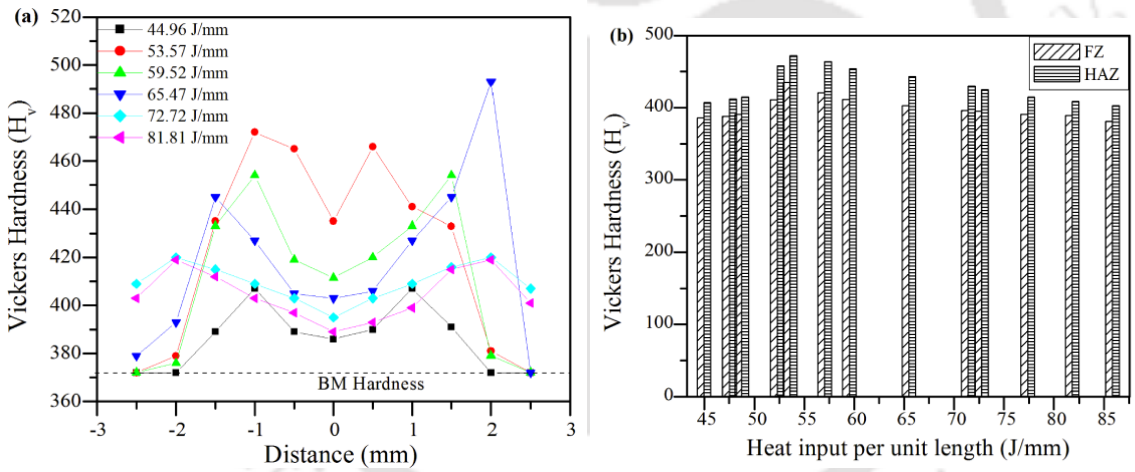

Fig. 4.18 Vickers hardness: (a) pattern in the different zones; (b) values for different heat input.

4.2.1.4 Temperature distribution

To measure the temperature during welding, K type thermocouples are fixed at middle upper surfaces of the plates in both sides as shown in Fig 4.19. Since the top plates of fixture are held very close so as to avoid misalignment, the space available for thermocouple attachment is very less. Therefore, a single thermocouple point could be attached at a distance of 5 mm from the weld centerline. Time- temperature history for three different heat input is plotted in Fig. 4.20. It can be seen that the peak temperature increases with increase in heat input. The heating

rate is almost similar whereas there is a variation of cooling rate due to presence of high conductive fixture and backing plates.

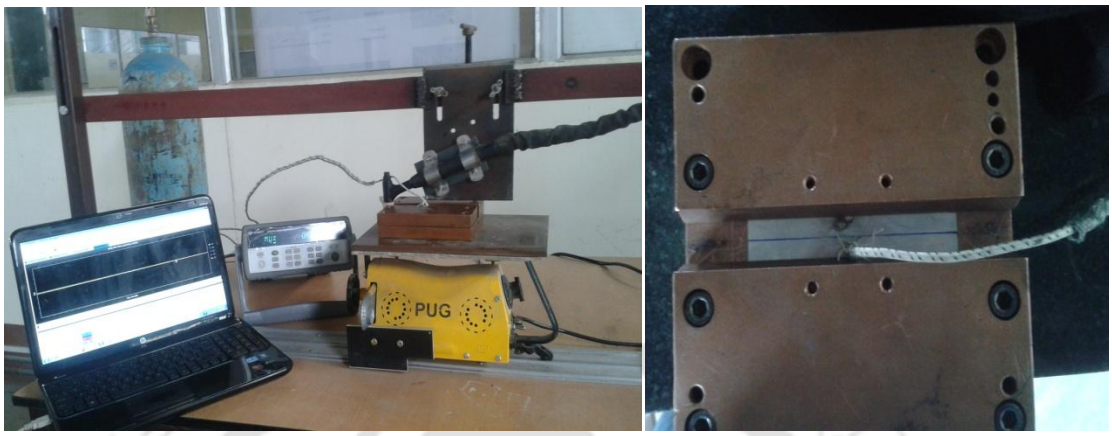

Fig. 4.19 Experimental measurement of temperature distribution.

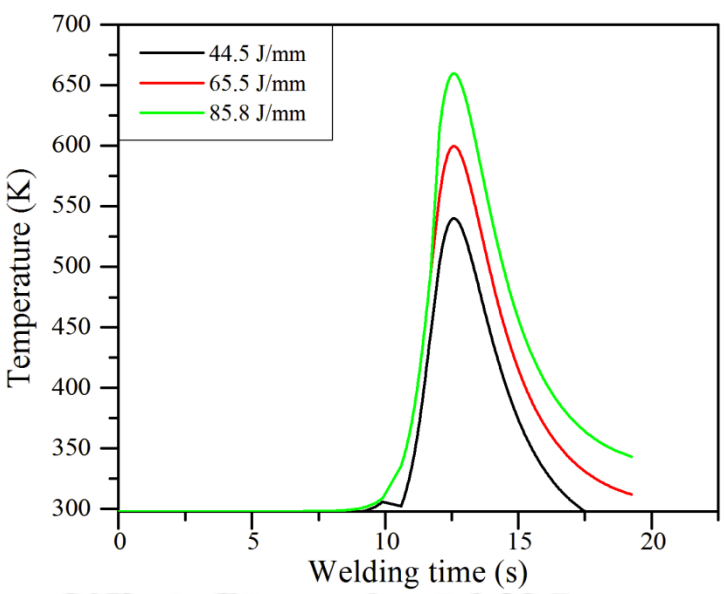

Fig. 4.20 Time-temperature history

4.2.1.5 Weld induced distortion

The basic need to study the angular distortion in welded plate is to investigate the residual stresses induced due to heating and cooling during welding which is detrimental to the integrity and the service behavior of the welded parts. In welding, highly localized heating is done on the plate or on the joint part which leads to non-uniform stress in the component because

of expansion and contraction of the heated region. At first compressive stresses induced in the cold metal at the time when weld pool is formed due to thermal expansion of the heat affected zone. If all the stresses generated from thermal expansion or contraction exceeds the yield strength of the particular metal distortion occurs due to the plastic deformation of the metal. Experiments have been performed to predict the distortions for different cases by co-ordinate measuring machine. Effects of process parameters viz. welding current and welding speed are studied on welding deformation in this section.

Figure 4.21(a) shows the pattern of residual distortion in cooled down specimen of thin sheet. It is obvious that the distribution of these two kinds of displacement is basically symmetrical with respect to the weld centerline. The deformation normal to the weld line is called transverse deformation and parallel to the weld line is called longitudinal deformation [Gao *et al*., 2003]. These deformations arise due to the shrinkage forces generated during the thermal cycle. Coordinate measuring machine is used to measure the distortion (displacement along Z-direction) of the sample. The deflection is measured by a simple method as shown Fig. 4.21(b). The deflection is measured by taking the centre of the weld line as the reference point. The difference of deflection for welded plate before and after welding is taken as height'd'. The height'd' is measured for both the identical joints and average value is taken for all the cases and is taken as the deflection at the indicated position. The distortion pattern for all the cases is same and is convex-concave type [Watanabe and Satoh, 1957]. The maximum value of deflection is at edge of the weld line for all the cases.

Distortion depends on welding conditions, geometry, restrains, and material properties. Co-ordinate-measuring machine is used to measure the distortion which determines the shape of the structure due to welding relative to a reference plane. The distortion due to welding is the difference between the initial shape (before welding) and the final shape (after welding) as the test plate is not perfectly straight. Here, 'after welding' means after complete cooling and release of the pressure from the suction table. Measurement has been done on several points along the lines indicated in Fig. 14.21(c) on a surface before and after the welding. The measurement is repeated for three times and the average value is considered for all the cases. Figure 4.22 shows the deformation of the welded sheets along the thickness direction corresponding to the highest heat input of 65.5 J/mm. The deformation is shown as longitudinal bending and transverse bending since the distortion is non-uniform along both the directions. It is obvious that there is

considerable amount of bending in both the directions due to the low stiffness of the sheets to be joined. The longitudinal bending (Fig. 4.22a) is more along the centerline that decreases gradually towards the edges. Transverse bending is shown in Fig. 4.22(b) at three different sections. It can be deduced that the maximum distortion is observed at the weld edge. Figure 4.23(a) depicts the comparison of longitudinal bending along the weld line (line 2) for all experimental conditions. The maximum deviation of deflection is found to ~ 1 mm between first and last experimental conditions. Figure 4.23(b) shows the deflection at the end of weld centerline (i.e. weld start or stop position). The trend infers that the deflection increases with heat input and becomes almost constant after a certain heat input. Once the molten pool extents to full depth, the heat transfer is enhanced in thickness direction. With further increase in heat input the size of the weld pool increases and becomes steady with further increase in heat input. It will try to equilibrate the butt joint with some optimum residual distortion in a large pool of weld volume. Also, the average temperature gradient between top and bottom surface does not increase with further increase in heat input.

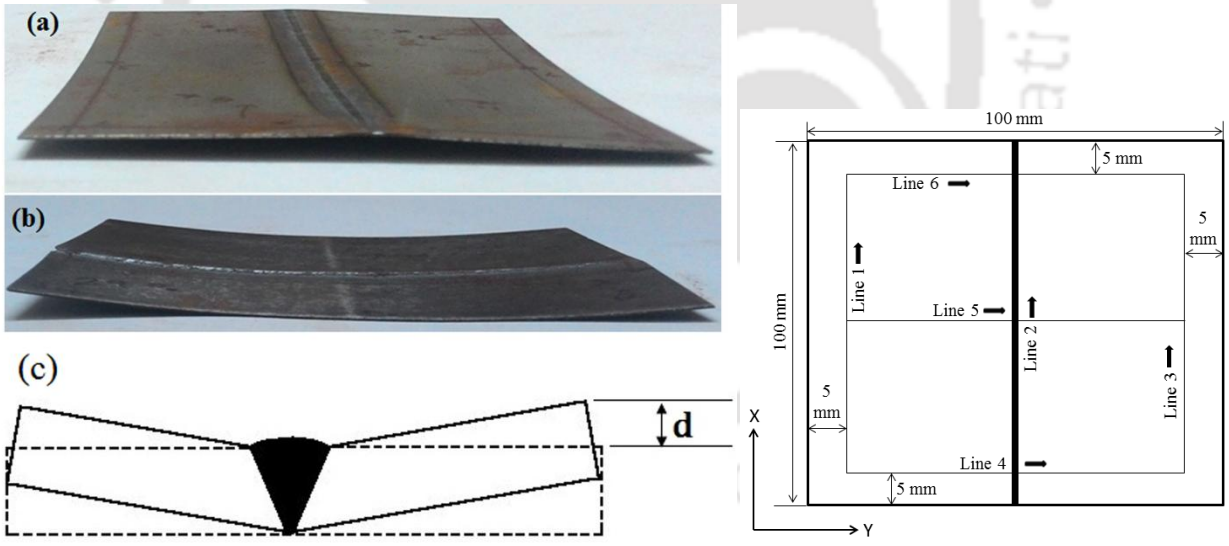

Fig. 4.21 Distortion pattern of the welded plates: (a) along the transverse direction; (b) along the weld direction; (c) Schematic of estimating the deflection in the butt joint.

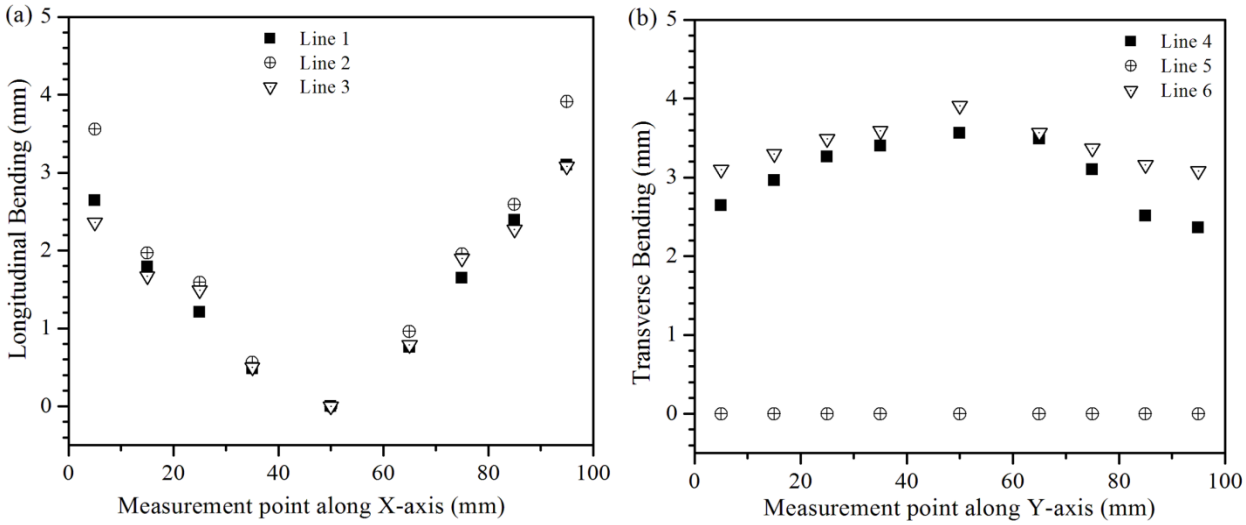

Fig. 4.22 Distortion at moderate heat input of 65.5 J/mm: (a) Longitudinal Bending; (b) Transverse Bending.

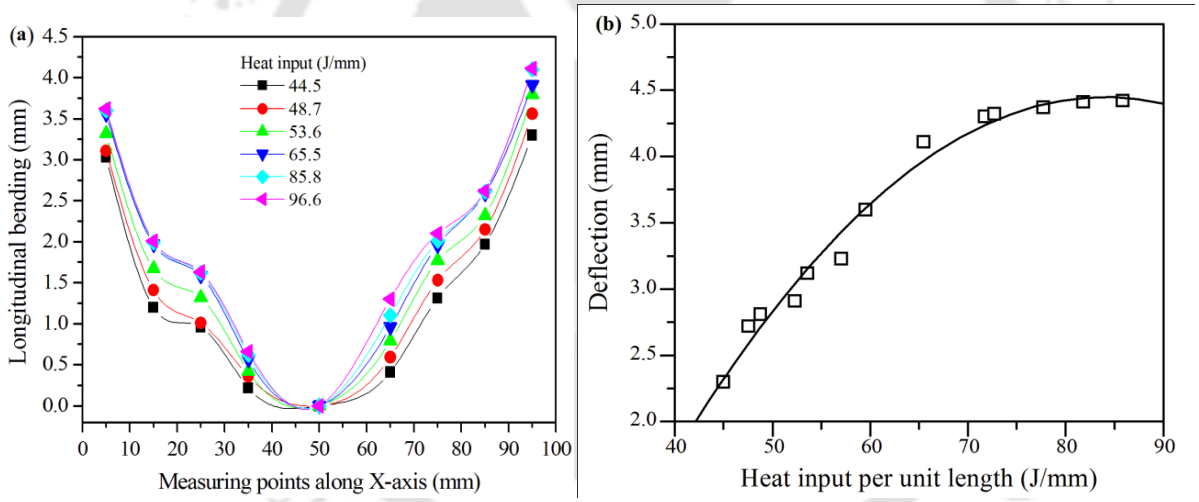

Fig. 4.23 (a) Comparison of longitudinal bending for different heat input; (b) Deflection at the weld edge along the centerline with respect to heat input.

4.2.2 MPAW of steels

Similar procedure is adopted to weld 500 µm of SS304 and mild steel individually. First bead on plate was carried out to find the optimized parameter and the butt weld is carried out. The welding parameters are chosen in three different speeds (2.75 mm/s, 4.2 mm/s, 5.26 mm/s) and current ranges of 7 - 20A with optimum combination of other fixed parameters (Table 4.5) similar to the one used with Ti6Al4V alloy. The fixture used here is different from the one used

in Ti6Al4V alloy welding. Also, no purging gas is used in the process. The schematic diagram of experimental set up is shown in Fig. 4.24. Fig. 4.25 shows the process map of the feasible range of most significant parameters i.e. welding speed and current to get a successful weld joint for all the materials. The suitable combination of welding current and speed is required to produce stable and defect-free weld. When the welding speed is increased, the proper welding current range shifts towards higher side. Only heating of the material takes place at low heat input while beyond a certain limit, burn out of the material occurs. Thus heat input can be considered to be one of the most important parameters in determining feasible range of welding condition. By comparison of the weld zone it can be concluded that the feasible parameter range of the mild steel is more i.e. for similar condition, more current can be employed to obtain a successful joint. This is due to higher conductivity of mild steel which causes the deposited heat to diffused away more rapidly. On the other side, the welding current is usually lower as compared to the welding of low carbon steel since the melting point of SS304 and electrical resistivity is less than low carbon steel. The thermal and mechanical properties of these two materials at room temperature are listed in Table 4.6.

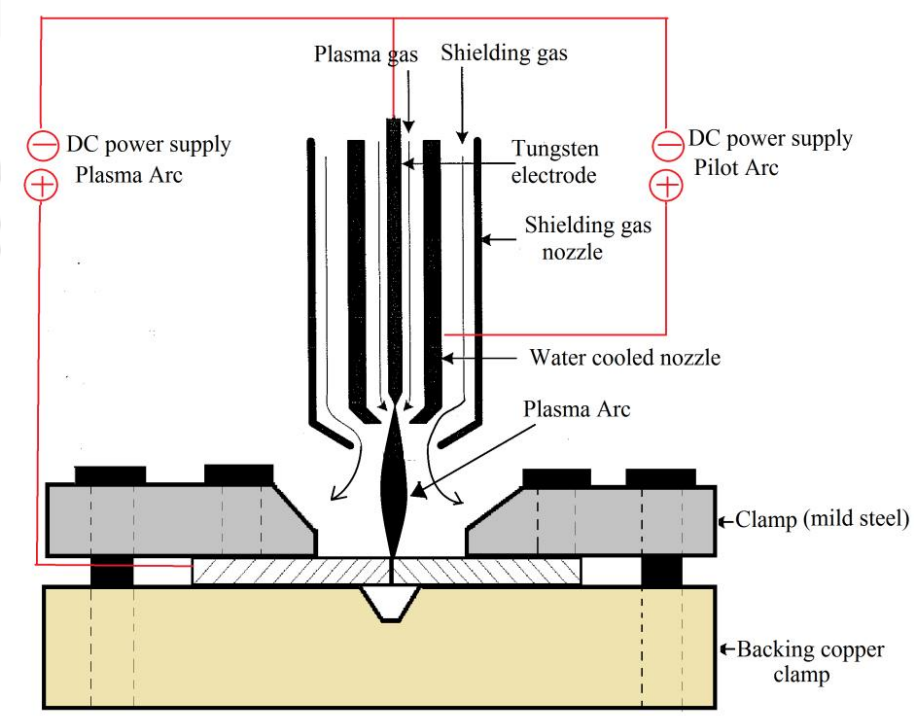

Fig. 4.24 Schematic diagram of experimental set up.

Table 4.5 MPAW process parameters used for two materials.

Welding Parameters	Values
Welding current (A)	10 - 13A
Welding speed (mm/s)	2.75, 4.2, 6.67
Copper Nozzle diameter (mm)	1.2
Electrode diameter (mm)	1.2
Plasma gas flow rate (lpm)	6
Nozzle to plate distance (mm)	2
Shielding gas flow rate (lpm)	0.4
Pre Flow (s)	4
Post Flow (s)	4
Torch Position	Vertical

Table 4.6 Constant material properties at ambient temperature [Mills, 2002].

Properties	Stainless steel	Low carbon steel
Density (Kg/m^3)	8000	7850
Thermal conductivity (W/mK)	16.2	43
Expansion coefficient (µm/mK)	17.2	12
Specific Heat (J/kgK)	530	510.78
Latent heat of fusion (kJ/kg)	260	270
Diffusivity ($\mu m^{2/}s$)	4.2	11.72
Meltingtemperature (K)	1723	1773
Solidus temperature (K)	1673	1723
Ultimate tensile strength (MPa)	754.7	330
Yield strength (MPa)	256	245
Young's Modulus (GPa)	200	200
Ductility(%)	60	36
Hardness (VHN)	176	108

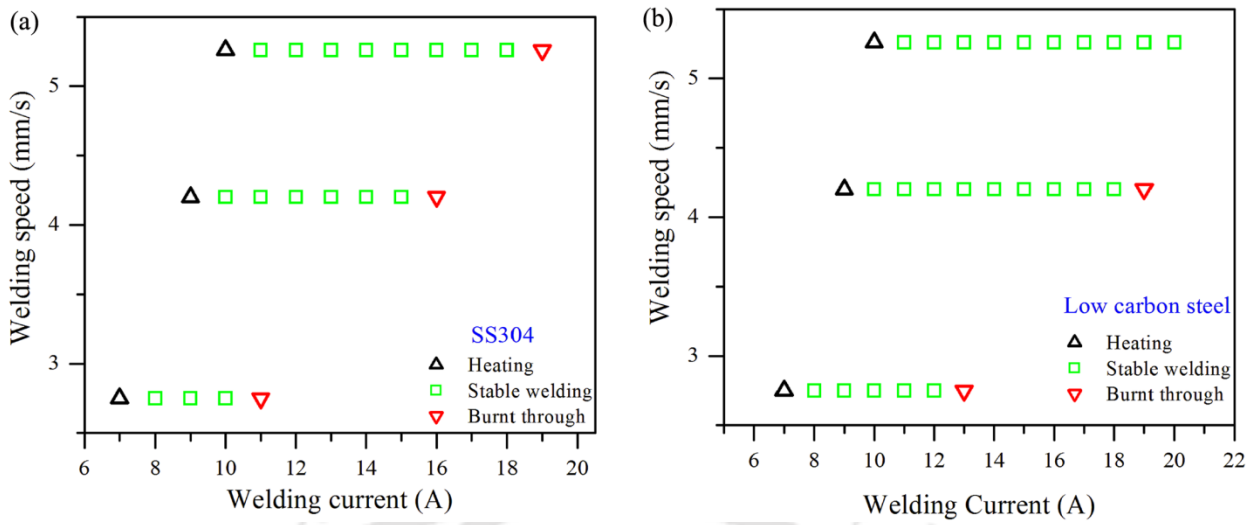

Fig. 4.25 Influence of welding speed and arc current: (a) SS304; (b) Low carbon Steel.

Figure 4.26(a) - (b) shows the weld bead produced for a full plate welding by bead on welding and butt welding respectively corresponding to a welding condition of 12 A and 4.2 mm/s. It is observed that the weld bead decreases slightly during butt welding of two sheets with similar process parameters. This is due to presence of slight gap between two sheets for actual butt joint as compared to bead-on-plate welding which may lead to the escape of heat. Figure 4.27 shows the weld macrographs obtained by butt welding of SS304 corresponding to certain welding conditions as summarized in Table 4.7. It is seen that the weld dimension increases with heat input.

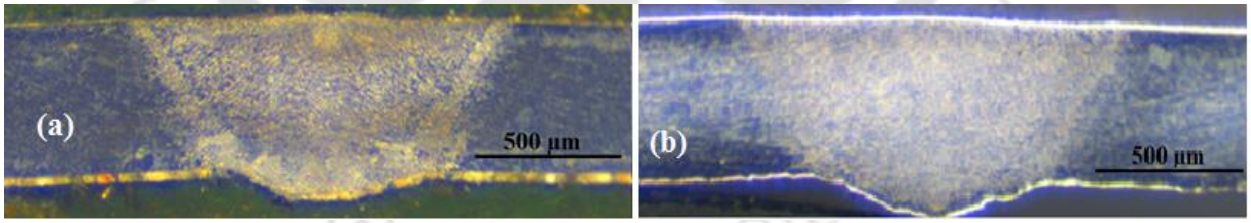

Fig. 4.26 Weld bead corresponding to a welding condition of 12 A and 4.2 mm/s (a) bead on plate; (b) butt welding.

It is well known fact that the welded microstructure depends on the heat-input in case of 304 stainless steel. Figure 4.28 shows the micrograph of fusion zone, HAZ and base metal for two different welding conditions. The parent material, HAZ and FZ could be discriminated easily. Dendrites can be observed extending from the fusion boundary to the weld centreline (Fig.

4.28b). Figure 4.29 shows the optical micrograph of fusion zones at three different heat inputs. The low heat input can be attributed to smaller dendrite sizes and lesser inter- dendritic spacing in the fusion zone. Since the cooling rate was moderate, δ-ferrite with skeletal morphology was formed in solidified weld metal for the condition of W2 (Fig. 4.29b). It is observed from Fig. 4.29 that a higher heat input renders the dendrite structure coarser due to a decrease in the cooling rate.

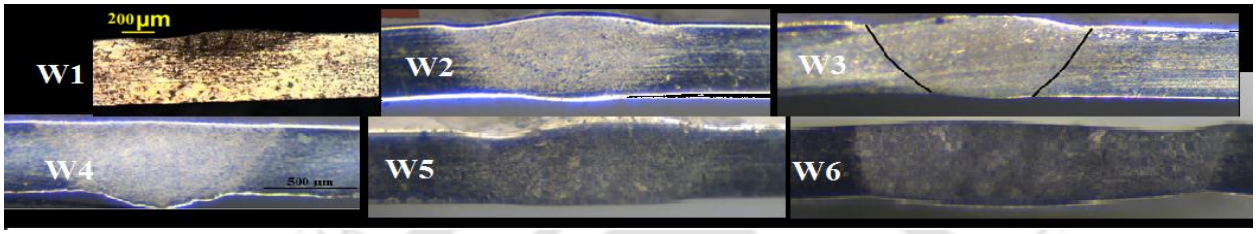

Fig. 4.27 Weld macrographs corresponding to the welding conditions of Table 4.7.

Table 4.7 Process parameters for SS304 butt welding.

Welding Condition	Current (A)	Welding speed (mm/s)	Heat input per unit length (J/mm)
W1	11	5.26	52.28
W2	10	4.2	59.52
W3	11	4.2	65.47
W4	12	4.2	71.42
W5	14	4.2	83.33
W6	10	2.75	90.90

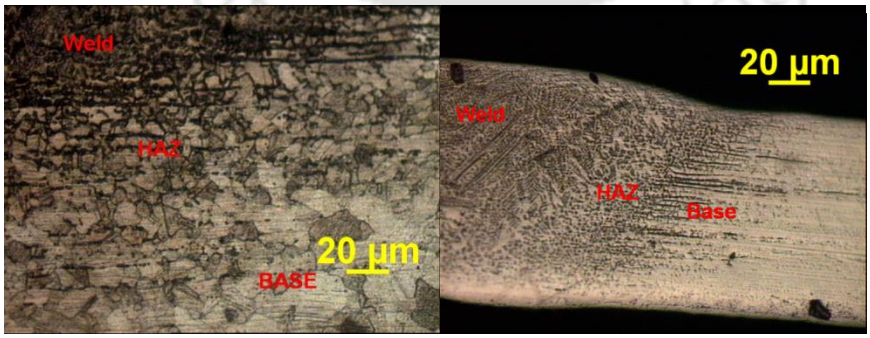

Fig. 4.28 Grain refinement in three zones: (a) W1; (b) W2.

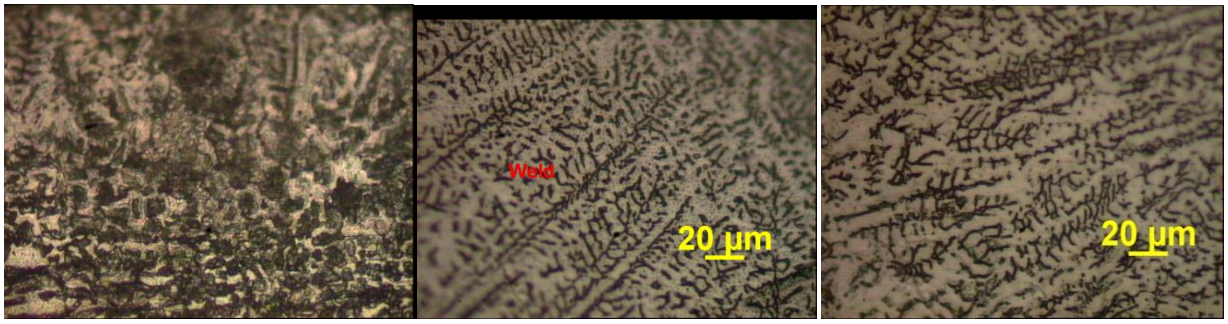

Fig. 4.29 Microstructure of fusion zone: (a) W1; (b) W2; (c) W3.

The mechanical properties determined for the weldment are tensile test and hardness test. Tensile test are carried out on a computer controlled universal testing machine as per ASTM standards (E-8). The tested tensile specimens are fractured in the base metal. The ductile fracture is observed in the tensile tested specimens. The tested welded specimens tensile strength (UTS) measured values are in the range of 600-760 MPa, whereas the base metal has shown tensile stress of 754 MPa. The weld joint efficiencies of over 90% are observed in majority of the samples and are comparable to the base metal strength. The details of tensile stress and yield stress measurements are given in Fig. 4.30b.

Vickers micro hardness tests are performed on a transverse section of the weld bead at 0.25mm below the top surface. The average hardness is found to be the highest in the fusion zone. Also hardness decreases with heat input. This can be attributed to the low heat input resulting in high cooling rate produced and hence increasing hardness in both HAZ and weld metal

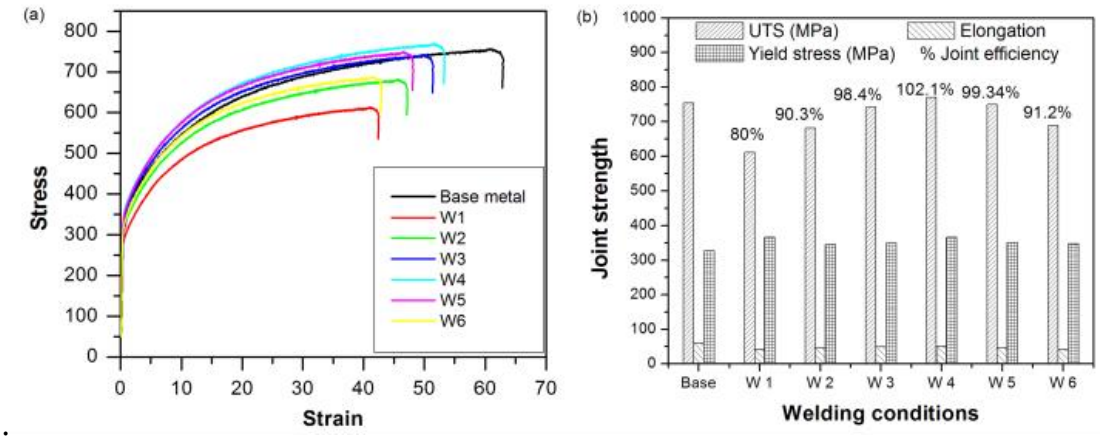

Fig. 4.30 (a)Tensile stress–strain curve; (b) Joint strength of the joints.

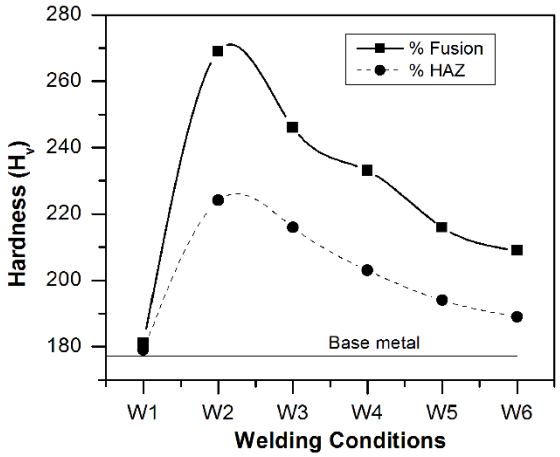

Fig. 4.31 Hardness values.

4.2.2.1 Comparison with low carbon steel

Figure 4.32 shows the weld bead obtained at similar welding condition for two materials. It is observed that the weld bead of carbon steel is smaller for the same welding condition but the total heat affected zone is higher [Fatima *et al.*, 2014]. Carbon steel has very high thermal conductivity which causes most of the heat to dissipate away. Whereas SS304 has lower thermal conductivity and the heat is highly concentrated in the weld zone causing it to form wider bead. Fig. 4.33 shows the weld macrograph at 10A and 4.2 mm/s. The weld bead formed by carbon steel is more elongated and the weld width is smaller as the heat is more distributed. Due to the low heat input (approximately 52-110 J/mm of the investigated region) by the micro plasma arc, the depth/width ratio is low and is not enough to produce a keyhole. In general, an elliptical shape is obtained.

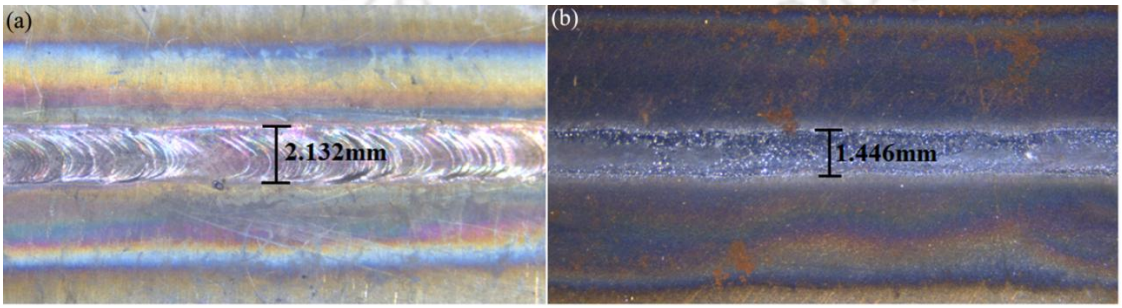

Fig. 4.32 Weld beads (bead on plate welding) obtained at 10 A, 4.2 mm/s: (a) SS304; (b) Low carbon Steel.

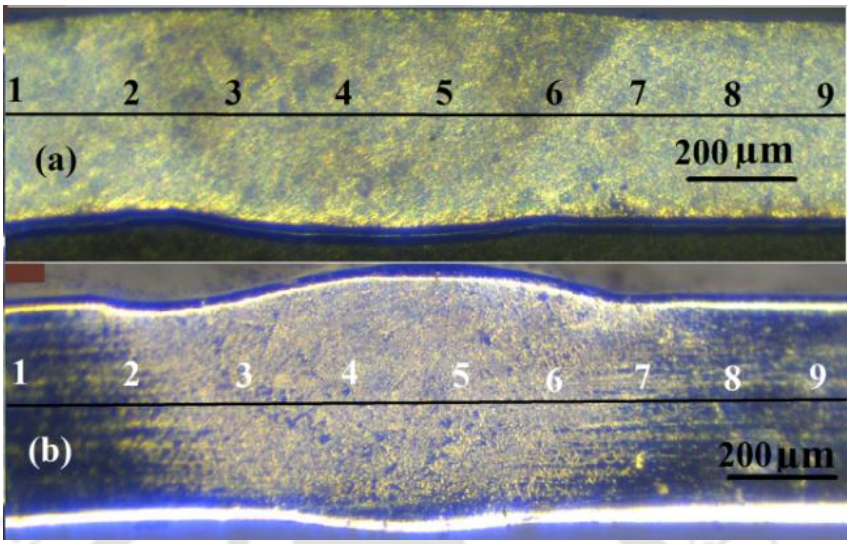

Fig. 4.33 Weld beads (bead on plate welding) obtained at 10 A, 4.2 mm/s: (a) Low carbon steel; (b) SS304.

Figure 4.34 shows the mechanical properties of the two materials at welding condition of 10 A, 4.2 mm/s. Transverse tensile strength of all the joints has been evaluated. The tensile testing was carried out in accordance with ASTM E-8 standard. Two specimens for tensile test are considered and the average values are considered. Tensile strength of SS304 welded joint is 784 MPa with 48% elongation while that of carbon steel welded joint is 363 MPa with 24% elongation. Joint efficiency is also being calculated for both the welded joints which are 104.78 and 110.19%, respectively. The yield strength for both the materials is 350MPa (SS304) and 255MPa (carbon steel) at the given welding condition. It is observed that the work hardening rate is more for SS304 than carbon steel. The micro-hardness test is carried out with Vickers pyramid indenter by 50 g load for 15 s along the middle line of the cross section (Fig. 4.33). The average hardness values for both the materials are evaluated. The hardness for the base materials is found to be 176 and 108 for SS304 and low carbon steel. Various factors can contribute to the hardening like grain size, phase composition and metallic inclusions. The hardness is found to be highest at the weld zone for SS304 as shown in Fig. 4.34b. This may be due to the formation of hard martensitic structure at the weld zone. While for low carbon steel, the highest is in the HAZ zone (Fig. 4.34b).This may be due to coarser grain in the HAZ of low carbon steel weldment

.

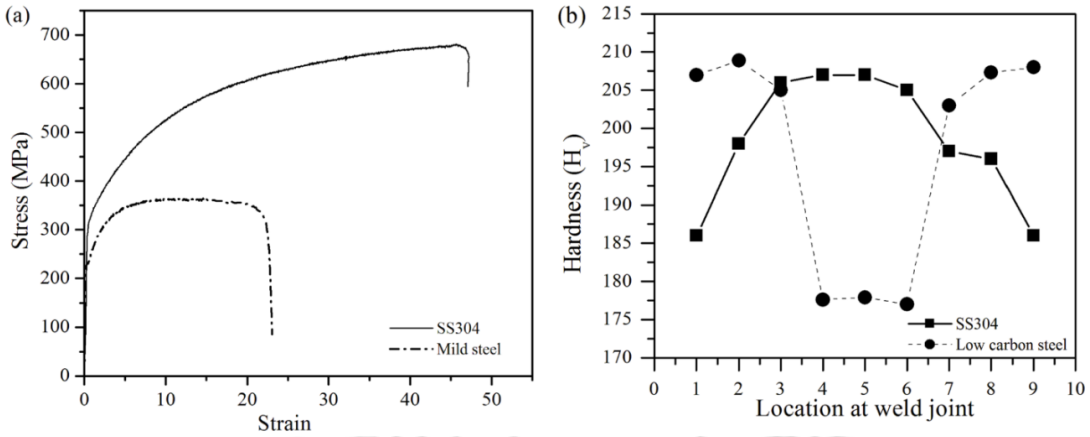

Fig. 4.34 (a) Stress strain diagram; (b) Hardness of the materials obtained at 10 A, 4.2 mm/s.

The weld-induced distortion is mainly influenced by welding conditions, geometric shape and restrains conditions. In the present investigation, the comparative analysis shows the distortion dependency on the difference in mechanical properties. Both the materials are distorted in a convex concave distortion. Fig. 4.35 shows the bending distortion (displacement along Z-direction) for the two materials in the longitudinal direction along the weld line and transverse direction corresponding to a welding condition of 4.2 mm/s speed and 10A current. It is seen that although the pattern of deflection of these materials is the same, the deflection is higher for SS304. This is because the coefficient of thermal expansion of SS304 is more than low carbon steel and thus SS304 expands and contracts at a faster rate than carbon steel resulting in greater warping.

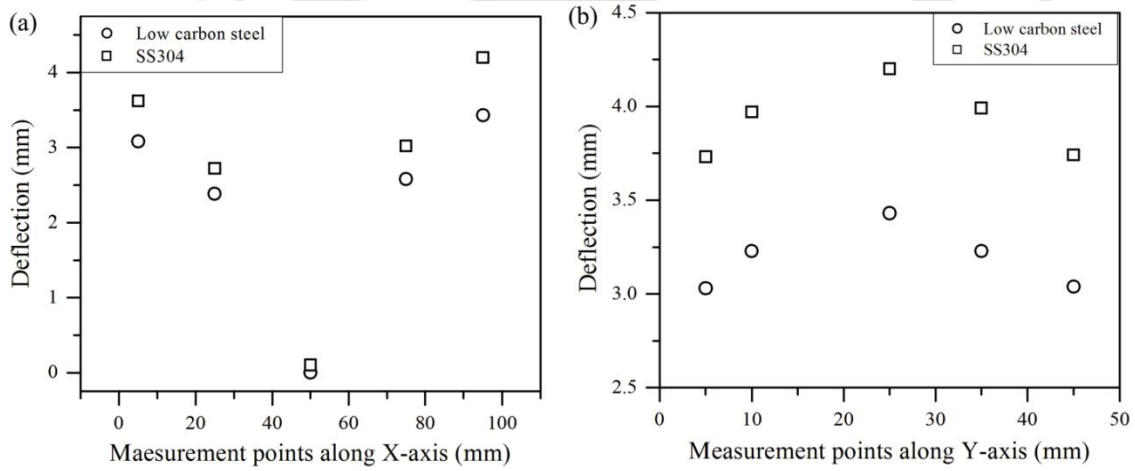

Fig. 4.35 Deflection comparison of the two materials at 4.2mm/s and 10A current (a) longitudinal direction along the weldline; (b) transverse direction at the weld stop edge.

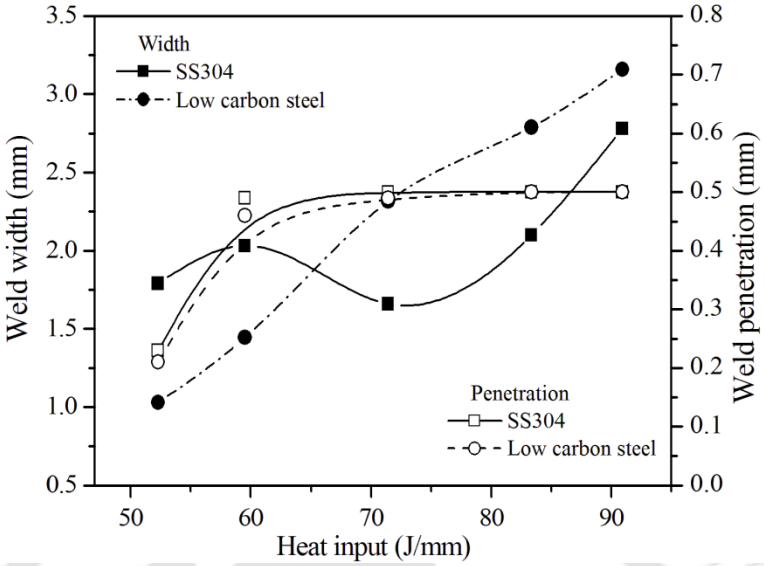

Fig. 4.36 Effect of heat input on weld dimensions.

The bead geometry which is specified by bead width, reinforcement, penetration, directly influences the load carrying capacity of the weldments. Fig. 4.36 revealed that both bead width and penetration of both the materials increases with increase with increase in heat input as greater amount of heat is available for forming the molten pool. However, at a critical value of heat input when full penetration of the SS304 weldment is obtained, the bead width decreases and thereafter the bead width increases. However, in case of low carbon steel, this effect is not obvious i.e. bead width increases with the increase in heat input for the entire range. Moreover the penetration increases more rapidly at lower heat input. Fig.4.37 shows the variation of mechanical properties with heat input. The ultimate tensile strength of the material first increases and then decreases with increase in heat input. The maximum UTS of 784MPa is obtained at 10A and 4.2mm/s (~ 59.5 J/mm) for stainless while 369MPa is obtained for low carbon steel at 12A and 42mm/s (~ 71.4). The lower strength at lower heat input is attributed to insufficient penetration. The value is found to be comparable to the base material in the investigated region indicating good strength of the weldment. The hardness value is found to be the highest at HAZ zone for all the cases in case of low carbon steel weldments. However, the hardness is highest in the weld zone for SS304. Fig. 4.37 reflects the average hardness values of HAZ zone for low carbon steel and weld zone for SS304 weldments. The hardness increases with increase in heat input. The deflection (Z-displacement) of the weld edge of the centreline is shown in Fig. 4.38.

The deflection increases with increase in heat input and becomes steady with further increase in heat input. Thus, it can be conclude that the heat input has significant effect on mechanical and microstructural characteristics of the plasma micro welded joints.

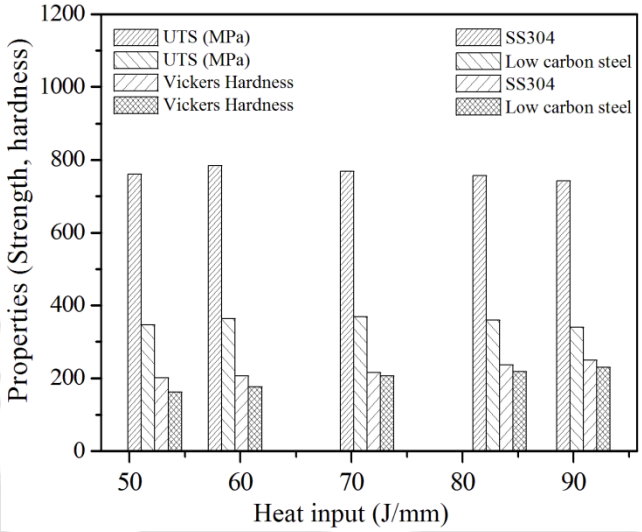

Fig. 4.37 Effect of heat input on mechanical properties.

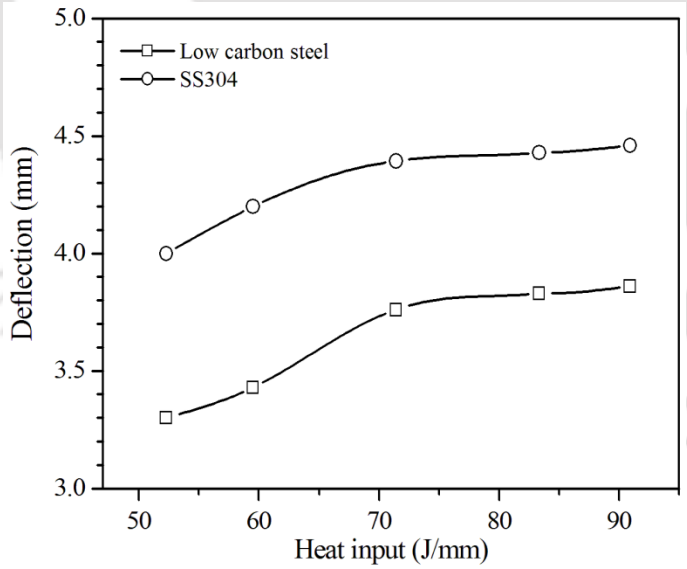

Fig. 4.38 Effect of heat input on deflection.

4.3 Laser microwelding

Pulse laser welding is carried out on 500 μm thick Ti6Al4V alloy in butt joint configuration using a 5 kW Nd:YAG laser system combined with a robotic arm as shown in Fig. 4.39. The schematic diagram of the experimental set-up is shown in Fig. 4.40(a). The

fundamental problem with welding of titanium is its strong affinity with surrounding elements at high temperature that causes embrittlement of the weldment. All parts of the heat-affected zone (HAZ) are necessary to shield from the atmosphere until the temperature drops below 650 K. Thus, additional shielding is generally provided for welding of titanium alloy [Donaiche, 2000]. The sheets to be joined are clamped carefully in a custom made fixture, designed and constructed for the operation of welding procedure in open air to prevent both oxygen contamination and distortion of the workpiece. The backing plate of the fixture is made of copper and the top plates used are made of aluminum. Both copper and aluminum have very high thermal conductivity which ensures low angular distortions of the joint due to intensive heat transfer [Klimpel and Lisiecki, 2007]. Also the problem of oxidation is reduced due high rate of heat diffusion through the backing plates. Industrially pure argon gas @ 8L/min is used as shielding gas and purging gas. The sheets are clamped properly so as to avoid distortion during the welding process and misalignment of the sheets along the weld line. Edge preparation is done to ensure full contact between the sheets along the weld line.

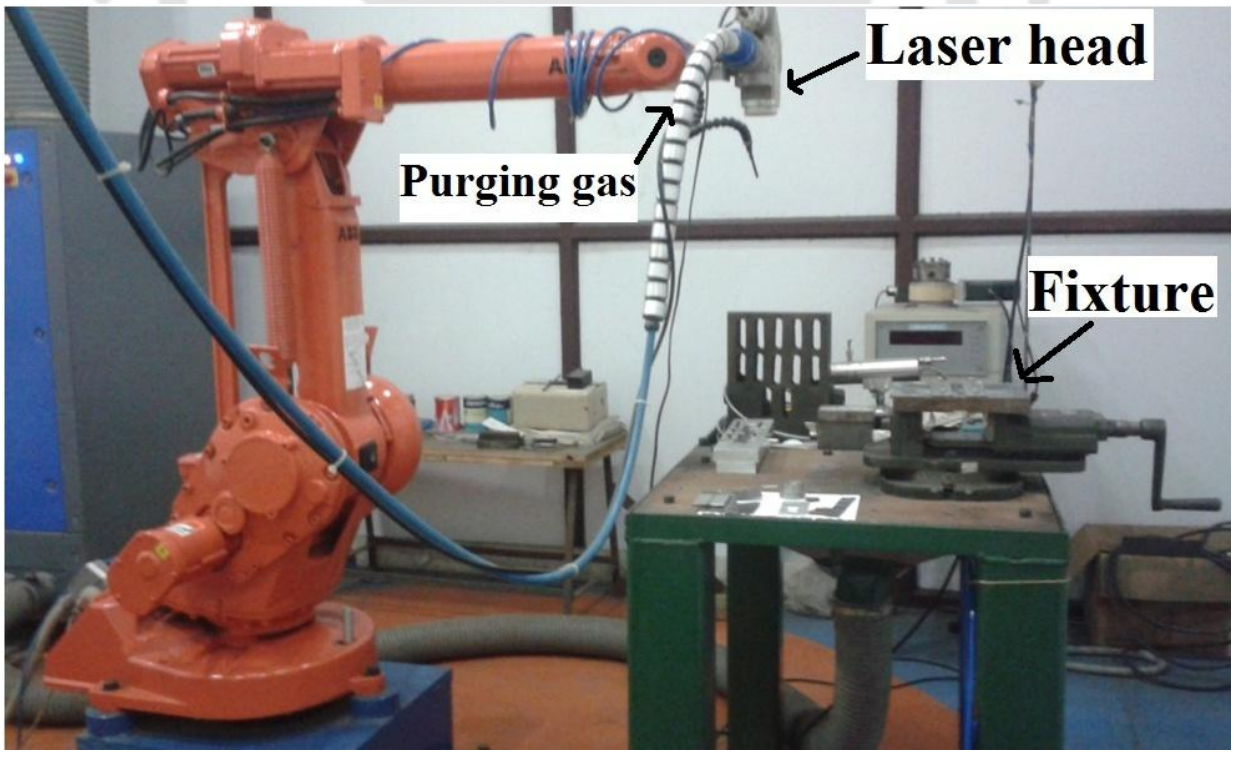

Fig. 4.39 Experimental Setup for laser micro welding.

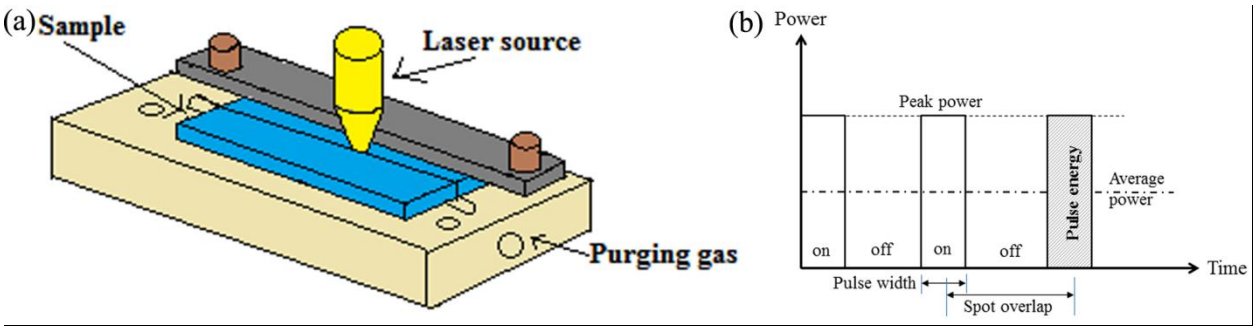

Fig. 4.40 Schematic diagram of: (a) experimental set-up, and (b) pulse characteristics.

Pulse welding is characterized by periodic heating of the weld pool by an incident high peak power and high density laser beam that allow melting and solidification to take place consecutively. The pulse laser is used generally for seam welding which is a series of overlapping spots to form a fusion zone [Tseng, 2000]. Apart from laser scanning speed and average power, the quality of weld joint depends on optimal combination of various pulse parameters such as pulse energy, pulse duration and repetition rate. In present work, the experiments are conducted by changing the laser scanning speed and pulse energy at constant pulse duration and frequency.

Since the pulse laser welding involves several process parameters. Careful selection of optimum parameters for successful weld joint needs a lot of trials. An approximate estimation of process parameters is supportive here to designate the domain of parameter selection for defect-free weld. The welding speed is defined by the spot overlap, the pulse repetition rate, and the focus diameter [Chmelíčková *et al.*, 2012] and is expressed as

$$U = 2r_{eff}(1 - S_0)F \tag{4.5}$$

where U is welding speed, S_o is spot overlap, F is pulse repetition rate, and r_{eff} effective spot radius of laser. The spot overlap of 60 %, 70 % and 80 % is considered in present investigation which corresponds to a speed of 6mm/s, 4.5mm/s and 3mm/s respectively. The maximum pulse duration is estimated as

$$t_{on}^{max} = \left(\frac{\rho C}{k}\right) r_{eff}^2 \tag{4.6}$$

where C, ρ, k are the specific heat, density, and conductivity of the material, respectively. The minimum energy of pulse required in welding is expressed as

$$E_{pl}^{min} = \frac{E_m}{1-R} \times \pi r_{eff}^2 t_{on}^{max} = \frac{\rho[C_p(T_m - T_0)+L]}{1-R} \quad (4.7)$$

where L, R, E_m, T_m and T_0 are the latent heat of fusion, reflectivity, melting energy per unit volume, melting temperature and ambient temperature respectively.

The numerical values of the physical properties used for the calculation is shown in Table 4.8. The maximum pulse duration and minimum energy are calculated to be around 1.9 ms and 4.8 J respectively. Thus pulse duration is fixed at 5 ms at constant pulse repetition rate of 20Hz in the present investigation whereas energy is varied from 5 J until the burnout of the material occurs. Laser is focused on 0.2mm below the surface to produce a spot diameter of 0.75mm on the top of the surface. The shape of the pulse is rectangular (Fig.1b).The average power (P_{av}) and the peak power (P_{pk}) during welding is estimated as

$$P_{av} = E_{pl}F; \qquad P_{pk} = \frac{E_{pl}}{t_{on}} \quad (4.8)$$

Considering the effect of laser scanning speed, the heat input per unit length (HI) based on average power is estimated as

$$HI = \frac{P_{av}}{U} \quad (4.9)$$

Table 4.9 Physical Properties of Ti6Al4V.

Parameters	Values
ρ	4430 kg mm^{-3}
R	0.55
C_p	526.3 J kg^{-1} K^{-1}
K	6.7 W m^{-1} K^{-1}
T_m	1933 K
T_0	298 K
L	370 $kJkg^{-1}$

The experiments are conducted over laser scanning speed of 3 - 6 mm/s, pulse energy of 5 – 14 J and heat input varies between 26.7 – 63.3 J/mm. Altogether 27 experiments are conducted at two pulse duration of 5 ms and 3 ms and at pulse frequency of 20 Hz. The peak power varies between 1.0 kW to 2.8 kW and the average power lies between 100 W to 280 W. Table 4.10 depicts the laser process parameters used in present investigation.

Table 4.10 Laser process parameters used in present investigation.

Exp. no.	Speed (mm/s)	Pulse Duration (ms)	Energy (J)	Peak power (kW)	Average Power (W)	Heat Input (J/mm)
1	3	5	5	1	100	33.33
2	3	5	6.5	1.3	130	43.33
3	3	5	8	1.6	160	53.33
4	3	5	9.5	1.9	190	63.33
5	3	5	11 (burnt)	2.2	220	73.33
6	4.5	5	6.5	1.3	130	28.8
7	4.5	5	8	1.6	160	35.5
8	4.5	5	9.5	1.9	190	42.22
9	4.5	5	11	2.2	220	48.8
10	4.5	5	12.5	2.5	250	55.55
11	4.5	5	14	2.8	280	62.22
12	4.5	5	15.5 (burnt)	3.1	310	68.66
13	6	5	8	1.6	160	26.66
14	6	5	9.5	1.9	190	31.66
15	6	5	11	2.2	220	36.66
16	6	5	12.5	2.5	250	41.66
17	6	5	14	2.8	280	46.66
18	4.5	3	9.5	3.17	190	42.22
19	3	3	9.5	3.17	190	63.33
20	6	3	9.5	3.17	190	31.66
21	4.5	3	8	2.67	160	35.55
22	3	3	8	2.67	160	53.33
23	6	3	8	2.67	160	26.66

4.3.1 Macro/microstructural characteristics

Figure 4.41(a) shows the feasible domain for a successful weld joint of welding speed and energy for a constant pulse width of 5ms and frequency of 20Hz. It is found that as the speed is increased, more energy is required to melt the metal. Beyond a certain limit of the laser power, burn out of the material occurs. The stable welding is obtained under the suitable combination of weld energy and speed within the range of the current study. Figure 4.41(b) shows the front and back surface appearance of a full penetration welded joint. It is observed that both bead formations are smooth and in a bright sliver color which indicates no oxidation in the joints.

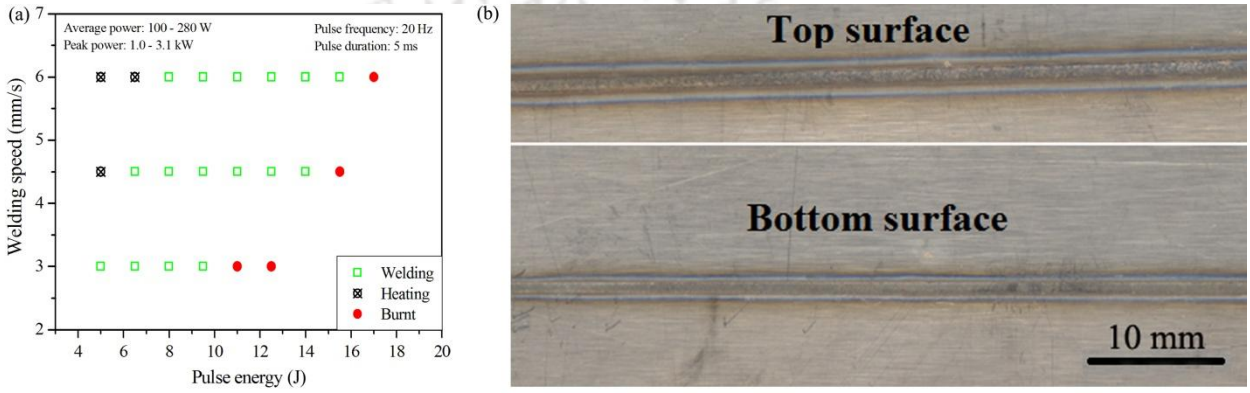

Fig. 4.41 (a) Process map for laser microwelding of Ti6Al4V butt joint configuration as a function of welding energy and speed; (b) Appearance of the weld surface.

Figure 4.42 presents the macrographs obtained at different welding conditions. Different types of profiles with variation of heat input per unit length are reflected. The macrograph reveals elliptical shape of the fusion zone at low heat input (Fig. 4.42a). As the heat input increases, the shape changes from trapezoidal to an hourglass shape. Macrographs reflecting the effect of pulse width are shown in Fig. 4.43 and Fig. 4.44. It is seen that the fusion area at higher pulse width is more. Also misalignment of the sample is observed when the heat input is very low. Thus, the optimum choice of heat input is important to decide to produce the full depth of penetration along with better quality.

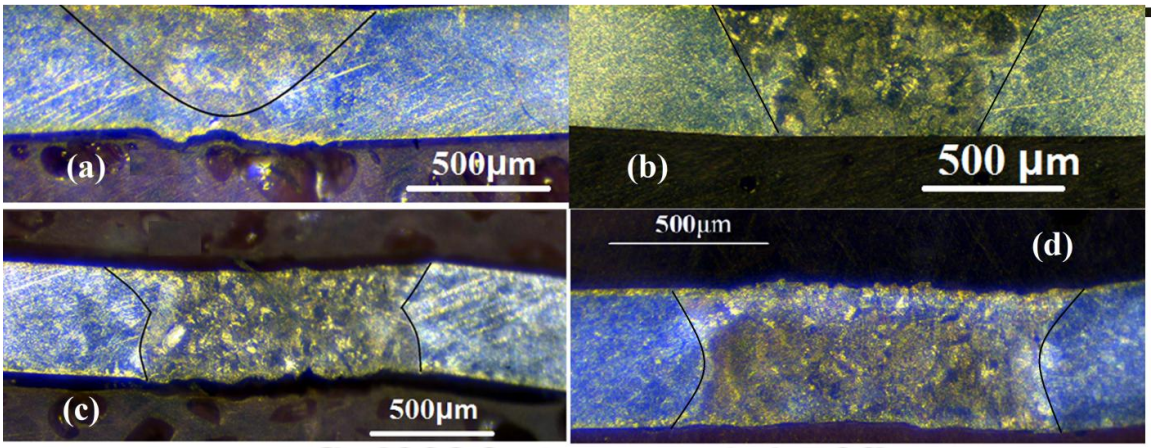

Fig. 4.42 Macrographs: (a) 33.33 J/mm; (b) 43.33 J/mm; (c) 53.33 J/mm; (d) 63.33 J/mm.

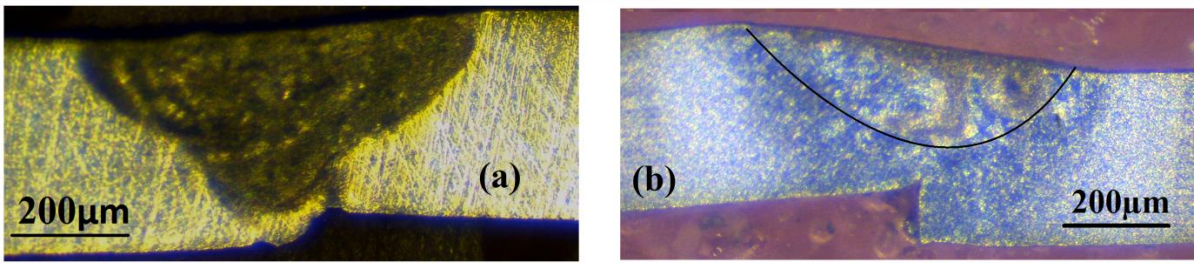

Fig. 4.43 Macrographs: (a) 26.6, 5ms; (b) 26.6, 3ms.

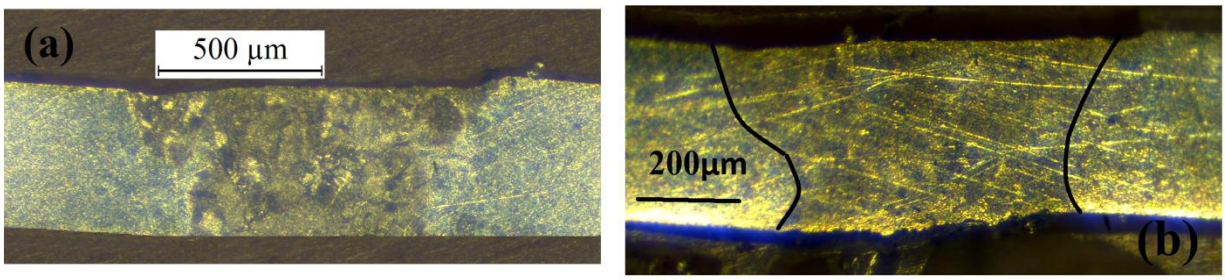

Fig. 4.44 Macrographs at 35.5 J/mm: (a) 5 ms; (b) 3 ms.

Figure 4.45 shows the grain refinement in the three zones due to laser micro welding corresponding to heat input of 53.5 J/mm. The HAZ zone is small which is typical, due to the high energy delivered in a short period. It is observed that a significant grain growth in the HAZ where the average prior-β grain size is ~ 35 µm. The evolution of the grain size of the prior-β phase in the HAZ and the FZ with respect to heat input is represented in Fig. 4.45 (b). From Fig. 4.45(b) it can be observed that very large prior-β grains in the FZ with an average size of 153 µm exist.

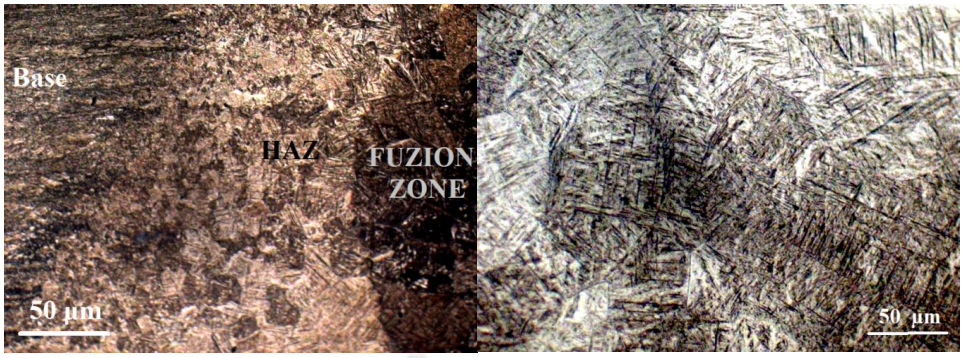

Fig. 4.45 (a) Macrographs showing different zones for Ti6Al4V weldment at heat input of 53.5 J/mm; (b) Prior-β grain size in the FZ and HAZ for the different welding conditions.

The rapid cooling rate in the weld pool, above the critical value for a full martensitic transformation, promoted the microstructural evolution to α' martensitic structure though the microstructure. The microstructures of Ti–6Al–4V alloy weld metal with different parameters are shown in Fig. 4.46. There is no essential distinction among the four macrographs, and the martensitic phase transformation of all joints occurs to a certain degree. However, the percentage of martensite decreases with increase in the heat input.

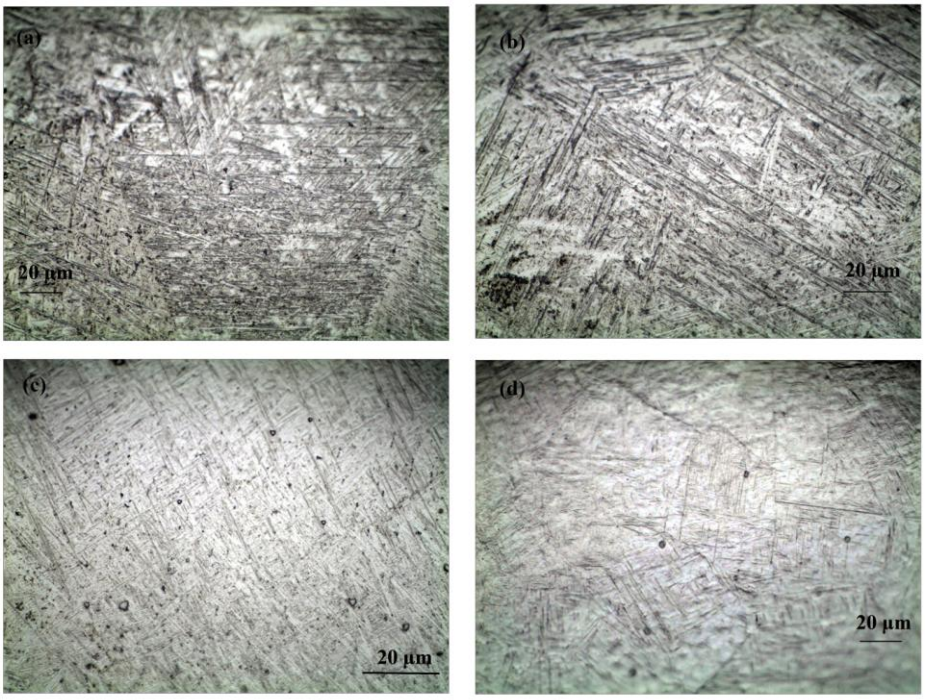

Fig. 4.46 Microstructure of fusion zone for Ti6Al4V weldment at welding conditions of :(a) 8 J, 5 ms, 6mm/s; (b)9.5 J, 5 ms, 6 mm/s; (c) 9.5 J, 5 ms, 4.5 mm/s; (d) 9.5 J, 5 ms, 3 mm/s.

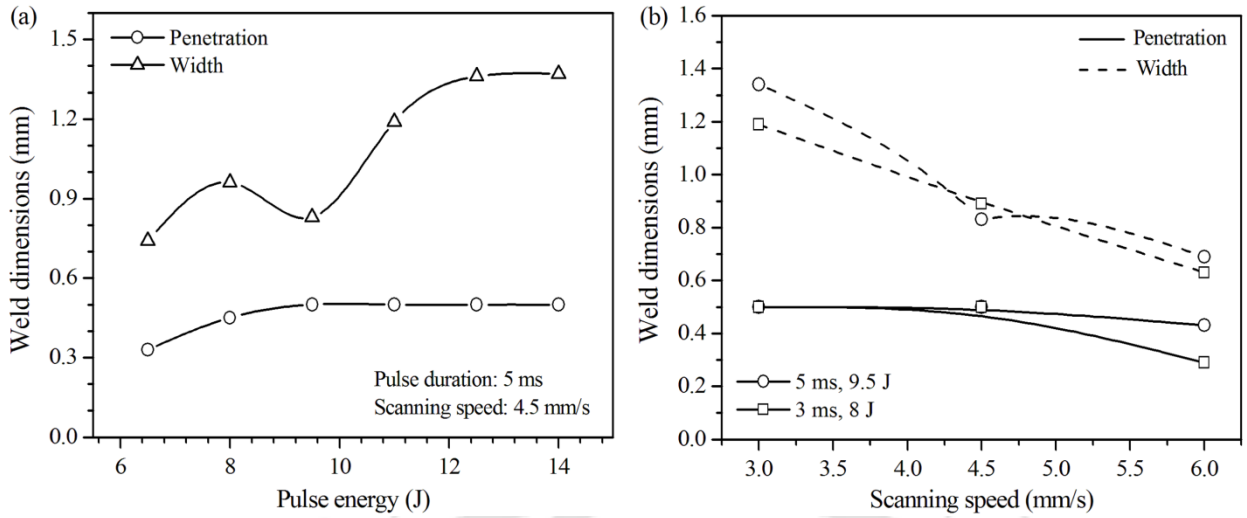

Fig. 4.47 Weld bead dimensions with (a) pulse energy, and (b) welding speed.

Figure 4.47 (a) shows the variation of weld dimensions with pulse energy (proportional to heat input per unit length). The weld penetration increases with increase in heat input and reaches in full depth at a threshold value of pulse energy between 8 J to 9.5 J. Once the molten pool extents to full depth, the heat transfer is enhanced in thickness direction that essentially reduces the weld width. The optimum (minimum) condition of weld width avails when full depth of penetration just reaches. With further increase in heat input the size of weld pool increases and becomes steady at pulse energy of 12.5 J. In case of very low heat input, misalignment is prone to occur that reduces the strength of the weld joint. Thus full penetration welds are always desirable. Fig. 4.47(b) indicates that with increase in pulse energy and decrease in welding speed is having similar effect on weld dimensions [Kou, 2003]. There is marginal difference in weld dimensions at low pulse energy viz. low pulse width. In laser welding, sufficient penetration with an acceptable weld surface (width) may be regarded as a signature of good weld joint. Low depth/width ratio as well as low heat input (less than 64 J/mm) by laser source are not enough to produce a keyhole and suggests the conduction mode of welding for the selected range of parameters. Also the macrostructures reveal no defects such as underfill, undercut, porosity and solidification cracking. Thus the weld bead obtained is of acceptable quality.

Energy dispersive X-ray (EDX) analysis is performed to find out the elemental distribution before and after welding in order to estimate the oxidation rate. EDX analysis confirms the presence of the alloying elements (Ti, Al, and V). The parent metal shows the presence of very little amount of oxygen (Fig. 4.48a). At high temperature during welding,

oxygen concentration increases which might lead to the decrease in usability of the fabricated sample in the industry. It is found to be the highest for lower scanning speed (3mm/s) as well the maximum heat input. The maximum oxygen percentage is ~ 11.4% which can be considered as in the acceptable range. This ascertains the robustness of the current laser micro welding method for titanium alloy.

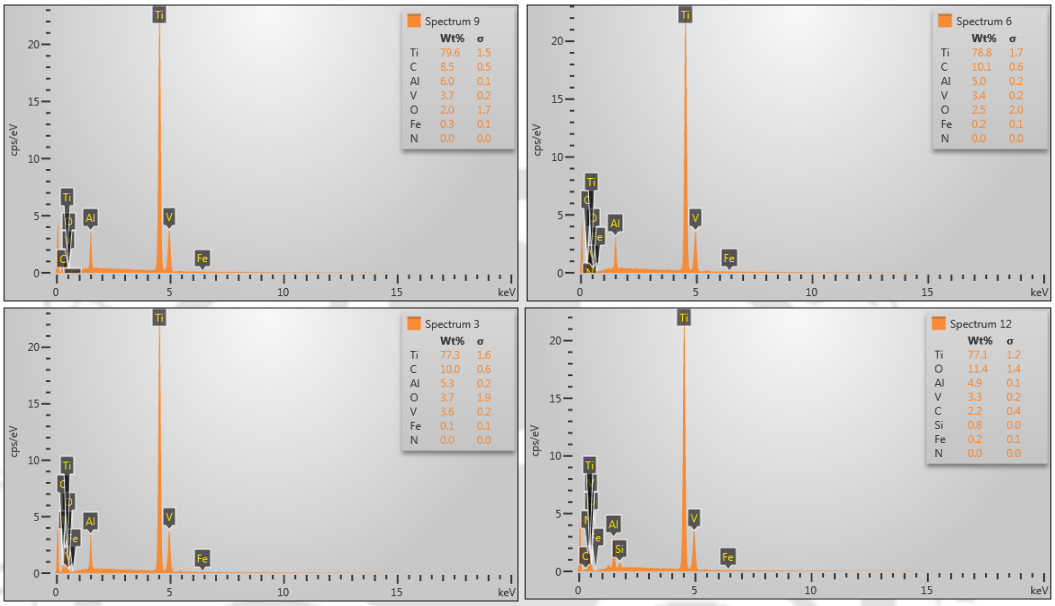

Fig. 4.48 EDX analysis of Ti6Al4V alloy:(a) at welding speed 6 mm/s, 5 ms, 8 J; (b) at welding speed 6 mm/s, 5 ms, 9.5 J; (c) at welding speed 4.5 mm/s, 5 ms, 9.5 J; (d) at welding speed 3 mm/s, 5 ms, 9.5 J .

4.3.2 Characteristics of mechanical properties

The strength of the joints is analyzed by tensile testing according to ASTM E8 standard. The test was carried at a constant rate of 0.2 mm/min where two specimens are prepared for each welding condition and the average value is considered. The stress-strain diagram of the welded specimens at different parameters is shown in Fig. 4.49(a). Overall, the strain hardening effect of titanium alloy is poor. With all other parameters remaining constant, the performance of stress-strain behavior i.e. yield strength and elongation is better in moderate pulse energy and then decreases with increase in pulse energy. Figure 4.49(b) indicates that the ultimate strength first increases and then decreases with increase in pulse energy. With increase in pulse energy, the heat input increases the volume of fusion zone and at very low heat input; the molten pool does

not produce full penetration welding. The strength of the weld joint is the lowest for low pulse energy because of partial penetration in this case. The joint efficiency of the weldment is also evaluated with reference to ultimate tensile strength (UTS) of the base material (~ 1119.40 MPa). The joint efficiently follows similar trend of UTS. The highest joint efficiency of 105.4% is obtained for moderate pulse energy. The UTS is the highest at the lowest welding speed of 3 mm/s (Fig. 4.49c). The yield stress follows similar trend to that of the ultimate tensile strength. Also, it can be concluded that the UTS of weld sample having larger pulse duration is more. Ductility loss is quantifiable in a maximum reduction of 30 % of the elongation from the base material, which drops from 16 % for the base material to 11%, in average. However, the ductility loss is not dramatic; this makes the laser beam welding suitable to gain high performance weld for Ti6Al4V.

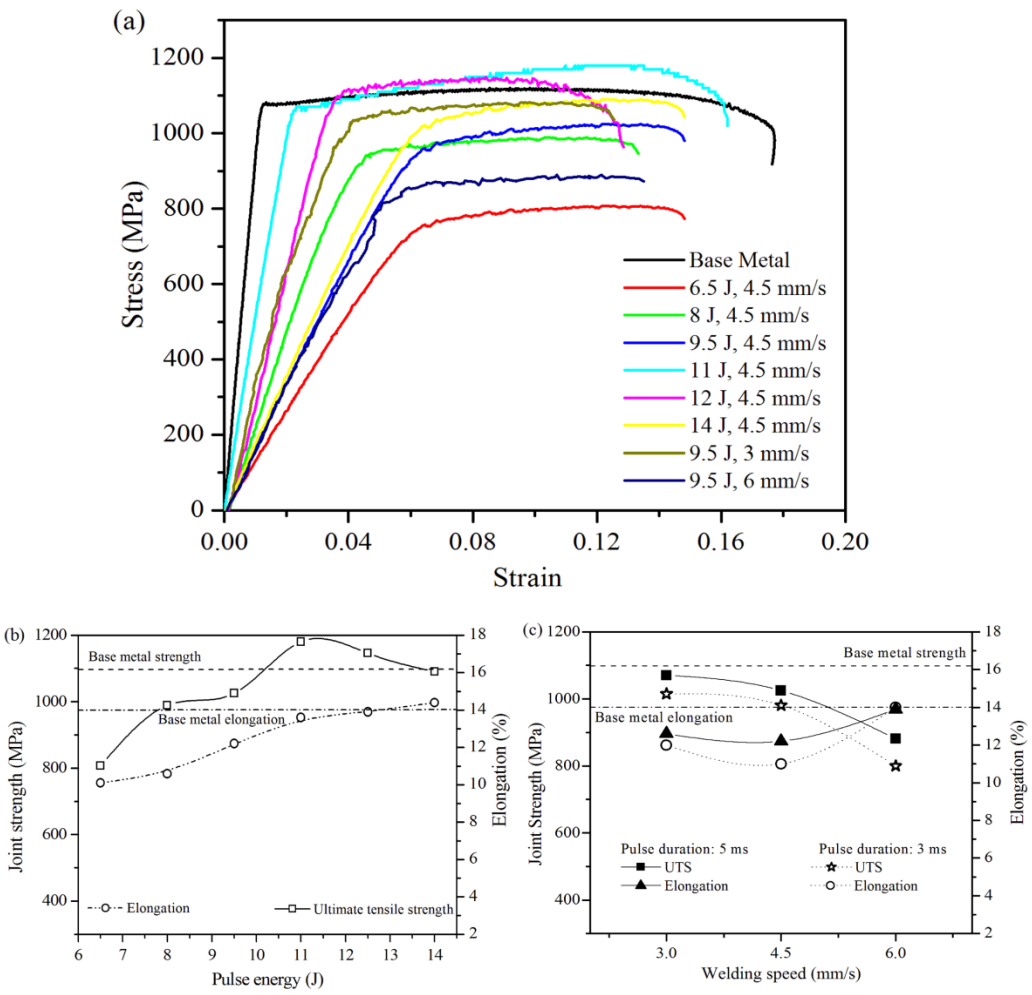

Fig. 4.49 (a) tensile stress–strain curve; strength and elongation variation with (a) pulse energy and (c) welding speed.

Vickers micro hardness tests are performed on a transverse section of the weld bead at 0.25mm below the top surface (Fig. 4.50). The average hardness is found to be the highest in the fusion zone regardless of the pulse energy and welding speed. In the present system, the cooling rate is very high which resulted in severe change in solidified microstructure as compared to base material. The hardness both in weld zone and HAZ zone are greater than the base metal. The micro hardness is found to decrease with increase in pulse energy and decrease in speed. At high heat input, the sample is subjected to slower cooling rate and results in coarse microstructure.

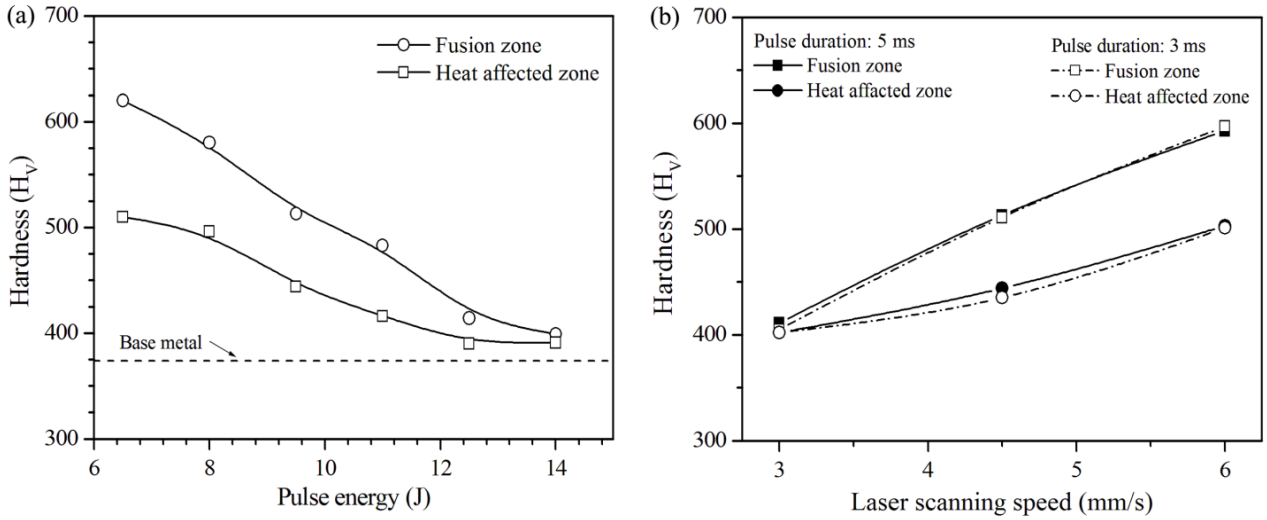

Fig. 4.50 Variation of hardness distribution with: (a) pulse energy; (b) welding speed.

Figure 4.51 exhibited several dimples along with little cleavage structure forming a river pattern. Also the dimples are shallow and non-uniform. Thus, the fractrographic analysis revealed a mixed mode of failure and the fracture mode is not completely ductile. This might be due to the presence of hardened martensitic structure present in the fusion zone. It is also seen that with decrease in speed the cleavage structure decreases and the dimples becomes deep and finer.

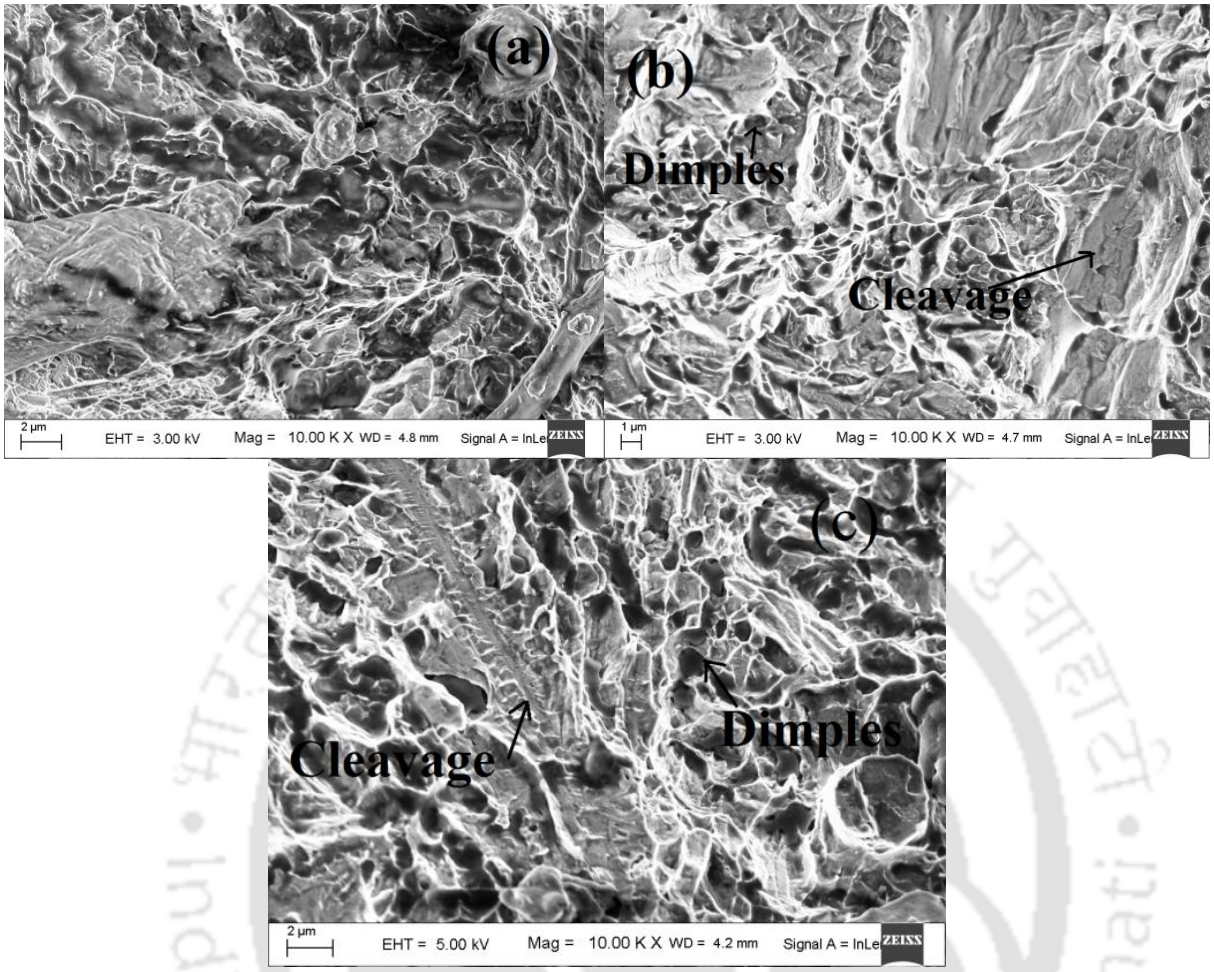

Fig. 4.51 Fracture surface of fusion zone of Ti6Al4V joints corresponding to 9.5 J, 5 ms and speed of: (a) 6 mm/s; (b) 4.5 mm/s; (c) 3 mm/s.

4.3.3 Distortion of laser welded structure

Distortion depends on welding conditions, geometry, restrains, and material properties. Co-ordinate-measuring machine is used to measure the distortion which determines the shape of the structure due to welding relative to a reference plane. The distortion due to welding is the difference between the initial shape (before welding) and the final shape (after welding) as the test plate is not perfectly straight. Here, 'after welding' means after complete cooling and release of the pressure from the suction table. Figure 4.52 shows the pattern of distortion along with the measurement points for the laser welded Ti6Al4V sheets for a certain welding conditions The plate has mainly significant transverse bending (uniform angular distortion) but the longitudinal

bending is very small. So the deflection is represented as angular distortion expressed by the following equation:

$$\theta = \tan^{-1}(p/b) \qquad (4.10)$$

Deflections are obtained for each case at three different sections of the plate, i.e. at the weld start edge, at the mid-section of the plate and at the weld stop edge. The angular distortion along the weld line corresponding to different welding conditions is demonstrated in Fig. 4.53. The distortion is found to be highest at the weld stop edge in comparison to weld start location for all the welding conditions. At the weld start location the heat input from the welding arc is absorbed by the base metal in front of the welding arc but at the weld stop location since there is no material in front of the welding arc, the heat is accumulated and therefore it results in higher angular distortions at the weld stop location in comparison to the weld start location. Also the distortion increases with increase in pulse energy and decreases with increase in speed. This is directly related to heat input which is proportional to pulse energy and indirectly to the welding speed. Also it is reflected that after a critical heat input, further distortion of the sheets is not observed as the process stabilizes itself. In Fig. 4.53, the trend infers that the deflection increases with heat input and becomes almost constant after a certain heat input. Once the molten pool extents to full depth, the heat transfer is enhanced in thickness direction. With further increase in heat input, the size of the weld pool increases and becomes steady with further increase in heat input. It will try to equilibrate the butt joint with some optimum residual distortion in a large pool of weld volume. Also, the average temperature gradient between top and bottom surface does not increase with further increase in heat input.

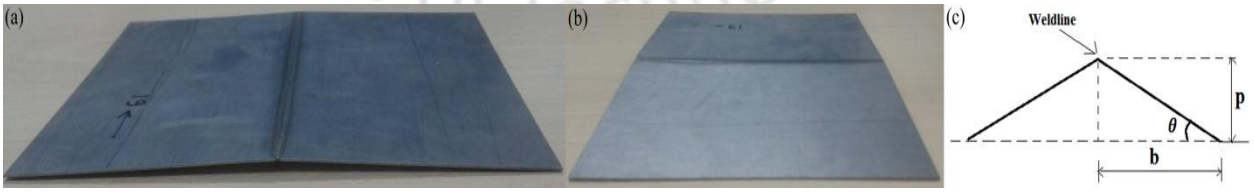

Fig. 4.52 Distortion pattern of the welded plates: (a) along the transverse direction; (b) along the weld direction; (c) schematic of estimating the deflection in the butt joint.

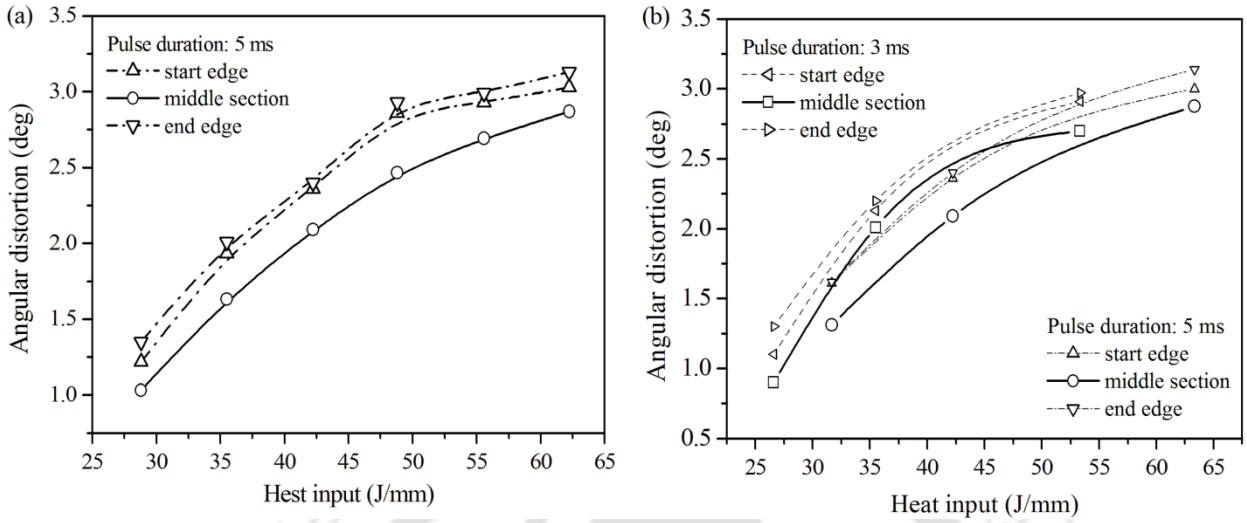

Fig. 4.53 Deflection along the weldline showing (a) the effect of pulse energy; (b) the effect of welding speed.

4.4 Comparative study between microplasma and laser microwelding of Ti6Al4V alloy

In this section, a comparative study is carried to investigate the effect of pulsed laser beam welding and plasma arc welding on weld joint characteristics of 0.5 mm thick Ti6Al4V alloy. The total heat input used in laser beam welding (LBW) is much less than that used in a plasma arc welding. It may be expected that LBW can be more effective for thin-plate joints as it may lead to less distortion and low HAZ. Thus, a comparison between the two processes on the weld quality is done corresponding to the same heat input of ~ 53 J/mm. For micro plasma welding, this heat input corresponds to the welding conditions of current of 9 A and welding speed of 4.2 mm/s. Whereas for laser micro welding this heat input corresponds to the welding speed of 3 mm/s, pulse energy of 8 J and pulse duration of 3 ms.

Figure 4.54 shows the weld macrographs obtained by laser and micro plasma welding. It is seen that fusion zone of laser welded micro joint is smaller than that by micro plasma welding. At this heat input α' martensite is formed in the fusion zone for both the process as revealed by Fig. 4.55. The figure shows the comparison of grain size in the fusion zone, for the two different welding processes. It is reflected that the laser welding produces more refined grains than that formed by plasma welding process for the same heat input. However the average grain size is

smaller in case of laser micro welding which is ~153 μm. While for micro plasma welding the average grain size is ~ 214 μm at the fusion zone. Also the distortion analysis of the weldments by the two process revealed that pattern is different. The results indicate that the out-of-plane deformation of thin-plate joint is much less in case of laser welding than that of microplasma welding. Also buckling can be prevented by the former process. However, the mechanical analysis showed that the strength of plasma weldment is more. Also less hardness is produced in case of micro plasma weldment. However, the oxygen concentration in the final weldment is much less in case of laser welding as suggested by EDX analysis.

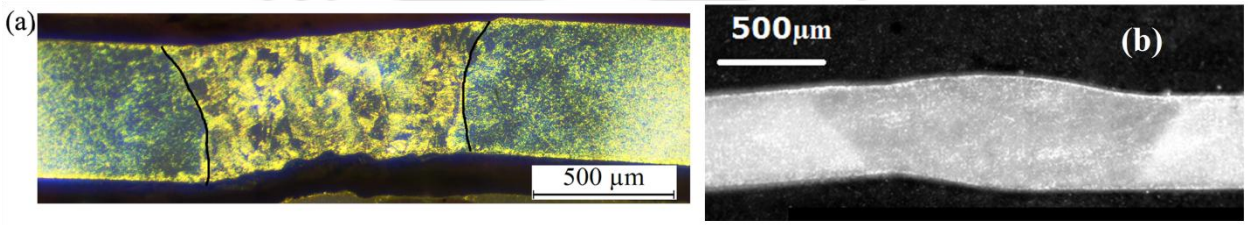

Fig. 4.54 Macrographs at welding conditions of 53.3 J/mm heat input per unit length: (a) laser weldment; (b) microplasma welding.

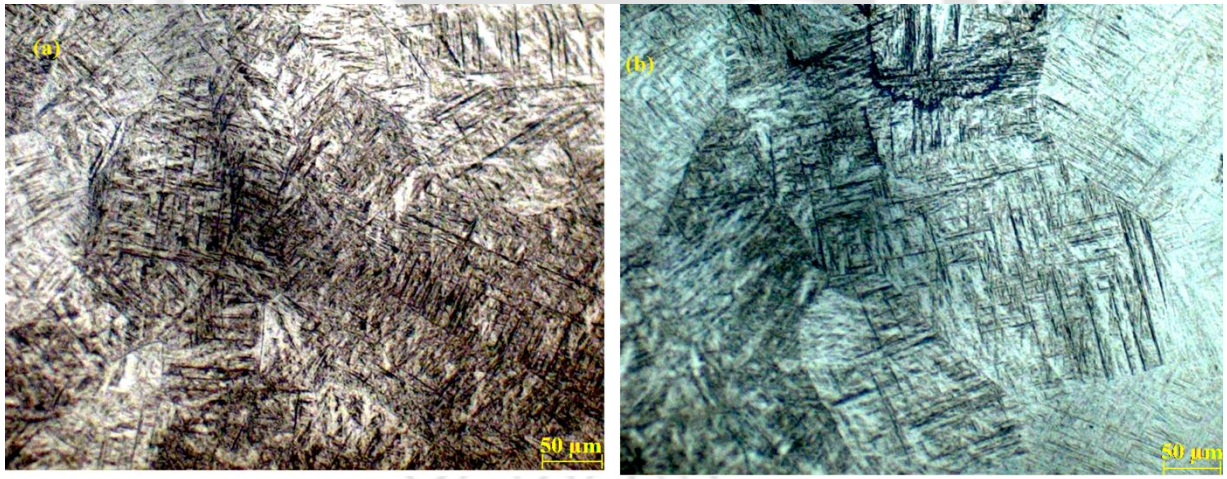

Fig. 4.55 Micrographs at welding conditions of 53.3 J/mm heat input per unit length: a) laser weldment; (b) microplasma welding.

4.5 Summary

A brief experimental investigation is undertaken in the present work to establish the microwelding processes for different materials in butt joint configuration. The micro plasma

welding is undertaken for wide variation of welding conditions for 500 μm of Ti6Al4V alloy. Low carbon steel and stainless steel are also welded by this method. The welding current is varied from 7 - 20 A and welding speed to 2 - 7 mm/s to get a defect-free weld joint. A study on laser microwelding using pulse Nd:YAG laser is also carried out on 500 μm thick Ti6Al4V alloy in butt joint configuration. The influence of laser scanning speed and pulse energy is analyzed to produce a defect-free joint. High peak power is actually dampen by pulsation of laser cratered to use in microwelding process. The feasible range of process parameters like laser scanning speed of 3-7 mm/s and peak power of 1-5 kW producing high quality weld joint using other favorable conditions that impede in oxidation of titanium alloy. The primary objective of experimental investigation is to develop an envelope of suitable combination of process parameters required for a successful weldment having good strength and ductility. The influence of process parameters on the weld geometry, weld-induced distortion and mechanical properties are studied systematically. It is thus obvious that the microstructure of titanium alloy greatly influences the mechanical properties of the welded joint. Although the solidification kinetics of Ti6Al4V is complex in nature, the direct relation with mechanical properties is more orthodox for very thin sheet where 2D heat transfer is appropriate than more complex 3D thermo-fluid material transport for thick sheet materials. Overall, the relation between heat transfer phenomena in terms of heat input and the mechanical properties is established in the present work through the microstructural characteristics at different welding conditions. Probably the established relation is not too drastic for thin sheet welded titanium alloy. The evidences from the weld macrographs and aspect ratio of weld dimensions generally confirm to the conduction mode laser welding. The experimental results suggested that the heat input per unit length is an important parameter for micro welding process. The experimentally measured weld pool dimensions are subsequently used to validate the calculated results from the numerical heat transfer model.

Chapter 5

Results and Discussions

5.0 Introduction

The present chapter describes the computed results of temperature and velocity field in microwelding processes obtained by finite element based numerical models. The numerical results are validated against in-house generated experimental data and also from independent literatures. The finite element software ABAQUS has been utilized to generate a sequentially coupled thermo-mechanical model to simulate plasma and laser microwelding processes by considering conduction mode heat transfer analysis. A well tested thermo-fluid model is also used to predict material flow field in laser microwelding process. A finite element based 3D heat transfer model is developed for ultra-short pulse laser processing using non-Fourier heat conduction. At first, the model has been calibrated using proper geometric shape, meshing, selecting material properties, optimizing the time step or load step. Finally, the numerical results are compared with experimentally measured results.

5.1 Model Geometry and Material Properties

The numerical simulation of temperature distribution and final weld dimensions in fusion welding greatly depends on the consideration of appropriate material properties. The accuracy of the computed results also relies on the appropriate mesh size and element type considered for the solution domain. The present section describes the properties of Ti6Al4v alloy, low carbon steel, and stainless steel used in numerical model. The model geometry and their mesh size considered for the 3D analyses of micro welding process are also presented in this section.

5.1 1 Model geometry

The geometrical configuration of the problem in Cartesian coordinate system along with the meshing pattern is shown in Fig. 5.1. The geometrical size of the welding plate and the simulation domain is same. Due to the intense heat source, high temperature gradient exists in the neighbourhood of welding pool. The welding line of microwelding is so narrow that sufficiently fine mesh is required to capture steep temperature gradient. This often leads to an excessive discretization and consequently a huge computational time. The heat input is constricted to a very small region without any effect towards the far end and thus the whole domain is divided into a non-uniform grid system. The application of constraint condition is significant in numerical modelling of welding process since it could affect both thermal and mechanical responses of the plate especially in case of thin sheets joining. Literature indicates that the maximum temperature increases by 3% while the depth of the weld pool got reduced when constrained was considered properly [Kohandehghan and Serajzadeh, 2011]. Moreover, utilizing fixtures leads to a different distribution of plastic strain and residual stress values.

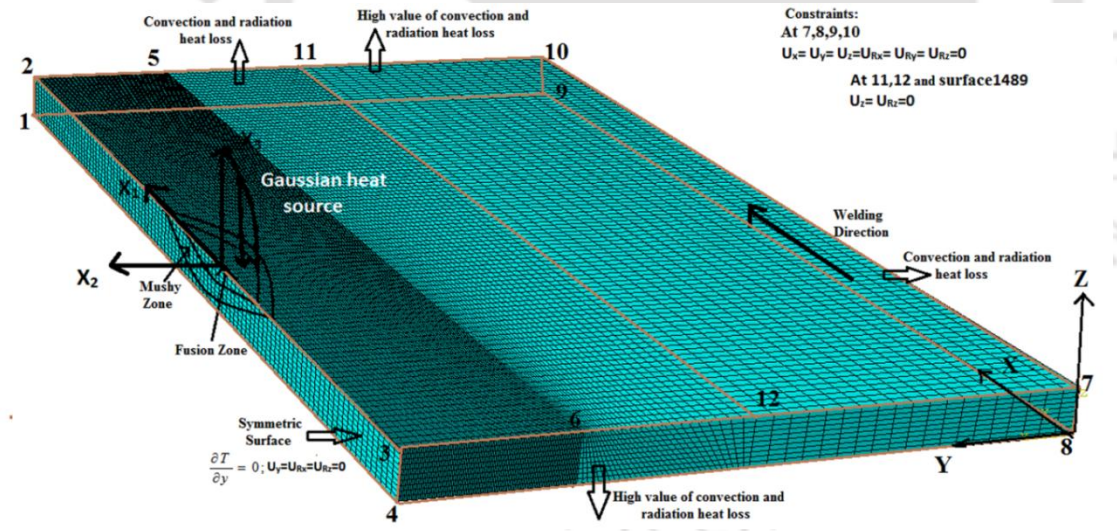

Fig. 5.1 Schematic representation of the solution geometry and boundary interactions.

5.1.2 Material Properties

The present section describes the properties of Ti6Al4v alloy, low carbon steel, and stainless steel used in numerical model. To consider the effect of fluid flow an artificial increase

in the value of the thermal conductivity in the weld pool is considered. The thermal conductivity for the simulation is expressed as

$$k = \begin{cases} k_0, & T < T_m \\ k_0 + k', & T \geq T_m \end{cases} \quad (5.1)$$

where k_0 is the thermal conductivity used while k' is the additional value due convective material flow in the weld pool, T_m is the melting point temperature. The thermal effects due to solidification of the weld pool are modelled by incorporating the latent heat for fusion. The constant values of various material properties used in computation is described in Table 5.1.

Table 5.1 Constant material properties at ambient temperature [Mills, 2000].

Properties	Ti6Al4V alloy	Stainless steel	Carbon steel
Density (Kg/m^3)	4430	8000	7850
Expansion coefficient (μm/mK)	10.5	17.2	12
Latent heat of fusion (kJ/kg)	370	260	270
Melting temperature (K)	1933	1723	1773
Solidus temperature (K)	1877	1673	1723
Poisson's ratio	0.3	0.33	0.29

The temperature dependent thermal properties for simulation are considered from literature [Mills, 2000; Lee and Lin, 1998] and are plotted in Fig. 5.2(a). The coefficient of thermal expansion is assumed constant ~ 10.5 x 10^{-6} K^{-1}), with temperature-dependent Young's modulus (Fig. 5.2.b) and constant Poisson's ratio (~ 0.3). The temperature dependent yield stress and tangent modulus are depicted in Fig. 5.2(b). The values for both the modulus and yield stresses are considered as constant beyond 1373 K. Annealing effect is also taken into account i.e. the effect of prior work hardening is removed by setting the equivalent plastic strain to zero.

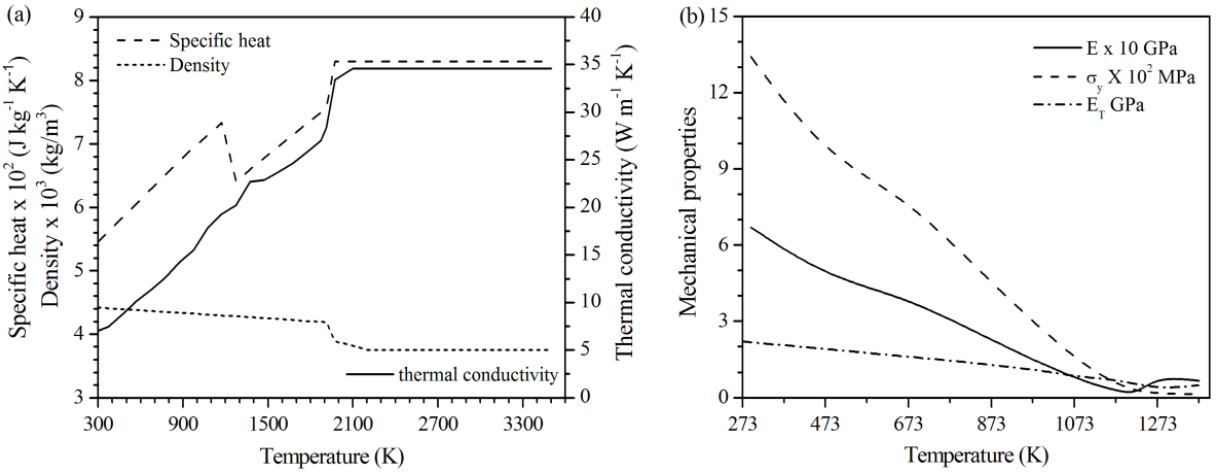

Fig. 5.2 Temperature dependent properties of Ti6Al4V: (a) thermal properties and (b) mechanical properties.

Figure 5.3(a) shows the temperature dependent thermal property of SS304 [Zhu and Chao 2014] as considered in the present work. The value of specific heat linearly increases from the room temperature upto 1700 K. The material assumes a mushy state at around 1700 K and the value of specific heat increases from 691 to 789 $Jkg^{-1}K^{-1}$. The value of the thermal conductivity increases linearly till 1700 K and reduces from 35.6 to 17.6 $Wm^{-1}K^{-1}$ at that temperature. The thermal conductivity again increases linearly from 17.6 to 22.0 $Wm^{-1}K^{-1}$ in the range of temperature from 1700 K to 3000 K. The temperature dependent mechanical properties are shown in Fig. 5.3(b)-(c) [Cheng, 2009]. The bilinear isotropic hardening model was employed and the model parameters were obtained through the fit shown in Fig. 5.3(c).

Figure 5.4(a) shows the temperature dependent thermal properties of low carbon steel [Mills, 2000, Yilbas *et al.*, 2010]. The value of the thermal conductivity reduces almost linearly up to 1073 K and becomes almost constant thereafter. The value of specific heat shows steep changes in the temperature range 873 to 1073 K. The temperature dependent mechanical properties are shown in Fig.5.4(b)-(c) [Yilbas *et al.*, 2010, Deng and Murakawa, 2008a].

5.2 Calibration of Numerical Model

The computed results of numerical model are sensitive to the element size, the distribution of elements within the solution geometry, the type of element used and the time steps or load steps. Thus, correct prediction of these parameters is necessary to improve the accuracy of the numerical model.

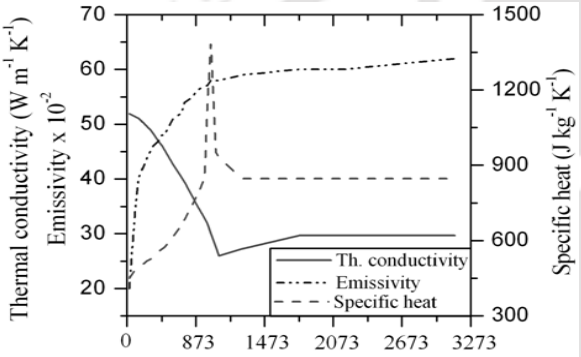

Fig. 5.4 Temperature dependent properties of low carbon.

5.2.1 Selection of mesh size

Mesh optimization in finite element simulation is one of the most important tasks. The type and number of elements used for the weld sample plays a vital role in accurate prediction by the simulation. The consideration of the element type, size and thus the number of elements is very crucial for the accuracy of the FE model. A very rough mesh may be too stiff to allow the structure to

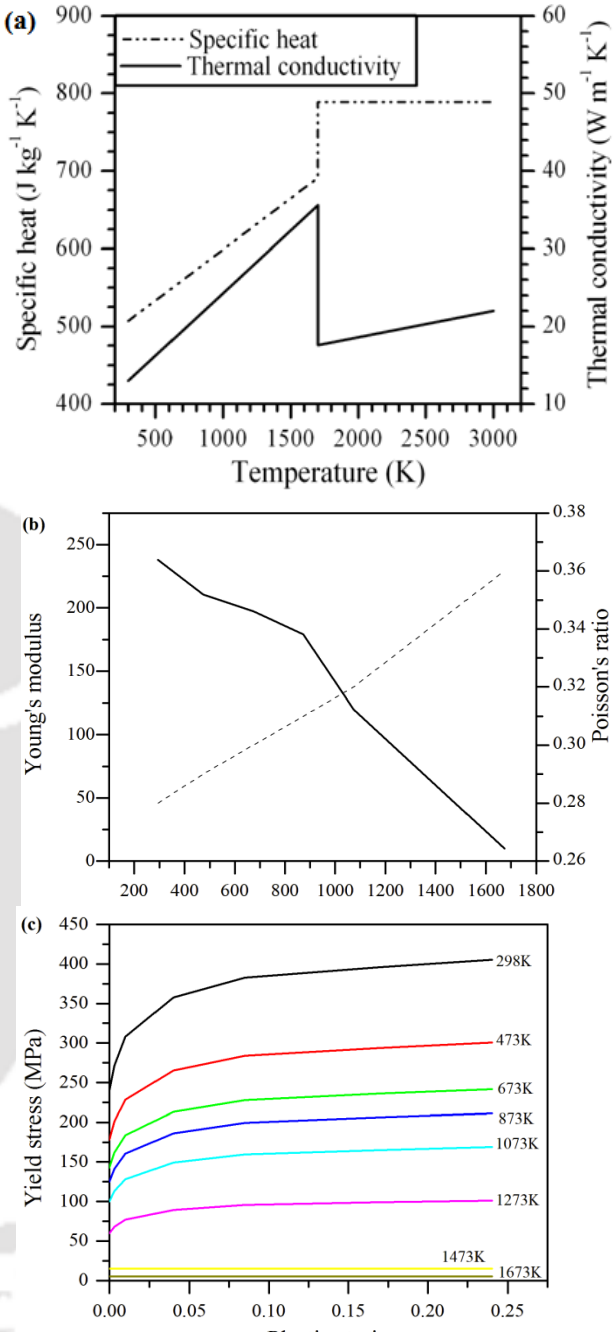

Fig. 5.3 Temperature dependent properties of SS304: (a) thermal properties [Zhu and Chao, 2004]; (b) mechanical properties; (c) Yield stress [Cheng, 2009].

respond to the thermal load in a proper way leading to wrong results. Whereas, too fine mesh in the model leads to a non-solvable problem due to the limited capacity of computer. Therefore, choosing optimum mesh for the model is one of the important steps to get reliable and accurate results.

For the heat-transfer analysis, the maximum temperature during welding was chosen to be the key parameter for the analysis [Goldak and Akhlaghi, 2005]. The model is meshed non-uniformly to minimize the simulation time by reducing the total number of nodes. Fine meshes are created in the region near the heat flux region while mesh size decreases gradually towards the outer portion of the model. Figure 5.4 shows a typical mesh considered for 3D heat transfer analysis. As the heat source is symmetric in the transverse direction, only a half section is considered for analysis where the original weld interface acts as the plane of symmetry. The model is divided into three parts based on mesh sizes. Constant mesh of smaller elements of size 0.10 mm x 0.10 mm with ten elements along the thickness is adopted upto 5 mm from the centre of the heat source as shown in Fig. 5.5 (upto the line 5-6) for micro plasma welding while 0.05 mm x 0.05 mm for laser microwelding. The mesh is progressively made coarser away from the beam to reduce the total number of nodes and elements and hence, the computational time. The solid element type used in the thermal analysis is an 8-node brick DC3XD8 diffusive heat transfer. The mechanical analysis employs similar geometry and meshing of thermal model. 8-noded linear brick C3D8 elements with reduced integration are used for mechanical analysis.

5.2.2 Selection of time step

The transient analysis in numerical modelling is required to simulate the micro welding which provides a natural way of coping with the non-linearity associated with the process. The transient analysis is carried out by dividing the total solution time into a large number of time increments. The time increment in a transient analysis can be controlled directly, or the software can control it automatically. The time increments can be selected automatically based on a user-prescribed maximum allowable nodal temperature change in an increment, $\Delta\theta_{max}$. The software (ABAQUS) will restrict the time increments to ensure that this value is not exceeded at any node (except nodes with boundary conditions) during any increment of the analysis. If $\Delta\theta_{max}$ is not

specified, fixed time increments equal to the user-specified initial time increment, Δt_0, will be used throughout the analysis.

The converged solutions of temperature are henceforth attempted in each of these small time steps. The computational time and the rate of convergence are greatly influenced by the choice of time step in transient analysis. In transient analysis with second-order elements there is a relationship between the minimum usable time increment and the element size. The integration procedure used in ABAQUS for transient heat transfer analysis introduces a relationship between the minimum usable time increment, element size and the material properties like

$$\Delta t_c \leq \frac{(\Delta d_n)^2 \rho C}{k} \tag{5.2}$$

where Δd_n is the minimum distance between the nodes, Δt_c the critical time step, and k, ρ and C represent the thermal conductivity, density and specific heat respectively at room temperature. If time increments smaller than this value are used in a mesh of second-order elements, spurious oscillations can appear in the solution, in particular in the vicinity of boundaries with rapid temperature changes [Hughes, 1977]. These oscillations are nonphysical and may cause problems if temperature-dependent material properties are present. In transient analyses using first-order elements the heat capacity terms are lumped, which eliminates such oscillations but can lead to locally inaccurate solutions for small time increments. If smaller time increments are required, a finer mesh should be used in regions where the temperature changes rapidly. It is worth noting that there is no upper limit on the time increment size (the integration procedure is unconditionally stable) unless nonlinearities cause convergence problems.

According to Eq. (5.2), the critical time steps for minimum nodal distance Δd_n = 0.1 mm and 0.05 mm, are 3.0 $x10^{-3}$ s and 6.78 $x10^{-4}$ s respectively for Ti6al4V. In the present analysis, the time step for micro plasma welding is considered as 1.0 $x10^{-3}$ s and for laser welding it is taken as 5.0 $x10^{-4}$ s.

5.2.3 Non-dimensional heat input index

The non-dimensional heat input index considers the combined effect of process parameters and thermal properties of substrate material and is defined by [De and Debroy, 2005]:

$$N_{HI} = \frac{\frac{\eta VI}{\pi r_{eff}^2 U}}{\rho C(T_L - T_o) + \rho L} \quad (5.3)$$

where V, I, η, r_{eff}, U, ρ, Cp, T_L, T_o, and L represent the voltage, current, efficiency, effective arc radius, weld velocity, density of the material, specific heat capacity of the material, liquidus temperature of the material, ambient temperature, and latent heat of fusion, respectively. In Eq. (5.3), the numerator can be expected as the whole incident welding heat source per unit volume. The denominator relates to the enthalpy which is necessary to heat the unit volume of the material from ambient temperature to liquidus temperature. Thus, the parameter embodies the combined effect of the welding process conditions and the material properties for the formation of weld pool. However to calculate the N_{HI}, the superheating of the substrate material beyond the melting is ignored. In several occasions, this non-dimensional heat input index is used to explain the numerical and experimental results.

5.3 Micro plasma welding of Ti6Al4V alloy

A three dimensional finite element based sequentially coupled thermo-mechanical model is developed for micro plasma welding process to analyse the differential influence of process parameters. The numerical simulation is performed considering a moving heat source which accounted the associated physical phenomena such as heat conduction, convection, and radiation heat loss from the surface. The highly conductive backing plate configuration is accounted for suitable heat transfer coefficient by neglecting the contact thermal resistance. The temperature dependent thermal and mechanical properties are considered for the analysis. It is emphasized that the large-displacement theory predicts the distortion satisfactorily for microwelding process as compared to high thickness materials. The characteristics of temperature field, plastic strain distribution and the residual stress are studied from numerical model. Relatively fair agreement between computed weld pool dimensions, time-temperature cycle, and distortion with experimental measurement shows the robustness of developed numerical model for micro plasma arc welding process.

5.3.1 Heat transfer analysis

Three dimensional computed temperature distributions corresponding to weld velocity of 4 mm/s and current 11 A at different locations is depicted in Fig. 5.5. The fusion zone and HAZ zone are represented by isotherm contours where the liquidus and solidus temperature of Ti6Al4V are 1933 K and 1877 K, respectively. The red colour represents the mushy zone bounded by liquidus and solidus temperature. HAZ zone is also represented by contours in the range of 1268 K to 1877 K [Donachie, 2000] since most of the solid state transformation occurs within this temperature range. It is also obvious from the simulation that the heat affected zone is confined in small area and it does not affect other part of the base metal.The peak temperature is achieved is 2273 K. This temperature is well below the vapourization temperature of titanium alloy and hence it can be concluded that the conduction mode heat transfer prevails against keyhole formation within this power density range used for microwelding of 500 μm thick plate. The compatibility of the developed numerical model is verified with experimentally measured results. Fig. 5.6(a)-(c) compares the numerically simulated and experimentally measured weld macrographs for three different cases. The cross-section of full-penetration weld resembles a trapezoidal shape. The shape and size of computed macrographs are well agreed with experimentally measured values. With increase in heat input the weld dimensions increases and the fusion zone becomes more parallel sided. It is also obvious that the fusion zone dimensions and peak temperature increases with current while decreases with increase in welding speed. Fig. 5.6(d) compares the experimentally measured and computed half width dimensions from numerical model. The maximum error is found to ~ 15%.

Figure 5.7(a) shows the comparison of temperature profile obtained by the effect of fixture at a distance of 1mm from the weld line for welding condition of 65.5 J/mm. This comparison is carried out so as to show the importance of using high heat transfer co-efficient at the interface of copper-Ti6Al4V while simulating the welding process. It is reflected that if the fixture effect is neglected, the cooling rate is greatly slowed down. The average cooling rate is calculated between the temperature where the dissolution of the primary α (940K) takes place and the β transus temperature (1273K) [Fan *et al.*, 2005]. It is estimated that the average cooling rate is around 610 K/s using copper fixture effect which is almost equal to the critical cooling

rate (683 K/s) of TiAl4V for a specific phase transformation [Poorhaydari *et al.*, 2005; Ahmed and Rack, 1998]. However, the typical cooling rate is

~ 100 K/s when fixture effect is neglected. This is because of the conductivity of copper that greatly increases the cooling rate of the material. Figure 5.7(b) shows the comparison between the temperature profile obtained by simulation considering the fixture effect and the experimental result. It is obvious that the temperature profile closely resembles to that by experiment and indicates the robustness of the numerical model.

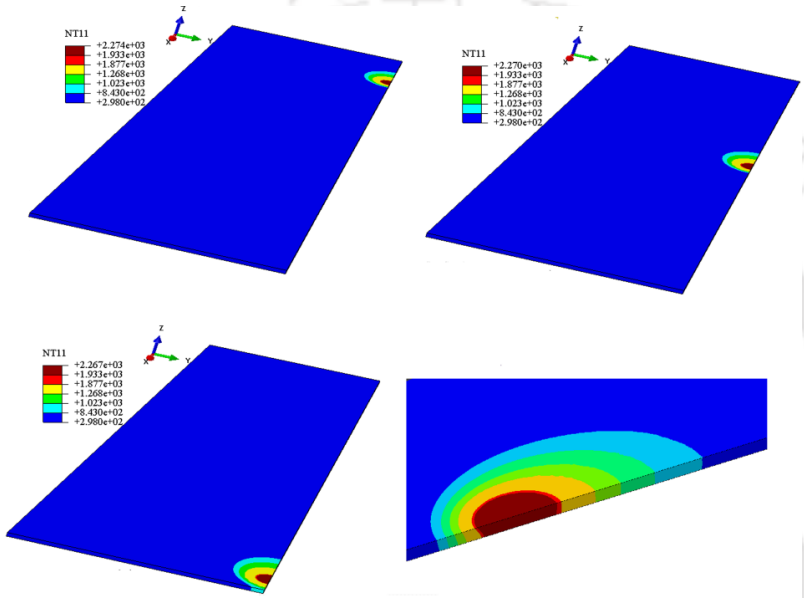

5.5 3D computed temperature distribution corresponding to velocity of 65.5 J/mm at different locations of the solution geometry.

Figure 5.8(a) shows the temperature profile along the weld line between the top and bottom surfaces. It is obvious that the peak temperature value does not vary much between the top surface and the bottom surface. This is due to the small thickness even temperature distribution takes through thickness direction. This confirms that angular distortion is insignificant in the present case [Deng *et al.*, 2013] as the temperature gradient through thickness is very less. It can also be observed that the temperature history curves of the two surfaces have no difference. There is rapid rise and drop of temperature once the peak temperature is reached i.e. the welding torch passes away. Also the temperature rises gradually from the start point and remains steady through the length of the plate and abruptly increases at the end point due to presence of edge. Figure 5.8(b) shows the temperature profile along the transverse direction (Y-

direction) in the middle of the plate. It is seen that peak temperature is highest at the centre of the plate and gradually deceases away from weld line. The temperature reaches to the ambient at about a distance of 6mm from the weld line. This indicates that the heat is distributed in a very small area and the cooling rate decreases as the peak temperature decreases.

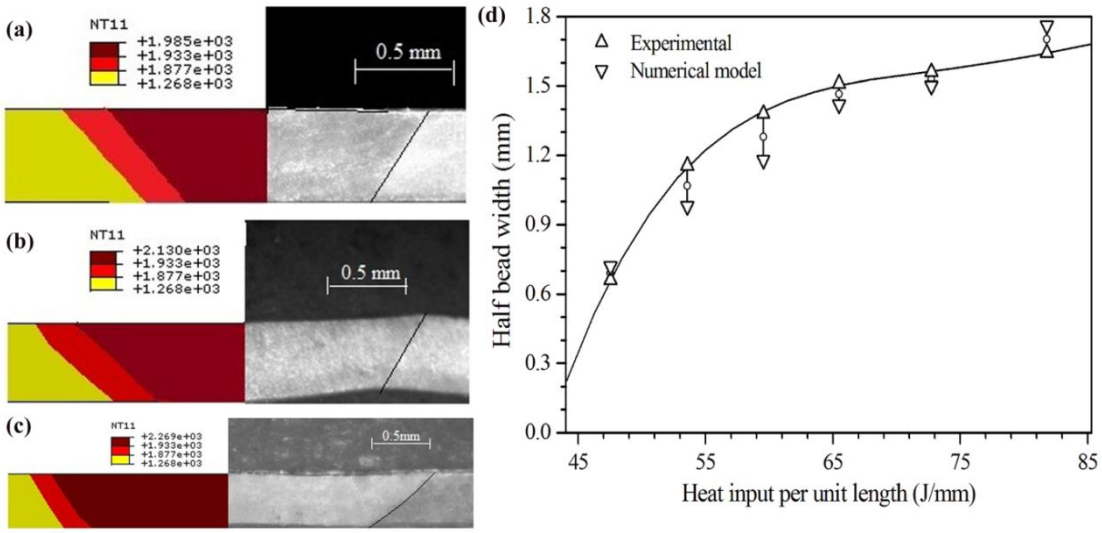

Fig. 5.6 Comparison of experimental (right) and computed (left) weld pool at welding conditions of (a)10 A and 5.26 mm/s, (b) 59.52 J/mm, (c) 65.5 J/mm; (d) Comparison between experimentally measured and computed half width dimensions.

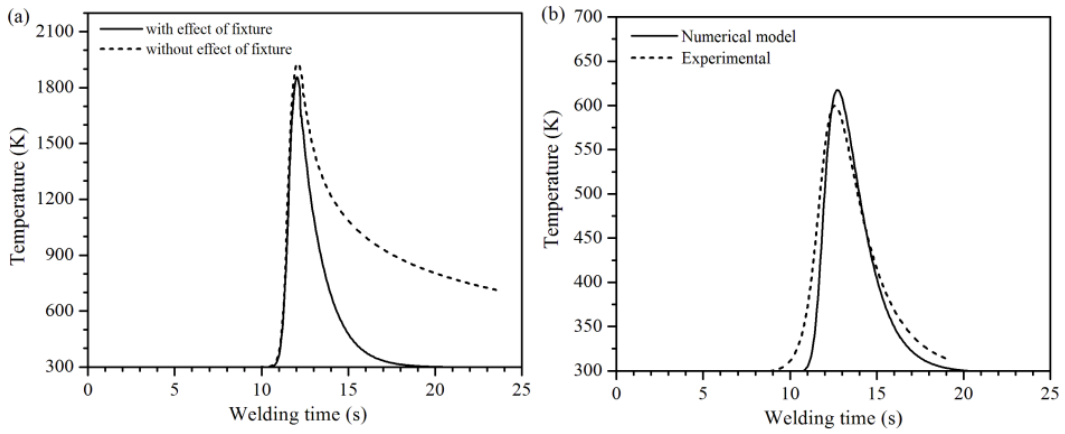

Fig. 5.7 Temperature profile at welding condition of 65.5 J/mm: (a) effect of fixture in simulation, (b) comparison between experimental and computed profile.

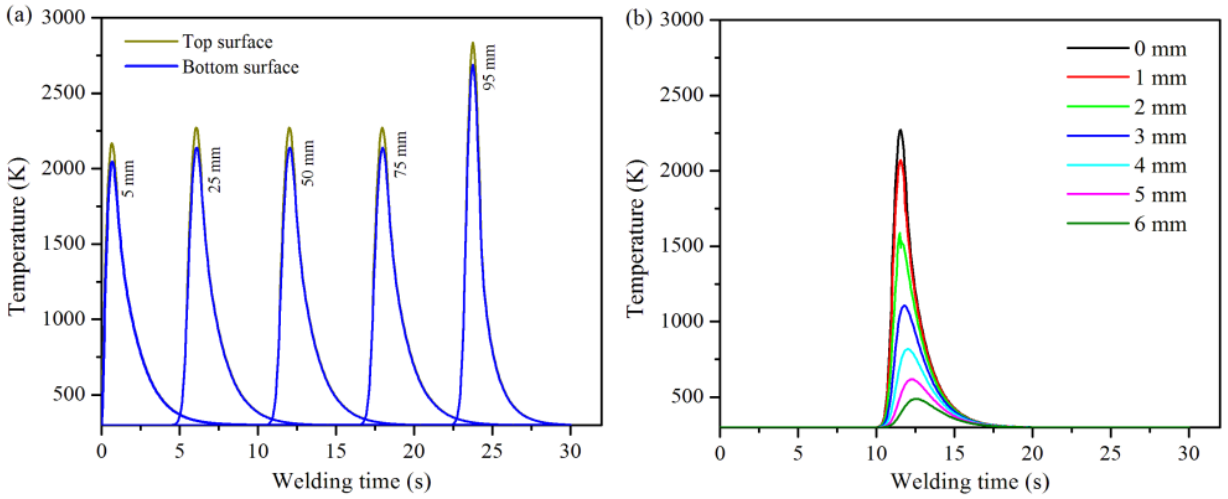

Fig. 5.8 Temperature profile between the top and bottom surface at welding condition of 65.5 J/mm: (a) along the weld line, (b) along the transverse direction at the middle of plate.

The numerical heat transfer model is utilized to demonstrate its capability in computing cooling rate (CR). The quality of the final weldment is greatly dependent on the welding process, the peak temperature reached, the thermal histories, and cooling rates. A quantitative knowledge of cooling rate in and around the weld zone is useful for understanding phase transformation kinetics which influences the final microstructure and mechanical properties of the joint. To keep the calculations simple, the thermodynamics and kinetics of the solidification process are not incorporated and the degree of undercooling is assumed as zero. Figure 5.9(a) depicts the estimated time-temperature history of micro plasma welding corresponding to three different heat input at the centre of the weld line. The cooling rate is estimated by the ratio of change in temperature with change of time and is defined by:

$$CR = \frac{dT}{dt} = \frac{T_2 - T_1}{t_2 - t_1} \tag{5.4}$$

where T_2 and T_1 are the temperatures corresponding to time t_2 and t_1 ($t_2 > t_1$). It is customary to note that the rate of change of temperature during heating period is also termed as cooling rate. From Fig. 5.9(a), it can be seen that the cooling rate is initially zero since there is little effect of welding heat source to develop the temperature. When the heat source approaches the point, the cooling rate increases gradually to half of the total welding time. At the half of the total welding time, cooling rate suddenly becomes zero since there is no change in temperature at that time.

The cooling rate further increases, attains maximum value, and reduces thereafter when the heat source moves away from the fixed region. The magnitude of the maximum cooling rate are 1675 K/s, 1496 K/s, and 1053 K/s corresponding to points 44.96 J/mm, 65.6 J/mm and 85.56 J/mm respectively. It is seen that the cooling rate decreases with increase in heat input. Thus, the microstructure that is formed after the welding process is dependent on the cooling rate as a function of the heat input. This explains the formation of different microstructures at the fusion zones for different heat input as reflected in Fig. 4.12 in the previous chapter.

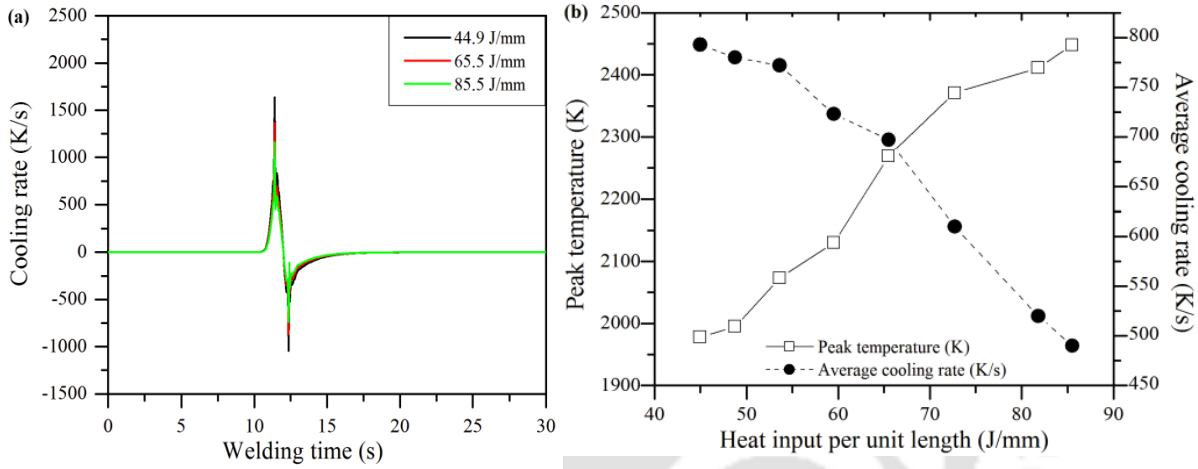

Fig. 5.9 (a) Estimated cooling rate for micro plasma welding corresponding to thermal cycles at the centre of the weldline; (b) Variation of peak temperatures and average cooling rates for different heat input per unit length.

The average cooling rate is calculated between the temperature where the dissolution of the primary α (940K) takes place and the β transus temperature (1273 K) [Fan *et al.*, 2005]. The average cooling rate at the fusion and peak temperature attained for different heat input estimated from the numerical simulation is demonstrated in Fig. 5.10(b). It is seen that the peak temperature increases with heat input as greater amount of heat is available for melting. However, the temperature is below the vaporization temperature of Ti6Al4V alloy. It is observed from Fig. 5.10(b) that cooling rate decreases with heat input. The average cooling rate is ~790 K/s for 44.96 J/mm while ~472 K/s for 85.5 J/mm. The variation of microstructure with heat input is reflected in Fig. 4.12 (Chapter 4). The critical cooling rate of Ti6Al4V for a specific phase transformation is 683 K/s [Ahmed and Rack, 1998]. If the cooling rate is higher than the

critical value, diffusion-less martensitic transformation occurs. While when cooling rate is less than the critical cooling rate, the transformation is diffusion controlled nucleation and growth process of secondary lamellae α.

The variation of microstructure in the different zones can be attributed to the heating and the cooling cycle of Ti6Al-4V alloy. At the end of solidification, the structure is completely beta. As the cooling process commences, transformation of beta to alpha occurs at temperatures below the alpha solves. The cooling rate is found to be about 707 K/s for a heat input of 65.5 J/mm at the weld line which is sufficient to form a martensitic structure [Ahmed and Rack, 1998]. The microstructure of the fusion zone consists mainly of coarse acicular structure with prior beat boundary (Fig. 4.12c). Such structure exhibits better ductility and acceptable strength level [El-Batahgy and DebRoy, 2014]. The transformation from beta to alpha in the present process occurs under moderate cooling rate and low heat input resulting in less amount of alpha prime martensite. The average cooling rates are calculated as 610 K/s, 542 K/s, 480 K/s at 1 mm, 2 mm, 3 mm from the weld line respectively corresponding to heat input of 65.5 J/mm. Also the material is heated to beta transus less than 3 mm from weld line. Thus no transformation occurred after 3 mm from the weld line. The HAZ zone consists of a mixture of primary alpha and transformed beta containing acicular alpha (Fig. 4.13). Thus, the cooling rate and peak temperature have a definite effect on microstructure developed.

5.3.2 Distortion and residual stress

The simulation for two different cases is presented to predict the residual stress and distortion (Eq. 3.14 of Chapter 3). The large deformation theory takes into account the non-linearity in deformation that mainly captures the minute deformation in a localized zone (Case – B). Since deflection is symmetrical along the weld line, the simulation for half of the plate is considered. To validate the model, the measured data for welding deformation (displacement along Z-direction) are compared with computed results for both the cases**.** Figure 5.10 shows the contours for the out of plane deformation computed for two different cases under the welding conditions of 4 mm/s and 11 A. The deformation mode for both the cases is similar and is of convex-concave type that is supported by experimental observation. The deflection is measured by considering the centre of the weld line as the reference point. However, the magnitudes of deflection are much smaller in case A. The maximum measured deflection for the same welding

condition is 4.11 mm at a point 5 mm from endpoint along the weld line. The maximum deflection is about 3.45 mm for case B which is comparable to measured values. Figure 5.11 shows the comparison of deflection for case A and case B with measured values along the weld line and corresponding to a welding conditions of 4 mm/s and 11 A. It can be concluded that the deflection pattern is same for all three cases i.e. it is of higher values at the ends while minimum at the centre of the weld line. Also deflection is slightly greater towards the end of the weld line than the start point for all the cases. It is also observed that deflection values predicted by case B are much close to the corresponding experimental values. However, the experimental value is significantly larger than the numerical result computed by case A. Thus, it can be concluded that for simulation of very thin plate it is necessary to consider both geometry and material nonlinear behaviour. Case B which takes into account this nonlinearity could closely predict the welding deformation even though there is buckling.

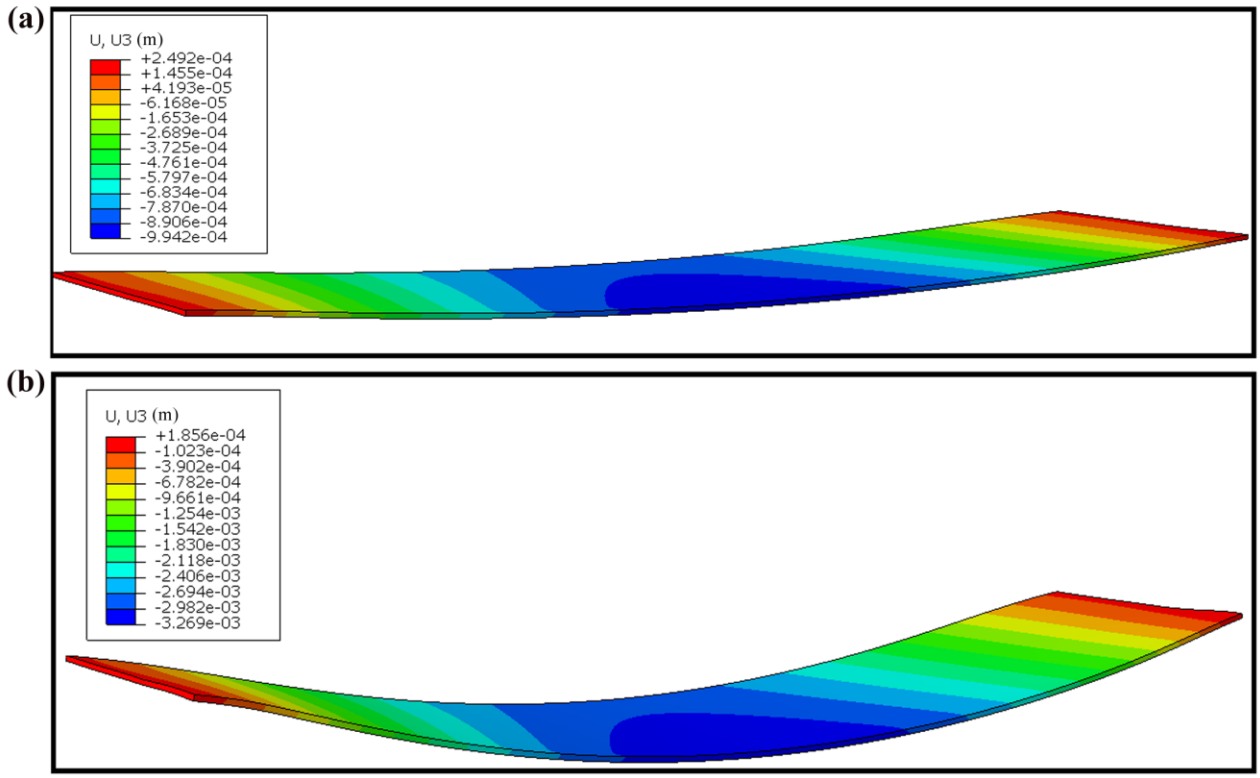

Fig. 5.10 Distortion pattern at welding speed 4 mm/s and current 11 A: (a) Case A - small deformation theory and (b) Case B – large deformation theory.

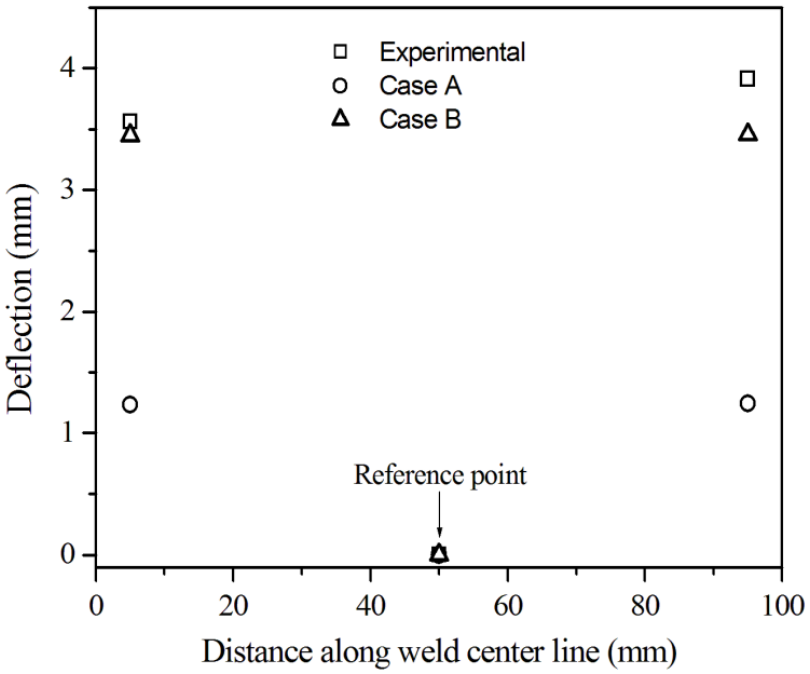

Fig. 5.11 Comparison of deflections at welding speed of 4 mm/s and current 11 A.

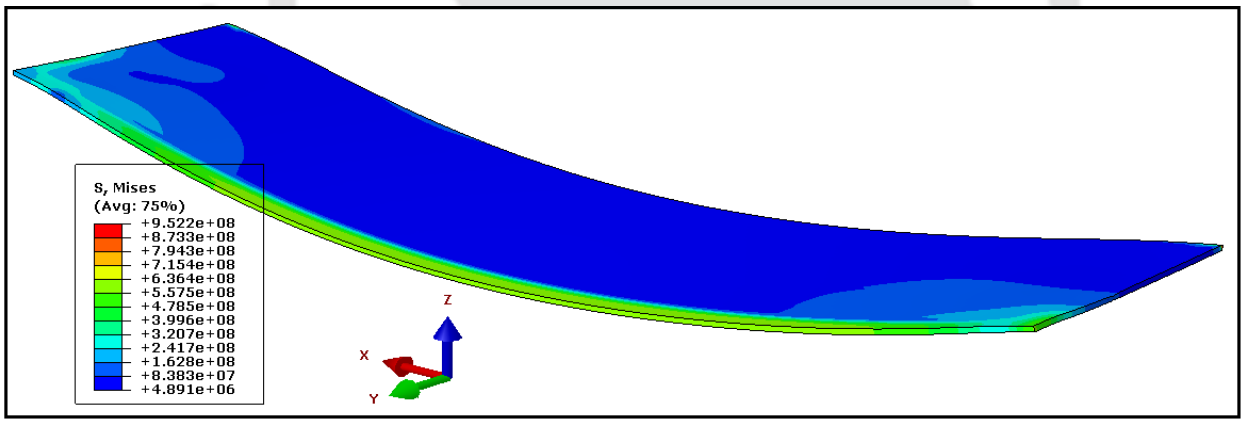

Fig. 5.12 Contour for von-Mises stress.

The residual stresses and plastic strain simulated for Case B is presented corresponding to welding conditions of 4 mm/s and 11 A. Figure 5.12 shows the contour for von-Mises stress for micro plasma welding corresponding to welding conditions of 4 mm/s and 11 A. Figure 5.13(a) shows the residual stress distributions at the top of the surface along X-axis. The material is subjected to significantly large longitudinal stress which is about ten times greater than transverse stress and almost equal to the total (von-Mises) maximum residual stress. The

longitudinal stress is almost uniformly distributed along the X-axis having a maximum value of 623 MPa in the weld joint area which almost reaches the material yield strength. It reduces to zero at the free surfaces of the starting and ending edges of the welding line. The weld joint experiences large longitudinal tensile stress. The transverse stress is negative towards the start and end of the weld indicating compressive residual stress. It gradually increases and become tensile along the length of the weld line. Thus, the weld joint is subjected to significant tensile stress along the length of the weld and plastic deformation. Figure 5.13(b) shows the distribution of residual stress on the top surface along the transverse direction (Y-direction) in the middle of the plate. Residual stresses exhibit a sharp decreasing trend in the area near the weld region (< 3 mm) and become almost zero away from the weld line. It is realized that the longitudinal stress has a high tensile value near the weld line due to the severe restraint condition and becomes compressive away from the weld line. However, the tensile stress is much higher than the compressive stress. This may be the primary reason for buckling of the plate. The transverse residual stress distribution is almost constant with respect to the longitudinal stress distribution. It can be concluded that most of the stress in the specimen is mainly due to the longitudinal stress and mostly concentrated in the weld area.

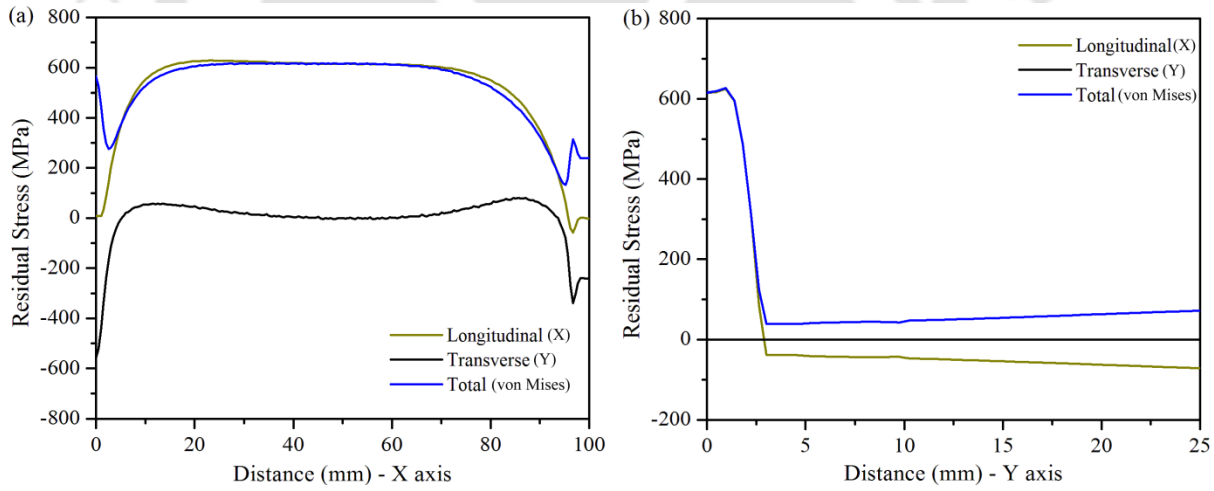

Fig. 5.13 Residual stress distributions at welding conditions of 4 mm/s and 11 A: (a) along the weld line and (b) along transverse direction at the middle of the plate.

Figure 5.14(a) shows the longitudinal stress distributions at the top and the bottom surface of the middle cross-section along Y-axis of the plate. The stresses are found to be different on the top surface and that of the bottom surface. The longitudinal residual stresses on the top surface are higher than those on the bottom surface within 3 mm distance. In the rest of the region, the longitudinal stress is positive before 4 mm distance on the top surface, becomes negative afterwards, and lower in magnitude as compared to bottom surface. On the top surface, the stresses are tensile in nature below 3 mm while compressive in the rest of the region. The tensile stresses are generated on the bottom surface that gradually decreases below 4mm and increases afterwards. This is the reason for significant longitudinal and transverse bending causing large out-of-plane deformation. Figure 5.14(b) represents the longitudinal and transverse plastic strain distribution (at the middle cross-section) along the transverse direction. The plastic zone is much smaller and the value of transverse plastic strain is larger than that of longitudinal plastic strain. The reason is that the restraint density in the longitudinal direction (parallel to welding direction) is stronger than that in the transverse direction (perpendicular to welding direction). The contours for plastic strain are represented in Fig. 5.15. It shows that the plastic strain is accumulated in very small region.

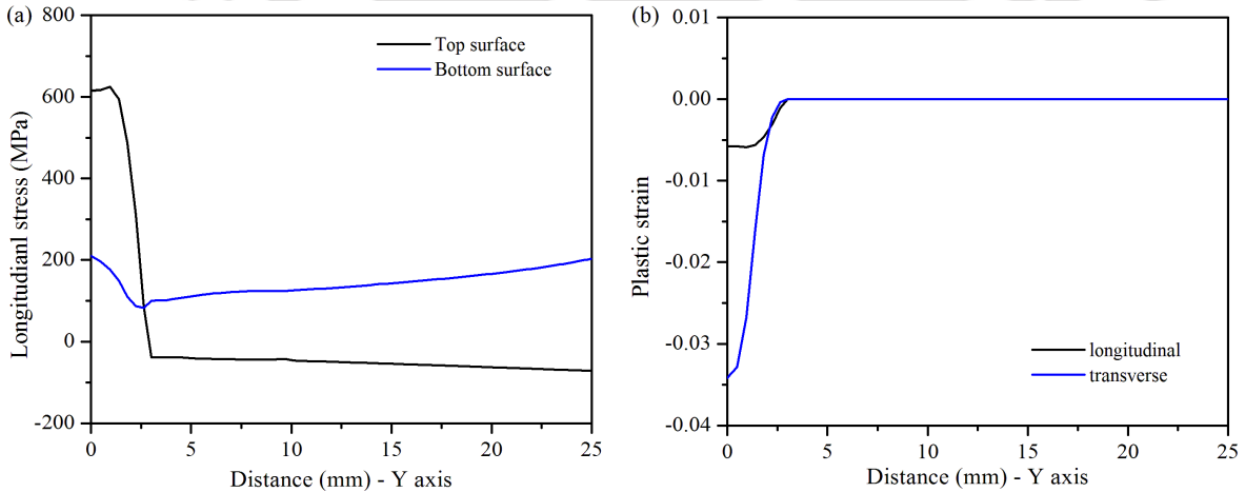

Fig. 5.14 (a) Longitudinal stress at the top and the bottom surface of the middle cross-section; (b) Longitudinal and transverse plastic strain distribution.

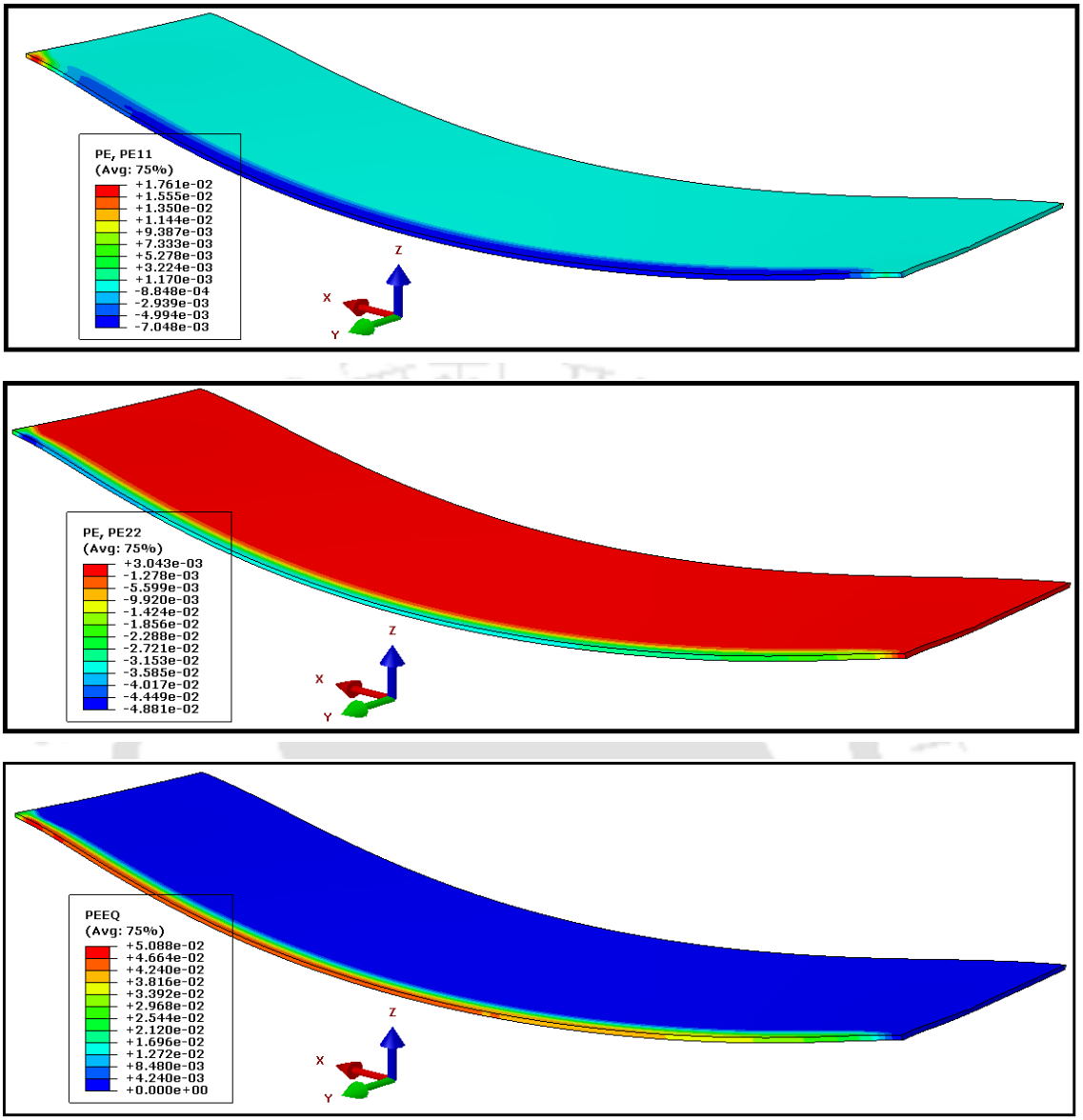

Fig. 5.15 Contours for plastic strain: (a) longitudinal plastic strain; (b) transverse plastic strain; (c) resultant magnitude of plastic strain.

Thus, the present methodology developed for microwelding of 500 μm thick Ti6Al4V plate is good alternative for joining of thin sheets. The prediction of temperature and distortion field using developed numerical model is relatively better for micro scale application. The accuracy of numerical model can be further improved by incorporating the residual stress generated due to volumetric change and transformation induced plasticity.

5.4 Micro Plasma Welding of Steels

Simulation is also carried out to predict the temperature field and distortion in plasma microwelding of SS304 stainless steel and low carbon steel. The analysis is performed in a comparative mode. Three dimensional computed temperature distribution corresponding to heat input of 59.4 J/mm for both the material is depicted in Fig. 5.16. The fusion zone and HAZ zone are represented by isotherm contours. The maroon and red color represents the fusion zone and mushy zone bounded by liquidus and solidus temperature respectively. It is obvious that the heat affected zone is confined in small area and it does not affect other part of the base metal. The peak temperature is achieved both the material is well below the vapourization temperature and hence it can be concluded that the conduction mode heat transfer prevails against keyhole formation within this power density range used for microwelding of 0.5 mm thick plate. It is also reflected that the temperature is more distributed in case of low carbon steel than the SS304. This is due to the fact that the thermal diffusivity of low carbon steel is higher as compared to stainless steel which leads to wider HAZ as compared to SS304. The peak temperature of SS304 weldment is more as the heat is highly concentrated.

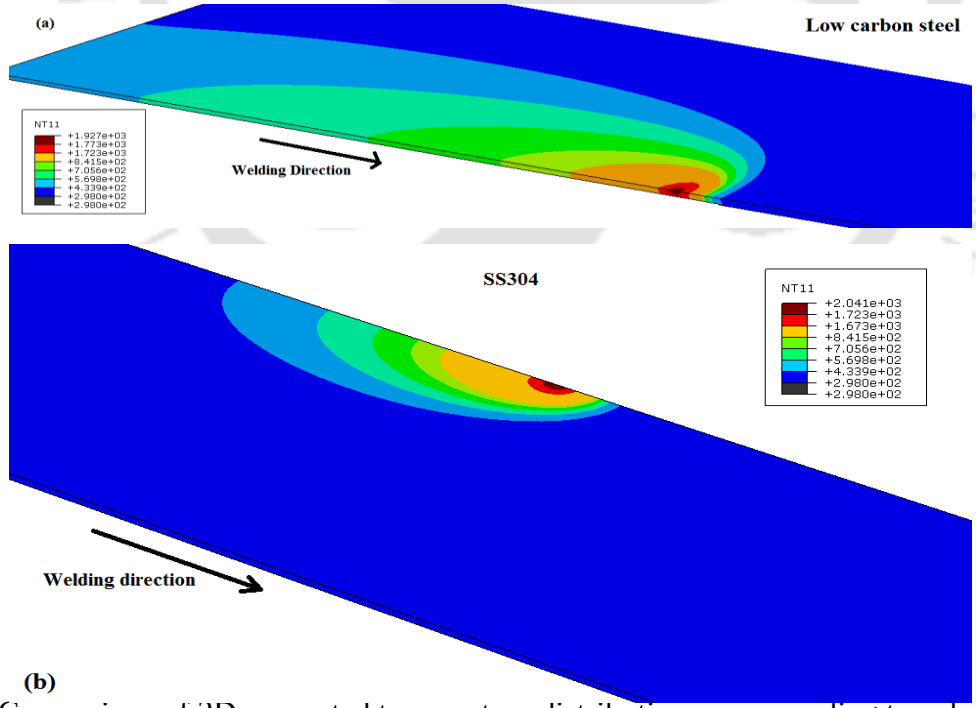

Fig. 5.16 Comparison of 3D computed temperature distribution corresponding to velocity 59.4 J/mm at the centre of the plate.

Figure 5.17 shows the temperature profile along the transverse direction (Y-direction) in the middle of the plate for both the materials corresponding to heat input per unit length of 59.4 J/mm. It is seen that peak temperature and cooling rate is highest at the centre of the plate and gradually deceases away from weld line. It can be also concluded that the temperature is higher for SS304 near the weld line while as we move away from the weld line temperature increases for low carbon steel. The peak temperature and cooling rate is higher for SS304 [Murugan *et al.*, 2011]. There is rapid rise and drop of temperature once the peak temperature is reached i.e. the welding torch passes away for ss304 while more time is needed for cooling in case of low carbon steel. This indicates that the heat is confined in a very small area in case of SS304 compared to low carbon steel.

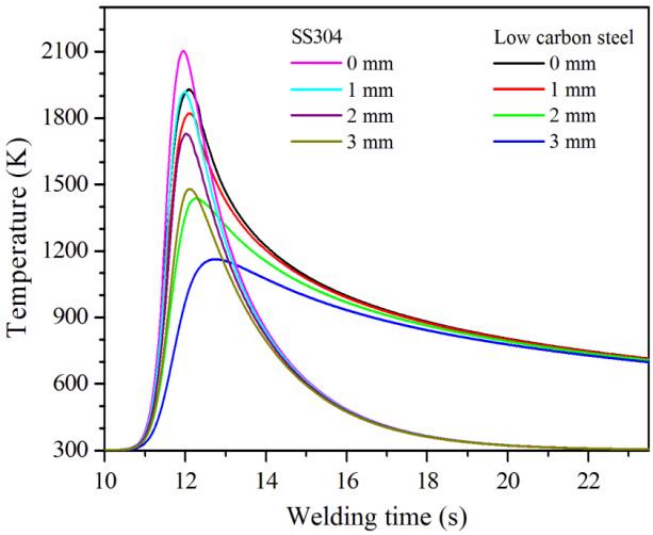

Fig. 5.17 Temperature profile along the transverse direction at the middle of the plate at welding condition of 59.4 J/mm heat input per unit length.

The compatibility of the developed numerical model is verified with experimentally measured results. Figures 5.18(a)-(b) and 5.19(a)-(b) compare the numerically simulated and experimentally measured weld macrographs for two different cases. The shape and size of computed macrographs are well agreed with experimentally measured values for both the materials. With increase in heat input the weld dimensions increases. It is also obvious that the fusion zone dimensions and peak temperature increases with increase in heat input. However, from Fig. 5.19(c) it is seen that the weld bead dimension does not decrease with heat input as in experimental measured widths. This effect is not taken into account as development of reinforcement is not accounted in the numerical modelling.

For simulation of very thin plate it is necessary to consider both geometry and material nonlinear behaviour. The simulation is carried out based on large deformation theory to predict the residual stress and distortion [Deng and Murakuwa, 2008a]. Since deflection is symmetrical

along the weld line, the simulation for half of the plate is considered. Figure 5.20 shows the contours for the out of plane deformation computed for two materials under the welding conditions of 59.4 J/mm heat input per unit length. The deformation mode for both the cases is

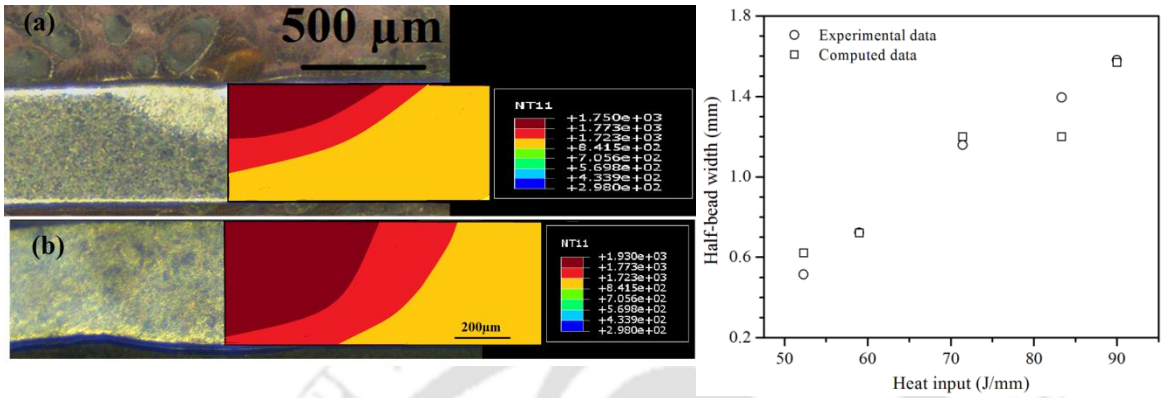

Fig. 5.18 Comparison of experimental (right) and computed (left) weld pool of low carbon steel at welding conditions of (a) 11 A and 5.26 mm/s, (b) 10 A and 4.2 mm/s, (c) Comparison between experimentally measured and computed half width dimensions.

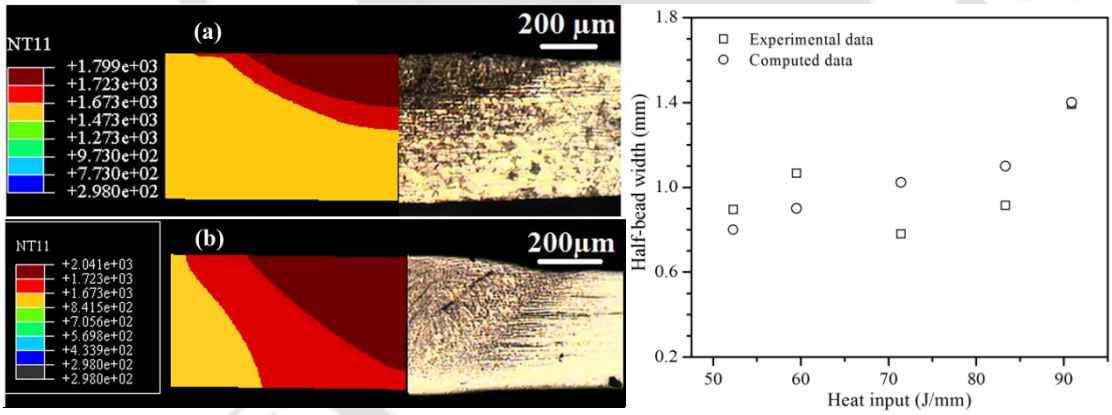

Fig. 5.19 Comparison of experimental (right) and computed (left) weld pool of SS304 at welding conditions of (a) 11 A and 5.26 mm/s, (b) 10 A and 4.2 mm/s, (c) Comparison between experimentally measured and computed half width dimensions.

similar and saddle type of buckling [Wang, *et al.*, 2014] takes place. However, the SS304 weldment (Fig. 5.20b) shows a non-uniform behaviour which is prone to occur in very thin sheet welding process. This result can be attributed to higher thermal expansion coefficient of SS304 which reveals a more realistic pattern for thin plate welding. The deflection is measured by

considering the centre of the weld line as the reference point. The maximum deflection is about 3.5596 and 3.96 mm for low carbon steel and ss304 respectively which is obtained at the edges of the weld line. The comparison of simulated and experimental values of out of plane deflection is shown in Fig. 5.21. Although correlated well with the deflection pattern obtained from experimental measurements, FE simulation predicts smaller values of angular distortions. This may be due to the fact that the effect of phase transformation has been neglected in the current model. The distortion for stainless is more than low carbon steel for the same welding condition.

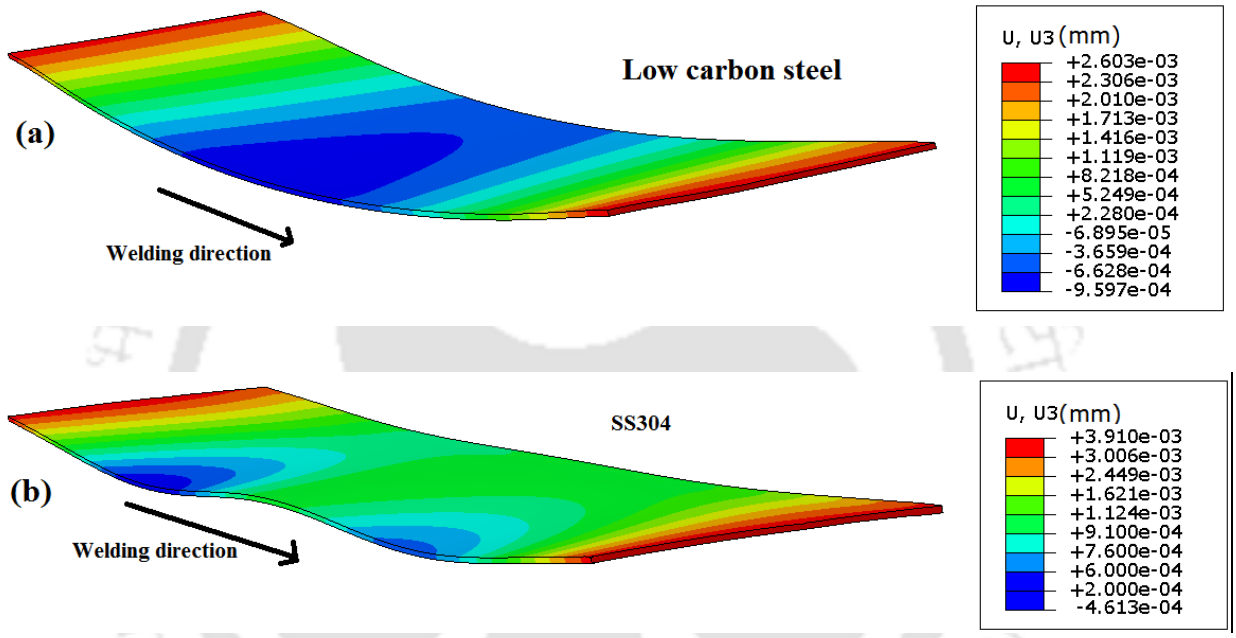

Fig. 5.20 Distortion pattern at welding speed 4 mm/s and current 10 A – large deformation theory (a) Low carbon steel; (b) SS304.

The residual stress patterns developed in low carbon steel and stainless steel weldments are highlighted in this section. Figure 5.22(a) highlights the residual stress developed in the two materials along the weldline on the top surface corresponding to a welding condition of 59.4 J/mm heat input per unit length. Both the materials are subjected to significantly large longitudinal stress which is almost equal to the von-Mises residual stress. The longitudinal stress is almost uniformly distributed along the X-axis having a maximum value of 247 MPa and 289 MPa for low carbon steel and ss304 respectively in the weld joint area, which almost reaches the material yield strength. It reduces to zero at the free surfaces of the starting and ending edges of

the welding line. The weld joint experiences large longitudinal tensile stress. The transverse stress is negative towards the start and end of the weld indicating compressive residual stress. It gradually increases and become tensile along the length of the weldline. In case of low carbon steel the transverse residual stress is uniformly distributed while in case of ss304, the transverse residual stress exhibited two peaks towards the edges of the weld line reaching a maximum value of 98MPa. This may be due the transient nature of temperature distribution near the start and end points of the welding. Thus, it can be deduced that the weld joint is subjected to significant tensile stress along the length of the weld subjecting to plastic deformation. Figure 5.22(b) shows the longitudinal stress distributions at the top and the bottom surface of the middle cross-section along Y-axis of the plate of the two materials. The stresses are found to be different on the top surface and that of the bottom surface. This is the reason for significant longitudinal and transverse bending causing large out-of-plane deformation.

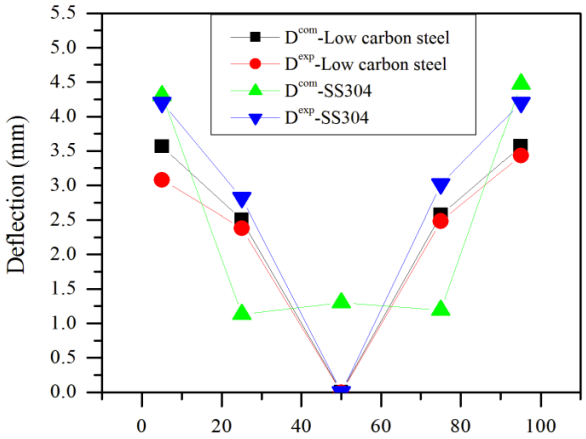

Fig. 5.21 Comparison of deflections along the longitudinal direction at welding condition of 59.4 J/mm heat input per unit length.

Figure 5.23 compares the distribution of residual stresses of both the materials on the top surface along the transverse direction (Y-direction) in the middle of the plate. The distribution in both the materials follow similar pattern. The von-Mises stresses exhibit a sharp decreasing trend in the area near the weld region (<3 mm) and become almost zero away from the weld line. It is also reflected that the longitudinal stress has a high tensile value near the weld line due to the severe restraint condition and becomes compressive away from the weld line. However, the tensile stress is much higher than the compressive stress. The transverse residual stress distribution is very less as compared to the longitudinal stress distribution. It has a maximum value of 6 MPa and 73 MPa for mild steel and ss304 respectively which is obtained in the HAZ region. Thus, it can be concluded that most of the stress in the specimen is mainly due to the longitudinal stress and mostly concentrated in the weld area. It can also be deduced from the

figures that the region of residual stress distribution in stainless steel weld joint is higher than that in mild steel weld joints near the weld area. However the value of residual stress increases in mild steel weldment compared to the stainless steel specimen. This can be attributed to the fact that the temperatures close to weld line are higher in stainless steel weldment while the temperature exhibits a lower value as we move away from the weld line. Additionally, the coefficient of thermal expansion of stainless steel is higher than that of mild steel. Thus, the residual stresses are formed over a larger region in the stainless steel weld joints.

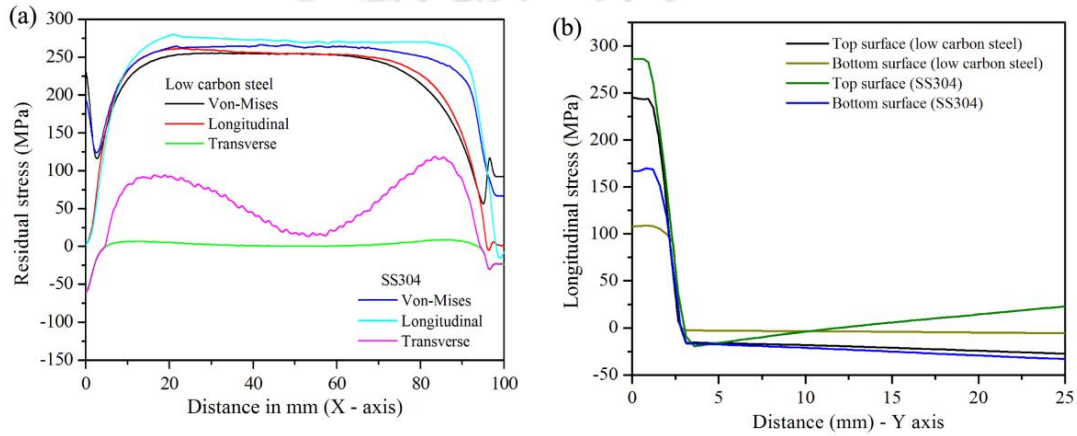

Fig. 5.22 Residual stress distributions at welding conditions of 59.4 J/mm: (a) along the weld line; (b) Longitudinal stress at the top and the bottom surface of the middle cross-section.

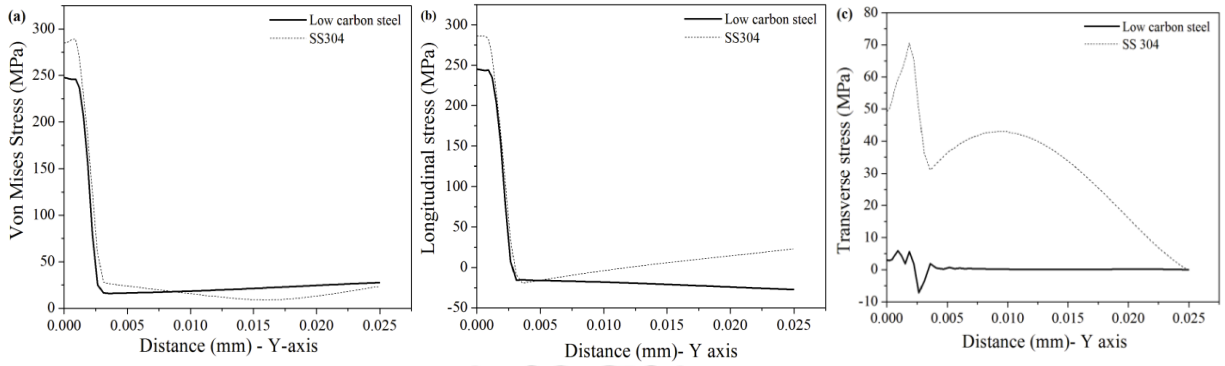

Fig. 5.23 Residual stress distributions at welding conditions of 4 mm/s and 10 A along transverse direction at the middle of the plate for both the materials (a) von-Mises stress; (b) Longitudinal stress; (c) transverse stress.

Figure 5.24 represents the longitudinal and transverse plastic strain distribution (at the middle cross-section) along the transverse direction for both the materials. The figure indicates

that the plastic strain distributions of both the materials are quite similar. The magnitude of longitudinal plastic strain is smaller than that of transverse plastic strain for both the materials. The reason is that the restraint density in the longitudinal direction (parallel to welding direction) is stronger than that in the transverse direction (perpendicular to welding direction). The plastic strain range concentrates in a narrow area near the weld region and becomes zero away from the weld line. It is also inferred that the value of plastic strain is higher for SS304.

Thus, the current investigation might extend an enhancement in both similar and dissimilar joining of the two materials. The study also revealed the relative importance of material properties on the joint characteristics of the weldment. Thermal conductivity and thermal expansion coefficient are important parameters which directly influence the final weld structure. The influence of material properties is better accredited by the development of physics based numerical model.

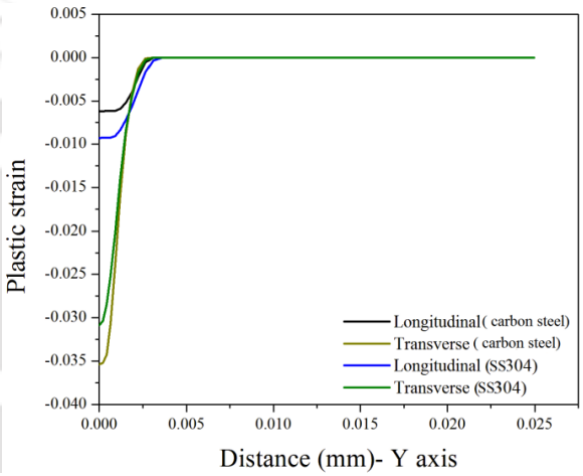

Fig. 5.24 Longitudinal and transverse plastic strain distribution.

5.5 Laser Microwelding

A three dimensional finite element based sequentially coupled thermo-mechanical model is developed for laser microwelding process to analyze the differential influence of process parameters. Typical “hourglass” type heat source is developed to account the temperature distribution of over penetrated weld sample. The temperature dependent thermal and mechanical properties are considered for the analysis. The distortion analysis is also performed using large-displacement theory that predicts the residual distortion satisfactorily for microwelding process as compared to relatively high thickness materials.

5.5.1 Heat transfer analysis

The simulation has been carried out to understand the effect of pulse in temperature distribution of laser micro welding. The influence of pulsation and its reflection through conventional experiments is difficult to capture. Therefore, the compatibility of the model to study the heat transfer in the weld pool is verified by comparing the results of the computed weld pool dimensions with the experimental results at various welding conditions. An attempt has been made to analyze the effect of pulse energy, pulse width and welding speed on temperature profile and weld pool dimensions. Three dimensional computed temperature distributions corresponding to weld velocity of 11 J, 5 ms and 4.5 mm/s. at different pulse time are depicted in Fig. 5.25. The fusion zone and HAZ zone are represented by isotherm contours where the liquidus and solidus temperature of Ti6Al4V are 1933K and 1877K, respectively. The red color represents the mushy zone bounded by liquidus and solidus temperature. The peak temperature and heat affected zone increase with time during welding during a pulse. It is obvious that the maximum temperature is reached at 11.1 s (Fig. 5.25d).

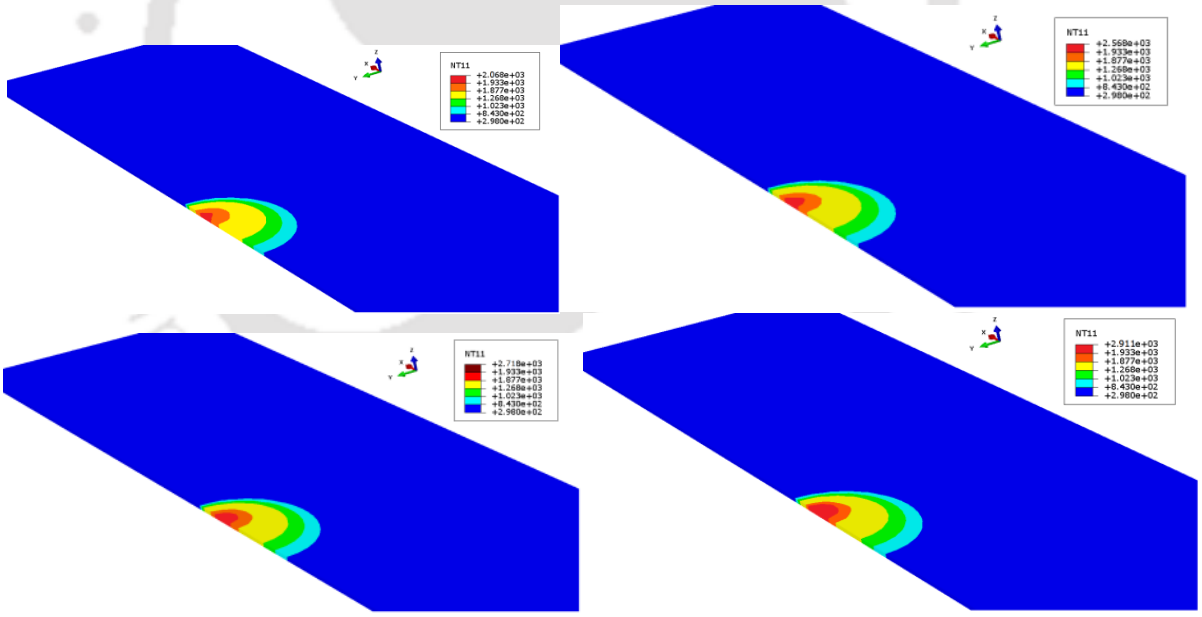

Fig. 5.25 3D temperature distribution of pulse laser welding corresponding to 8 J, 5 ms, 4.5 mm/s at time (a) 11.095 s; (b) 11.097 s (c) 11.098 s; (d) 11.1 s.

Figure 5.26(a) shows the temperature profile along the transverse direction (Y-direction) in the middle of the plate at welding condition of 11 J, 5 ms and 4.5 mm/s. It is seen that peak

temperature is highest at the center of the plate and gradually decreases away from weld line. The temperature reaches to the ambient at about a distance of 5 mm from the weld line. This indicates that the heat is distributed in a very small area and the cooling rate decreases as the peak temperature decreases. Also the pulse effect decreases away from the centerline. Figure 5.26(b) shows the temperature profile along the weld line at the center point of the weld centerline showing the effect of pulse. The average power is considered for calculation of the heat input in case of continuous welding i.e. pulse on and pulse off effect is not taken into account. It is found that the peak temperature computed by considering the average power is ~ 2300 K which is well below the vaporization temperature of Ti6Al4V. Also it is demonstrated that when the pulse effect is taken into consideration, the average temperature at the can be calculated to be around 2527 K. Thus the temperatures calibrated by both the process are fairly similar. However, the profile predicted by the model showing the pulse time effect can help in better understanding of the pulse laser microwelding as it can better reflect the pulse effect at each node.

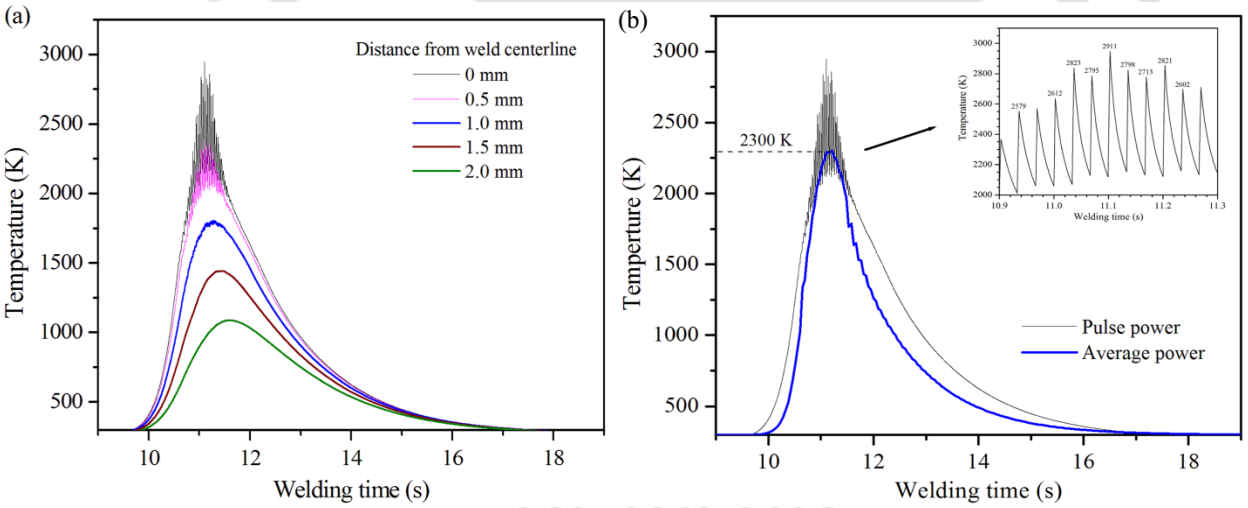

Fig. 5.26 Temperature profile for welding condition of 11 J, 5 ms and 4.5 mm/s: (a) along the transverse direction at the middle of plate; (b) comparison of temperature profile of pulse and continuous welding.

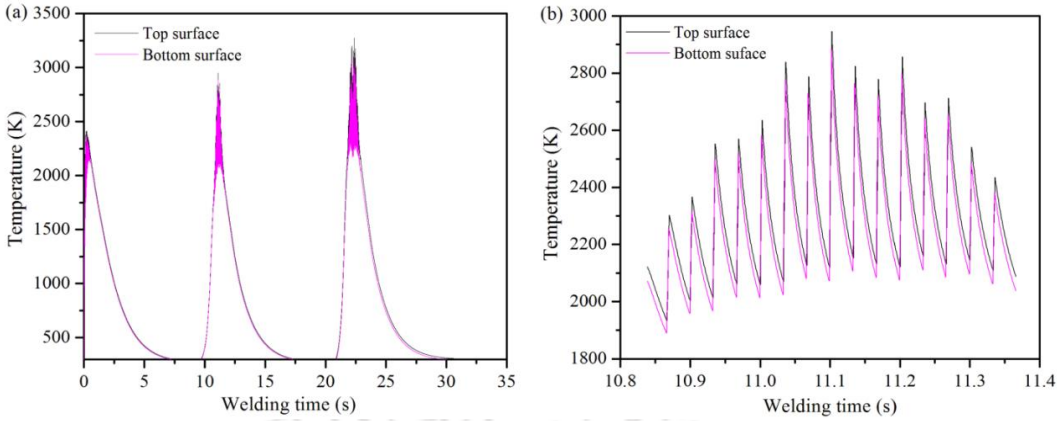

Fig. 5.27 Temperature profile between the top and bottom surface at welding condition of 11 J and 4.5 mm/s: (a) along the weld line, (b) zoomed profile of the center of the plate.

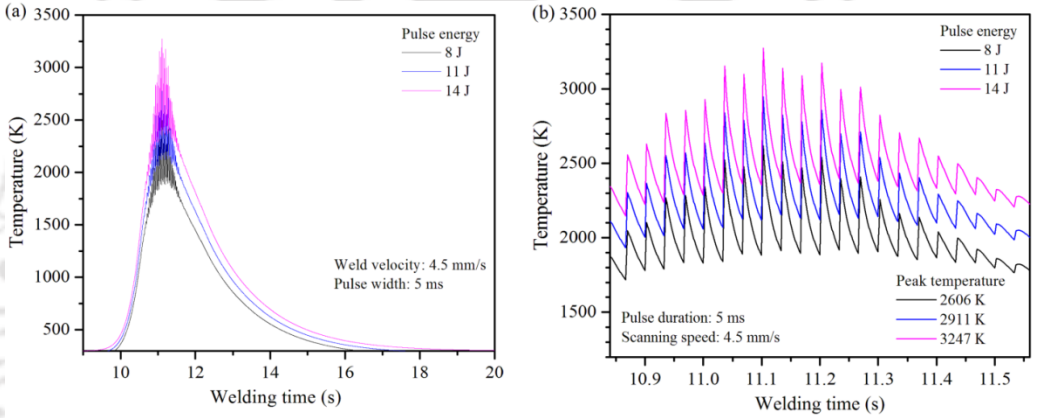

Fig. 5.28 Temperature profile at the center of the plate for welding condition of 8 J and 4.5 mm/s, 11 J and 4.5 mm/s and 14 J and 4.5 mm/s at constant pulse width of 5ms.

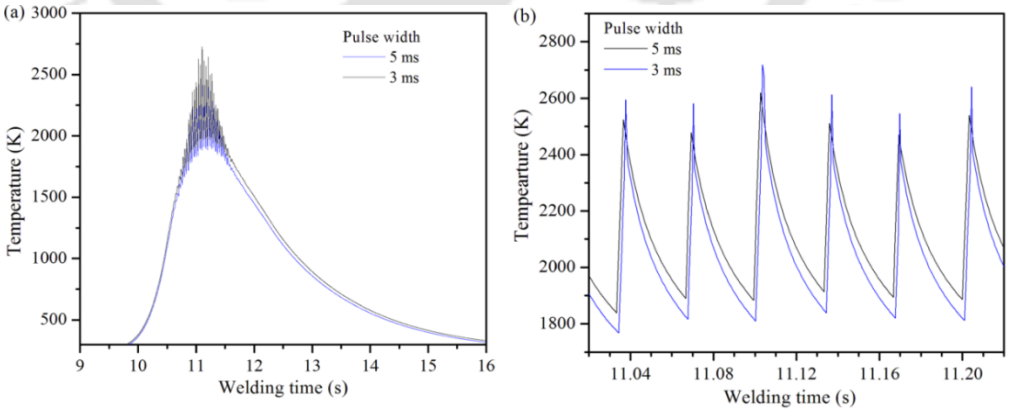

Fig. 5.29 Temperature profile at the center of the plate for welding condition of 8 J, 4.5 mm/s, 5 ms and 8 J, 4.5 mm/s, 3 ms.

Figure 5.27(a)-(b) shows the temperature profile along the weld line between the top and bottom surfaces at the center point of the weld centerline. It is obvious that the peak temperature value does not vary much between the top surface and the bottom surface. This is due to the small thickness even temperature distribution takes through thickness direction. It can also be observed that the temperature history curves of the two surfaces have no difference. Figures 5.28(a)-(b) shows the temperature profiles at the center point of the weld line for three different welding conditions. It is seen that the peak temperature decreases as the heat input decreases. Though the peak temperature is found to be very high but the average temperature is not much. Figure 5.29(a)-(b) shows the effect of pulse width on the temperature profile. The welding condition chosen for this analysis is 8 J, 4.5 mm/s for two different pulse width – 5 ms and 3 ms. It is known that as the pulse width decreases at constant frequency, the pulse on time decreases. At constant pulse energy, as the pulse width decreases the peak power increases leading to an increase in the applied heat input but remains on the joint for a shorter duration. The increase in peak power leads to an increase in peak temperature as evident from the Fig. 5.29(b). However the temperature profiles remain almost similar.

As described in chapter 3, the heat source model predicted by Eq. (3.5) at a low heat input i.e. below heat input of 50 J/mm while at a high heat input, heat source model given by Eq. (3.8) and Eq. (3.9) is used. The compatibility of the model is verified by comparing the results of the computed weld pool dimensions as shown in Fig. 5.30. The fusion zone and HAZ zone are represented by isotherm contours where the liquidus and solidus temperature of Ti6Al4V are 1933 K and 1877 K, respectively. The red colour represents the mushy zone bounded by liquidus and solidus temperature. HAZ zone is also represented by contours in the range of 1268 – 1877 K [Donachie, 2000] since most of the solid state transformation occurs within this temperature range. The shape and size of computed macrographs well agreed with experimentally measured values. The peak temperature is achieved is also reflected in the Fig. 5.29. It is seen that the peak temperature increases with increase in heat input. Figure 5.31 compares the experimentally measured and computed half width dimensions from numerical model. The maximum error is found to ~14%. This explains the robustness of the process.

Table 5.2 Dimension of the hourglass heat source

Dimensions	Z_t	Z_b	Zm	r_t	r_b	r_m
Exp.10	0.5	0	0.25	0.595	0.515	.43
Exp.7	0.5	0	0.25	0.67	.665	.59

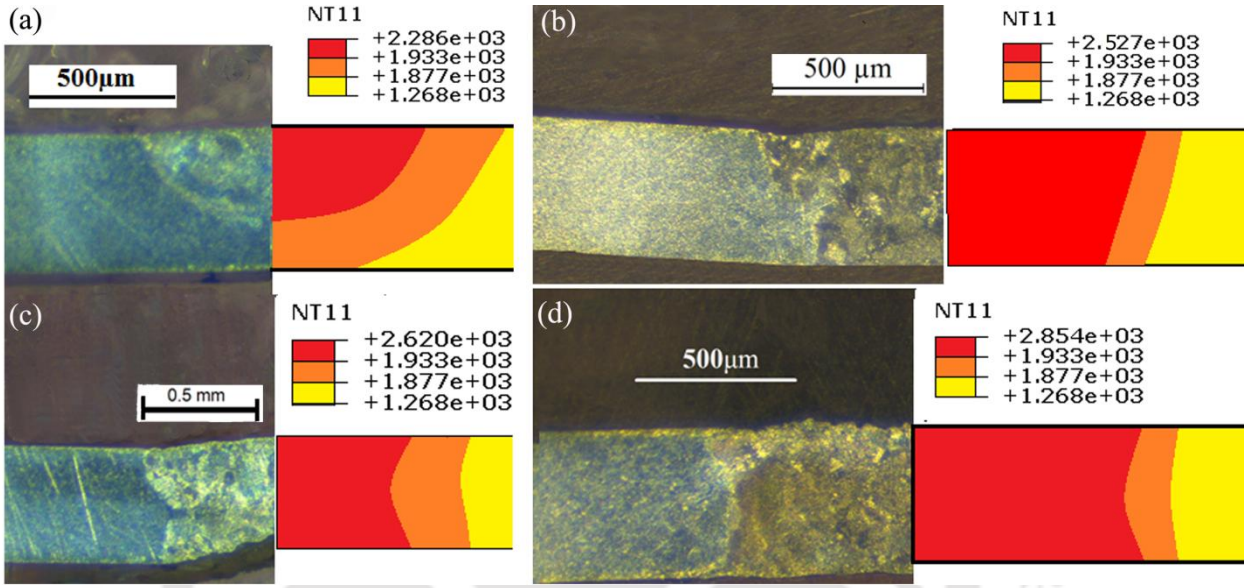

Fig. 5.30 Comparison of experimental (right) and computed (left) weld pool at welding conditions of (a) 6.5 J, 4.5 mm/s, 5 ms; (b) 11 J, 4.5 mm/s, 5 ms (c) 8 J, 3 mm/s, 3 ms; (d) 9.5 J, 3 mm/s, 5 ms;

5.5.2 Welding distortion

Ti6Al4V weldment exhibits highly localized residual stress. The large deformation theory is used to simulate welding residual stress and deformation in the butt welded joint since the stiffness of the plate is very less [Deng and Murakawa, 2008]. Figure 5.32 shows the contour of the deflection distribution computed by the large deformation theory. From this figure, it can be observed that a large transverse bending and negligible longitudinal bending are produced after welding. At the weld stop edge, the maximum deflection is observed which is about 3.557 mm which is almost equivalent to experimental measurement of 3.91 mm at the same point

corresponding to a welding condition of 4.5 mm/s speed and 11 J pulse energy. Figure 5.33 shows the deflection distributions of the plate along the middle section calibrated through both experimental measurement and simulation. It is clear that the deflection mode and values predicted through simulation is much close to the experimental values. Also the longitudinal bending is not significant for such welding. This suggests that when the thermo-elastic–plastic FEM in the simulation welding deformation of a thin plate welding joint or structure it is necessary to consider geometrically nonlinear phenomenon carefully. Otherwise, it may produce very large error.

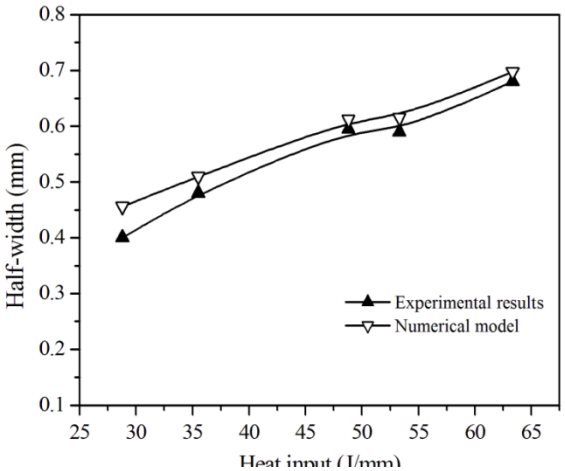

Fig. 5.31 Comparison between experimentally measured and computed half width dimensions.

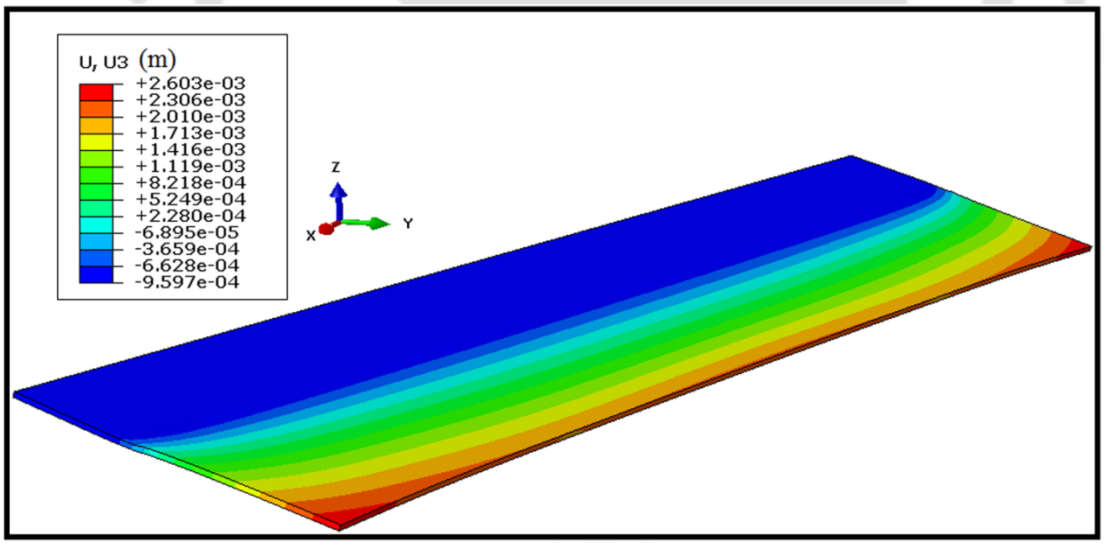

Fig. 5.32 Distortion pattern at welding speed 4.5 mm/s and energy of 11 J using large deformation theory.

5.5.3 Welding residual stress

The residual stresses can be found after the whole process of welding is completed and structure is cooled down to the room temperature. By directional the welding stresses subdivide into longitudinal (parallel to the welding direction) and transversal (perpendicular to the weld seam) and through thickness stress. Figure 5.34(a) refer to the residual stress distributions computed by the large deformation theory corresponding to a welding condition of 4.5 mm/s speed and 11 J pulse energy at the top of the surface along the weldline. The material is subjected to significantly large longitudinal stress which is more than twice the transverse stress and almost equal to the total (von-Mises) maximum residual stress. The longitudinal stress is almost uniformly distributed along the X-axis having a maximum value of 593 MPa in the weld joint area which almost reaches the material yield strength. It reduces to zero at the free surfaces of the starting and ending edges of the welding line. Thus the weld joint experiences large longitudinal tensile stress. It can also be deduced from the figure that the transverse stress is negative towards the start and end of the weld indicating compressive residual stress. It gradually increases and become tensile reaching a maximum value of 223 MPa along the length of the weldline. The transverse residual stress also exhibits two peaks towards the end of the weld line. Thus, the weld joint is subjected to significant tensile stress along the length of the weld and is subjected to high plastic deformation at high temperature.

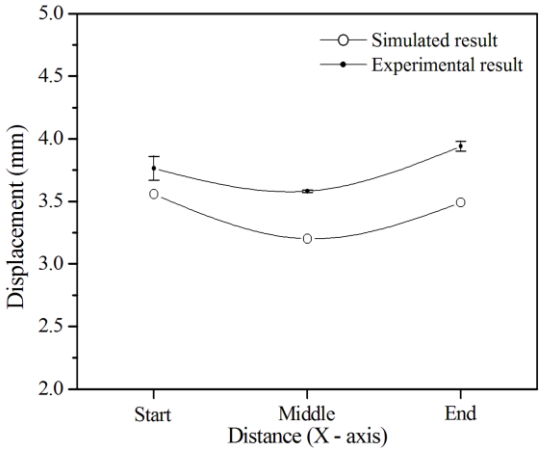

Fig. 5.33 Comparison of deflections at welding speed of 4.5 mm/s and pulse energy of 11 J at pulse duration of 5 ms.

Figure 5.34(b) shows the longitudinal residual stress distributions at the top surface and bottom surface of the middle cross-section along the transverse direction (Y-direction), which is computed by the large deformation theory corresponding to a welding condition of 4.5 mm/s speed and 11 J pulse energy. The longitudinal residual stress exhibit a sharp decreasing trend in the area near the weld region (<2 mm) and becomes negative away from the weld line. It is

realized that the longitudinal stress has a high tensile value near the weld line due to the severe restraint condition and becomes compressive away from the weld line. However, the tensile stress is much higher than the compressive stress. It is also reflected that there is a slight difference between the longitudinal stress of the top surface and that of the bottom surface. The longitudinal stress in the bottom surface is larger than the top surface. This supports the premise that the welded sheets are bended to a concave structure in the longitudinal direction.

Figure 5.34(c) shows the transverse residual stress distributions of the middle section along the transverse direction. There is a significant difference between the transverse residual stress of the top surface and that of the bottom surface. The transverse residual stress exhibits a high value near the weld region but reduces away from the weldline. It is very clear that the transverse residual stress of the top surface is much larger and tensile in nature than that of the bottom surface which is compressive in nature. The difference resulted in the large transverse bending deformation and very less bending along the longitudinal direction. It can also be concluded that most of the stress in the specimen is mainly mostly concentrated in the weld area.

Figure 5.35(a) shows comparison of the von-Mises stress for three different welding conditions the longitudinal direction of the weldline. It is seen that the von-Mises stress increases with heat input. However no particular trend can be demonstrated from the comparison. From the Fig. 5.35(b) it can be concluded that the residual stress is more for greater pulse width as the heat is applied for more time for the same total pulse duration.

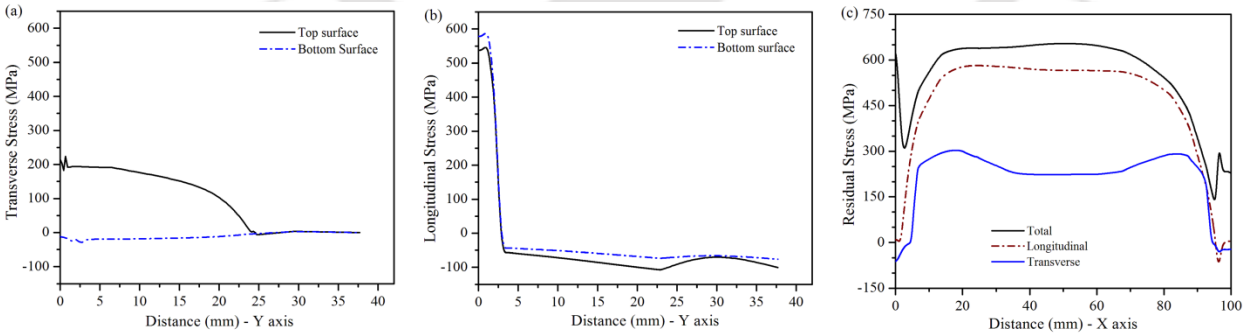

Fig. 5.34 Residual stress distributions at welding conditions of 4.5 mm/s and 11 J: (a) along the weld line and (b) Longitudinal residual stress along transverse direction at the middle of the plate; (c) Transverse residual stress along transverse direction at the middle of the plate.

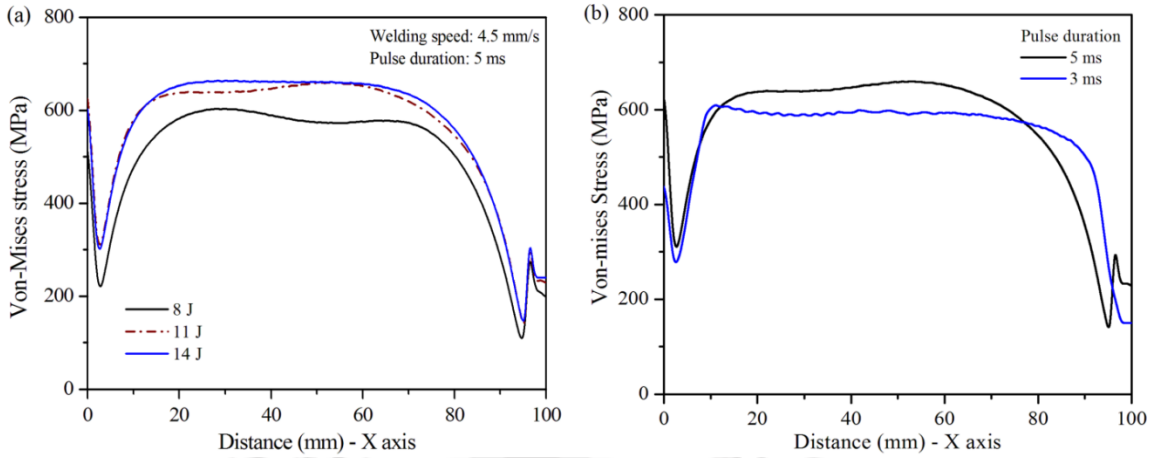

Fig. 5.35 Residual stress comparison for different conditions: (a) von-Mises stress for three different welding conditions; (b) von-Mises stress for three different pulse width.

5.5.4 Plastic strain distribution

Figure 5.36(a) represents the longitudinal and transverse plastic strain distribution (at the middle cross-section) along the transverse direction corresponding to welding condition of 11 J and 4.5 mm/s. From the figure, it is known that the range of the longitudinal plastic strain distribution is larger than that of the transverse plastic strain distribution. The transverse plastic strain range concentrates almost only in the fusion zone and the HAZ, while the longitudinal plastic strain range distributes in a relatively large range. Generally, the range and magnitude of the plastic strain component are mainly governed by the peak temperature and the restraint conditions. During welding, because the restraint intensity in the longitudinal direction (welding direction) is larger than that in the transverse direction, the range of the longitudinal plastic strain is relatively large. From the Fig. 5.36(b) it can be concluded that the plastic strain values for the three cases are found to be the same suggesting that the strain developed mainly depends on the constraints and property of the material rather than the external load.

5.6 Full plate welding

This section describes the simulation considering full plate geometry corresponding to the heat input of ~ 53 J/mm. The simulation is carried out to bring out a comparative study between micro plasma welding and laser welding. The computational time is greatly increased as compared to the half plate simulation. For micro plasma welding this heat input corresponds to

the welding conditions of current of 9 A and welding speed of 4.2 mm/s. Whereas for laser micro welding this heat input corresponds to the welding speed of 3 mm/s, pulse energy of 8 J and pulse duration of 5 ms. Simulation for laser micro welding is carried out taking the average power over the whole cycle.

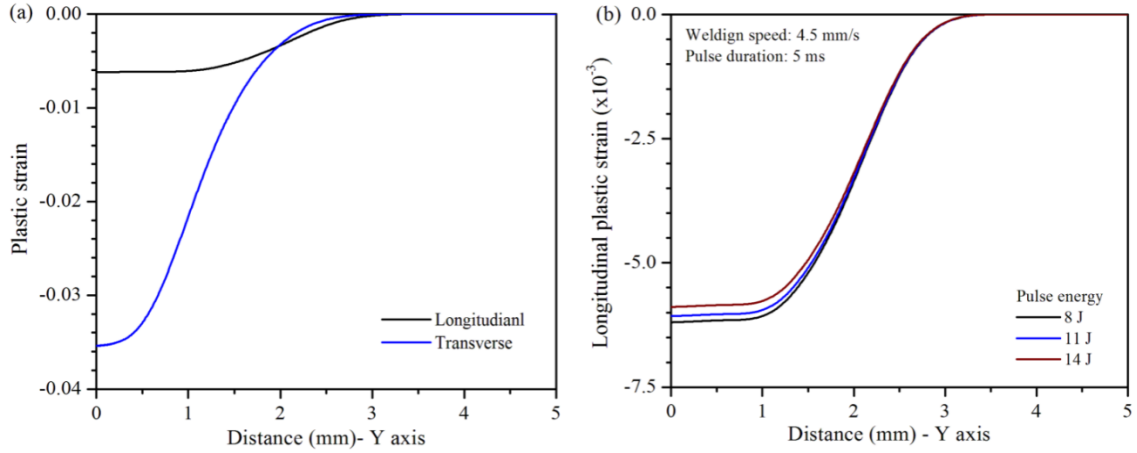

Fig. 5.36 Plastic strain distribution: (a) longitudinal and transverse for 11 J, 4.5 mm/s; (b) comparison of plastic strain for three cases.

Comparison of experimental and computed weld pool at specified welding conditions are depicted for laser micro welding (Fig. 5.37) and micro plasma welding (Fig. 5.38). The red color represents the fusion zone bounded by liquidus temperature while the yellow color represents the mushy zone bounded by solidus and liquidus temperature. It is reflected that though the peak temperature for laser microwelding is higher yet fusion zone is smaller than that of micro plasma welding. However, it is confirmed that for both the processes the heat affected zone is confined in small area. Figure 5.39(a) also highlighted that the peak temperature and cooling rate are higher for laser microwelding for the same heat input. At this heat input, the average cooling rates calculated between the temperature where the dissolution of the primary α (940 K) takes place and the β transus temperature (1273 K) are found to be 746 K/s and 943 K/s for microplasma and laser micro welding respectively. Thus the cooling rate for both the process is sufficiently high to form α' martensite at this heat input in the fusion zone. The magnitude of the maximum cooling rate is 2453 K/s and 1373 K/s for laser micro welding and micro plasma welding respectively (Fig. 5.39b).

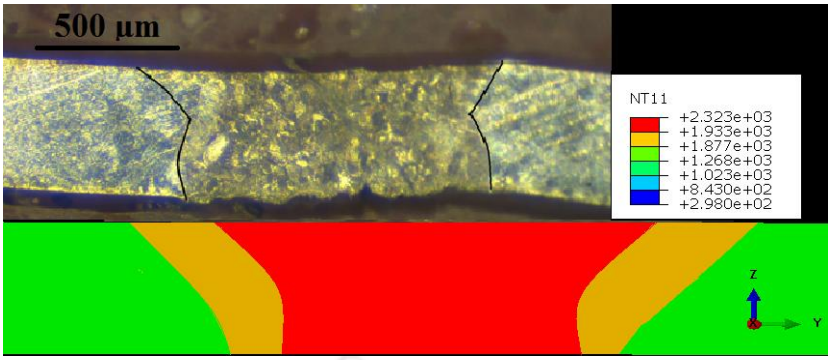

Fig. 5.37 Comparison of experimental (top) and computed (bottom) weld pool at welding conditions of ~ 53 J/mm for laser micro welding.

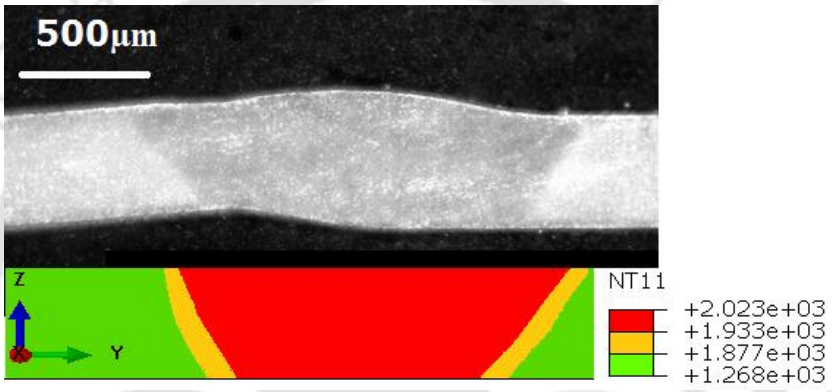

Fig. 5.38 Comparison of experimental (top) and computed (bottom) weld pool at welding conditions of ~ 53 J/mm for micro plasma welding.

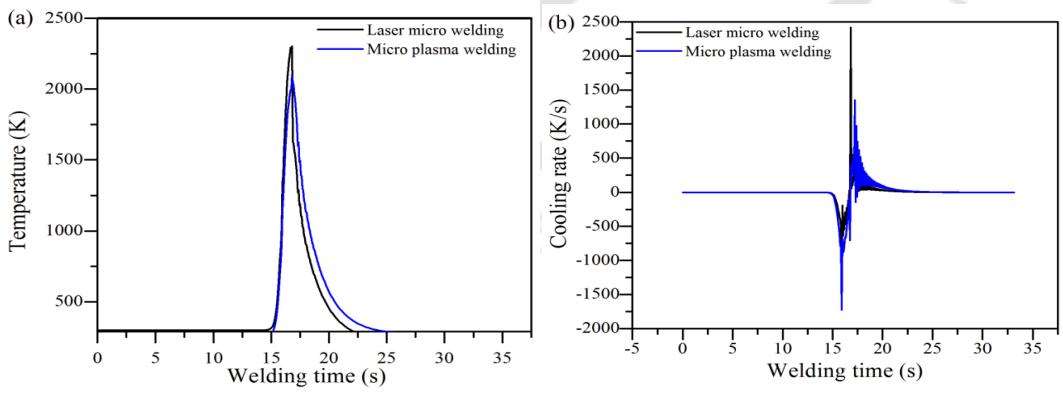

Fig. 5.39 Comparative analysis at welding conditions of ~ 53 J/mm: (a) Temperature profile at the middle of weldline; (b) Cooling rate.

Figure 5.40 and 5.41 demonstrates the deflection contours for laser microwelding and plasma micro welding respectively. It is highlighted that uniform negative bending occurs in case of laser micro welding without much deformation along the longitudinal direction. However, in case of micro plasma welding the pattern is convex-concave type. In this case, the deformation mainly takes place along the longitudinal direction. Moreover, the magnitude of deformation for laser is less than that of micro plasma welding.

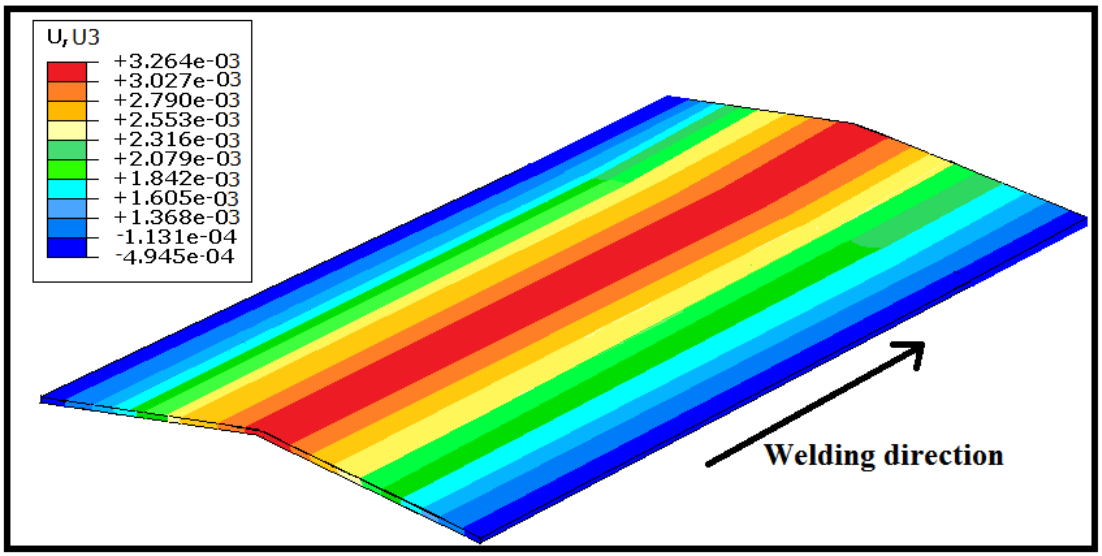

Fig. 5.40 Distortion pattern for full plate geometry at for ~ 53 J/mm for laser micro welding.

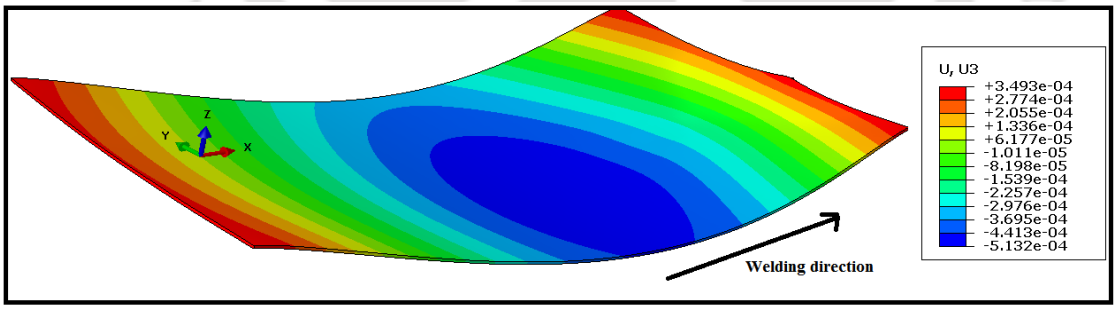

Fig. 5.41 Distortion pattern for full plate geometry at for ~ 53 J/mm for micro plasma welding.

5.7 Heat Transfer and Fluid Flow in Laser Microwelding

The compatibility of the model to study the heat transfer and fluid flow behaviour in the weld pool is verified by comparing the results of the computed weld pool dimensions with the experimental data reported in independent literature [Kleine *et al.*, 2004]. The laser micro

welding conditions are illustrated in Table 5.3. The experiments involved micro welding of 304 Stainless Steel and Titanium with a single mode fiber laser focussed on the top surface of the sample with a beam diameter of 25 μm in Argon shielding gas environment. The welding speed and pulse frequency was kept constant at 4 mm/sec and 200 Hz, respectively. Peak power of 40 W, 60 W, 80 W and 100 W were used for two different laser pulse lengths (2 ms and 4 ms). It is evident from Table 5.3 that both the weld penetration and weld width increases with increase in peak power for the same welding conditions. It is also observed that for the same peak power weld dimensions increase with increase in pulse length. This is due to the fact that energy per unit length increases with increase in either laser power or pulse length. In numerical simulation of pulsed laser microwelding, the average power is calculated over energy distribution per cycle. Obviously, the average power will be less than peak power as observed in Table 5.4. However, the average power is calculated based on pulse energy over one cycle time assuming rectangular shape of energy distribution over pulse length.

Table 5.3 Laser welding conditions used to validate numerical model [Kleine *et al.*, 2004].

Data set index	Material	Peak power (W)	Pulse frequency (Hz)	Pulse length (ms)	Pulse energy (J)	Weld speed (mm/s)	Average power (W)	P/v (J/mm)	Spot diameter (μm)
1		40			0.080		16	4	
2		60		2	0.120		24	6	
3		80			0.160		32	8	
4	Stainless	100	200		0.200	4	40	10	25
5	steel	40			0.160		32	8	
6		60		4	0.240		48	12	
7		80			0.320		64	16	
8		100			0.400		80	20	
9	Titanium	80	200	4	0.320	4	64	16	25

Table 5.4 Experimentally measured weld dimensions [Kleine *et al.*, 2004].

Data set index	Weld width (mm)	Weld penetration (mm)	Width/penetration ratio
1	0.07	0.06	0.89
2	0.15	0.13	0.86
3	0.17	0.25	1.46
4	0.20	0.34	1.70
5	0.13	0.08	0.60
6	0.17	0.18	1.06
7	0.24	0.29	1.23
8	0.26	0.42	1.64
9	0.30	0.35	1.17

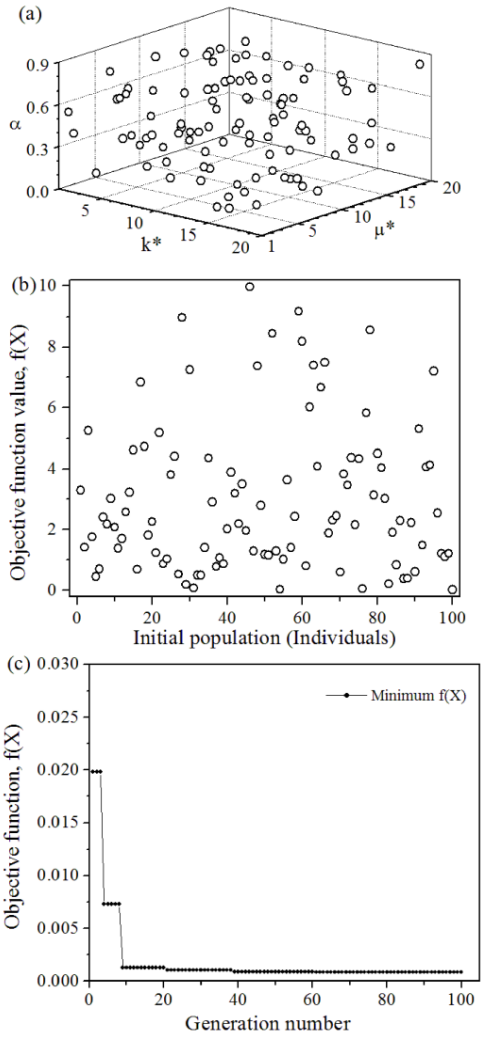

Fig. 5.42 Optimisation of unknown parameters, (a) initial population, (b) objective function valuefor initial population, and (c) performance of HM algorithm.

The estimation of uncertain parameters involves some sort of inverse analysis where the numerical model is integrated with Harmony Search (HS) algorithm and an optimum set of uncertain parameters comes out from this integrated approach. HM is a real number based metaheuristic algorithm where the concept of improvisation technique of the musicians is used [Geem, 2009]. Figure 5.42 depicts the performance of HS algorithm to estimate the optimum set of unknown parameters. An initial population is created within feasible range of unknown parameters. Table 5.5 describes the range of parameters in non-dimensional form. The reference value for thermal conductivity and viscosity are respectively 22.8 W $m^{-1}K^{-1}$ and $6.7x10^{-3}$ kg $m^{-1}s^{-1}$ for Stainless Steel and 9.63 W $m^{-1}K^{-1}$ and $4.9x10^{-3}$ kg $m^{-1}s^{-1}$ for Titanium which are room temperature values [Bag *et al.*, 2009; Mishra and DebRoy, 2005; Quintino *et al.*,

2007]. Figure 5.42(a) illustrates the distribution of randomly generated initial population (~ 100). It is observed that the individuals are diversely distributed over the solution space and it is assumed that each individual has potential to achieve global optimum value. Figure 5.42(b) furnishes the computed values of objective function of initial population. The objective function value tends toward zero are good initial individuals as compared to higher objective functional value (~ 10.0). The f(**X**) values are also diversely distributed over feasible solution space and each of individuals has scope of further improvement over generations. The performance of optimiization algorithm is depicted in Fig. 5.42(c) with plotting minimum value of f(**X**) in each generation. The algorithm has stopped after 100 generations since it was observed no further improvement of f(**X**) after 100 generations. To improve the performance of HS algorithm, variable values of PAR and BW (function of generation number) are considered in present case. The optimum value of f(**X**) is achieved as ~ 4.18×10^{-3} and corresponding optimum values of unknown parameters is described in Table 5.5.

Table 5.5 Optimization of unknown parameters.

Non-dimensional form			In dimension		
Unknown parameters	Permissible range	Estimated optimum value	Unknown parameters	Effective values (SS304)	Effective values (Ti)
α	0.1 – 0.9	0.61	α	0.61	0.61
k^*	1 - 20	7.33	k_{eff}	167 $Wm^{-1}K^{-1}$	70.58 $Wm^{-1}K^{-1}$
μ^*	1 - 20	5.61	μ_{eff}	0.037 kg m^{-1} s^{-1}	0.027 kg m^{-1} s^{-1}

The optimum value of absorption coefficient (~ 0.61) is almost in similar range of literature reported value [Quintino *et al.*, 2007]. The enhancement of material properties at high temperature with several folds is also reported in several literatures [Bag *et al.*, 2009; Mishra and DebRoy, 2005] and the results reported in Table 5.5 are within the limit. However, the exact value of enhancement depends on the process itself as well as process parameters. There is no strict guideline or methodology to decide the enhancement factor. In essence, the enhancement of material properties at several folds yields the effect of uniform turbulence within small weld pool.

Figure 5.43 depicts the computed temperature and velocity fields for single pulsed fiber laser during welding of 304 Stainless Steel using optimum set of known parameters depicted in Table 5.5. The temperature field is depicted by isotherm contour and velocity of liquid metal is indicated by the arrow vector line. Both the velocity and peak temperature increased with the peak power for a constant pulse length and same welding conditions. The temperature coefficient of surface tension $d\gamma/dT$ is negative as the molten metal on the surface flows from the centre to the outward periphery of the liquid pool. The buoyancy force acts in the upward direction. As a result, the fluid flow makes a circulation loop in the clockwise direction. The magnitude of velocity vector is more

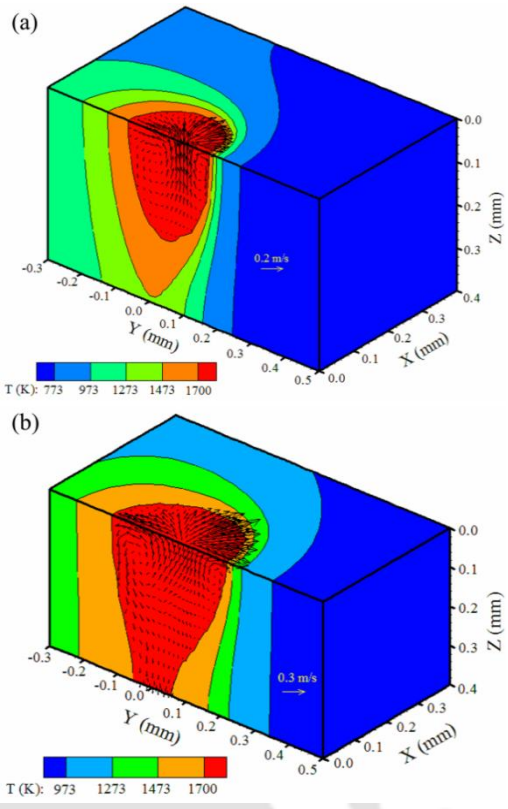

Fig. 5.43 Three-dimensional temperature and velocity distribution corresponding to welding conditions of (a) dataset # 3 and (b) dataset #8 in Table 5.4.

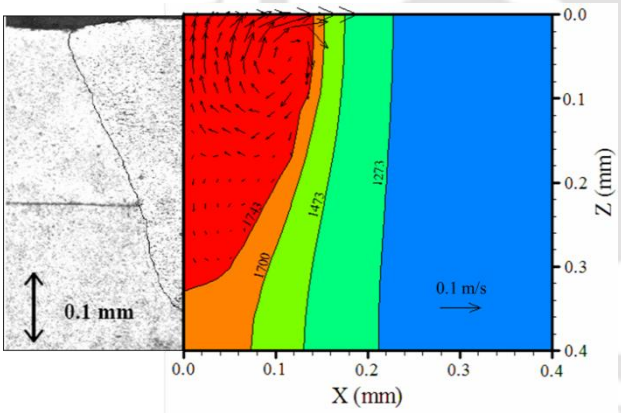

Fig. 5.44 Comparison between numerically obtained and experimentally measured weld macrographs corresponding to welding conditions of dataset #9 in Table 5.4.

at the top of weld pool and it reduces along depth direction. It is evident from Fig. 5.44(a) that the partial penetration of weld occurs and the solidus isotherm of SS304 and decides the weld pool shape and size. The maximum order of magnitude of velocity in this case is ~ 390 mm/s. Fig. 5.43(b) depicts the full depth penetration at average laser power of 80 W and the magnitude of maximum velocity vector is ~ 520 mm/s.

Figure 5.44 compares the numerically obtained and experimentally measured weld macrographs of the cross-section of a typical titanium weld corresponding to data set #9 in Table 1. The macrograph shows the boundary between the resolidified weld metal and the non-melted pool. The shape and size of computed macrograph is well agreed with experimentally measured penetration. This indicates the robustness of integrated modelling in laser micro welding process. Overall comparison of computed weld dimensions with experimentally measured results is described in Fig. 5.45. It is noteworthy that the optimum set of unknown parameters is used to calculate weld pool dimensions for all data sets of Table 5.3. The optimization calculation is performed using few experimental data from Table 5.3 and an average value i.e. optimized values of unknown parameters are used to predict all data sets. Hence the discrepancy between computed and experimental results occurs in few cases. Fig. 5.45 also shows the error percentage between the experimentally measured and calculated weld pool dimensions. The maximum error for this case was found to be 30% and only for one data set. Most of the cases the error percentage is below 15 %.

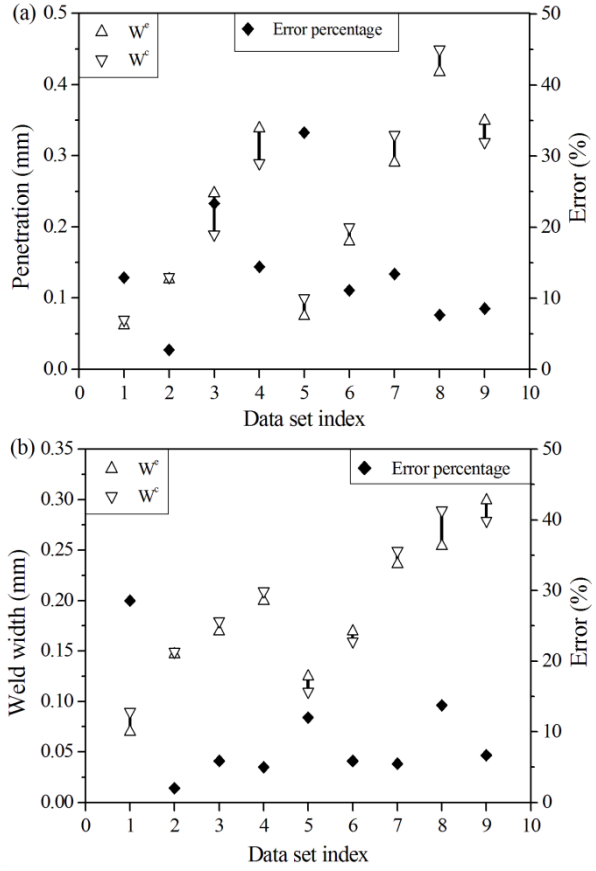

Fig. 5.45 Comparison between experimentally measured and computed weld dimensions from numerical model using optimum set of unknown parameters.

Experimental measurement of flow field is extremely difficult or nearly impossible for laser micro welding process. Hence the reliability of numerical model is analysed using various dimensionless numbers and the expected value of maximum velocity is estimated using order-of-magnitude analysis under various driving forces. Fig. 5.46(a) depicts the peak temperature and average temperature gradient calculated from numerical model. The average

temperature gradient is seen to have a linear increase with power. The peak temperature also increases with laser power since the energy per unit length increases with increase in average power. It is noteworthy that peak temperature and average temperature gradient are higher in Titanium than in Stainless steel for the similar welding conditions. The relative importance of the mode of heat transfer i.e. by conduction or convection is evaluated by Peclet number (Pe) which is expressed as:

$$Pe = \frac{V_r \rho C L_r}{k} \tag{5.5}$$

where V_r is the typical velocity of the weld pool, ρ is the density, C is the specific heat, L_r is the characteristic length taken as the pool radius, and k is the thermal conductivity. When the value of Pe is greater than one, convection plays an important role in the heat transfer phenomenon within the weld pool. The calculated value of Pe for all data sets (Table 5.3) is shown in Fig. 5.46(b). To calculate Pe, the physical properties value reported in Table 4 is used. Since the Pe is greater than one, it is justifiable to use heat transfer and fluid flow model instead of only heat conduction analysis. It has been observed that the Peclet number increases linearly with increase in peak power. It is due to the fact that the value of maximum velocity increases with power due to the increase in temperature gradient. The relative importance of various driving forces in fluid motion can be evaluated in terms of various dimensionless numbers as used by He and his co-workers [He *et al.*, 2004]. The ratio of buoyancy force to viscous force is determined by Grashof number

$$Gr = \frac{g \beta L_b^{\,3} \Delta T \rho^2}{\mu^2} \tag{5.6}$$

where g is the gravitational acceleration, β is the thermal expansion coefficient of the liquid, ΔT is the temperature difference between the peak temperature in the weld pool land solidus temperature, L_b is a characteristic length for the buoyancy force in the liquid pool, which is approximated by one-eighth of the width of weld pool, ρ is the density, μ is the viscosity. The Surface tension Reynolds number, *Ma*, is used to describe the ratio of surface tension gradient force to viscous force, and is calculated as [He *et al.*, 2003]:

$$Ma = \frac{\rho \Delta T L_r \left| \frac{d\gamma}{dT} \right|}{\mu^2} \tag{5.7}$$

The importance of surface tension and buoyancy can be found by ratio of surface tension Reynolds number to Grashof number:

$$R_{S/B} = \frac{Ma}{Gr} \tag{5.8}$$

Using the physical properties from Table 5.6 and also the values calculated in present work, the Grashof number, and surface tension Reynolds number is calculated by Eq. (5.6) and (5.7). Fig. 5.47(a) indicates a similar trend of increase in the effect of buoyance force as well as surface tension gradient force increases with increase in peak power. However, it is interesting to note that the Ma is least in case of Ti whereas Gr is the maximum for Ti as compared to all other data sets of stainless steel. The ratio of surface tension force to buoyancy force (Eq. 5.8) is calculated and found to be order of ~ $2x10^6$. Therefore it can be expected that the liquid flow is mainly driven by Marangoni convection and to a much less extent by the buoyancy force. Fig. 5.47(b) shows the different values of $R_{S/B}$ for all data sets. It is observed that $R_{S/B}$ is the maximum for data set #1 i.e. at low average laser power or lowest energy per unit length. This signifies that the effect of buoyancy force increases with increase in laser power.

In order to calculate the approximated magnitude of velocity vector the order-of-magnitude analysis is performed. The order of the maximal velocity under the influence of surface tension force can be approximated by [He *et al.*, 2004]:

$$V_{ST}^{\max} = \left(\left| \frac{d\gamma}{dT} \right| \left| \frac{dT}{dy} \right| \frac{W^{1/2}}{0.664 \rho^{1/2} \mu^{1/2}} \right)^{2/3} \tag{5.9}$$

where d*T*/dy is the average temperature gradient in the weld pool, *W* is the weld pool radius. An order of magnitude of the maximum velocity due to buoyancy driven flow is estimated as [He *et al.*, 2004]:

$$V_G^{\max} = \sqrt{g \beta \Delta T p} \tag{5.10}$$

The values of expected maximum velocity from order-of-magnitude analysis using optimum set of unknown parameters are plotted for the different data sets and presented in Fig. 5.48. These values are in well agreement with those of the calculated using the heat transfer and fluid flow model.

Table 5.6 Constant values of material properties used in numerical calculation [He *et al.*, 2004; Du *et al.*, 2003].

Material	ρ (kg m^{-3})	μ (kg m^{-1} s^{-1})	β (K^{-1})	$\frac{d\gamma}{dT}$ (kg s^{-2} K^{-1})	T_S(K)	T_L(K)
Ti	4200	0.027	$1x10^{-4}$	$0.35x10^{-4}$	1743	1813
SS304	7200	0.037	$1.95x10^{-5}$	$0.43x10^{-3}$	1700	1727

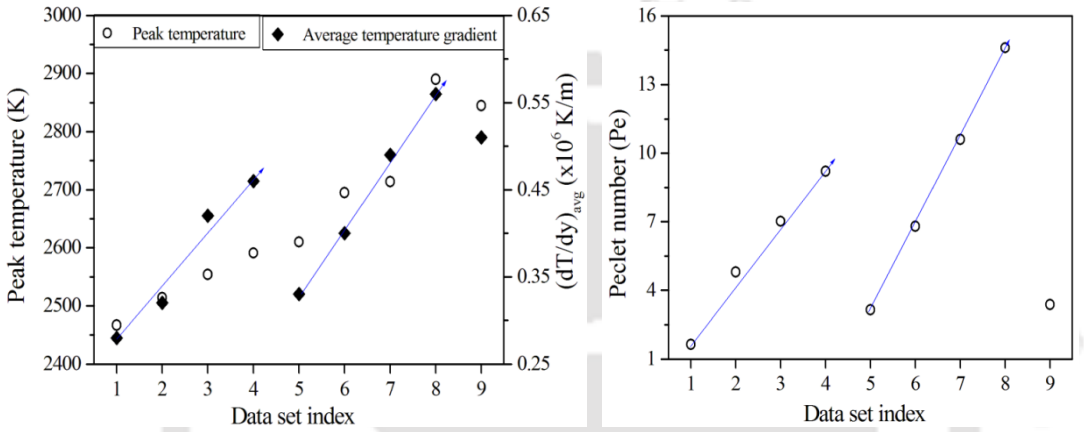

Fig. 5.46 Estimation of (a) peak temperature and average temperature gradient, and (b) Peclet number from numerical model.

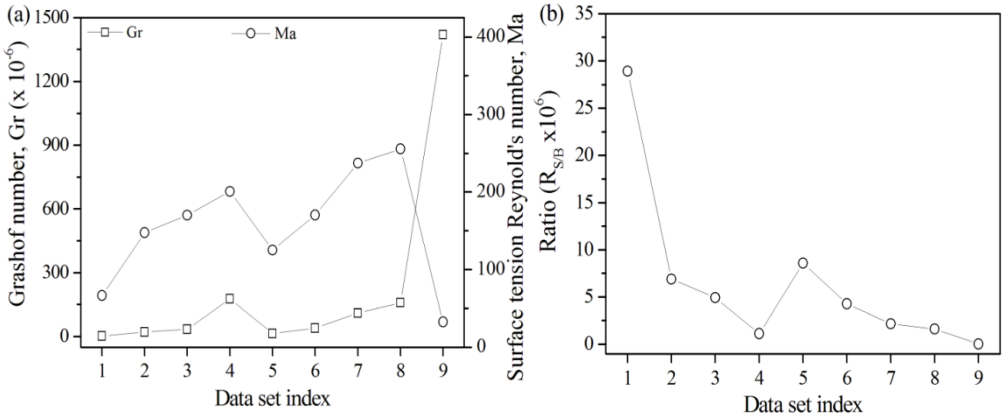

Fig. 5.47 Estimation of: (a) dimensionless numbers, and (b) expected maximum velocity from order-of-magnitude analysis using optimum set of unknown parameters.

An integrated modelling approach is presented in present course of action during reliable modelling of laser micro welding. The analysis of various dimensionless numbers indicates that the fluid flow analysis is important even in micro-scale welding process. The identification of unknown parameters using HS algorithm further strengthen the reliability of numerical modelling. Enhancement of material properties like thermal conductivity and viscosity over their molecular values dim the effect of uniform turbulence.

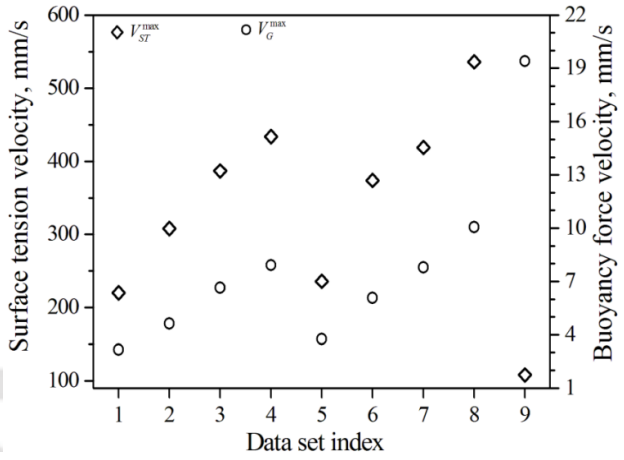

Fig. 5.48 Ratio of surface tension Reynolds number and Grashof number for all data set.

5.8 Laser Transmission Welding

The basic principle of laser transmission welding is passing or transmitting laser radiation through one piece of plastic to create a weld. Unlike standard welding where the energy is applied at the surface of the materials, transmission welding aims to apply the energy in between two plastic pieces at their interface. The upper layer needs to be transparent to laser wavelengths in the infrared and near-infrared spectrum. The true dimension of the sample that is used for this study is shown in Fig. 5.49. A distributed heat flux given by Eq. (3.50) is applied on the material body on which the laser is being focussed. The moving load is implemented into ABAQUS through DFLUX subroutine which has been written to describe the spatial and temporal variation of the heat source. The time is calculated based on the welding speed and heat source location. Thus, a nodal temperature history is obtained as a function of time. Heat transfer between the two materials has been

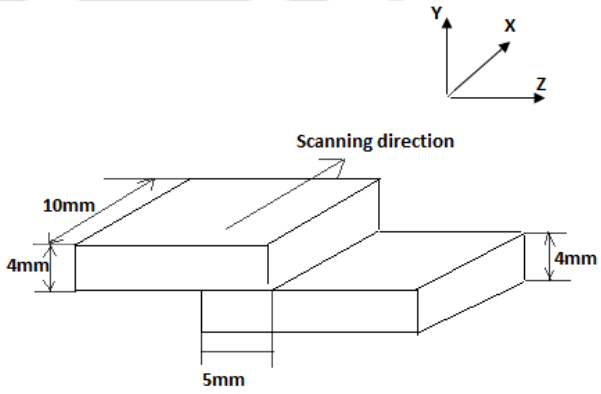

Fig. 5.49 3D geometry of the model (similar materials).

modelled by using the surface interaction technique option in ABAQUS. The heat flow across interface occurs via contact conduction, which was defined by the GAP CONDUCTION. Due to presence of loading and material symmetries, only one half of the model is considered. The FE continuum solid element type used in the thermal analysis is an 8-node brick DC3XD8 diffusive heat transfer. The material properties used in the simulation are provided in Table 5.7 and Table 5.8 as collected from matweb.com. It is noteworthy that the term melting point, when applied to polymers, suggests not a solid–liquid phase transition but a transition from a crystalline or semi-crystalline phase to a solid amorphous phase. It is more properly called the crystalline melting temperature.

Table 5.7 Material property of the material used for simulation.

Material	Density (kg/m^3)	Thermal conductivity (W/m-K)	Specific Heat (J/kg-K)	Crystalline melting point (K)	Emissivity
Polypropylene	920	0.16	80	438	0.97

Results are validated from experimental data collected from independent data [Ghorbel *et al.*, 2009]. Three dimensional computed temperature distribution corresponding to velocity of 2 mm/s and power density of 2.8 W/mm^2 at three different locations is depicted in Fig. 5.50. Fig. 5.51 compares the numerically simulated and experimentally measured [Ghorbel *et al.*, 2009] weld macrographs of the cross-section of the two joining materials. The shape and size of computed macrograph well agreed with experimentally measured values. Computed temperature contours at two different velocities (2mm/sec and 5mm/sec) are shown in Fig. 5.52. Thus it is seen that the weld dimension decreases with increase in velocity. It is because as velocity is increased, less irradiation time is available resulting in less energy deposit and thus both weld width and penetration decreases.

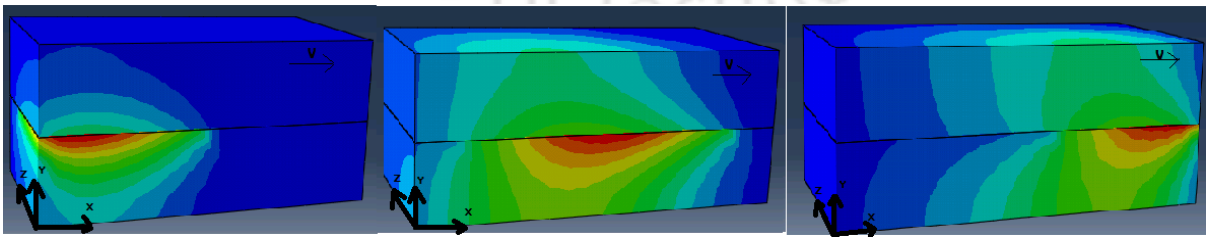

Fig. 5.50 3D computed temperature distribution corresponding to velocity of 2 mm/s and power density of 2.8 W/mm^2 at three different locations.

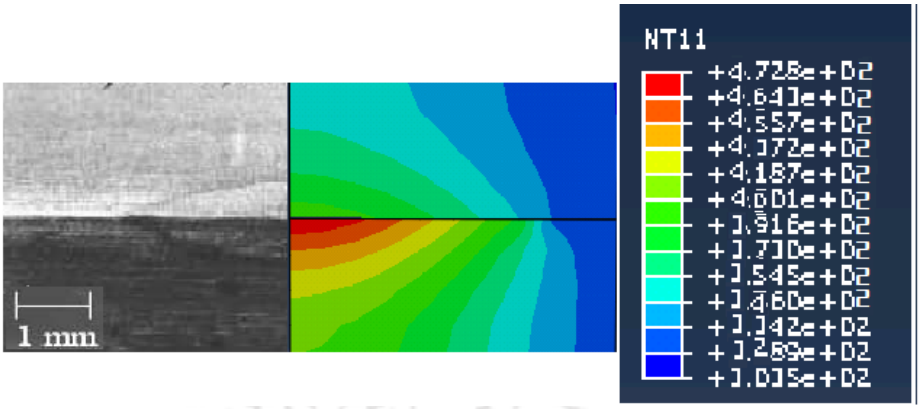

Fig. 5.51 Comparison between numerically obtained and experimentally measured weld macrographs [Ghorbel *et al*., 2009] at power density of 2.8 W/mm^2 and velocity 2 mm/s.

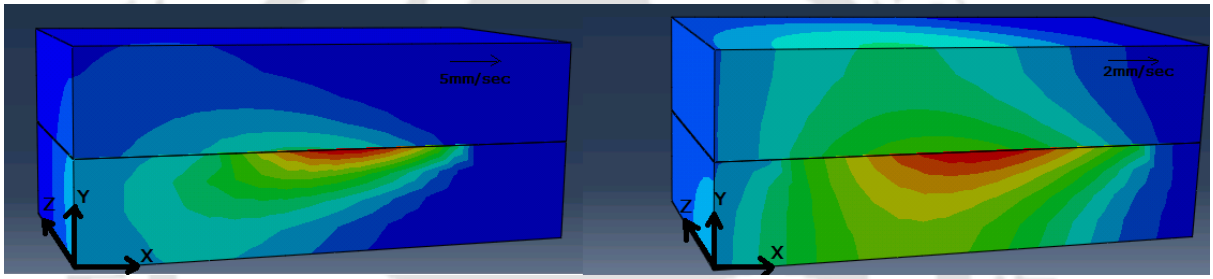

Fig. 5.52 Computed temperature contours at two different velocities.

It is obvious from above mentioned results that the discrepancy in the temperature distribution of the transparent part may be due to improper value of the gap heat transfer coefficient considered for present analysis. However the profile of temperature matched reasonably well with the experimental one. The effect two different velocities on the temperature profile indicate that the weld dimension decreases with increase in velocity. Figure 5.53 shows the temperature profile for dissimilar materials corresponding to velocity of 800 mm/s and power of 4W at three different locations. Figure 5.54 demonstrates the temperature profile at the centre of the plate and the cross-sectional view (Fig. 5.55b).

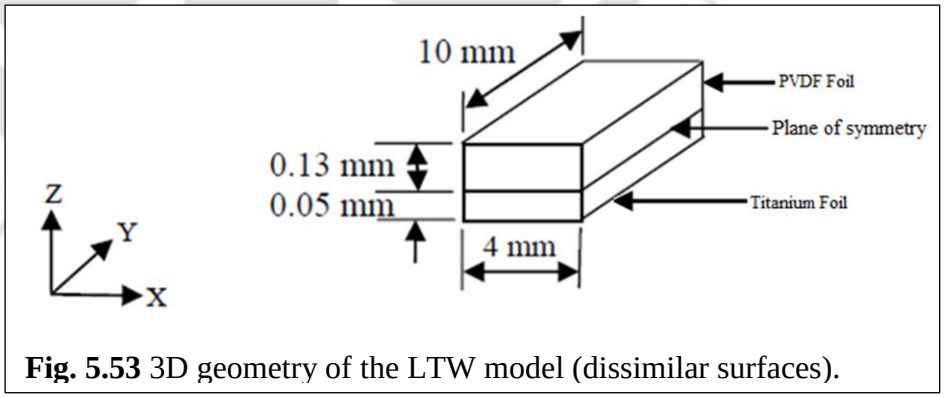

Fig. 5.53 3D geometry of the LTW model (dissimilar surfaces).

Table 5.8 Material property of the materials used for simulation (dissimilar surfaces).

Material	Density (kg/mm^3)	Thermal conductivity (W/m-K)	Specific Heat (J/kg-K)	Melting Point (K)
PVDF	1790	0.13	1214	443
Titanium	4440	17	530	1918

A more general 3-D finite element model for LTW for similar and dissimilar materials is developed including the effect of contact resistance due to the presence of any air gap due to roughness at the weld interface.Capable of calculating the contact conduction without approximating it based on roughness value and temperature developed at the two surface. The present model seems capable of predicting the thermal profile with a fair degree of precision.

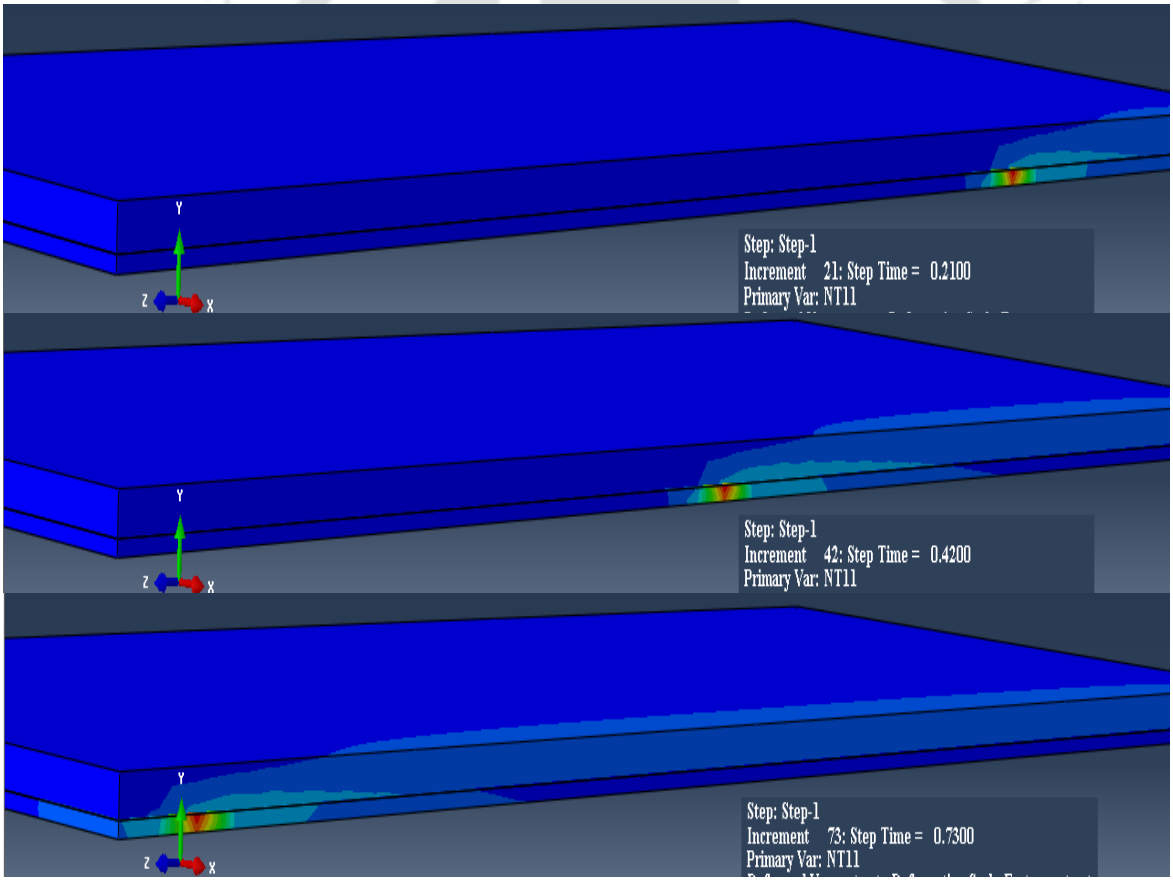

Fig. 5.54 3D computed temperature distribution corresponding to velocity of 800 mm/s and power of 4W at three different locations.

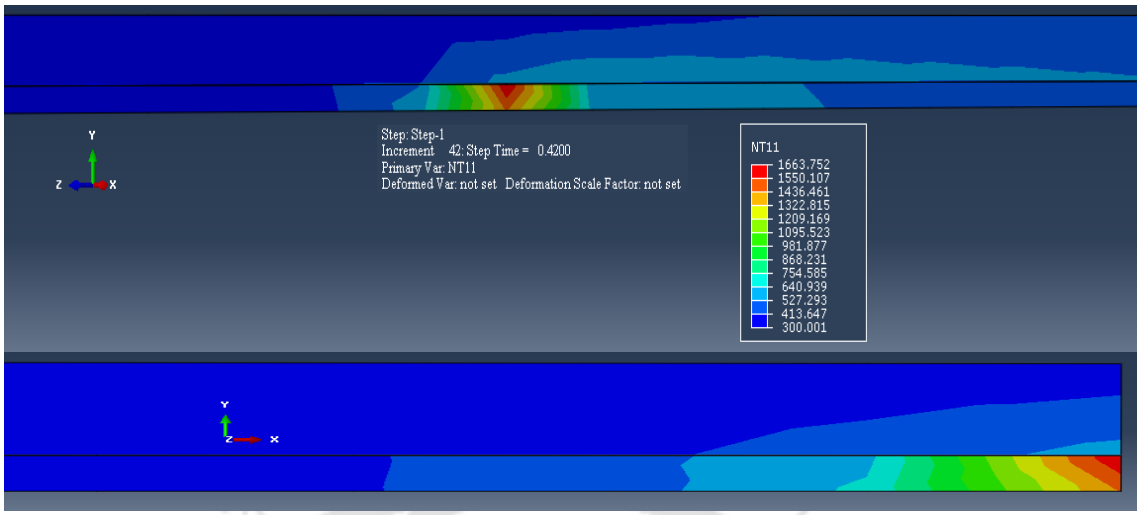

Fig. 5.55 (a) The temperature profile at the centre of the plate (b) the cross-sectional View.

5.9 Ultra-shot Pulse Laser Heating

Fourier's law is commonly used for the description of heat conduction in long pulse laser where heat transfer occurs without any time lag after the application of heat flux. However, Fourier's law is valid under the assumption of local thermodynamic equilibrium, which is violated in very small dimensions and short timescales. Therefore, the heat transfer on microscale or nanoscale substrate with femtosecond or picosecond pulse laser heating has very different physical basis as compared to micro, nano and mili-second pulse laser source. Hence an attempt has been made to understand the heat transfer phenomenon in ultra-short pulse laser heating process using dual phase lag model. The temperature distribution for an ultra-short pulse laser of 100 fs pulse duration is simulated on gold film of 0.1 μm (100 nm) thickness. The developed numerical model under consideration is validated by comparing the simulated results with the experimental data published in literature [Qiu *et al.*, 1994]. Table 5.59 depicts the process parameters and thermal properties of gold used in present simulation. Fig. 5.56 depicts typical three dimensional temperature distribution of ultra-short pulse laser heating of 100 fs pulse width, 2.66 kW peak

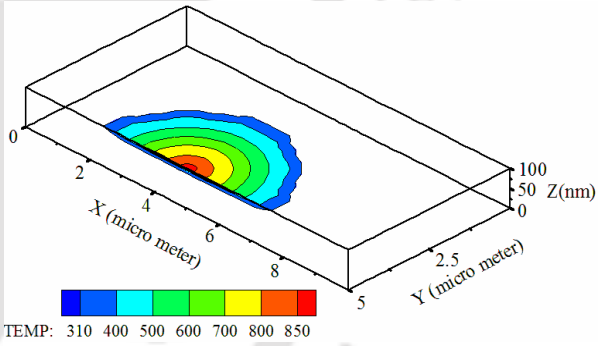

Fig. 5.56 3D temperature distribution of ultra-short pulse laser heating at 100 fs width.

laser power, and 76 MHz pulse repetition rate. The process parameters are similar to the experimental investigation conducted by Qui *et al.* [1994]. The simulated temperature distribution is at the time when peak temperature is the maximum for the first pulse and it is beyond the pulse duration (~ 100 fs). It has been observed from experiment that for pulse of 100 fs and 630 nm wavelength, the radiation penetration depth is almost 15 nm which is much less than the film thickness of 100 nm. There is rapid surface temperature drop observed in the experimental analysis.

Table 5.59 Experimental conditions and thermal properties of gold film [Qui *et al.*, 1993].

Thermal conductivity (W/mK)	315
Thermal diffusivity (m^2/s)	$1.2x10^{-4}$
Relaxation time due to heat flux (ps)	0.05
Relaxation time due temperature gradient (ps)	0.1
Melting temperature (K)	1337
Density (g/cm^3)	19.3
Heat capacity (J/kgK)	136.0
Laser wavelength (nm)	630
Pulse duration (fs)	100
Pulse energy (nJ)	0.266
Pulse repetition rate (MHz)	76
Laser absorption coefficient	0.21

Figure 5.57 depicts the normalized temperature change at the front surface of the gold film of 100 nm. The process parameters are similar to the experimental investigation on gold film. In present analysis, two relaxation parameters are considered as $\tau_q = 0.05$ ps and $\tau_t = 0.1$ ps which is very much analogous to the measured value of specified material [Qiu and Tien, 1993]. However, the relaxation parameters vary a lot depending upon other factors such as dependency on temperature, homogeneity in structure of materials and surface condition[Tzou and Chiu, 2001; Qui *et al.*, 1994]. Therefore, a feasible range of parameters is considered in present investigation. The peak temperature reaches at 0.15 ps and decreases further which is quite consistent with the experimental data [Qui *et al.*, 1994; Tzou, 1995]. The calculated normalized surface temperature $(\Delta T/(\Delta T)_{max})$ is well agreed with analytical solution [Tzou, 1996] as well as finite difference solution by Tzou and Chiu [2001] Although the pulse duration is 100 fs, the peak temperature reaches after 150 fs due to lagging effect of two relaxation times. The thermal inertia produced by differential effect of relaxation develops the lag in temperature inside the body. Therefore, it is necessary to investigate the effect of various uncertain

parameters used for numerical model of heat transfer and an optimum combination of these parameters improves the reliability of physical modelling approach.

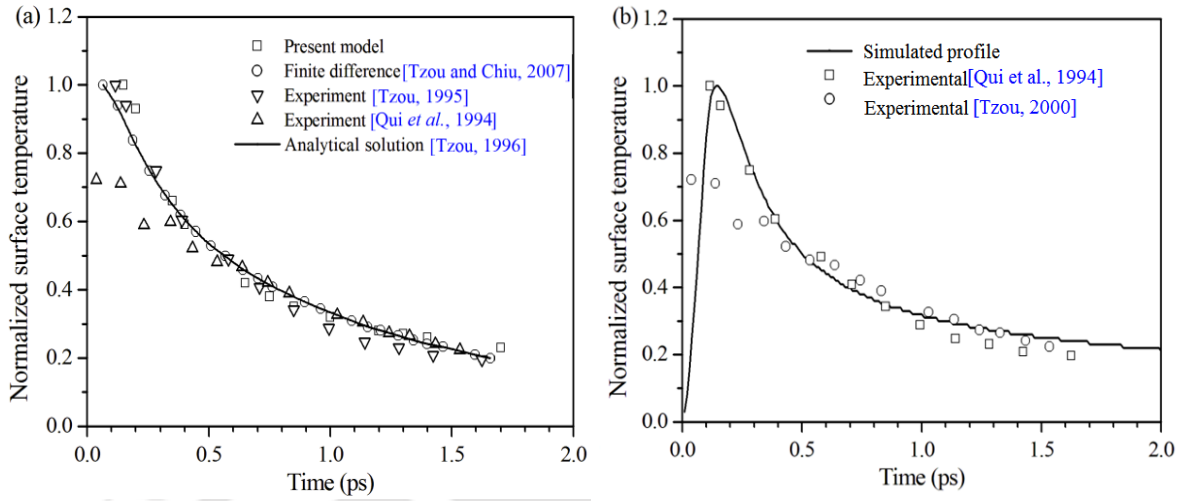

Fig. 5.57 Comparison of normalized surface temperature between experimental and simulated data: (a) discrete data points, and (b) continuous time-temperature profile.

Figure 5.58 depicts three dimensional temperature distribution of laser heating at different time phases of a pulse. The dimension of the solution domain is similar to Fig. 5.58. It is obvious that the maximum temperature is reached at 150 fs (Fig. 5.58d) although the pulse width is 100 fs. The depth of heat affected zone increases with time during cooling phase of the pulse. Even for pulse off-time, the size of heat affected zone is the maximum. This is due to the effect of relaxation to diffuse heat inside the body.

Figure 5.59 describes the variation of temperature at different location of the solution geometry. Here z = 0 represents the top surface of the gold film on which laser pulse irradiates. The depth of heat affected zone is not very high after single pulse which may be the case of an ultra-short pulse heating. However, the time temperature history for multiple pulses predicts higher temperature at various depths. It is observed from Fig. 5.59(a) that the time to reach peak temperature increases along the depth direction. It confirms the finite speed of propagation of thermal wave.

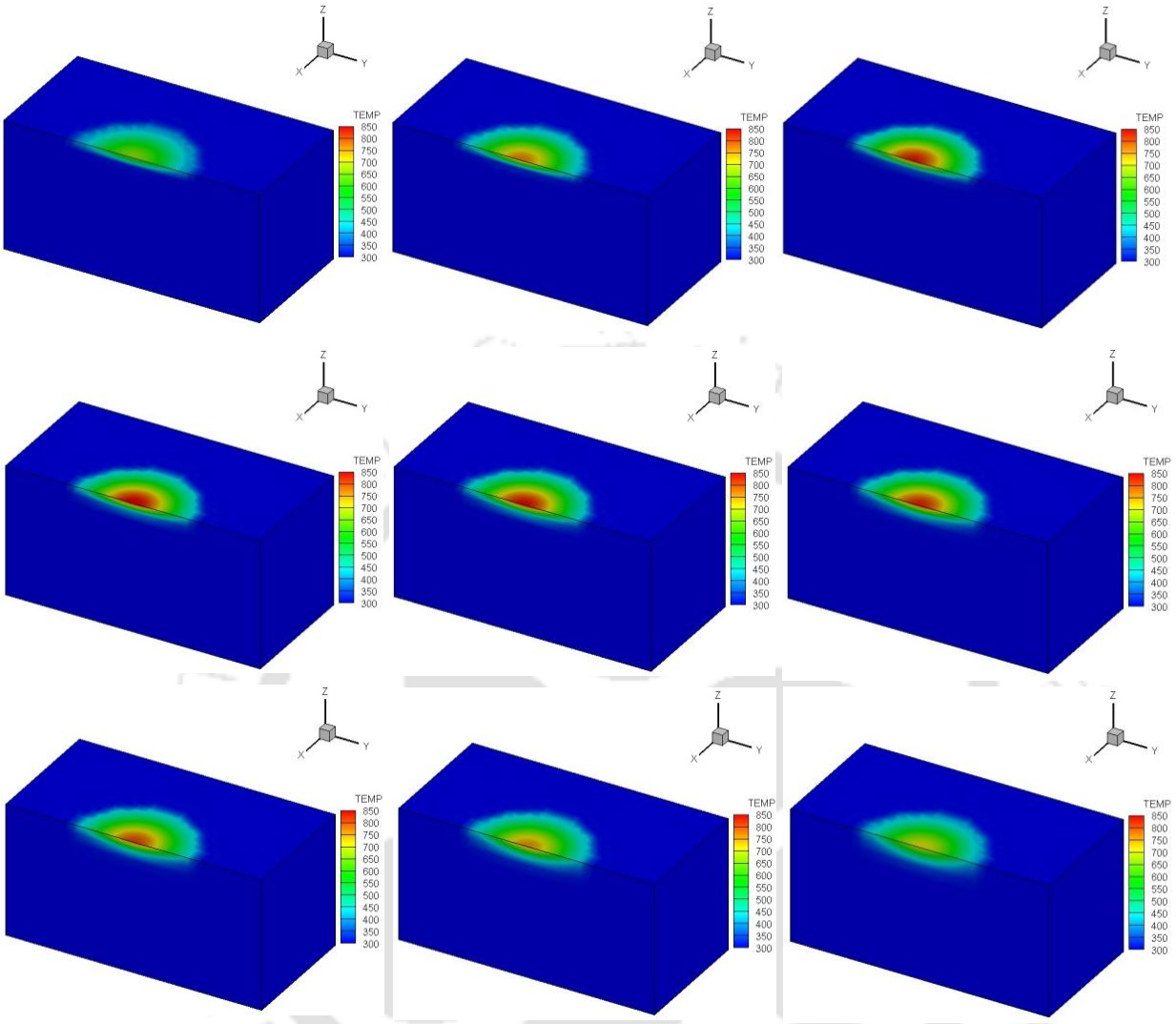

Fig. 5.58 3D temperature distribution of ultra-short pulse laser heating at time (a) 80 fs, (b) 100 fs, (c) 120 fs, (d) 150 fs, (e) 170 fs, (f) 190 fs, (g) 210 fs, (h) 250 fs, (i) 300 fs.

Figure 5.59 also demonstrates the ability of the ultra-short pulse laser to control the depth of penetration (in order of nanometres). It is therefore extensively used in micro and nanomaterial processing of electronic industry. In Fig. 5.59(b), Y = 0.00 μm represents the center of the heat source on the top surface and the distance is calculated from this point in Y- direction. As the effective radius of the laser source in the present work is 2.5 μm, the analysis in Fig. 5.59(b) is done for 0 to 2.5 μm. The heat source has been modelled as Gaussian distributed flux for surface heating. The maximum temperature is generated at the centre point and the

temperature decreases away from the centre. It is observed that the temperature at the centre of laser beam (Y = 0) and at Y = 0.25 μm are almost coinciding. The point Y = 0.25 μm lies very close to the center of the heat source and due to bell shape of the Gaussian distribution it receives almost same amount of heat. However, the time to reach peak temperature for all the points is same since all the points lie within the beam radius and receives the flux at the same time. Hence a special variation of temperature exists.

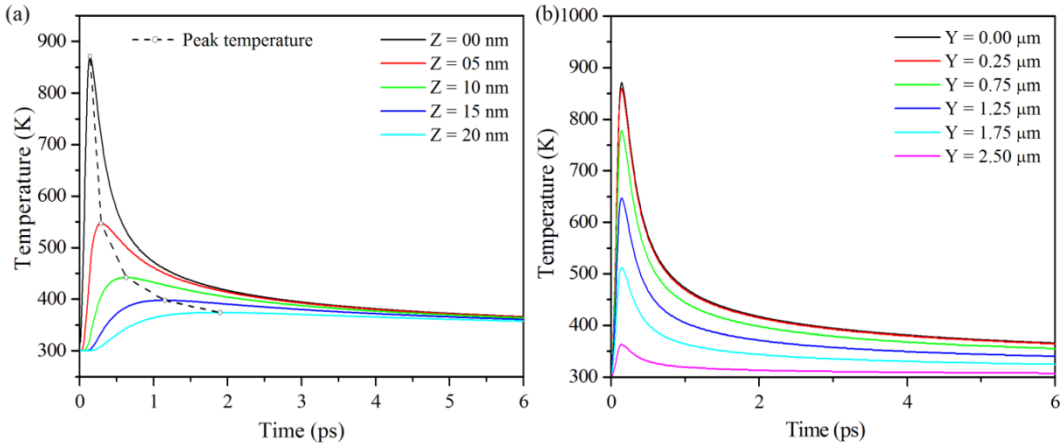

Fig. 5.59 Variation of temperature profile (a) at various depths normal to the surface, and (b) on surface in Y direction of the heat source point.

Figure 5.60(a) depicts the time-temperature history for several pulses for the duration of 110 ns. Since the frequency of the pulse considered in the present work is 76 MHz which provides the cycle time of 13.16 ns, a pulse train with 8 pulses is simulated. It is obvious that after every pulse the base and the peak temperature are increasing slightly which should be the case practically. In order to reach certain temperature (like melting point of gold 1337 K) multiple pulses is required. Practically, in the material processing of very thin films (order of nm) by ultra-short pulse laser, the temperature is raised by multiple pulses to keep track the thermal shock distortion as low as possible. It is noteworthy that the temperature decrement is very rapid for single pulse (in order of few picoseconds) and it is not observable to see all picosecond effect on nanosecond scale. Therefore, Fig. 5.60(b) shows temperature profile for the duration of 2 ps. There is rapid decrement of peak temperature from 860 K to 400 K within a span of 0.15 ps to 2 ps. The estimated cooling rate and heating rate for this process are ~

$2.5x10^{14}$ K/s and ~ $37x10^{14}$ K/s, respectively which is analogous to thermal shock that may produce thermal fatigue.

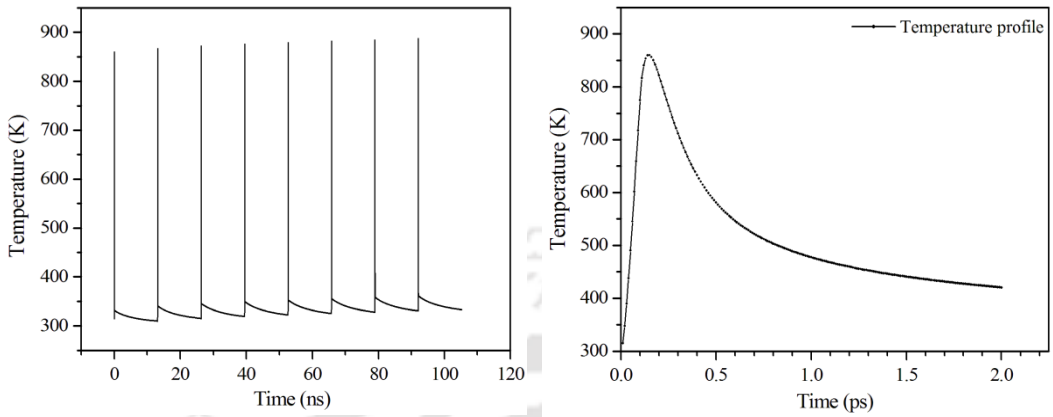

Fig. 5.60 Simulation of time-temperature profile: (a) multiple pulses up to 110 ns, and (b) single pulse.

With the increase of pulse width of an ultra-short pulse laser, the interaction time of laser increases and consequently the peak temperature (Fig. 5.61a). The longer pulse generates higher temperature but the time span to reach peak temperature is also increases (Fig. 5.61b). For 100 fs pulse, peak temperature reaches in 150 fs i.e. even after 100 fs the temperature goes on increasing for another 50 fs. This phenomenon is due to thermal inertia which occurs in almost every pulse heating process. However its effect is nullified when the pulse duration is above microseconds or the relaxation parameter is less than the pulse width of laser heating process. In present simulation, the thermal inertia phenomenon occurs only for few femtoseconds to few picoseconds. It is obvious that the thermal inertia is affected by proper choice of relaxation parameters.

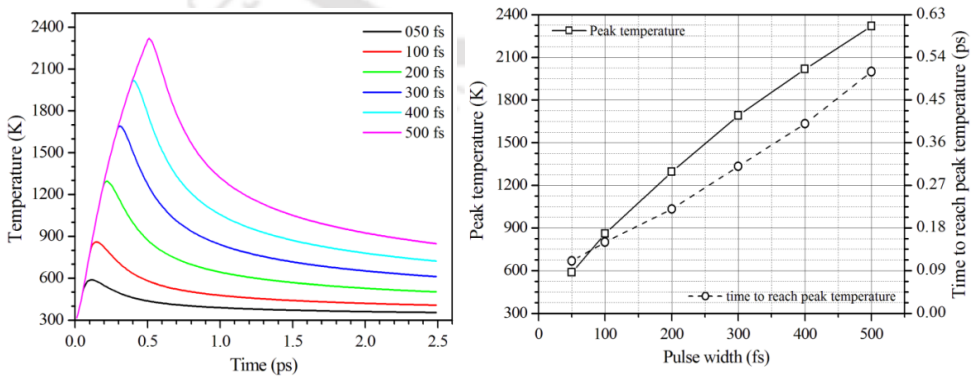

Fig. 5.61 Effect of pulse width on (a) surface temperature, and (b) peak temperature to reach.

In dual phase lag model, τ_t is the delay in establishing the temperature gradient across the target (gold film) and τ_t is also known as microstructural inertia [Tzou, 1995]. By increasing the value of τ_t, the lag in establishing the temperature gradient will increase. However, the amount of heat conducted depends on temperature gradient. Thus, by increasing τ_t the amount of heat conducted will decrease and the surface temperature will not increase. This effect is clearly observed in Fig. 5.62 in which the peak temperature reduces by increasing τ_t. As τ_t does not contribute much to the thermal inertia hence there is not much increase in the time span to reach peak temperature upon increasing τ_t. Let us assume that a slice from the work piece of thickness δz. The temperature on top and bottom of the film is T_1 and T_2 respectively and both are same (i.e. ambient temperature) before application of heat flux so that no heat is getting conducted. The instant the heat flux was applied on the top surface T_1 started to increase, thus a temperature gradient is created ($\Delta T = T_1 - T_2$) and heat starts getting conducted into the film. Now τ_t can be assumed as the amount of time required to affect T_2 (increase or decrease). If τ_t is large then T_2 which was initially at ambient temperature will change (increase) after large amount of time (τ_t). Thus higher temperature gradient (ΔT) will be created for larger instance of time due to which amount of heat conducted into the film will increase and thus very less heat will get accumulated on the surface leading to decrease in the peak temperature. If τ_t is very small, then T_2 will increase very quickly which will not allow a decent temperature gradient to get established. So heat will be conducted into the medium slowly causing the accumulation of heat on the surface which further leads to high peak temperature. Finally, by increases τ_t peak temperature should reduce which is observed in Fig. 5.62(b). This is also explanation on why Fourier model predicts more surface temperature than non-Fourier model. In Fourier model as τ_t is 0, so in no time T_2 starts to increase (due to infinite speed of propagation of heat wave) which causes a lot of heat to get accumulated on the surface leading to a high value of peak temperature.

The relaxation time due to heat flux τ_q is mainly responsible for thermal inertia. By increasing τ_q the thermal inertia by the heating pulse increases. This causes temperature to increase even after pulse is off. Thus time at which peak temperature reaches will increase and is clearly observed in the Fig. 5.63. τ_q also causes delay in establishing the heat flux and associated conduction through the target. On increasing τ_q heat flux remains unsteady for longer duration of

time. In the absence of constant heat flux, the heat supply decreases and further causes the reduction of peak temperature. Therefore, increase in τ_q causes decrease in peak temperature which can be observed in Fig. 5.63(b). In present case, the pulse width is 0.1 ps so the peak temperature does not reach at the end of the pulse but roughly after pulse width plus the τ_q amount of time. It is an observation from present set of calculation and may not true always. However, the above data shows the effect of thermal inertia and how the time of peak temperature increases with increase in τ_q. For metals, $\tau_q$is in order of sub picosecond and hence present analysis is done by varying τ_q in the required order.

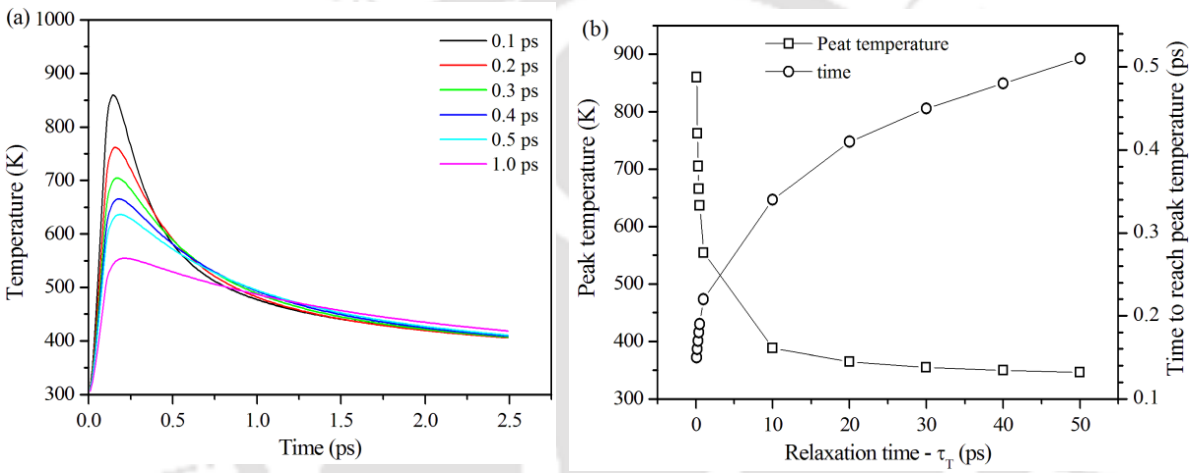

Fig. 5.62 Effect of relaxation time due to temperature gradient: (a) on temperature profile and (b) time elapsed to reach peak temperature.

Let us assume that the RHS of Eq. (3.22) is represented as $F(t,x)$ and τ_t is constant (0.1 ps). $F(t,x)$is a function of space and time which corresponds to amount of heat conducted into the target after applying the heat flux q which further changes the temperature of the target. Now Eq. (3.22) is written as

$$q = F(t,x) - \tau_q \frac{\partial q}{\partial t} \qquad (5.11)$$

Form Eq. (5.11) it can be concluded why τ_q is called lag time or relaxation time. When the heat flux is applied at any target the entire heat is not conducted into the target instantaneously due to the finite speed of thermal wave. So on applying q amount of heat flux $\left\{F(t,x) - \tau_q \frac{\partial q}{\partial t}\right\}$ amount of heat is conducted into the surface, which is less than $F(t,x)$ and would have been conducted in case of Fourier law. So $\tau_q \frac{\partial q}{\partial t}$ amount of heat flux gets lagged behind due to the transient behavior of the heat flux for short period of time τ_q. It is obvious from Eq. (5.11) that by increasing τ_q the amount of heat (i.e. q) to be conducted decreases. Thus less heat is conducted into the surface which reduces the peak temperature. Hence, upon increasing τ_q the peak temperature decreases which can be observed in Fig. 5.63(b). It is observed from Fig. 9(a) that the temperature profile is wavy in nature at $\tau_q = 1\ ps$. Since the ration $\frac{\tau_T}{\tau_q} =$ 0.1 is low for this case, the system predicts wavy nature of temperature profile.

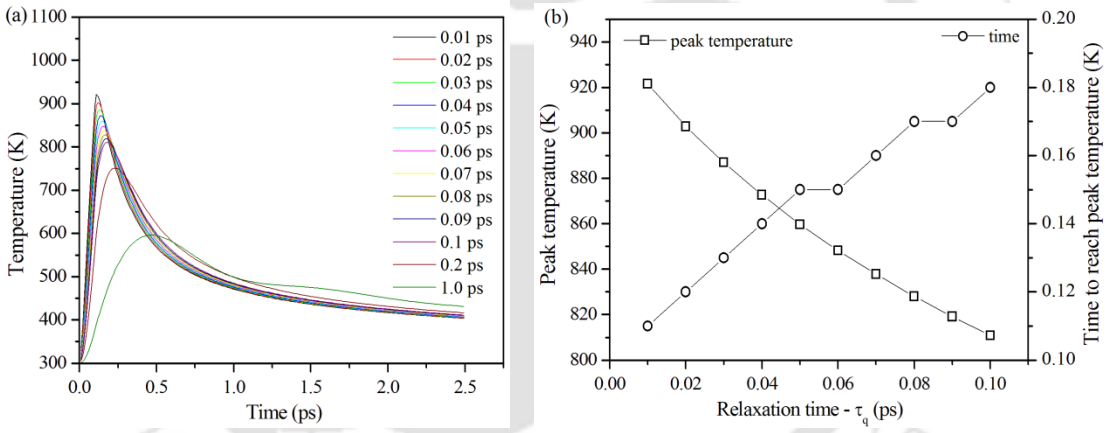

Fig. 5.63 Effect of relaxation time due to heat flux: (a) on temperature profile and (b) to reach peak temperature.

A comparative analysis is performed on the effect of τ_q (relaxation time due to heat flux) and τ_t (relaxation time due to temperature gradient) to reach maximum temperature i.e. peak temperature. The range of values of τ_q in Fig. 5.64(a) and the range of values of τ_t in Fig. 5.64(b) are kept same in plotting of their respective temperature profile so that their affect can be compared. The fixed values of other relaxation parameters i.e. τ_t and τ_q in this analysis are considered as same which are best suited for the verification of experimental results i.e. τ_t = 0.1

ps and τ_q = 0.05 ps. A black dot at the end of the temperature curve denotes the maximum value of temperature. Since the pulse width used in each case is 0.1 ps so a dotted line is drown perpendicular to the x-axis (i.e. time axis) at 0.1 ps in both the Figs 5.64(a) and 5.64(b) to denote the end of the pulse on-time (after this time no heat is supplied for the rest of the cycle i.e. 0.1 ps to 13.15 ns). It is obvious that τ_q mainly corresponds to thermal inertia and it is observed that for a particular value of τ_q (Fig. 10a) the peak temperature is reached at much greater time than for the same value of τ_t (Fig. 5.64b). For instance when $\tau_q = 20.0$ ps the peak temperature is reached at 2.07 ps whereas it is 0.41 s for the same value of $\tau_t = 20.0$ ps. It is observed from Fig. 5.64(a) that by varying τ_q from 0.1 ps to 50 ps the time of peak temperature goes up from 0.18 ps to 3.26 ps whereas it is from 0.15 ps to 0.51 ps by varying τ_t from 0.1 ps to 50 ps. Hence in the modelling of ultra-short pulse laser heating where duration of heat transfer (or the duration for which temperature will increase) is very important factor in order to precisely control the heat affected zone. The analysis reveals the fact that τ_q is more significant parameter thenτ_t . It is observed from Fig. 5.64(c) that the time of peak temperature increases gradually as τ_q is increased gradually. There is almost linear variation in the time of peak temperature and τ_q. For instance, peak temperature reaches in 0.11, 0.12, 0.13, 0.14, 0.15 ps for τ_q equal to 0.01, 0.02, 0.03, 0.04 and 0.05 ps, respectively. Time to reach peak temperature is exactly equal to the sum of pulse width and theτ_q. However this relation is lost by varying τ_q beyond 0.1 ps.

Thus, a robust mathematical process simulation model for ultra-short pulse laser heating is developed using finite element method. Overall, the experimental measurement of ultra-fast heating process is expensive for a thin film. Hence the demand of a reliable quantitative heat transfer model using lagging phenomena is ever increasing. The present work is a contribution in this direction. The detail derivation of the finite element model can be enhanced further for ultra-short pulse laser welding process. However, further validation of calculated results of temperature distribution for different process conditions is necessary to reliably establish the process model reported in this work.

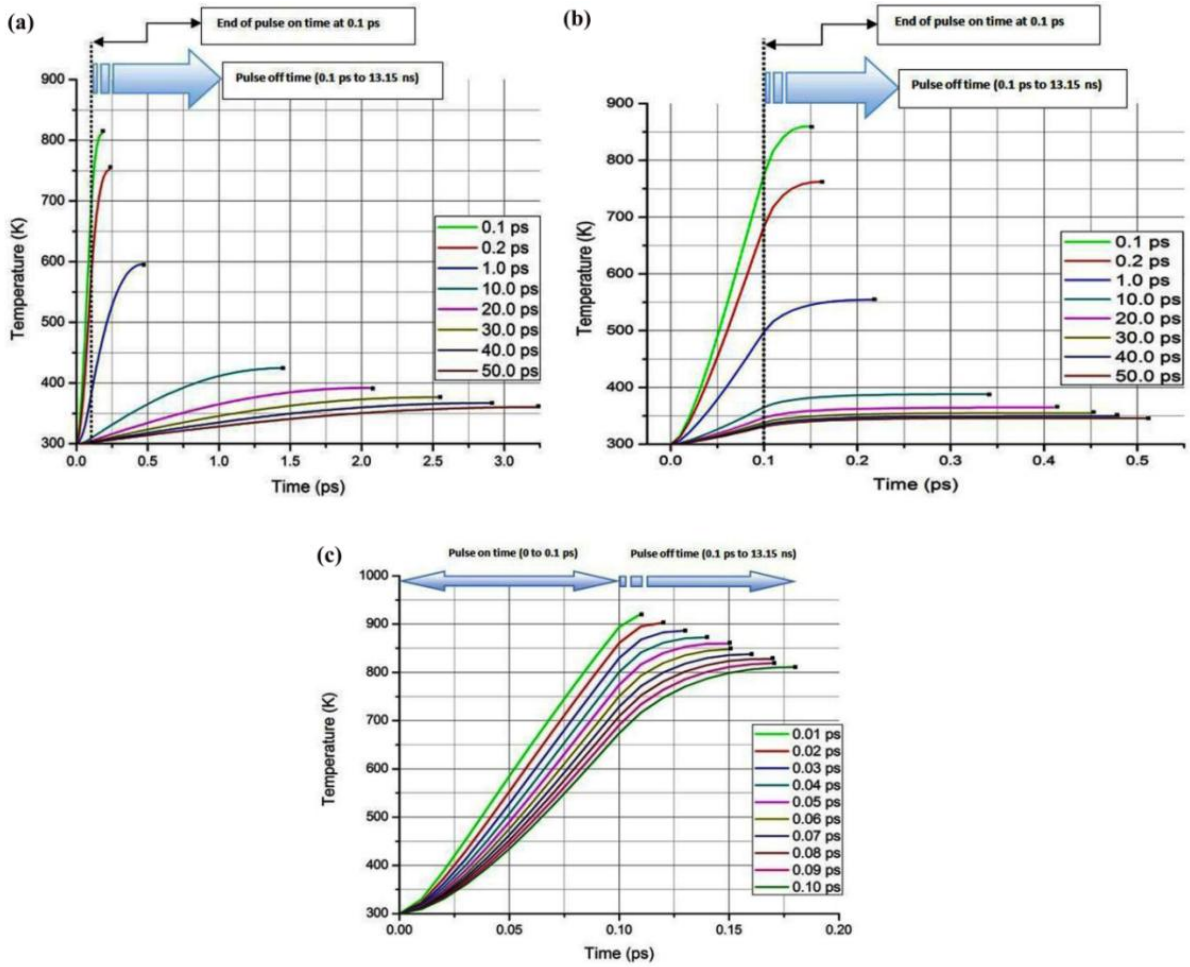

Fig. 5.64 (a) Temperature profile for different values of τ_q (0.1 to 50 ps) for τ_t = 0.1 ps; (b) Temperature profile for different values of τ_t (0.1 to 50 ps) for τ_q = 0.05 ps; (c) Temperature profile at the various values of τ_q (0.01 to 0.1 ps) and τ_t = 0.1 ps.

5.10 Summary

A three-dimensional sequentially coupled thermo-mechanical model has been developed to simulate the distribution of temperature and residual distortion during plasma and laser microwelding processes. The temperatures are well below the vaporization temperature of the materials and hence it can be concluded that the conduction mode heat transfer prevails against keyhole formation within this power density range used for microwelding of 0.5 mm thick plate. It is also obvious that the heat affected zone is confined in small area due to effect of copper fixture. The fusion zone geometry calculated from model is in good agreement with the

experimentally measured weld pool dimensions. The error is at the maximum of 15%. The distortion increases with increase in heat input due to greater amount of heat available at a specific area. The out of plane deformation predicted by considering the non-linearity matches well with the experimental values. However, the consideration of phase transformation effect may reduce the difference. The residual stress is mainly due to the longitudinal stress and the plastic zone is very small. Thus the residual stress feature is highly localized and leads to less distortion.

A three-dimensional numerical heat transfer and fluid flow model has been also been developed thereafter to simulate the evolution of temperature and velocity fields during laser microwelding of 304 stainless steel and titanium. HS algorithm is utilised to identify the suitable values of a set of unknown variables that are required for modelling calculations. The integrated model inherently identifies the optimum values of three significant input variables that are well within the range of similar value reported earlier. The computed results match well with the experimental values collected from independent literature. Error analysis has been performed to check the performance of the numerical model. It was found that most of the cases maximum the error is below 15%. The velocity and peak temperature increase with the increase in peak power for the same pulse length. Though the fusion zone was small, yet the Peclet number was found to be greater than one, which enhances the importance of convection in heat transfer analysis of the weld pool. The fluid flow was mainly driven by Marangoni force and to a much smaller extent by buoyancy force as indicated by order-of-magnitude analysis.

The heat transfer process for ultra-short pulse laser heating is simulated using Non-Fourier dual phase lag heat conduction model over nanometre film thickness. The various features of the developed numerical model have been illustrated by quantitative analysis of transient heat transfer. The model results are validated with experimental results of thin gold film. The developed model confirms the belief on the effect of significant parameters like pulse width and relaxation times. An attempt has been made to understand the physical significance of two relaxation parameters and their effect on the time-temperature history. Decreasing the pulse width, the thermal inertia effect increases rapidly. The relaxation in heat flux is the main reason for thermal inertia that increases with the magnitude of relaxation time. For these particular process parameters, the heat affected zone is controlled in such a way that the surface is confined

to a very low depth. The simulation is performed for multi pulses in which the rise of the peak and base temperature is observed after every pulse. However, the influence of pulse shape on heating process is important to make the model more reliable and robust that precisely controls the temperature of nanoscale system.

A 3D numerical model is also developed which accounted for all physical phenomena associated with the LTW. The model involving moving distributed heat flux for laser transmission welding has been implemented into FE thermal simulations to predict temperature field during the process. The simulated results are validated by comparing with experimental results collected from independent literature. The profile of the fusion zone of the absorbing part agreed well with the experimental one. The LTW is being applied in joining various thermoplastics, various dissimilar materials, plastics to metals etc. Thus process is being extended to joining of micro parts for applications in various industries. Also the clear weld technique for joining two clear thermoplastic parts even introduced some great flexibility into laser welding.

Chapter 6

Conclusions and Future Scope

6.0 Introduction

With the miniature of the products, the demands for micro scale manufacturing process are ever increasing. Microwelding is one of such developed joining process where the intense and regulated heat source from laser or plasma is useful to fuse the material over a narrow zone. Therefore, the evolution of parametric domain for defect free weld joint is significant contribution in the present research work. Laser or plasma microwelding of several materials such as stainless steel, low carbon steel and titanium alloy are investigated in the present work. However, fusion microwelding involves a complex interaction of heat transfer, material flow, evolution of solidified microstructures, and temperature induced strains and stresses. A concrete thermo-mechanical model is always better path to understand the micro welding processes. The numerical models developed in this work both for the conduction and transport phenomena based heat transfer analyses are based on finite element method. The primary achievement of the present work lies in the identification of process window for microwelding of several materials and development of a three dimensional thermo-mechanical model to simulate the evolution of temperature and residual distortion in microwelding process. A well tested thermo-fluid model is also used to analyze the material flow in laser microwelding process. Temperature dependent material properties and latent heat of melting and solidification are included thoroughly into both the conduction and convective heat transfer models. Optimization algorithm is also incorporated with numerical model to identify the most suitable unknown model input parameters. In general, two fusion welding processes are studied i.e. micro plasma welding and laser micro welding. Calculated results from numerical model are validated against experimental data. A 3D numerical model using ABAQUS is also developed including the effect of contact resistance due

to the presence of any air gap at the weld interface. A simulation work is also carried out on the effect of ultra-short pulse laser processing over a nano-film thickness using non-Fourier heat conduction model.

6.1 Conclusions

The following conclusions are arrived at in the course of reviewing literatures, developing the computational exercise, and conducting the experiments on micro plasma arc and laser micro welding processes. Thus, the present methodology developed for microwelding of 500 μm thick materials is good alternative for joining of thin sheets. The prediction of temperature and distortion field using developed numerical model is relatively better for micro scale application. The accuracy of numerical model can be further improved by incorporating the residual stress generated due to volumetric change and transformation induced plasticity.

- The conduction based numerical model attempt to consider Gaussian distributed surface heat flux or volumetric heat source. It is realized that the surface heat flux may not be sufficient for micro welding process with concentrated heat intensity. In that case, the volumetric heat source is more appropriate and *a-priori* knowledge of solidified weld dimensions from experiment is required. However, the conduction heat transfer analysis with the volumetric heat source term tends to become inadequate in the cases when the welding conditions confirm to very high heat input. An "hour-glass" type heat source model to simulate the laser micro welding at higher heat input is required. Thus, an accurate heat source is a necessity for the reliability of the numerical model.
- In numerical modeling of fusion welding process, the input model parameters such as arc efficiency, effective thermal conductivity, and effective viscosity cannot be assigned with confidence based on scientific principles alone. But, the parameters like welding power, welding speed etc. can be correctly specified. To estimate the correct values of uncertain model parameters, an effort towards integration of suitable optimization tool with numerical model is required.
- The optimized values of unknown model input parameters are successfully achieved by intrinsically supporting the process FE model through Harmony search optimization process. The integrated model is also developed to the extent that the same can compute quantitative

information of thermal cycles and cooling rate using the optimum value of unknown model parameters.

- The fluid flow in small weld pool in case of microwelding is significant since it considers realistic physical phenomena and enhances the reliability of temperature estimation as compared to only conduction mode heat transfer analysis. Also, the Peclet number was found to be greater than one, which ensures the importance of convection in heat transfer analysis of the weld pool. The fluid flow was mainly driven by Marangoni force and to a much smaller extent by buoyancy force as indicated by order-of-magnitude analysis in case of laser microwelding process.
- The investigation is carried out on plasma microwelding of titanium alloy, austenitic stainless steel, and low carbon steel. Laser micro welding of Ti6Al4V is also carried out. The formation of oxides influences the mechanical properties of the welded joints. Thus, the extra shielding gas is used to avoid oxidation problem of titanium alloy. The specifically designed fixture reduces the distortion of thin sheet in plasma microwelding process.
- The heat input per unit length is an important parameter to obtain a stable welding. There is a positive correlation between welding speed and welding current for microplasma welding with all other process parameters remaining constant. When the welding speed is increased, the proper welding current range shifts toward the higher-current side. It is found the weld bead increases with current up to a certain limit after which burn out of the material occurs. The selective welding speed and arc current for welding indicates that there may be a process map that produces successful joints in plasma micro welding process. This graph can be used to determine the type of weld at different parameters and can further be used for predicting the weld types at higher currents and speeds.
- In microwelding of titanium alloy, the fusion zone mainly consists of α' martensitic phase and of a small quantity of β phase. This is because the cooling rate is greater than the critical cooling rate i.e. around 600 K/s. The mono-phase martensitic structure greatly contributes to the mechanical properties of the welded joints. With further increases in heat input lamellar α growth takes place which lowers the strength. Overall, the heat input must be kept moderate (i.e. optimum) for better mechanical properties. The tensile strength of joints obtained under the current study is almost similar to that of base metal, and it is well in accordance with the relationship between microstructure and mechanical properties of welded joints.

Microhardness of fusion zone is higher than that of the base metal due to the formation of α' martensitic phase.

- The temperatures are well below the vaporization temperature of the materials and hence it can be concluded that the conduction mode heat transfer prevails against keyhole formation within this power density range used for microwelding of 0.5 mm thick plate. Although the consideration of actual material flow is more realistic, the conduction only heat transfer analysis facilitates the coupled thermo-mechanical analysis. The fusion zone geometry calculated from only heat conduction model is in good agreement with the experimentally measured weld pool dimensions. The error is at the maximum of ~ 15%.
- It is found that the longitudinal bending is higher compare to the transverse bending in the welded sheets. The deflection increases with heat input and becomes almost constant with further increase in heat input. The distortion increases with increase in heat input due to greater amount of heat available at a specific area. The residual stress is mainly due to the longitudinal stress and the plastic zone is very small. Thus the residual stress feature is highly localized and leads to less distortion. The out of plane deformation predicted by considering the non-linearity matches well with the experimental values. However, the consideration of phase transformation effect may reduce the difference.
- A suitable combination of process parameters i.e. pulse energy, pulse width and welding speed for pulse Nd:YAG laser micro welding of 500 µm thick Ti6Al4V is evaluated. The distortion increases with increase in heat input due to greater amount of heat available at a specific area. The hardness is found very high in the fusion zone due to presence of fine martensitic structure. The deflection pattern and value predicted by the current model matches well with the experimental values. The residual stress feature is highly localized. The longitudinal residual stress is much higher than that of transverse residual stress. The plastic zone is very small and depends on the constraints and property of the material rather than the difference in heat input.
- The feasible range of the process parameters for micro plasma arc welding of 500 µm thick low carbon steel and SS304 is evaluated. SS304 requires less heat input to produce similar fusion zone of low carbon steel which means faster welding for the same heat input at similar welding speed. Slower diffusion of heat in SS304 results in concentration of the heat effected zone of the material within a narrow area. On the other hand, due to greater diffusivity of low

carbon steel, the heat gets dissipated more quickly so that the peak temperature is lower in low carbon steel at the weld line as compared to SS304.

- The hardness value is found to be highest at the fusion zone for SS304 weldment while at the HAZ for low carbon steel. Due to higher expansion coefficient and greater concentration of temperature with a small area, the distortion is more for SS304 weldments. The out of plane deformation predicted by considering the nonlinearity agrees well with the experimental values. However the distortion pattern of SS304 shows a buckling behaviour. The residual stress is mainly due to the longitudinal stress and the plastic zone is very small for both the materials.
- The LTW is being applied in joining various thermoplastics, various dissimilar materials, plastics to metals etc. Thus process is being extended to joining of micro parts for applications in various industries. The 3-D finite element model for LTW for similar and dissimilar materials is developed including the effect of contact resistance due to the presence of any air gap and due to roughness at the weld interface is capable of calculating the contact conduction without approximating it based on roughness value and temperature developed at the two surface.
- The heat transfer process for ultra-short pulse laser heating is simulated using the non-Fourier dual phase lag heat conduction model over nanometer film thickness. The model results are validated with experimental results of a thin gold film. By decreasing the pulse width, the thermal inertia effect increases rapidly. The relaxation in heat flux is the main reason for thermal inertia that increases with the magnitude of relaxation time. For these particular process parameters, the heat affected zone is controlled in such a way that the surface is confined to a very low depth. The simulation is performed for multipulses in which the rise of the peak and base temperature is observed after every pulse. However, the influence of pulse shape on heating process is important to make the model more reliable and robust that precisely controls the temperature of nanoscale system.
- Finally, the calculation method and quantitative knowledge extracted from this research work in fusion welding process will expected to serve as a basis for the control of fusion welding processes aimed at achieving enhanced reliability. Titanium and its alloys have replaced many materials and have been utilized for diverse application due to biocompatibility. Thus, the present study is mainly focused on microjoining of 500 μm titanium alloys to find out

feasible range of process variables both for micro plasma arc welding and Nd:YAG pulse laser welding. Also micro plasma arc welding has been performed to join 500 μm thick SS304 and low carbon steel in butt joint configuration as both the material are most widely used. Welding speed range of 2-7 mm/s and current of 5-20 A have been found suitable for microplasma welding of 500 μm. This envelope of parameters can be further extended to join sheets of various thicknesses. Laser microwelding with a constant pulse repetition rate of 20 Hz, pulse width of 3-5 ms and pulse energy of more than 5 J upto a certain threshold limit, has been found suitable to join 500 μm thick Ti6Al4V alloy. The laser microwelding can be further utilized to join thin sheets by varying other parameters like pulse repetition rate etc. The laser micro welded joint as compared to micro plasma weld produces smaller heat effect zone and refined grain size with lesser distortion.

6.2 Scope of future work

The development of micro welding system is primary target of the present work. An effort has been put forward to develop the process window of successful butt weld joint for three different types of materials. However the experimental processes and the analysis techniques can be improved in several ways. The experimental measurement of residual stress development in microwelding process is worthy to investigate. However, the theoretical prediction of residual stresses or distortion in the micro joining process is ever challenging that includes the effect of phase transformation and transformation induced plasticity. The effect of pulse shaping in heat transfer phenomena specifically for microwelding process can be a future direction of investigation. The modulation of pulse is helpful in joining of difficult-to-weld materials and also dissimilar combination of materials. Utilization of the gap-conduction to simulate heat transfer phenomena including the effect of contact resistance between the workpiece and fixture certainly can enhance the reliability of modeling approach.

Appendix A

The Fourier law of heat conduction in x direction under the assumption of reaching equilibrium condition instantaneously is expressed as

$$q = -k\frac{\partial T}{\partial x} \tag{A1}$$

where q is the applied heat flux, $\frac{\partial T}{\partial x}$ is the temperature gradient and k is the thermal conductivity of the medium. In ultra-fast process, if we consider two intrinsic delay times i.e. dual phase lags to reach in equilibrium condition at finite time, the modified version of Fourier heat conduction is expressed as

$$q(t + \tau_q) = -k\frac{\partial T(t+\tau_T)}{\partial x} \tag{A2}$$

where$\tau_q$and τ_T are two relaxation times. The first order expansion of Eq. (A2) for dual phase lag model is represented by

$$q + \tau_q \frac{\partial q}{\partial t} = -k\left\{\frac{\partial T}{\partial x} + \tau_T \frac{\partial}{\partial t}\left(\frac{\partial T}{\partial x}\right)\right\} \tag{A3}$$

Now differentiating Eq. (A1) we get

$$\frac{\partial q}{\partial x} = -k\frac{\partial^2 T}{\partial x^2} \tag{A4}$$

This equation is one-dimensional energy equation for incompressible solids with no internal heat generation or absorption. One-dimensional unsteady state heat conduction without internal heat generation is given by

$$\frac{\partial^2 T}{\partial x^2} = \frac{\rho c}{k}\frac{\partial T}{\partial t} \tag{A5}$$

From Eqs. (A4) & (A5) it can be written as

$$\frac{\partial q}{\partial x} = -\rho c\frac{\partial T}{\partial t} \tag{A6}$$

Now differentiating Eq. (A3) we get

$$\frac{\partial q}{\partial x} + \tau_q \frac{\partial}{\partial x}\left(\frac{\partial q}{\partial t}\right) = -k\left[\frac{\partial^2 T}{\partial x^2} + \tau_T \frac{\partial}{\partial x}\left\{\frac{\partial}{\partial t}\left(\frac{\partial T}{\partial x}\right)\right\}\right] \tag{A7}$$

Now rearranging the Eq. (A7), it is obtained as

$$\frac{\partial q}{\partial x}+\tau_q\frac{\partial}{\partial t}\left(\frac{\partial q}{\partial x}\right)=-k\left\{\frac{\partial^2 T}{\partial x^2}+\tau_T\frac{\partial^2}{\partial x^2}\left(\frac{\partial T}{\partial t}\right)\right\} \quad \text{(A8)}$$

Substituting the relation of Eq. (A6) in Eq. (A8), we get

$$\frac{\partial T}{\partial t}+\tau_q\frac{\partial^2 T}{\partial t^2}=\frac{k}{\rho c}\left\{\frac{\partial^2 T}{\partial x^2}+\tau_T\frac{\partial^2}{\partial x^2}\left(\frac{\partial T}{\partial t}\right)\right\} \quad \text{(A9)}$$

where thermal diffusivity $\alpha=\frac{k}{\rho c}$. Therefore, non-Fourier heat conduction equation in x-direction is represented as

$$\frac{\partial T}{\partial t}+\tau_q\frac{\partial^2 T}{\partial t^2}-\alpha\frac{\partial^2 T}{\partial x^2}-\alpha\tau_T\frac{\partial^2}{\partial x^2}\left(\frac{\partial T}{\partial t}\right)=0 \quad \text{(A10)}$$

Therefore, the non-Fourier heat conduction equation with double phase lag in three dimensions form is written as

$$\dot{T}+\tau_q\ddot{T}-\alpha\left(\frac{\partial^2 T}{\partial x^2}+\frac{\partial^2 T}{\partial y^2}+\frac{\partial^2 T}{\partial z^2}\right)-\tau_T\alpha\left(\frac{\partial^2 \dot{T}}{\partial x^2}+\frac{\partial^2 \dot{T}}{\partial y^2}+\frac{\partial^2 \dot{T}}{\partial z^2}\right)=0 \quad \text{(A11)}$$

or $$\frac{\partial T}{\partial t}+\tau_q\frac{\partial^2 T}{\partial t^2}-\alpha\nabla^2 T-\tau_T\alpha\nabla^2\frac{\partial T}{\partial t}=0 \quad \text{(A12)}$$

where $\dot{T}=\frac{\partial T}{\partial t}$ and $\ddot{T}=\frac{\partial^2 T}{\partial t^2}$

Appendix B

The governing equation of DPL model is given by

$$\dot{T} + \tau_q \ddot{T} - \alpha \nabla^2 T - \tau_T \alpha \nabla^2 \dot{T} = 0 \tag{B1}$$

The boundary condition for DPL model is represented as

$$k_n \left(\frac{\partial T}{\partial n} + \tau_T \frac{\partial \dot{T}}{\partial n}\right) = q + \tau_q \frac{\partial q}{\partial t} - h_{eff}(T - T_0) \tag{B2}$$

Using Galerkin's weighted residue technique, if w_1 is the weighted residual function of governing equation over an elemental volume 'dV' and $w_2$is the weighting function of boundary condition over elemental surface 'dS' then

$$\int_v w_1 R_1 dV + \int_s w_2 R_2 dS = 0 \tag{B3}$$

where R is the residual and is represented as $R_1 = \dot{T} + \tau_q \ddot{T} - \alpha \nabla^2 T - \tau_T \alpha \nabla^2 \dot{T}$

and $R_2 = k_n \left(\frac{\partial T}{\partial n} + \tau_T \frac{\partial \dot{T}}{\partial n}\right) - q - \tau_q \frac{\partial q}{\partial t} + h_{eff}(T - T_0)$

Therefore, $\int_v w_1 R_1 dV$ becomes

$$\int_v w_1 \dot{T} dV + \int_v \tau_q w_1 \ddot{T}\, dV - \int_v \alpha w_1 \left(\frac{\partial^2 T}{\partial x^2} + \frac{\partial^2 T}{\partial y^2} + \frac{\partial^2 T}{\partial z^2}\right) dV - \int_v \tau_T \alpha w_1 \left(\frac{\partial^2 \dot{T}}{\partial x^2} + \frac{\partial^2 \dot{T}}{\partial y^2} + \frac{\partial^2 \dot{T}}{\partial z^2}\right) dV = 0 \tag{B4}$$

Integrating by parts and using greens theorem of the components of Eq. (B4),

$$\int_v \alpha w_1 \left(\frac{\partial^2 T}{\partial x^2} + \frac{\partial^2 T}{\partial y^2} + \frac{\partial^2 T}{\partial z^2}\right) dV = \int_s \alpha w_1 \frac{\partial T}{\partial n} dS - \int_v \alpha \left(\frac{\partial w_1}{\partial x}\frac{\partial T}{\partial x} + \frac{\partial w_1}{\partial y}\frac{\partial T}{\partial y} + \frac{\partial w_1}{\partial z}\frac{\partial T}{\partial z}\right) dV \tag{B5}$$

and

$$\int_v \tau_T \alpha w_1 \left(\frac{\partial^2 \dot{T}}{\partial x^2} + \frac{\partial^2 \dot{T}}{\partial y^2} + \frac{\partial^2 \dot{T}}{\partial z^2}\right) dV = \int_s \tau_T \alpha w_1 \frac{\partial \dot{T}}{\partial n} dS - \int_v \tau_T \alpha \left(\frac{\partial w_1}{\partial x}\frac{\partial \dot{T}}{\partial x} + \frac{\partial w_1}{\partial y}\frac{\partial \dot{T}}{\partial y} + \frac{\partial w_1}{\partial z}\frac{\partial \dot{T}}{\partial z}\right) dV \tag{B6}$$

Eq. (B4) takes the form after using greens theorem and integrating by parts

$$\int_v w_1 \dot{T} dV + \int_v \tau_q w_1 \ddot{T}\, dV - \left\{\int_s \frac{w_1 k_n}{\rho c}\left(\frac{\partial T}{\partial n} + \tau_T \frac{\partial \dot{T}}{\partial n}\right) dS\right\} + \int_v \alpha\left(\frac{\partial w_1}{\partial x}\frac{\partial T}{\partial x} + \frac{\partial w_1}{\partial y}\frac{\partial T}{\partial y} + \frac{\partial w_1}{\partial z}\frac{\partial T}{\partial z}\right) dV +$$
$$\int_v \tau_T \alpha\left(\frac{\partial w_1}{\partial x}\frac{\partial \dot{T}}{\partial x} + \frac{\partial w_1}{\partial y}\frac{\partial \dot{T}}{\partial y} + \frac{\partial w_1}{\partial z}\frac{\partial \dot{T}}{\partial z}\right) dV = 0 \quad \text{(B7)}$$

Now Fourier heat conduction law in three dimensional forms is written as

$$q = -k\nabla T \quad \text{(B8)}$$

Differentiating Fourier's equation with respect to time

$$\frac{\partial q}{\partial t} = -k\nabla \dot{T} \quad \text{(B9)}$$

Now substituting $\frac{\partial q}{\partial t} = -k\left(\frac{\partial \dot{T}}{\partial x} + \frac{\partial \dot{T}}{\partial y} + \frac{\partial \dot{T}}{\partial z}\right)$ in Eq. (B2)

$$k_n\left[\frac{\partial T}{\partial n} + \tau_T \frac{\partial \dot{T}}{\partial n}\right] = q - \tau_q k\left(\frac{\partial \dot{T}}{\partial x} + \frac{\partial \dot{T}}{\partial y} + \frac{\partial \dot{T}}{\partial z}\right) - h_{eff}(T - T_0) \quad \text{(B10)}$$

Now $\int_s w_2 R_2 dS$ becomes

$$\int_s \frac{w_2 k_n}{\rho c}\left(\frac{\partial T}{\partial n} + \tau_T \frac{\partial \dot{T}}{\partial n}\right) dS = \int_s \frac{q}{\rho c} w_2\, dS - \int_s \tau_q \frac{k}{\rho c} w_2 \left(\frac{\partial \dot{T}}{\partial x} + \frac{\partial \dot{T}}{\partial y} + \frac{\partial \dot{T}}{\partial z}\right) dS - \int_s \frac{h_{eff}}{\rho c} w_2 T dS +$$
$$\int_s \frac{h_{eff} T_0}{\rho c} w_2\, dS \quad \text{(B11)}$$

If $w_1 = w_2 = w$, the derivation from Eqs. (B4) & (B12) is written as

$$\int_v w \dot{T} dV + \int_v \tau_q w \ddot{T}\, dV - \int_s \frac{q}{\rho c} w\, dS + \int_s \tau_q \frac{k}{\rho c} w \left(\frac{\partial \dot{T}}{\partial x} + \frac{\partial \dot{T}}{\partial y} + \frac{\partial \dot{T}}{\partial z}\right) dS + \int_s \frac{h_{eff}}{\rho c} w T dS -$$
$$\int_s \frac{h_{eff} T_0}{\rho c} w\, dS + \int_v \alpha\left(\frac{\partial w}{\partial x}\frac{\partial T}{\partial x} + \frac{\partial w}{\partial y}\frac{\partial T}{\partial y} + \frac{\partial w}{\partial z}\frac{\partial T}{\partial z}\right) dV + \int_v \tau_T \frac{k}{\rho c}\left(\frac{\partial w}{\partial x}\frac{\partial \dot{T}}{\partial x} + \frac{\partial w}{\partial y}\frac{\partial \dot{T}}{\partial y} + \frac{\partial w}{\partial z}\frac{\partial \dot{T}}{\partial z}\right) dV = 0 \quad \text{(B12)}$$

If we consider an element of 'n' nodes and temperature at corresponding nodes are $T_1, T_2 \ldots\ldots\ldots T_n$ and the nodal shape functions are $N_1, N_2 \ldots\ldots\ldots\ldots N_n$. The temperature T in term of shape function of an element is represented as

$$T = N_1 T_1 + N_2 T_2 + \ldots\ldots\ldots + N_n T_n \qquad \text{i.e. } T = [N]\{T\} \quad \text{(B13)}$$

$$\frac{\partial T}{\partial x} = \lfloor N_x \rfloor \{T\}; \frac{\partial T}{\partial y} = \lfloor N_y \rfloor \{T\}; \frac{\partial T}{\partial z} = \lfloor N_z \rfloor \{T\}; \frac{\partial T}{\partial t} = \dot{T} = \lfloor N \rfloor \{\dot{T}\}; \frac{\partial^2 T}{\partial t^2} = \ddot{T} = \lfloor N \rfloor \{\ddot{T}\}; \frac{\partial}{\partial x}\left(\frac{\partial T}{\partial t}\right) = \frac{\partial \dot{T}}{\partial x} = [N_x]\{\dot{T}\}$$

It is assumed that the weight function w is equal to shape function. Therefore,

$$\frac{\partial w}{\partial x} = [N_x]; \frac{\partial w}{\partial y} = [N_y]; \frac{\partial w}{\partial z} = [N_z] \tag{B14}$$

The form of the Eq. (B12) is as follows:

$$\int_v \rho c[N][N]\{\dot{T}\}dV + \int_v \tau_q \rho c[N][N]\{\ddot{T}\}dV + \int_s \tau_q k\left[[N][N_x] + [N][N_y] + [N][N_z]\right]\{\dot{T}\}dS + \int_s h_{eff}[N][N]\{T\}dS + \int_v k\left[[N_x][N_x] + [N_y][N_y] + [N_z][N_z]\right]\{T\}dV + \int_v \tau_T k\left[[N_x][N_x] + [N_y][N_y] + [N_z][N_z]\right]\{\dot{T}\}dV = \int_s q\{N\}dS + \int_s h_{eff}T_0\{N\}dS \tag{B15}$$

Now the final algebraic equation over the special domain is written as

$$[K]\{T\} + [M]\{\ddot{T}\} + [C]\{\dot{T}\} = \{F\} \tag{B16}$$

where the coefficients [K] , [M]and [C]are

$$[K] = [K]_v + [K]_s \tag{B17}$$

$$[K]_v = \int_v k\left[[N_x][N_x] + [N_y][N_y] + [N_z][N_z]\right]dV \tag{B18}$$

$$[K]_s = \int_s h_{eff}[N][N]\,dS \tag{B19}$$

$$[M] = \int_v \tau_q \rho c[N][N]\,dV \tag{B20}$$

$$[C] = [C]_{v1} + [C]_{v2} + [C]_{s1} \tag{B21}$$

$$[C]_{v1} = \int_v \rho c[N][N]dV \tag{B22}$$

$$[C]_{v2} = \int_v \tau_T k\left[[N_x][N_x] + [N_y][N_y] + [N_z][N_z]\right]dV \tag{B23}$$

$$[C]_{s1} = \int_s \tau_q k\left[[N][N_x] + [N][N_y] + [N][N_z]\right]dS \tag{B24}$$

$$\{F\} = \{F\}_1 + \{F\}_2 \tag{B25}$$

$$\{F\}_1 = \int_s h_{eff}T_0\{N\}dS \tag{B26}$$

$$\{F\}_2 = \int_s q\{N\}dS \tag{B27}$$

The matrix [K], [M] and [C] can be calculated by numerical integration. Gauss quadrature method is used for numerical integration.

To get temperature distribution Newmark method [28] is used. The function and its first time derivative are approximated according to

$$\{\dot{T}^{t+\Delta t}\} = \{\dot{T}^{t}\} + [(1-\delta)\{\ddot{T}^{t}\} + \delta\{\ddot{T}^{t+\Delta t}\}]\,\Delta t \tag{B28}$$

and

$$\{T^{t+\Delta t}\} = \{T^{t}\} + \{\dot{T}^{t}\}\Delta t + \left[\left(\frac{1}{2}-\beta\right)\{\ddot{T}^{t}\} + \beta\{\ddot{T}^{t+\Delta t}\}\right](\Delta t)^2 \tag{B29}$$

where β and δ are parameter that can be determined to obtain accuracy and stability. With reference to the final Eq. (B16) the updated value of [K] at time $t+\Delta t$ is expressed as

$$[\hat{K}] = [[K] + a_0[M] + a_1[C]] \tag{B30}$$

Also the updated value of load vector at time $t+\Delta t$ is expressed as

$$\{\hat{F}^{t+\Delta t}\} = \left\{\{F^{t+\Delta t}\} + [M]\left(a_0\{T^{t}\} + a_2\{\dot{T}^{t}\} + a_3\{\ddot{T}^{t}\}\right) + [c]\left(a_1\{T^{t}\} + a_4\{\dot{T}^{t}\} + a_5\{\ddot{T}^{t}\}\right)\right\} \tag{B31}$$

where $a_0 = \frac{1}{\beta(\Delta t)^2}$, $a_1 = \frac{\delta}{\beta\Delta t}$, $a_2 = \frac{1}{\beta\Delta t}$, $a_3 = \frac{1}{2\beta} - 1$, $a_4 = \frac{\delta}{\beta} - 1$, $a_5 = \frac{\Delta t}{2}\left(\frac{\delta}{\beta} - 2\right)$

Now the temperature T at time $t+\Delta t$ is calculated by

$$[\hat{K}]\{T^{t+\Delta t}\} = \{\hat{F}^{t+\Delta t}\} \tag{B32}$$

$$\text{i.e.}\{T^{t+\Delta t}\} = \left[[K] + \frac{1}{\beta(\Delta t)^2}[M] + \frac{\delta}{\beta\Delta t}[C]\right]^{-1}\left\{\{F^{t+\Delta t}\} + [M]\left(\frac{1}{\beta(\Delta t)^2}\{T^{t}\} + \frac{1}{\beta\Delta t}\{\dot{T}^{t}\} + \left(\frac{1}{2\beta} - 1\right)\{\ddot{T}^{t}\}\right) + [c]\left(\frac{\delta}{\beta\Delta t}\{T^{t}\} + \left(\frac{\delta}{\beta} - 1\right)\{\dot{T}^{t}\} + \frac{\Delta t}{2}\left(\frac{\delta}{\beta} - 2\right)\{\ddot{T}^{t}\}\right)\right\} \tag{B33}$$

The matrix relation gives temperature vector $\{T^1\}$ at the end of time step Δt in terms of known temperature given as vector $\{T^2\}$ at the start of the time step. Knowing the $\{T^2\}$ we can determine $\{T^3\}$ and thus proceed for subsequent step. It is noteworthy that the estimation of load vector is done on previous load step i.e. $\{F^{t+\Delta t}\} = \{F^{t}\}$. Therefore, $\{\dot{T}\}$and$\{\ddot{T}\}$at time $t+\Delta t$ calculated by

$$\{\ddot{T}^{t+\Delta t}\} = \frac{1}{\beta(\Delta t)^2}\left(\{T^{t+\Delta t}\} - \{T^{t}\}\right) - \frac{1}{\beta\Delta t}\{\dot{T}^{t}\} - (\frac{1}{2\beta} - 1)\{\ddot{T}^{t}\} \tag{B34}$$

$$\{\dot{T}^{t+\Delta t}\} = \{\dot{T}^{t}\} + \Delta t(1-\delta)\{\ddot{T}^{t}\} + \delta\Delta t\{\ddot{T}^{t+\Delta t}\} \tag{B35}$$

Appendix C

Hourglass heat source model

For a high heat input, at any plane perpendicular to the Z-axis, the heat intensity distribution of a laser heat source:

$$\dot{Q}(Z, r) = q_o \exp\left[-d\frac{r^2}{{r_{eff}}^2}\right] \quad \text{(C1)}$$

where P refers to laser power, r_{eff} is effective radius of laser beam on the work piece surface, d is the power density distribution factor of heat source and r is the radial co-ordinate. For simplicity and to reduce the number of process parameters, it is assumed 1 – R = α, R and α are reflectivity and absorption coefficient of the material.

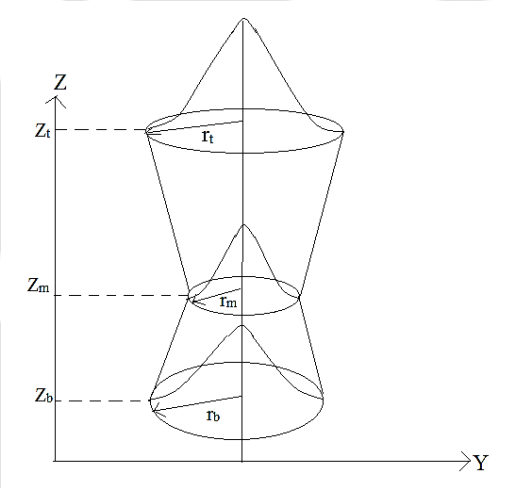

Fig. C1 Hourglass heat source model.

For the upper cone,

$$\frac{r_o - r_m}{r_t - r_m} = \frac{Z_o - Z_m}{Z_t - Z_m} \quad \text{(C2)}$$

$$r_o = \frac{Z_o - Z_m}{Z_t - Z_m}(r_t - r_m) + r_m \quad \text{(C3)}$$

For the lower cone,

$$r_o = \frac{Z_o - Z_b}{Z_m - Z_b}(r_b - r_m) + r_m \quad \text{(C4)}$$

The thermal energy conservation energy,

$$\eta P = \int_0^H \int_0^{2\pi} \int_0^{r_o} \dot{Q}(Z,r)\, r\, dr\, d\theta\, dh = \int_0^H \int_0^{2\pi} \int_0^{r_o} \frac{\alpha dP}{\pi {r_{eff}}^2} \exp\left[-d\frac{r^2}{{r_{eff}}^2}\right] r\, dr\, d\theta\, dh$$

$$= \int_0^H \int_0^{2\pi} \int_0^{r_o} q_o \exp\left[-d\frac{r^2}{{r_{eff}}^2}\right] r\, dr\, d\theta\, dh \quad \text{(C5)}$$

1st integration,

$$\int_0^{r_o} q_o \exp\left[-d\frac{r^2}{{r_{eff}}^2}\right] r\, dr = \frac{-q_o {r_o}^2}{2d}[\exp(-d) - 1] = \frac{q_o {r_o}^2}{2d}[1 - \exp(-d)] \quad \text{(C6)}$$

Thus eq. (C5) becomes

$$\int_0^H \int_0^{2\pi} \frac{q_o {r_o}^2}{2d}[1 - \exp(-d)]\, d\theta\, dh = \frac{q_o \pi}{d}[1 - \exp(-d)] \int_0^H {r_o}^2 dh \quad \text{(C7)}$$

For the upper cone,

$${r_o}^2 = \left[\frac{Z_o - Z_m}{Z_t - Z_m}(r_t - r_m) + r_m\right]^2 \quad \text{(C8)}$$

Putting, $h = Z_o - Z_m$ and $H = Z_t - Z_m$, the eq. (C8) becomes

$${r_o}^2 = \left[\frac{h}{H}(r_t - r_m) + r_m\right]^2 = \frac{[H.r_m + h.r_t - h.r_m]^2}{H^2} = \frac{[H^2.{r_m}^2 + h^2.{r_t}^2 + h^2.{r_m}^2 + 2.H.h.r_m.r_t - 2.h^2.r_m.r_t - 2.H.h.{r_m}^2]}{H^2} \quad \text{(C9)}$$

Thus, for the upper cone,

$$\int_0^H {r_o}^2 dh = \int_0^H \frac{[H^2.{r_m}^2 + h^2.{r_t}^2 + h^2.{r_m}^2 + 2.H.h.r_m.r_t - 2.h^2.r_m.r_t - 2.H.h.{r_m}^2]}{H^2}\, dh = \frac{H[{r_m}^2 + r_m.r_t + {r_t}^2]}{3} \quad \text{(C10)}$$

Thus, eq. (C5) becomes

$$\eta P = \frac{q_o \pi}{d}[1 - \exp(-d)]\frac{H[{r_m}^2 + r_m.r_t + {r_t}^2]}{3} \quad \text{(C11)}$$

Therefore,

$$q_o = \frac{3d\eta P}{\pi.[1 - \exp(-d)].H[{r_m}^2 + r_m.r_t + {r_t}^2]} \quad \text{(C12)}$$

Now, eq. (C1) becomes

$$\dot{Q}(Z,r) = \frac{3d\eta P}{\pi.[1 - \exp(-d)].(Z_t - Z_m)[{r_m}^2 + r_m.r_t + {r_t}^2]} \exp\left[-d\frac{r^2}{{r_{eff}}^2}\right]; \quad \text{for upper cone } (Zo \geq Zm) \quad \text{(C13)}$$

$$\dot{Q}(Z,r) = \frac{3d\eta P}{\pi.[1 - \exp(-d)].(Z_m - Z_b)[{r_m}^2 + r_m.r_t + {r_t}^2]} \exp\left[-d\frac{r^2}{{r_{eff}}^2}\right]; \quad \text{for lower cone } (Zo < Zm) \quad \text{(C14)}$$

References

Abe, N., Funada, Y., Imanaka, T. and Tsukamoto, M., 2005. Micro welding of thin stainless steel foil with a direct diode laser. *Transactions of JWRI, 34 (1)*, pp.19-23.

Acherjee, B., Kuar, A., Mitra, S. and Mitra, D., 2010. Finite element simulation of laser transmission welding of dissimilar materials between polyvinylidene fluoride and titanium. *International Journal of Engineering, Science and Technology*, *2*(4), pp.176-186.

Acherjee, B., Kuar, A.S., Mitra, S. and Misra, D., 2012. Effect of carbon black on temperature field and weld profile during laser transmission welding of polymers: A FEM study. *Optics & Laser Technology*, *44*(3), pp.514-521.

Ahmed, T. and Rack, H.J., 1998. Phase transformations during cooling in α+ β titanium alloys. *Materials Science and Engineering: A*, *243*(1), pp.206-211.

Akbari, M., Saedodin, S., Toghraie, D., Shoja-Razavi, R. and Kowsari, F., 2014. Experimental and numerical investigation of temperature distribution and melt pool geometry during pulsed laser welding of Ti6Al4V alloy. *Optics & Laser Technology*, *59*, pp.52-59.

Akman, E., Demir, A., Canel, T. and Sınmazçelik, T., 2009. Laser welding of Ti6Al4V titanium alloys. *Journal of materials processing technology*, *209*(8), pp.3705-3713.

Assuncao, E. and Williams, S., 2013. Comparison of continuous wave and pulsed wave laser welding effects.*Optics and Lasers in Engineering*, *51*(6), pp.674-680.

Atma Raj, M.R. and Joy Varghese, V.M., 2014. Determination of Distortion Developed During TIG welding of low carbon steel plate. *International Journal of Engineering Research and General Science*, 2(5), pp.756-767.

Attarha, M.J. and Sattari-Far, I., 2011. Study on welding temperature distribution in thin welded plates through experimental measurements and finite element simulation. *Journal of Materials Processing Technology*, *211*(4), pp.688-694.

Azizpour, M., Ghoreishi, M. and Khorram, A., 2015. Numerical Simulation of Laser Beam Welding of Ti6Al4V Sheet. *Journal of Computional Applied Research in Mechanical Engineering*, *4*(2), pp.145-154.

Bag, S., 2011. A perspective review on laser assisted microjoining. *Recent Patents on Mechanical Engineering*, *4*(2), pp.153-167.

Bag, S. and De, A., 2010. Computational modelling of conduction mode laser welding process, laser welding. *InTech. doi*, *10*(5772), pp.9861.

Bag, S., Trivedi, A. and De, A., 2009. Development of a finite element based conduction mode heat transfer model for laser welding process using an adaptive volumetric heat source. *International Journal of Thermal Science*, *48*(10), pp.1923-31.

Bagger, C., Laursen, S. and Olsen, F., 1992. Comparison of a pulsed CO2 laser and a pulsed Nd: YAG laser for welding. In *Proceedings of ICALEO*, 92, pp. 537-546.

Baker, T.S., 1985. *Fatigue Crack Propagation and Fracture Toughness of Plasma Arc Welded Ti-6Al-4V Alloy*. Royal aircraft establishment, Technical report no:85066.

Balasubramanian, T.S., Balakrishnan, M., Balasubramanian, V. and Manickam, M.M., 2011. Influence of welding processes on microstructure, tensile and impact properties of Ti-6Al-4V alloy joints. *Transactions of Nonferrous Metals Society of China*, *21*(6), pp.1253-1262.

Balasubramanian, T.S., Balakrishnan, M., Balasubramanian, V. and Manickam, M.A.M., 2013. Effect of welding processes on joint characteristics of Ti–6Al–4V alloy. *Science and Technology of Welding and Joining*. *16(8)*, pp.702-708.

Bammann, D.J., Prantil, V.C. and Lathrop, J.F., 1995. *A model of phase transformation plasticity* (No.SAND--95-8513C; CONF-9509118--3). Sandia National Labs., Livermore, CA (United States).

Banas, C.M., 1974. Electron beam, laser beam and plasma arc welding studies.

Banerjee, A., Ogale, A.A., Das, C., Mitra, K. and Subramanian, C., 2005. Temperature distribution in different materials due to short pulse laser irradiation. *Heat Transfer Engineering*, *26*(8), pp.41-49.

Barreda, J.L., Santamarıa, F., Azpiroz, X., Irisarri, A.M. and Varona, J.M., 2001. Electron beam welded high thickness Ti6Al4V plates using filler metal of similar and different composition to the base plate. *Vacuum*, *62*(2), pp.143-150.

Bashenko, V.V. and Sosnin, N.A., 1988. Optimization of the plasma arc welding process. *Welding Journal*, *67*(10), pp.233-237.

Batool, S., Khan, M., Jaffery, S.H.I., Khan, A., Mubashar, A., Ali, L., Khan, N. and Anwar, M.N., 2015.Analysis of weld characteristics of micro-plasma arc welding and tungsten inert gas welding of thin stainless steel (304L) sheet. *Proceedings of the Institution of Mechanical Engineers, Part L: Journal of Materials Design and Applications*, pp.1464420715592438.

Becker, F. and Potente, H., 2002. A step towards understanding the heating phase of laser transmission welding in polymers. *Polymer Engineering & Science*, *42*(2), pp.365-374.

Benyounis, K.Y., Olabi, A.G. and Hashmi, M.S.J., 2005. Effect of laser welding parameters on the heat input and weld-bead profile. *Journal of Materials Processing Technology*, *164*, pp.978-985.

Beranoagirre, A., Olvera, D. and de Lacalle, L.L., 2012. Milling of gamma titanium–aluminum alloys. *The International Journal of Advanced Manufacturing Technology*, *62*(1-4), pp.83-88.

Blackburn, J.E., Allen, C.M., Hilton, P.A., Li, L., Hoque, M.I. and Khan, A.H., 2010. Modulated Nd: YAG laser welding of Ti–6Al–4V. *Science and Technology of Welding and Joining*, *15*(5), pp.433-439.

Bortoleto, E.M., Sarmiento, G.S. and Fioranelli, A., 2000. Using Abaqus User Subroutines to Develop a New Finite Element Modeling Tool for Heat Treatment Simulation.

Boyer, R.R., 1996. An overview on the use of titanium in the aerospace industry. *Materials Science and Engineering: A*, *213*(1), pp.103-114.

Brockmann, R., Honekamp, M., Dickmann, K., Meier, S., Lefsch, H. and Matthes, K.J., 2001. Modern welding processes for microsystems engineering and electronics taking particular account of the laser. *Schweissen und Schneiden(Germany)*, *53*(10), pp.230-236.

Buvanashekaran, G., Shanmugam, S.N., Sankaranarayanasamy, K. and Sabarikanth, R., 2009. A study of laser welding modes with varying beam energy levels. *Proceedings of the Institution of Mechanical Engineers, Part C: Journal of Mechanical Engineering Science*, *223*(5), pp.1141-1156.

Caiazzo, F., Curcio, F., Daurelio, G. and Minutolo, F.M.C., 2004. Ti6Al4V sheets lap and butt joints carried out by CO_2 laser: mechanical and morphological characterization. *Journal of Materials Processing Technology*, *149*(1), pp.546-552.

Camilleri, D., Comlekci, T. and Gray, T.F., 2005.Computational prediction of out-of-plane welding distortion and experimental investigation. *The Journal of Strain Analysis for Engineering Design*, *40*(2), pp.161-176.

Cao, X. and Jahazi, M., 2009. Effect of welding speed on butt joint quality of Ti–6Al–4V alloy welded using a high-power Nd: YAG laser. *Optics and Lasers in Engineering*, *47*(11), pp.1231-1241.

Cao, X., Kabir, A.S.H., Wanjara, P., Gholipour, J., Birur, A., Cuddy, J. and Medraj, M., 2014. Global and local mechanical properties of autogenously laser welded Ti-6Al-4V. *Metallurgical and Materials Transactions A*, *45*(3), pp.1258-1272.

Casalino, G., Mortello, M., Contuzzi, N. and Minutolo, F.M.C., 2015.Finite element model for laser welding of titanium.*Procedia CIRP*, *33*, pp.435-440.

Cattaneo, C., 1958. A form of heat conduction equation which eliminates the paradox of instantaneous propagation. *Compte Rendus*, *247*(4), pp.431-433.

Chang, W.S. and Na, S.J., 2002a. A study on heat source equations for the prediction of weld shape and thermal deformation in laser microwelding. *Metallurgical and Materials Transactions B*, *33*(5), pp.757-764.

Chang, W.S. and Na, S.J., 2002b. A study on the prediction of the laser weld shape with varying heat source equations and the thermal distortion of a small structure in micro-joining. *Journal of materials processing technology*, *120*(1), pp.208-214.

Chakraborty, N. and Chakraborty, S., 2005. Influences of sign of surface tension coefficient on turbulent weld pool convection in a gas tungsten arc welding (GTAW) process: A comparative study. *Journal of heat transfer*, *127*(8), pp.848-862.

Chen, J.K., Beraun, J.E., Grimes, L.E. and Tzou, D.Y., 2002. Modeling of femtosecond laser-induced non-equilibrium deformation in metal films. *International Journal of Solids and Structures*, *39*(12), pp.3199-3216.

Chan, C., Mazumder, J. and Chen, M.M., 1984. A two-dimensional transient model for convection in laser melted pool. *Metallurgical Transactions A*, *15*(12), pp.2175-2184.

Chen, J.C. and Pan, C.X., 2011. Welding of Ti-6Al-4V alloy using dynamically controlled plasma arc welding process. *Transactions of Nonferrous Metals Society of China*, *21*(7), pp.1506-1512.

Chen, W. and Molian, P., 2008. Dual-beam laser welding of ultra-thin AA 5052-H19 aluminum. *The International Journal of Advanced Manufacturing Technology*, *39*(9-10), pp.889-897.

Chen, M., 2009. Gap bridging in laser transmission welding of thermoplastics. Thesis, Queen's University, Kingston, Ontario, Canada.

Cheng, P.Y., 2009. Influence of residual stress and heat affected zone on fatigue failure of welded piping joints. Thesis, North Carolina State University, Raleigh, North Carolina.

Cherepanov, A.N. and Shapeev, V.P., 2009. Numerical investigation of the process of welding of thin metal plates. *Computational Technologies*, *14*(3), pp.96-106.

Cherepanov, A.N., Shapeev, V.P., Fomin, V.M. and Semin, L.G., 2006. Numerical simulation of thermophysical processes at laser beam welding. *Journal of Applied Mechanics and Technical Physics*, (5), pp.88-96.

Chmelíčková, H. and Šebestová, H., 2012. Pulsed Laser Welding. Nd YAG Laser, Dr. Dan C.Dumitras (Ed.), InTech.

Choobi, M.S., Haghpanahi, M. and Sedighi, M., 2010. Investigation of the effect of clamping on residual stresses and distortions in butt-welded plates. *Scientia Iranica. Transaction B, Mechanical Engineering*, *17*(5), p.387.

Choobi, M.S., 2013. Investigating the effect of geometrical parameters on distortions in butt-welded plates. *The Journal of Strain Analysis for Engineering Design*, *48*(4), pp.258-268.

Chung, C.K. and Lin, Y.C., 2005. Simulation and fabrication for pin-to-plate microjoining by Nd: YAG laser. *Microsystem technologies*, *12*(1-2), pp.104-109.

Coelho, J.P., Abreu, M.A. and Pires, M.C., 2000. High-speed laser welding of plastic films. *Optics and lasers in engineering*, *34*(4), pp.385-395.

Cui, C., Hu, B., Zhao, L. and Liu, S., 2011. Titanium alloy production technology, market prospects and industry development. *Materials & Design*, *32*(3), pp.1684-1691.

Darcourt, C., Roelandt, J.M., Rachik, M., Deloison, D. and Journet, B., 2004, December. Thermomechanical analysis applied to the laser beam welding simulation of aeronautical structures. In *Journal de Physique IV (Proceedings)* (Vol. 120, pp. 785-792). EDP sciences.

De, A. and DebRoy, T., 2005. Reliable calculations of heat and fluid flow during conduction mode laser welding through optimization of uncertain parameters. *Welding Journal*, *84*(7), pp.101-112.

De, A. and DebRoy, T., 2011. A perspective on residual stresses in welding. *Science and Technology of Welding and Joining*, *16*(3), pp.204-208.

De, A., Maiti, S.K., Walsh, C.A. and Bhadeshia, H.K.D.H., 2003. Finite element simulation of laser spot welding. *Science and Technology of Welding and Joining*, *8*(5), pp.377-384.

DebRoy, T. and David, S.A., 1995. Physical processes in fusion welding. *Reviews of modern physics*, *67*(1), p.85.

Del Coz Diaz, J.J., Rodríguez, P.M., Nieto, P.G. and Castro-Fresno, D., 2010. Comparative analysis of TIG welding distortions between austenitic and duplex stainless steels by FEM. *Applied Thermal Engineering*, *30*(16), pp.2448-2459.

Deng, D., 2009. FEM prediction of welding residual stress and distortion in carbon steel considering phase transformation effects.*Materials & Design*, *30*(2), pp.359-366.

Deng, D., Liang, W. and Murakawa, H., 2007. Determination of welding deformation in fillet-welded joint by means of numerical simulation and comparison with experimental measurements. *Journal of Materials Processing Technology*, *183*(2), pp.219-225

Deng, D. and Murakawa, H., 2006. Numerical simulation of temperature field and residual stress in multi-pass welds in stainless steel pipe and comparison with experimental measurements.*Computational materials science*, *37*(3), pp.269-277.

Deng, D. and Murakawa, H., 2008a. Finite element analysis of temperature field, microstructure and residual stress in multi-pass butt-welded 2.25 Cr–1Mo steel pipes. *Computational materials science*, *43*(4), pp.681-695.

Deng, D. and Murakawa, H., 2008b. FEM prediction of buckling distortion induced by welding in thin plate panel structures. *Computational Materials Science*, *43*(4), pp.591-607.

Deng, D., Murakawa, H. and Liang, W., 2007. Numerical simulation of welding distortion in large structures. *Computer methods in applied mechanics and engineering*, *196*(45), pp.4613-4627.

Deng, D., Zhou, Y., Bi, T. and Liu, X., 2013. Experimental and numerical investigations of welding distortion induced by CO_2 gas arc welding in thin-plate bead-on joints. *Materials & Design*, *52*, pp.720-729.

Denney, P.E. and Metzbower, E.A., 1989. Laser beam welding of titanium.*Welding Journal*, *68*(8), pp.342s-346s.

Desai, R.S. and Bag, S., 2014. Influence of displacement constraints in thermomechanical analysis of laser micro-spot welding process. *Journal of Manufacturing Processes*, *16*(2), pp.264-275.

Deshpande, A.A., Short, A.B., Sun, W., McCartney, D.G., Xu, L. and Hyde, T.H., 2012. Finite element-based analysis of experimentally identified parametric envelopes for stable keyhole plasma arc welding of a titanium alloy. *The Journal of Strain Analysis for Engineering Design*, *47*(5), pp.266-275.

Deshpande, A.A., Xu, L., Sun, W., McCartney, D.G. and Hyde, T.H., 2011. Finite-element-based parametric study on welding-induced distortion of TIG-welded stainless steel 304 sheets. *The Journal of Strain Analysis for Engineering Design*, *46*(4), pp.267-279.

Dhinakaran, V., Shanmugam, N.S. and Sankaranarayanasamy, K., 2015. Some studies on temperature field during plasma arc welding of thin titanium alloy sheets using parabolic Gaussian heat source model. *Proceedings of the Institution of Mechanical Engineers, Part C: Journal of Mechanical Engineering Science*, pp.1-17.

Dhorajiya, A.P., Mayeed, M.S., Auner, G.W., Baird, R.J., Newaz, G.M., Patwa, R. and Herfurth, H., 2010. Finite element thermal/mechanical analysis of transmission laser microjoining of titanium and polyimide. *Journal of Engineering Materials and Technology*, *132*(1), p.011004.

Donachie, M.J., 2000. *Titanium: a technical guide*. ASM international.

Du, H., Hu, L., Liu, J. and Hu, X., 2004. A study on the metal flow in full penetration laser beam welding for titanium alloy. *Computational Materials Science*, *29*(4), pp.419-427.

Ducharme, R., Williams, K., Kapadia, P., Dowden, J., Steen, B. and Glowacki, M., 1994. The laser welding of thin metal sheets: an integrated keyhole and weld pool model with supporting experiments. *Journal of physics D: Applied physics*, *27*(8), pp.1619.

Eesley, G.L., 1983. Observation of nonequilibrium electron heating in copper. *Physical review letters*, *51*(23), pp.2140.

El-Batahgy, A. and DebRoy, T., 2014.Nd-YAG laser beam and GTA welding of Ti-6Al-4V alloy. *International Journal of Engineering Technology Research*, *2*, pp.43-50.

El Kadiri, H., Bienvenu, Y., Solanki, K., Horstemeyer, M.F. and Wang, P.T., 2006. Creep and tensile behaviors of Fe–Cr–Al foils and laser microwelds at high temperature. *Materials Science and Engineering: A*, *421*(1), pp.168-181.

Elias, C.N., Lima, J.H.C., Valiev, R. and Meyers, M.A., 2008.Biomedical applications of titanium and its alloys.*Journal of The Minerals, Metals & Materials Society*, *60*(3), pp.46-49.

Elmer, J.W., Palmer, T.A., Babu, S.S., Zhang, W. and DebRoy, T., 2004. Phase transformation dynamics during welding of Ti–6Al–4V. *Journal of Applied Physics*, *95*(12), pp.8327-8339.

Faller, K. and Froes, F.S., 2001. The use of titanium in family automobiles: Current trends. *The Journal of The Minerals, Metals & Materials Society*, *53*(4), pp.27-28.

Fan, Y., Cheng, P., Yao, Y.L., Yang, Z. Egland, K., 2005. Effect of phase transformations on laser forming of Ti–6Al–4V alloy. *Journal of Applied Physics*, *98*(1), p.013518.

Fraser, F.W., 1982. Laser welding of titanium alloy, advanced processing method for titanium, Ed.: F. Dennis, *Conference Proceeding of the Metallurgical Society of AIME*, Warrendale, PA, pp. 175–187.

Frewin, M.R. and Scott, D.A., 1999. Finite element model of pulsed laser welding.*Welding Journal*, *78*, pp.15-s.

Fujimoto, J.G., Liu, J.M., Ippen, E.P. and Bloembergen, N., 1984. Femtosecond laser interaction with metallic tungsten and nonequilibrium electron and lattice temperatures. *Physical Review Letters*, *53*(19), pp.1837.

Gao, X.L., Zhang, L.J., Liu, J. and Zhang, J.X., 2013. A comparative study of pulsed Nd: YAG laser welding and TIG welding of thin Ti6Al4V titanium alloy plate. *Materials Science and Engineering: A*, *559*, pp.14-21.

Gao, X.L., Zhang, L.J., Liu, J. and Zhang, J.X., 2014. Effects of weld cross-section profiles and microstructure on properties of pulsed Nd: YAG laser welding of Ti6Al4V sheet. *The International Journal of Advanced Manufacturing Technology*, *72*(5-8), pp.895-903.

Geem, Z.W., Tseng, C.L. and Williams, J.C., 2009. Harmony search algorithms for water and environmental systems. In *Music-Inspired Harmony Search Algorithm* (pp. 113-127). Springer Berlin Heidelberg.

Georgiev, D.G., Sultana, T., Mian, A., Auner, G., Herfurth, H., Witte, R. and Newaz, G., 2005. Laser fabrication and characterization of sub-millimeter joints between polyimide and Ti-coated borosilicate glass. *Journal of Materials Science*, *40*(21), pp.5641-5647.

Ghorbel, E., Casalino, G. and Abed, S., 2009. Laser diode transmission welding of polypropylene: Geometrical and microstructure characterisation of weld. *Materials & Design*, *30*(7), pp.2745-2751.

Gianola, D.S. and Eberl, C., 2009. Micro-and nanoscale tensile testing of materials. *Journal of Material Research and Technology*, *61*(3), pp.24-35.

Goldak, J.A. Akhlaghi, M., 2005. Computational Welding Mechanics, first ed.Springer Science & Business Media.

Goldak, J., Chakravarti, A. and Bibby, M., 1984.A new finite element model for welding heat sources.*Metallurgical transactions B*, *15*(2), pp.299-305.

Grewell, D. and Benatar, A., 2003. Modeling heat flow for a moving heat source to describe scan micro-laser welding. In *ANTEC 2003 Conference Proceedings* (pp. 1045-1050).

Guo, K.W., 2009. A review of micro/nano welding and its future developments. *Recent patents on Nanotechnology*, *3*(1), pp.53-60.

Ishida, T., 1987. Interfacial phenomena of plasma arc welding of mild steel and aluminium. *Journal of materials science*, *22*(3), pp.1061-1066.

Ismail, S., Idris, M., Okamoto, Y., Okada, A. and Uno, Y., 2011. Experimental investigation on micro-welding of thin stainless steel sheet by fiber laser. *American Journal of Engineering and Applied Sciences*, *4*(3), pp.314-320.

Haberstroh, E. and Luetzeler, R., 2001. Influence of carbon black pigmentation on the laser beam welding of plastics micro parts. *Journal of Polymer Engineering*, *21*(2-3), pp.119-130.

Hallum, D.L. and Baeslack, W.A., 1990. Nature of grain refinement in titanium alloy welds by microcooler inoculation. *Welding Journal*, *69*(9), pp.326s-336s.

He, X., DebRoy, T. and Fuerschbach, P.W., 2004. Composition change of stainless steel during microjoining with short laser pulse. *Journal of Applied Physics*, *96*(8), pp.4547-4555.

He, X., Elmer, J.W. and DebRoy, T., 2005. Heat transfer and fluid flow in laser microwelding. *Journal of Applied Physics*, *97*(8), p.084909.

Hilton, P., Blackburn, J. and Chong, P., 2007, November. Welding of Ti-6Al-4V with fibre delivered laser beams. In *Proceedings of ICALEO* (pp. 887-895).

Ho, C.Y., Wen, M.Y. and Ma, C., 2010, March. Computer simulation for laser welding of thermoplastic polymers. In *Computer Engineering and Applications (ICCEA), 2010 Second International Conference on* (Vol. 1, pp. 362-364). IEEE.

Hu, A., Zhou, Y. and Duley, W.W., 2011. Femtosecond laser-induced nanowelding: fundamentals and applications. S*ignificance*, *9*, pp.10.

Huang, H., Wang, J., Li, L. and Ma, N., 2016. Prediction of laser welding induced deformation in thin sheets by efficient numerical modeling. *Journal of Materials Processing Technology*, *227*, pp.117-128.

Hughes, T.J., 1977. Unconditionally stable algorithms for nonlinear heat conduction. *Computer methods in applied mechanics and engineering*, *10*(2), pp.135-139.

Jaidi, J. and Dutta, P., 2013. Three-dimensional turbulent weld pool convection in gas metal arc welding process. *Science and Technology of Welding & Joining. 9(5)*, pp.407-414.

Jiang, Y., Xu, B., Lu, Y., Xiang, Y., Liu, C. and Xia, D., 2008. Application prospects of plasma welding within remanufacturing engineering. In *World congress on maintenance, Beijing* (p. 2).

Joseph, D.D. and Preziosi, L., 1989. Heat waves. *Reviews of Modern Physics*, *61*(1), p.41-73.

Josserand, E., Jullien, J.F., Nelias, D., Boitout, F. and Deloison, D., 2007. Numerical simulation of welding-induced distortions taking into account industrial clamping conditions. *Mathematical Modeling of weld phenomena*, *8*, pp.1105-1124.

Kabir, A.S.H., 2013. *Nd: YAG Laser Welding of Ti-6Al-4V Alloy*. Concordia University.

Kabir, A.S.H., Cao, X., Medraj, M., Wanjara, P., Cuddy, J. and Birur, A., 2010, October. Effect of welding speed and defocusing distance on the quality of laser welded Ti–6Al–4V. In *Proceedings of the Materials Science and Technology (MS&T) 2010 Conference, Houston, TX* (pp. 2787-2797).

Kaplan, A., 1994. A model of deep penetration laser welding based on calculation of the keyhole profile. *Journal of Physics D: Applied Physics*, *27*(9), p.1805.

Karimzadeh, F., Salehi, M., Saatchi, A. and Meratian, M., 2005.Effect of microplasma arc welding process parameters on grain growth and porosity distribution of thin sheet Ti6Al4V alloy weldment. *Materials and Manufacturing Processes*, *20*(2), pp.205-219.

Karimzadeh, F., Ebnonnasir, A. and Foroughi, A., 2006.Artificial neural network modeling for evaluating of epitaxial growth of Ti6Al4V weldment. *Materials Science and Engineering: A*, *432*(1), pp.184-190.

Kashaev, N., Ventzke, V., Fomichev, V., Fomin, F. and Riekehr, S., 2016. Effect of Nd: YAG laser beam welding on weld morphology and mechanical properties of Ti–6Al–4V butt joints and T-joints. *Optics and Lasers in Engineering*, *86*, pp.172-180.

Kawahito, Y., Kito, M. and Katayama, S., 2007. Adaptive Gap Control in Butt Welding with a Pulsed YAG Laser. *TRANSACTIONS-JWRI*, *36*(2), p.5.

Keanini, R.G., 1993. Simulation of weld pool flow and capillary interface shapes associated with the plasma arc welding process. *Finite Elements in Analysis and Design*, *15*(1), pp.83-92.

Keshava Murthy, K., Sundaresan, S., 1998. Phase transformations in a welded near- titanium alloy as a function of weld cooling rate and post-weld heat treatment conditions. 33, pp.817-826.

Kennish, Y.C., Shercliff, H.R. and McGrath, G.C., 2002, May. Heat flow model for laser welding of polymers. In Proceedings of the 60th Annual Technical Conference of the Society of Plastics Engineers (ANTEC 2002) (pp. 1132-1136). Society of Plastics Engineers.

Khurram, A. and Shehzad, K., 2012. FE Simulation of Welding Distortion and Residual Stresses in Butt Joint Using Inherent Strain. *International Journal of Applied Physics and Mathematics*, *2*(6), pp.405.

Khorram, A., Yazdi, M.S., Ghoreishi, M. and Moradi, M., 2010.Using ANN approach to investigate the weld geometry of Ti 6Al 4V titanium alloy. *International Journal of Engineering and Technology*, *2*(5), pp.491.

Kihara, H. and Masubuchi, K., 1954. Studies on the shrinkage and residual welding stress of constrained fundamental joint. *Reports of Transportation Technical Research Iinstitute*, (7).

Kim, B.C., Kim, T.H., Kim, K.B., Kim, J.S. and Lee, H.Y., 2002. Investigation on the effect of laser pulse shape during Nd: YAG laser microwelding of thin Al sheet by numerical simulation. *Metallurgical and Materials Transactions A*, *33*(5), pp.1449-1459.

Kleine, K.F., Fox, W.J. and Watkins, K.G., 2004, October.Micro welding with pulsed single mode fiber lasers.In *Proceedings of the 23rd International Congress on Applications of Lasers & Electro-Optics (ICALEO)* (pp. 4-7).

Klimpel, A. and Lisiecki, A., 2007. Laser welding of butt joints of austenitic stainless steel AISI 321. *Journal of Achievements in Materials and Manufacturing Engineering*, *25*(1), pp.63-66.

Kohandehghan, A.R. and Serajzadeh, S., 2011. Arc welding induced residual stress in butt-joints of thin plates under constraints. *Journal of Manufacturing Processes*, *13*(2), pp.96-103.

Kong, F., Ma, J. and Kovacevic, R., 2011. Numerical and experimental study of thermally induced residual stress in the hybrid laser–GMA welding process. *Journal of Materials Processing Technology*, *211*(6), pp.1102-1111.

Kou, S., 2003. Welding metallurgy. *New York*.

Krasnoperov, M.Y., Pieters, R.R.G.M. and Richardson, I.M., 2004. Weld pool geometry during keyhole laser welding of thin steel sheets. *Science and Technology of Welding and Joining*, *9*(6), pp.501-506.

Kritskiy, A., 2009. Laser welding of nylon tubes to plates using conical mirrors, MSc thesis, Queen's University.

Lathabai, S., Jarvis, B.L. and Barton, K.J., 2001. Comparison of keyhole and conventional gas tungsten arc welds in commercially pure titanium. *Materials Science and Engineering: A*, *299*(1), pp.81-93.

Lee, C.H. and Chang, K.H., 2009. Finite element simulation of the residual stresses in high strength carbon steel butt weld incorporating solid-state phase transformation. *Computational Materials Science*, *46*(4), pp.1014-1022.

Lee, K.S. and Geem, Z.W., 2005. A new meta-heuristic algorithm for continuous engineering optimization: harmony search theory and practice. *Computer Methods in Applied Mechanics and Engineering*, *194*(36), pp.3902-3933.

Lee, D. and Kannatey-Asibu, E., 2008. Numerical analysis on the feasibility of laser microwelding of metals by femtosecond laser pulses using ABAQUS. *Journal of Manufacturing Science and Engineering*, *130*(6), p.061014.

Lee, R.S. and Lin, H.C., 1998. Process design based on the deformation mechanism for the non-isothermal forging of Ti–6Al–4V alloy. *Journal of Materials Processing Technology*, *79*(1), pp.224-235.

Liang, W., Sone, S., Tejima, M., Serizawa, H. and Murakawa, H., 2004. Measurement of Inherent Deformations in Typical Weld Joints Using Inverse Analysis (Part 1): Inherent Deformation of Bead on Welding (Mechanics, Strength & Structural Design). Transactions of JWRI, *33*, pp.45–51.

Liang, W., Deng, D. and Murakawa, H., 2005.Measurement of Inherent Deformations in Typical Weld Joints Using Inverse Analysis (Part 2).Transactions of JWRI, *34*(1), pp.113–123.

Liang, W., Deng, D., Sone, S. and Murakawa, H., 2005. Prediction of welding distortion by elastic finite element analysis using inherent deformation estimated through inverse analysis. *Welding in the World*, *49*(11-12), pp.30-39.

Lindgren, L.E., 2007. Computational welding mechnaics, First Ed. Addison-Woodhead Publication Ltd, Cambridge, England.

Lisiecki, A., 2012. Welding of titanium alloy by different types of lasers. *Archives of Materials Science and Engineering*, *58*(2), pp.209-218.

Li, Y., Feng, Y.H., Zhang, X.X. and Wu, C.S., 2013. An improved simulation of heat transfer and fluid flow in plasma arc welding with modified heat source model. *International Journal of Thermal Sciences*, *64*, pp.93-104.

Liu, H., Nakata, K., Yamamoto, N. and Liao, J., 2012. Microstructural characteristics and mechanical properties in laser beam welds of Ti6Al4V alloy. *Journal of Materials Science*, *47*(3), pp.1460-1470.

Liu, J., Staron, P., Riekehr, S., Stark, A., Schell, N., Huber, N., Schreyer, A., Müller, M. and Kashaev, N., 2015.In situ study of phase transformations during laser-beam welding of a TiAl alloy for grain refinement and mechanical property optimization. *Intermetallics*, *62*, pp.27-35.

Liu, J., Watanabe, I., Yoshida, K. and Atsuta, M., 2002. Joint strength of laser-welded titanium. *Dental materials*, *18*(2), pp.143-148.

Long, H., Gery, D., Carlier, A. and Maropoulos, P.G., 2009. Prediction of welding distortion in butt joint of thin plates. *Materials & Design*, *30*(10), pp.4126-4135.

Luo, W., 2002. Effect of micro-plasma arc melting on the corrosion resistance of a 0Cr19Ni9 stainless steel SAW joint. *Materials Letters*, *55*(5), pp.290-295.

Luo, C. and Lin, L., 2002. The application of nanosecond-pulsed laser welding technology in MEMS packaging with a shadow mask. *Sensors and Actuators A: Physical*, *97*, pp.398-404.

Mackerle, J., 2002. Finite element analysis and simulation of welding-an addendum: a bibliography (1996-2001). *Modelling and Simulation in Materials Science and Engineering*, *10*(3), p.295.

Mackwood, A.P. and Crafer, R.C., 2005. Thermal modelling of laser welding and related processes: a literature review. *Optics & Laser Technology*, *37*(2), pp.99-115.

Mahdavi, M., Fesanghary, M. and Damangir, E., 2007. An improved harmony search algorithm for solving optimization problems. *Applied Mathematics and Computation*, *188*(2), pp.1567-1579.

Majumdar, B., Galun, R., Weisheit, A. and Mordike, B.L., 1997. Formation of a crack-free joint between Ti alloyand Al alloy by using a high-power CO2 laser. *Journal of Materials Science*, *32*(23), pp.6191-6200.

Mahmood, T., Mian, A., Amin, M.R., Auner, G., Witte, R., Herfurth, H. and Newaz, G., 2007. Finite element modeling of transmission laser microjoining process. *Journal of Materials Processing Technology*, *186*(1), pp.37-44.

Marimuthu, S., Eghlio, R.M., Pinkerton, A.J. and Li, L., 2013. Coupled computational fluid dynamic and finite element multiphase modeling of laser weld bead geometry formation and joint strengths. *Journal of Manufacturing Science and Engineering*, *135*(1), p.011004.

Mastrocinque, E., Corrado, G., Caiazzo, F., Pasquino, N. and Sergi, V., 2012. Effect of defocusing on Bead-on-Plate of Ti6Al4V by Yb: YAG disk laser. *In Advanced Materials Research* (Vol. 383, pp. 6258-6264). Trans Tech Publications.

Masubuchi, K., 1953. Buckling type deformation of thin plate due to welding. In *Proceedings of the 3rd Japan National Congress for Applied Mechanics* (pp. 107-111).

Mayboudi, L.S., Birk, A.M., Zak, G. and Bates, P.J., 2006, January. Thermal Imaging Studies and 3-D Thermal Finite Element Modeling of Laser Transmission Welding of a Lap-Joint. In *ASME 2006 International Mechanical Engineering Congress and Exposition* (pp. 423-432). American Society of Mechanical Engineers.

Mayboudi, L., Birk, A.M., Zak, G. and Bates, P.J., 2007. A 3-D thermal model of laser transmission contour welding for a lap joint. In *ANTEC-CONFERENCE PROCEEDINGS*- (Vol. 5, p. 2796).

Mayboudi, L.S., Birk, A.M., Zak, G. and Bates, P.J., 2007. Laser transmission welding of a lap-joint: Thermal imaging observations and three–dimensional finite element modeling. *Journal of Heat Transfer*, *129*(9), pp.1177-1186.

McDill, J.M.J., Oddy, A.S., Goldak, J.A. and Bennison, S., 1990. Finite element analysis of weld distortion in carbon and stainless steels. *The Journal of Strain Analysis for Engineering Design*, *25*(1), pp.51-53.

McKelliget, J.W., 1990. Numerical computation of coupled heat transfer, fluid flow, and electromagnetism: the inductively coupled plasma torch. *Advanced Computational Methods in Heat Transfer: Phase change and combustion stimulation*, *3*, p.309.

McLay, R. and Carey, G.F., 1989. Coupled heat transfer and viscous flow, and magnetic effects in weld pool analysis. *International Journal for Numerical Methods in Fluids*, *9*(6), pp.713-730.

Mehdi, B., Badji, R., Ji, V., Allili, B., Bradai, D., Deschaux-Beaume, F. and Soulié, F., 2016. Microstructure and residual stresses in Ti-6Al-4V alloy pulsed and unpulsed TIG welds. *Journal of Materials Processing Technology*, *231*, pp.441-448.

Mazumder, J. and Steen, W.M., 1980. Heat transfer model for CW laser material processing. *Journal of Applied Physics*, *51*(2), pp.941-947.

Marya, S.K., 1996. Effect of minor chemistry elements on GTA weld fusion zone characteristics of a commercial grade titanium. *Scriptamaterialia*, *34*(11), pp.1741-1745.

Masubuchi, K., 1953. Buckling type deformation of thin plate due to welding.In *Proceedings of the 3rd Japan National Congress for Applied Mechanics* (pp. 107-111).

Mian, A., Newaz, G., Vendra, L., Rahman, N., Georgiev, D.G., Auner, G., Witte, R. and Herfurth, H., 2005. Laser bonded microjoints between titanium and polyimide for applications in medical implants. *Journal of Materials Science: Materials in Medicine*, *16*(3), pp.229-237.

Michaleris, P. ed., 2011. *Minimization of welding distortion and buckling: modelling and implementation*. Elsevier.

Mills, K.C., 2002. *Recommended values of thermophysical properties for selected commercial alloys*. Woodhead Publishing.

Mishra, S. and DebRoy, T., 2005. A heat-transfer and fluid-flow-based model to obtain a specific weld geometry using various combinations of welding variables. *Journal of Applied Physics*, *98*(4), p.044902.

Mollicone, P., Camilleri, D. and Gray, T., 2008. Procedural influences on non-linear distortions in welded thin-plate fabrication. *Thin-walled Structures*, *46*(7), pp.1021-1034.

Monfared, A.H., 2012. Numerical simulation of welding distortion in thin plates. *Journal of Engineering Physics and Thermophysics*, *85*(1), pp.187-194.

Mueller, R., 1994. A model for predicting keyhole and fusion zone depths in blind keyhole welding. In *Laser Materials Processing* (Vol. 2500, p. 509).

Mueller, S., Stiles, E. and Dienemann, R., 2006. Study of porosity formation during laser welding of Ti6Al4V. In *Proceedings of 25th International Congress on Applications of Lasers and Electro-Optics ICALEO 2006* (pp. 133-138).

Murugan, S., Rai, S.K., Kumar, P.V., Jayakumar, T. and Raj, B., 2001. Temperature distribution and residual stresses due to multipass welding in type 304 stainless steel and low carbon steel weld pads. *International Journal of Pressure Vessels and Piping*, *78*(4), pp.307-317.

Mys, I. and Schmidt, M., 2006, February. Laser micro welding of copper and aluminum. *In Lasers and Applications in Science and Engineering* (pp. 610703-610703). International Society for Optics and Photonics.

Naeem M., 2008.Microwelding performance comparison between a low power (125w) pulsed Nd:YAG laser and a low power (100-200W) single mode fiber laser. *Proceedings of the 3rd Pacific International Conference on Application of Lasers and Optics*. Beijing, China.

Nélias, D., Jullien, J.F. and Deloison, D., 2010. Experimental investigation and finite element simulation of laser beam welding induced residual stresses and distortions in thin sheets of AA 6056-T4. *Materials Science and Engineering: A*, *527*(12), pp.3025-3039.

Neto, O.D. and Lima, C.A.S., 1994. Nonlinear three-dimensional temperature profiles in pulsed laser heated solids. *Journal of Physics D: Applied Physics*, *27*(9), p.1795.

Newaz, G., Mian, A., Sultana, T., Mahmood, T., Georgiev, D.G., Auner, G., Witte, R. and Herfurth, H., 2006. A comparison between glass/polyimide and titanium/polyimide microjoint performances in cerebrospinal fluid. *Journal of Biomedical Materials Research Part A*, *79*(1), pp.159-165.

Nguyen, N.T., Ohta, A., Matsuoka, K., Suzuki, N. and Maeda, Y., 1999. Analytical solutions for transient temperature of semi-infinite body subjected to 3-D moving heat sources. *Welding Journal*, *78*, pp.265-s.

Nichols, K.G., 1969. Review of laser microwelding and micromachining. *Electrical Engineers, Proceedings of the Institution of*, *116*(12), pp.2093-2100.

Nomoto, T., Terasaki, T. and Maeda, K., 1997.Study of parameters controlling weld buckling. *Transaction of the Japan Society of Mechanical Engineering, Series A*, *63*(609), pp.591-596.

Nordin, M.C., Edwards, G.R. and Olson, D.L., 1987. The influence of yttrium microadditions on titanium weld metal cracking susceptibility and grain morphology. *Welding Journal, Research Supplement*, *66*.

Norris, J.T., Roach, R., Fuerschbach, P.W. and Bernal, J.E., 2005, March. Thin Plate Gap Bridging Study for Nd: YAG Pulsed Laser Lap Welds. *In Proceedings of the 7th International Conference on Trends in Welding Research* (pp. 155-160).

O'Brien, R.W., 2007. *Predicting weld distortion in the design of automotive components* (Doctoral dissertation, Durham University).

Oddy, A.S., Goldak, J.A. and McDill, J.M.J., 1990. Numerical analysis of transformation plasticity in 3D finite element analysis of welds. *European journal of mechanics. A. Solids*, *9*(3), pp.253-263.

Oden, J.T., Kikuchi, N. and Song, Y.J., 1982. Penalty-finite element methods for the analysis of Stokesian flows. *Computer Methods in Applied Mechanics and Engineering*, *31*(3), pp.297-329.

Otani, T., 2006. Titanium Welding Technology. *SHINNITTETSU GIHO*, *385*, pp.81.

Quintino, L., Costa, A., Miranda, R., Yapp, D., Kumar, V. and Kong, C.J., 2007. Welding with high power fiber lasers–a preliminary study. *Materials & Design*, *28*(4), pp.1231-1237.

Owen, R.A., Preston, R.V., Withers, P.J., Shercliff, H.R. and Webster, P.J., 2003. Neutron and synchrotron measurements of residual strain in TIG welded aluminium alloy 2024. *Materials Science and Engineering: A*, *346*(1), pp.159-167.

Park, M.J., Yang, H.N., Jang, D.Y., Kim, J.S. and Jin, T.E., 2004. Residual stress measurement on welded specimen by neutron diffraction.*Journal of Materials Processing Technology*, *155*, pp.1171-1177.

Patankar, S.V. and Spalding, D.B., 1972. A calculation procedure for heat, mass and momentum transfer in three-dimensional parabolic flows. *International journal of heat and mass transfer*, *15*(10), pp.1787-1806.

Pattee, F.M., 1975. *Buckling distortion of thin aluminum plates during welding* (Doctoral dissertation, Massachusetts Institute of Technology).

Peters, M., Kumpfert, J., Ward, C.H. and Leyens, C., 2003. Titanium alloys for aerospace applications. *Advanced engineering materials*, *5*(6), pp.419-427.

Poorhaydari, K., Patchett, B.M. and Ivey, D.G., 2005. Estimation of cooling rate in the welding of plates with intermediate thickness, *Welding Journal*, *84*, pp. 149-155.

Potente, H. and Fiegler, G., 2004. Laser transmission welding of thermoplastics: Modelling of flows and temperature profils. In *ANTEC. conference proceedings* (Vol. 1, pp. 1193-1199). Society of Plastics Engineers.

Potente, H., Fiegler, G., Haferkamp, H., Fargas, M., Von Busse, A. and Bunte, J., 2006. An approach to model the melt displacement and temperature profiles during the laser through-transmission welding of thermoplastics. *Polymer Engineering & Science*, *46*(11), pp.1565-1575.

Prabhakaran, R., Kontopoulou, M., Zak, G., Bates, P. and Baylis, B., 2003. *Laser transmission welding of glass reinforced nylon 6* (No. 2003-01-1133). SAE Technical Paper.

Prasad, K.S., Rao, C.S. and Rao, D.N., 2014. Study on Weld Quality Characteristics of Micro Plasma Arc Welded Austenitic Stainless Steels. *Procedia Engineering*, *97*, pp.752-757.

Prasad, K.S., Rao, C.S. and Rao, D.N., 2012a. Effect of pulsed current micro plasma arc welding process parameters on fusion zone grain size and ultimate tensile strength of Inconel 625 sheets. *ActaMetallurgica Sinica (English letters)*, *25*(3), pp.179-189.

Prasad, K.S., Rao, C.S. and Rao, D.N., 2012b. Study on Weld Quality Characteristics of Pulsed Current Micro Plasma Arc Welding of Inconel 625 Sheets. *Journal of Minerals and Materials Characterization and Engineering*, *11*(02), p.133.

Prasad, K.S., Rao, C.S. and Rao, D.N., 2011. A study on weld quality characteristics of pulsed current micro plasma arc welding of SS304L sheets. *International Transaction Journal of Engineering, Management & Applied Sciences & Technologies*, *2*(4), pp.437-446.

Pitscheneder, W., DebRoy, T., Mundra, K. and Ebner, R., 1996. Role of sulfur and processing variables on the temporal evolution of weld pool geometry during multikilowatt laser beam welding of steels: The beneficial effects of sulfur on weld pool size and shape are strongly dependent on controlling convective heat transfer. *Welding Journal*, *75*(3), pp.71-s.

Pitscheneder, W., Ebner, R., Hong, T., DebRoy, T., Mundra, K. and Benes, R., 1997. Experimental and numerical investigation of transport phenomena in conduction mode weld pools. *Numerical Analysis of Weldability*, pp.3-25.

Qiu, T.Q. and Tien, C.L., 1993. Heat transfer mechanisms during short-pulse laser heating of metals. *Journal of Heat Transfer*, *115*(4), pp.835-841.

Qiu, T.Q., Juhasz, T., Suarez, C., Bron, W.E. and Tien, C.L., 1994. Femtosecond laser heating of multi-layer metals—II. Experiments. *International Journal of Heat and Mass Transfer*, *37*(17), pp.2799-2808.

Rai, R., Burgardt, P., Milewski, J.O., Lienert, T.J. and DebRoy, T., 2008.Heat transfer and fluid flow during electron beam welding of 21Cr–6Ni–9Mn steel and Ti–6Al–4V alloy. *Journal of Physics D: Applied Physics*, *42*(2), p.025503.

Rai, R., Elmer, J.W., Palmer, T.A. and DebRoy, T., 2007. Heat transfer and fluid flow during keyhole mode laser welding of tantalum, Ti–6Al–4V, 304L stainless steel and vanadium. *Journal of physics D: Applied physics*, *40*(18), p.5753.

Raja, V.B., Kumar, K.P., Elangovan, K. and Manoharan, N., 2009. Effect of Welding Processes on Microstructure of Ti6Al4V Weldments. T*he International Journal on Design and Manufacturing Technology*, *3*(1), pp.12-18.

Reddy, J.N. and Gartling, D.K., 2010. *The finite element method in heat transfer and fluid dynamics*. CRC press.

Rohde, M., Markert, C. and Pfleging, W., 2010. Laser micro-welding of aluminum alloys: experimental studies and numerical modeling. *The International Journal of Advanced Manufacturing Technology*, *50*(1-4), pp.207-215.

Roy, G., Braid, M. and Shen, G., 2003. Application of ADINA and hole drilling method to residual stress determination in weldments. *Computers & structures*, *81*(8), pp.929-935.

Rosenthal, D., 1941. Mathematical theory of heat distribution during welding and cutting. *Welding journal*, *20*(5), pp.220s-234s.

Russek, U.A., Palmen, A., Staub, H., Pöhler, J., Wenzlau, C., Otto, G., Poggel, M., Koeppe, A. and Kind, H., 2003, July. Laser beam welding of thermoplastics. In *High-Power Lasers and Applications* (pp. 458-472). International Society for Optics and Photonics.

Russek, U.A., Aden, M., Poehler, J., Palmen, A. and Staub, H., 2004. Laser beam welding of thermoplastics parameter influence on weld seam quality-experiments and modeling.

Sánchez-Tovar, R., Montañés, M.T., García-Antón, J., Guenbour, A. and Ben-Bachir, A., 2011. Corrosion behaviour of micro-plasma arc welded stainless steels in H 3 PO 4 under flowing conditions at different temperatures. *Corrosion Science*, *53*(4), pp.1237-1246.

Sarkani, S., Tritchkov, V. and Michaelov, G., 2000.An efficient approach for computing residual stresses in welded joints.*Finite Elements in Analysis and Design*, *35*(3), pp.247-268.

Schajer, G.S. ed., 2013. *Practical residual stress measurement methods*. John Wiley & Sons.

Schajer, G.S., 1988. Measurement of non-uniform residual stresses using the hole-drilling method. Part I—Stress calculation procedures. *Journal of Engineering Materials and Technology*, *110*(4), pp.338-343.

Schauer, D.A., Giedt, W.H. and Shintaku, S.M., 1978. *Electron beam welding cavity temperature distributions in pure metals and alloys* (No. UCRL-80723). California Univ., Livermore (USA). Lawrence Livermore Lab..

Schenk, T., Richardson, I.M., Kraska, M. and Ohnimus, S., 2009. A study on the influence of clamping on welding distortion.*Computational Materials Science*, *45*(4), pp.999-1005.

Schulz, J. and Haberstroh, E., 2000. Welding of polymers using a diode laser. In *Proceedings of the 58th Annual Technical Conference (ANTEC 2000), Society of Plastics Engineers, Orlando, FL* (pp. 1196-1201).

Semak, V.V., Knorovsky, G.A. and MacCallum, D.O., 2003. On the possibility of microwelding with laser.*Journal of Physics D: Applied Physics*, *36*(17), pp.2170-74.

Sepokurov, A.S., Sergatskii, G.I. and Alikin, A.P., 1971. Use of microplasma welding in component construction. *Chemical and Petroleum Engineering*, *7*(11), pp.979-980.

Shanmugam, N.S., Buvanashekaran, G. and Sankaranarayanasamy, K., 2012. Some studies on weld bead geometries for laser spot welding process using finite element analysis. *Materials & Design*, *34*, pp.412-426.

Shao, J. and Yan, Y., 2005. Review of techniques for on-line monitoring and inspection of laser welding. In *Journal of Physics: Conference Series* (Vol. 15, No. 1, p. 101). IOP Publishing.

Short, A.B., McCartney, D.G., Webb, P. and Preston, E., 2011. Influence of nozzle orifice diameter in keyhole plasma arc welding. *Science and Technology of Welding and Joining*, *16*(5), pp.446-452.

Short, A., 2009. *Plasma arc welding for fabricating titanium aero-engine structures* (Doctoral dissertation, PhD thesis, University Of Nottingham, Nottingham, UK).

Singh, S., Yadaiah, N., Bag, S. and Pal, S., 2014. Numerical simulation of welding-induced residual stress in fusion welding process using adaptive volumetric heat source. *Proceedings of the Institution of Mechanical Engineers, Part C: Journal of Mechanical Engineering Science*, p.0954406214525601.

Song, S.P., Paradowska, A.M. and Dong, P.S., 2014. Investigation of residual stresses distribution in titanium weldments. In *Materials Science Forum*, 777, pp. 171-175.

Sonti, N. and Amateau, M.F., 1989. Finite-element modeling of heat flow in deep-penetration laser welds in aluminum alloys. *Numerical heat transfer*, *16*(3), pp.351-370.

Spina, R., Tricarico, L., Basile, G. and Sibillano, T., 2007.Thermo-mechanical modeling of laser welding of AA5083 sheets.*Journal of materials processing technology*, *191*(1), pp.215-219.

Squillace, A., Prisco, U., Ciliberto, S. and Astarita, A., 2012. Effect of welding parameters on morphology and mechanical properties of Ti–6Al–4V laser beam welded butt joints. *Journal of Materials Processing Technology*, *212*(2), pp.427-436.

Sudnik, W., Radaj, D. and Erofeew, W., 1996. Computerized simulation of laser beam welding, modelling and verification. *Journal of Physics D: Applied Physics*, *29*(11), pp.2811.

Sun, J., Liu, X., Tong, Y. and Deng, D., 2014.A comparative study on welding temperature fields, residual stress distributions and deformations induced by laser beam welding and CO_2 gas arc welding. *Materials & Design*, *63*, pp.519-530.

Sun, W., Mohammed, M.B., Xu, L., Hyde, T.H., McCartney, D.G. and Leen, S.B., 2014. Process modelling and optimization of keyhole plasma arc welding of thin Ti-6Al-4V. *The Journal of Strain Analysis for Engineering Design*, *49*(6), pp.410-420.

Sun, Z., Pan, D. and Zhang, W., 2002, April. Correlation between welding parameters and microstructures in TIG, plasma and laser welded Ti-6 Al-4 V alloy. *6 th International Conference: Trends in Welding Research* (pp. 760-767).

Syahroni, N. and Hidayat, M.I.P., 2012. *3D Finite Element Simulation of T-Joint Fillet Weld: Effect of Various Welding Sequences on the Residual Stresses and Distortions*. InTech.

Taha, Z.A., Roy, G.G., Hajim, K.I. and Manna, I., 2009. Mathematical modeling of laser-assisted transmission lap welding of polymers. *Scripta Materialia*, *60*(8), pp.663-666.

Tam, S.C., Lindgren, L.E. and Yang, L.J., 1989. Computer simulation of temperature fields in mechanised plasma-arc welding. *Journal of Mechanical Working Technology*, *19*(1), pp.23-33.

Tamaki, T., Watanabe, W. and Itoh, K., 2006.Laser micro-welding of transparent materials by a localized heat accumulation effect using a femtosecond fiber laser at 1558 nm. *Optics Express*, *14*(22), pp.10460-10468.

Taylor, G.A., Hughes, M., Strusevich, N. and Pericleous, K., 2002. Finite volume methods applied to the computational modelling of welding phenomena. *Applied Mathematical Modelling*, *26*(2), pp.311-322.

Teng, T.L. and Lin, C.C., 1998. Effect of welding conditions on residual stresses due to butt welds. *International Journal of Pressure Vessels and Piping*, *75*(12), pp.857-864.

Terasaki, T., Maeda, K., Murakawa, H. and Nomoto, T., 1998. Critical conditions of plate buckling generated by welding. *Transaction of the Japan Society of Mechanical Engineering, Series A*, *64*(625), pp.2239-2244.

Thomas, G., Ramachandra, V., Nair, M.J., Nagarajan, K.V. and Vasudevan, R., 1992. Effect of preweld and postweld heat treatment on the properties of GTA welds in Ti-6Al-4V sheet. *Welding journal*, *71*(1), pp.15s-20s.

Tian, L., Luo, Y., Wang, Y. and Wu, X., 2014. Prediction of transverse and angular distortions of gas tungsten arc bead-on-plate welding using artificial neural network. *Materials & Design*, *54*, pp.458-472.

Trivedi, A., Bag, S. and De, A., 2013. Three-dimensional transient heat conduction and thermomechanical analysis for laser spot welding using adaptive heat source. *Science and Technology of Welding & Joining*, *12*(1), pp. 24-31.

Tsay, L.W. and Tsay, C.Y., 1997. The effect of microstructures on the fatigue crack growth in Ti 6Al 4V laser welds. *International Journal of Fatigue*, *19*(10), pp.713-720.

Tsai, C.L., Park, S.C. and Cheng, W.T., 1999. Welding distortion of a thin-plate panel structure. *Welding Journal*, *78*, pp.156-s.

Tseng, K.H., Hsieh, S.T. and Tseng, C.C., 2013. Effect of process parameters of micro-plasma arc welding on morphology and quality in stainless steel edge joint welds. *Science and Technology of Welding & Joining*, *8(6)*, pp.423-430.

Tzeng, Y.F., 2000. Parametric analysis of the pulsed Nd: YAG laser seam-welding process. *Journal of Materials Processing Technology*, *102*(1), pp.40-47.

Tsirkas, S.A., Papanikos, P. and Kermanidis, T., 2003. Numerical simulation of the laser welding process in butt-joint specimens. *Journal of Materials Processing Technology*, *134*(1), pp.59-69.

Tzou, D.Y., 1995. Experimental support for the lagging behavior in heat propagation. *Journal of Thermophysics and Heat Transfer*, *9*(4), pp.686-693.

Tzou, D.Y. 1998. Macro-to Microscale Heat Transfer. The lagging behaviour. Series in Chemical and Mechanical Engineering. *Journal of Non Equilibrium Thermodynamics*, *23*(2), pp.192-193.

Tzou, D.Y. and Chiu, K.S., 2001. Temperature-dependent thermal lagging in ultrafast laser heating. *International Journal of Heat and Mass Transfer*, *44*(9), pp.1725-1734.

Ueda, Y., Murakawa, H. and Ma, N., 2007. Computational approach to welding deformation and residual stress. *Tokyo: Sanpo Publication*.

Utsumi, A., Ooie, T., Yano, T. and Katsumura, M., 2007. Direct bonding of glass and metal using short pulsed laser. *JLMN-J Laser Micro/Nanoengineering*, *2*(2), pp.133-6.

Van de Ven, J.D. and Erdman, A.G., 2007a. Bridging gaps in laser transmission welding of thermoplastics. *Journal of Manufacturing Science and Engineering*, *129*(6), pp.1011-1018.

Van de Ven, J.D. and Erdman, A.G., 2007b. Laser transmission welding of thermoplastics—Part I: Temperature and pressure modeling. *Journal of Manufacturing Science and Engineering*, *129*(5), pp.849-858.

Veiga, C., Davim, J.P. and Loureiro, A.J.R., 2012. Properties and applications of titanium alloys: a brief review. *Reviews on Advance Material Science*, *32*(2), pp.133-148.

Ventrella, V.A., Berretta, J.R. and De Rossi, W., 2010. Pulsed Nd: YAG laser seam welding of AISI 316L stainless steel thin foils. *Journal of Materials Processing Technology*, *210*(14), pp.1838-1843.

Vernotte, P., 1958. La veritable equation de la chaleur. *Comptes Rendus Hebdomadaires des Seances de l Academie des Sciences*, *247*(23), pp.2103-2105.

Voropai, N.M., Shcherbak, V.V. and Grigor'ev, A.A., 1971. Pulsed microplasma welding of thin aluminum gaskets. *Chemical and Petroleum Engineering*, *7*(11), pp.977-978.

Wang, Y. and Chen, Q., 2002. On-line quality monitoring in plasma-arc welding. *Journal of Materials Processing Technology*, *120*(1), pp.270-274.

Wang, M., Jiang, M.L., Wei, Q. and Gu, K.F., 2011. Technique of Laser-TIG Hybrid T-Shape Joint Welding of Titanium Alloy. In *Advanced Materials Research* (Vol. 291, pp. 841-847). Trans Tech Publications.

Wang, X., Li, P., Xu, Z., Song, X. and Liu, H., 2010. Laser transmission joint between PET and titanium for biomedical application. *Journal of Materials Processing Technology*, *210*(13), pp.1767-1771.

Wang, R., Rashed, S., Serizawa, H., Murakawa, H. and Zhang, J., 2008.Numerical and experimental investigations on welding deformation. *Transaction of JWRI*, *37*(1), pp. 79-90.

Wang, J., Rashed, S. and Murakawa, H., 2014. Mechanism investigation of welding induced buckling using inherent deformation method. *Thin-Walled Structures*, *80*, pp.103-119.

Wang, S.H., Wei, M.D. and Tsay, L.W., 2003. Tensile properties of LBW welds in Ti–6Al–4V alloy at evaluated temperatures below 450 C. *Materials Letters*, *57*(12), pp.1815-1823.

Wang, S. and Wu, X., 2012. Investigation on the microstructure and mechanical properties of Ti–6Al–4V alloy joints with electron beam welding. *Materials & Design*, *36*, pp.663-670.

Wang, H.G., Wu, C.S. and Zhang, M.X., 2005. Finite element method analysis of temperature field in keyhole plasma arc welding. *Transactions-China Welding Institution*, *26*(7), p.49.

Wang, H.G., Wu, C.S. and Zhang, M.X., 2005. Finite element method analysis of temperature field in keyhole plasma arc welding. Transactions of the China Welding Institution, *26*(7), p.49.

Watanabe, M. and Satoh, K., 1957. On the type of distortion in various welded joints: shrinkage distortion in welded joint (Report 5). *Journal of Japan Welding Society*, *26*(6), pp.399-405.

Watanabe, M. and Satoh, K., 1958. Fundamental study on buckling of thin steel plate due to bead-welding. *Journal of the Japan Welding Society*, *27*(6), pp.313-320.

Withers, P.J. and Bhadeshia, H.K.D.H., 2001.Residual stress. Part 1–measurement techniques. *Materials Science and Technology*, *17*(4), pp.355-365.

Wong, J., Froba, M., Elmer, J.W., Waide, P.A. and Larson, E.M., 1997. In-situ phase mapping and transformation study in fusion welds. *Journal of Materials Science*, *32*(6), pp.1493-1500.

Wu, K.C., 1981. Correlation of properties and microstructure in welded Ti-6Al-6V-2Sn. *Welding Journal*, *60*(11), pp.219s-226s.Wu, C.S., Hu, Q.X. and Gao, J.Q., 2009. An adaptive heat source model for finite-element analysis of keyhole plasma arc welding. *Computational Materials Science*, *46*(1), pp.167-172.

Wu, C.S., Wang, H.G. and Zhang, Y.M., 2006. A new heat source model for keyhole plasma arc welding in FEM analysis of the temperature profile. *Welding Journal*, *85*(12), pp.284.

Wu, C.S., Wang, L., Ren, W.J. and Zhang, X.Y., 2014. Plasma arc welding: Process, sensing, control and modeling. *Journal of Manufacturing Processes*, *16*(1), pp.74-85.

Xu, P.Q., Yao, S., He, J.P., Ma, C.W. and Ren, J.W., 2009.Numerical analysis for effect of process parameters of low-current micro-PAW on constricted arc. *The International Journal of Advanced Manufacturing Technology*, *44*(3-4), pp.255-264.

Yang, H.Q., 1991. Non-Fourier effect on heat conduction during welding. *International Journal of Heat and Mass Transfer*, *34*(11), pp.2921-2924.

Yang, Y.P., Brust, F.W., Dong, P., Zhang, J. and Cao, Z., 2000. Modeling procedure development of buckling distortion in thin plate welding. *ASME-PUBLICATIONS-PVP*, *410*(1), pp.103-108.

Yang, J., Sun, S., Brandt, M. and Yan, W., 2010. Experimental investigation and 3D finite element prediction of the heat affected zone during laser assisted machining of Ti6Al4V alloy. *Journal of Materials Processing Technology*, *210*(15), pp.2215-2222.

Ye, X.H. and Chen, X., 2002.Three-dimensional modelling of heat transfer and fluid flow in laser full-penetration welding.*Journal of Physics D: Applied Physics*, *35*(10), p.1049.

Yilbas, B.S., Arif, A.F.M. and Aleem, B.A., 2010. Laser welding of low carbon steel and thermal stress analysis. *Optics & Laser Technology*, *42*(5), pp.760-768.

Yovanovich, M.M., 2005. Four decades of research on thermal contact, gap, and joint resistance in microelectronics. *IEEE transactions on components and packaging technologies*, *28*(2), pp.182-206.

Yunlian, Q., Ju, D., Quan, H. and Liying, Z., 2000. Electron beam welding, laser beam welding and gas tungsten arc welding of titanium sheet. *Materials Science and Engineering: A*, *280*(1), pp.177-181.

Yoshioka, S., Miyazaki, T., Kimura, T., Komatsu, A. and Kinoshita, N., 1993. Thin-plate welding by a high-power density small diameter plasma arc. *CIRP Annals-Manufacturing Technology*, *42*(1), pp.215-218.

Zain-ul-Abdein, M., Nelias, D., Jullien, J.F. and Deloison, D., 2009.Prediction of laser beam welding-induced distortions and residual stresses by numerical simulation for aeronautic application.*Journal of Materials Processing Technology*, *209*(6), pp.2907-2917.

Zeng, P., Mei, L. and Lei, L.P., 2013. Thermal-Elastic-Plastic Finite Element Analysis for Laser Welding Deformation of Thin Plate. In *Advanced Materials Research* Vol. 650, pp. 572-576). Trans Tech Publications.

Zhang, Y.M. and Li, P.J., 2001. Modified active control of metal transfer and pulsed GMAW of titanium.*Welding Journal(USA)*, *80*(2), p.54.

Zhang, D.K. and Niu, J.T., 2009. Application of artificial neural network modeling to plasma arc welding of aluminum alloys. *Acta Metallurgica Sinica (English letters)*, *13*(1), pp.194-200.

Zhao, H., White, D.R. and DebRoy, T., 1999. Current issues and problems in laser welding of automotive aluminium alloys. *International Materials Reviews*, *44*(6), pp.238-266.

Zhong, X.M., Murakawa, H. and Ueda, Y., 1995. Buckling Behavior of Plates under Idealized Inherent Strain (Mechanics, Strength & Structural Design).

Zhou Y., 2008. Microjoining and nanojoining,Woodhead Publishing Limited,CRC Press, Cambridge, England.

Zhou, W. and Chew, K.G., 2003.Effect of welding on impact toughness of butt-joints in a titanium alloy. *Materials Science and Engineering: A*, *347*(1), pp.180-185.

Zhu, X.K. and Chao, Y.J., 2004. Numerical simulation of transient temperature and residual stresses in friction stir welding of 304L stainless steel. *Journal of materials processing technology*, *146*(2), pp.263-272.

Zienkiewicz, O.C., Taylor, R.L. and Too, J.M., 1971. Reduced integration technique in general analysis of plates and shells. *International Journal for Numerical Methods in Engineering*, *3*(2), pp.275-290.

Zou, D., Gao, L., Li, S. and Wu, J., 2011. An effective global harmony search algorithm for reliability problems. *Expert Systems with Applications*, *38*(4), pp.4642-4648.

Bibliography

1. J. A. Goldak and M. Akhalaghi: Computational Weld Mechanics, Springer Science and Business Media, Inc. New York, First edition, 2005.
2. U. S. Dixit: Finite Element Methods For Engineers Cengage Learning India, First edition, 2009.
3. Y. Zhou: Microjoining and nanojoining,Woodhead Publishing Limited,CRC Press, Cambridge, England, 2008.
4. M.J. Donachie: Titanium: a technical guide. ASM international, 2000.
5. S. Kou. Welding metallurgy. New York, 2003.
6. J.N., Reddy and D.K. Gartling: The finite element method in heat transfer and fluid dynamics. CRC press, 2000.
7. J.F. Lancaster: The physics of welding. Physics in technology, 1984.

List of publications

Referred Journal

1. M. Baruah and S. Bag: Influence of pulsation in thermo-mechanical analysis on laser microwelding of Ti6Al4V alloy, ***Optics and Laser Technology***, 90, 40 - 51, 2017.
2. M. Baruah and S. Bag: Microstructural influence on mechanical properties in plasma microwelding of Ti6Al4V alloy, ***Journal of Materials Engineering and Performance***, 25(11), 4718 - 4728, 2016.
3. M. Baruah and S. Bag: Influence of heat input in microwelding of titanium alloy by micro plasma arc, ***Journal of Materials Processing Technology***, 231, 100 - 112, 2016.
4. S. Kumar, S. Bag and **M. Baruah**: Finite element model for femtosecond laser pulse heating using dual phase lag effect, ***Journal of Laser Applications***, 28(3), 032008:1 - 14, 2016.
5. M. Baruah and S. Bag: Numerical modelling of heat transfer and fluid flow in laser microwelding, ***International Journal of Mechatronics and Manufacturing Systems***, 6(13), 310 - 334, 2013.
6. M. Baruah and S. Bag: Characteristic difference of thermo-mechanical behavior in plasma microwelding of steels (**under review**).
7. M. Baruah, S. Kumar and S. Bag: Probing phase lag effect in ultra-short pulse laser heating of nano-film (**under review**).
8. T. Saikia, **M. Baruah** and S. Bag: Micro-plasma arc welding of maraging steel (**under review**)

Referred Conference

9. M. Baruah and S. Bag: Effect of peak power on joint characteristics of pulse laser welding of 0.5 mm Ti6Al4V sheets, AIMTDR 2016, 16^{th} - 18^{th} December, 2016, Pune.
10. M. Baruah and S. Bag: Analysis of temperature of microplasma arc welding of 0.5 mm Ti6Al4V sheets, 1rst International Conference on Materials, Manufacturing and Design Engineering (iCMMD 2016), 20 – 21^{st} December, 2016, Vidyavihar, Raigad, Maharashtra, India.
11. M. Baruah and S. Bag: Influence of gap conductance in thermal analysis of laser transmission welding, Recent Trend in Mechanical Engineering, 21^{st} – 22^{nd} October, 2016, Institute of Engineers (India, Assam State Centre), Guwahati.
12. M. Baruah and S. Bag: Micro-plasma Arc Welding of Ti6Al4V sheets, 3^{rd} International Conference on Lasers and Plasma Application in Materials Science (LAPAMS), 15^{th} – 17^{th} January, 2015, Kolkata.
13. R. Majumdera, **M. Baruah** and S. Bag: Influence of plasma gas flow rate on weld-induced distortions in plasma microwelding of low carbon steel, 30th National Conference of Production Engineers, Agartala, Tripura July 18-19, 2015

14. M. Baruah and S. Bag: Investigation on micro plasma welding of titanium alloy, Advancements in Welding, Cutting & Surfacing Technologies for Improved Economy, Reliability & Sustainable Environment, IIW International Congress 2014, 9 – 11th April, 2014, New Delhi.

15. M. Baruah and S. Bag: Experimental and Numerical Investigation of Micro Plasma Welded Ti-6Al-4V sheets, International Symposium on Aspects of Mechanical Engineering & Technology for Industry (AMETI 2014), 6 – 8th December, 2014, NERIST, Arunachal Pradesh.

16. M. Baruah and S. Bag: A perspective on thermal analysis of laser transmission welding, National Conference on Manufacturing: Vision for Future (MVF 2013), IIT Guwahati, Assam, 12 – 13th October, 2013.

Acknowledgement

This thesis is the result of five years of work at IIT Guwahati whereby I have been accompanied and supported by many people. First and foremost I would like to express my special appreciation and sincere gratitude to my supervisor, Dr. Swarup Bag. He has been a tremendous mentor for me. I would like to thank him for encouraging my research and for allowing me to grow as a research scientist. I owe him lots of gratitude for his guidance.

I would like to convey my deep regards to my doctoral committee chairman, Professor P. S. Robi for his valuable support and suggestions from time to time to carry out my research work. His guidance and help in my research has really been invaluable. I would also like to thank my doctoral committee members Dr. Pankaj Biswas and Dr. Nanda Kishore for their insightful comments and encouragement which incented me to widen my research from various perspectives. I am also grateful to the head of the Mechanical Engineering Department Professor A. K. Das for providing excellent facilities and environment to conduct research work. I would also like to thank Professor Debabrata Chakraborty and Professor Rita Sarmah for their advice on both researches as well as on my career.

I would also like to thanks Mr. Saiffuddin Ahmed, Mr. Jiten Basumatary, Mr. Sanjib Sarma, for their support in carrying out the research work in the laboratories. I am very much thankful to workshop superintendent Mr. N.K. Das, and workshop technicians Mr. Dilip Chetri, Mr. Mrinal Sarma, Mr. Manoj Kr. Baishya for providing their expertise knowledge that greatly assisted the experimental work and their willingness to help me in fabricating the experimental setup precisely and accurately. I also gratefully acknowledge the kind support and assistance from Advanced Manufacturing Center, CSIR-CMERI, Durgapur, West Bengal, India to carry out my research work.

I am extremely grateful to my Father for his love, prayers, care and support for educating and preparing me for my future. Also I express my thanks to my sister, brother and brother in law for their support and valuable prayers. My special thanks go to my friends for their mental support and keen interest shown to complete this thesis successfully.

And finally I would thank the Almighty God for his showers of blessings throughout my life and during period of research work to complete the research successfully.

January 2017

Mayuri Baruah

IIT Guwahati